

200 / 200507

CCMS-87-04  
VPI-E-87-3

111-24

69602-CR

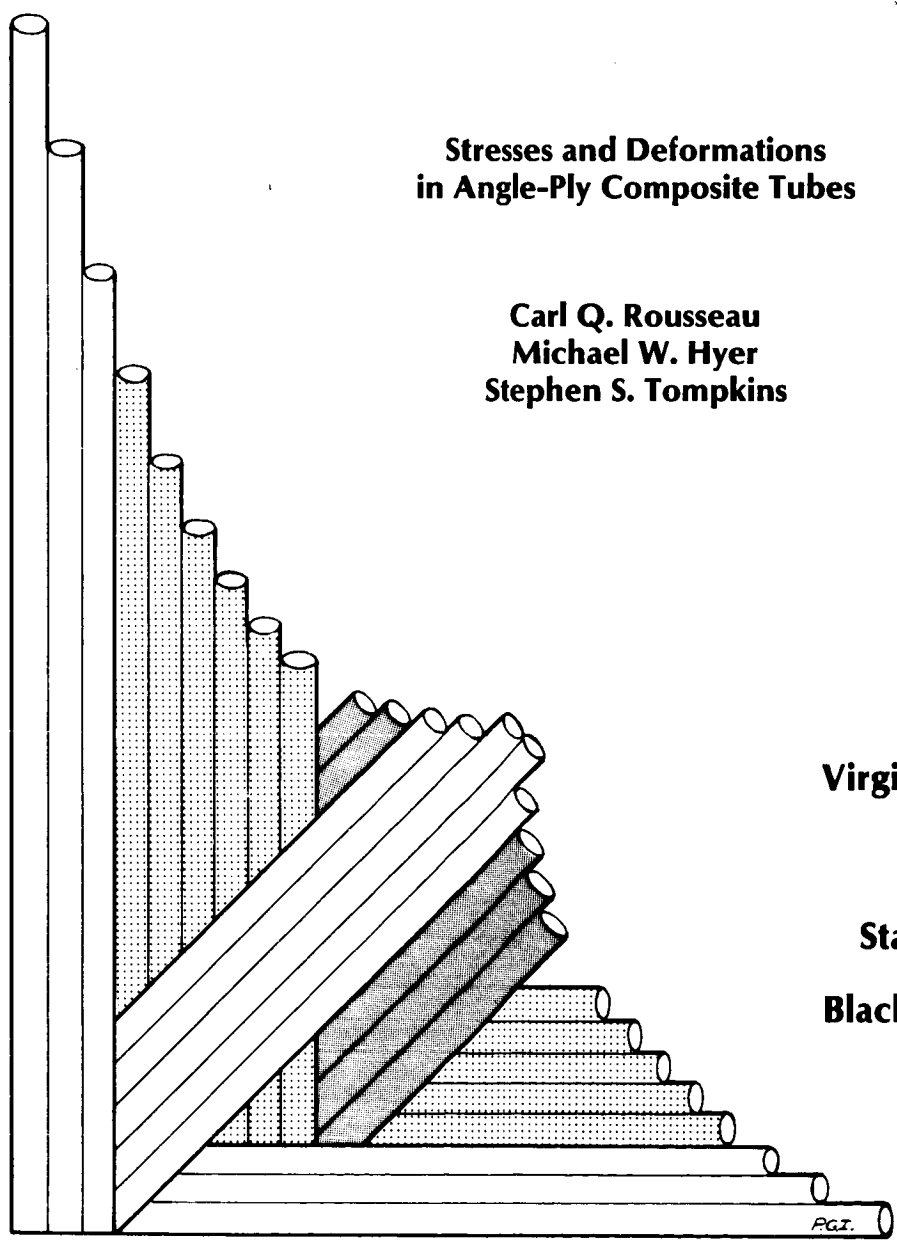
P. 211

VIRGINIA TECH  
**CENTER FOR  
COMPOSITE MATERIALS  
AND STRUCTURES**

V 1610169

**Stresses and Deformations  
in Angle-Ply Composite Tubes**

**Carl Q. Rousseau  
Michael W. Hyer  
Stephen S. Tompkins**



**Virginia Polytechnic  
Institute  
and  
State University  
Blacksburg, Virginia  
24061**

(NASA-TM-89365) STRESSES AND DEFORMATIONS  
IN ANGLE-PLY COMPOSITE TUBES (Virginia  
Polytechnic Inst. and State Univ.) 244 p  
Avail: NTIS HC A11/MF A01 CSCL 11D

N87-26148

Unclas  
0069602

G3/24

College of Engineering  
Virginia Polytechnic Institute and State University  
Blacksburg, Virginia 24061

March 1987

CCMS-87-04  
VPI-E-87-3

***Stresses and Deformations***  
***in Angle-Ply Composite Tubes***

Carl Q. Rousseau<sup>1</sup>  
Michael W. Hyer<sup>2</sup>  
Stephen S. Tompkins<sup>3</sup>

Dept of Engineering Science & Mechanics

Interim Report 62  
The NASA-Virginia Tech Composites Program  
NASA Grant NAG-1-343

Prepared for:

Applied Materials Branch  
National Aeronautics and Space Administration  
Langley Research Center  
Hampton, VA 23665

---

<sup>1</sup> Graduate Student, Dept of Engineering Science & Mechanics, VPI & SU

<sup>2</sup> Professor, Dept of Mechanical Engineering, University of Maryland

<sup>3</sup> NASA Langley Research Center, Applied Materials Branch

## Stresses and Deformations in Angle-Ply Composite Tubes

### **ABSTRACT**

The objective of this study was to investigate, both experimentally and analytically, the stresses and deformations in angle-ply composite tubes subjected to axisymmetric thermal loading. For the theoretical portion a generalized plane strain elasticity analysis was developed. The analysis included mechanical and thermal loading, and temperature-dependent material properties. Using the elasticity analysis and a temperature range of 116 K to 450 K, stress levels were found to be high for the specific designs considered, compared to material failure levels. In addition, the use of temperature-dependent material properties was found to have a significant effect on the predicted stresses and deformations. The elasticity analysis was also used to study the effect of including a thin metallic coating on a graphite-epoxy tube. The stresses in the coatings were found to be quite high, exceeding the yield stress of aluminum. An important finding in the analytical studies was the fact that even tubes with a balanced-symmetric lamination sequence exhibited shear deformation, or twist. The radial location of an off-axis ply was found to influence its effect on the overall torsional tube response. For the experimental portion an apparatus was developed to measure torsional and axial response in the temperature range of 140 K to 360 K. Eighteen specimens were tested, combining three material systems, eight lamination sequences, and three off-axis ply orientation angles. For the twist response, agreement between analysis and experiment was found to be good. The axial response of the tubes tested was found to be greater than predicted by a factor of three. As a result of the study it is recommended that the thermally-induced axial deformations be investigated further, both experimentally and analytically.

## **Acknowledgements**

The authors would like to express their thanks for support of this work from the NASA-Virginia Tech Composites Program through NASA Grant NAG 1-343, and the faculty and students of the program.

# Table of Contents

<b>1.0 Introduction</b>	<b>1</b>
1.1 Introduction	1
1.2 Summary of Specific Study Objectives	3
1.3 Overview of the Thesis	4
<b>2.0 Theoretical Formulation</b>	<b>6</b>
2.1 Literature Review	6
2.2 Derivation of Elasticity Solution	8
2.3 General Form of Solution for a Single Layer	10
2.4 Axisymmetric Solution	14
2.5 Boundary Conditions	20
2.6 Temperature-Dependent Material Properties	24
<b>3.0 Analytical Predictions</b>	<b>27</b>
3.1 Temperature Dependency of Material Properties	29
3.2 Tube Response	33
3.3 Comparison of Coated and Uncoated Tubes	59

3.4 Stresses in the Coatings .....	74
<b>4.0 Experimental Apparatus .....</b>	<b>78</b>
4.1 Design .....	78
4.2 Data Acquisition .....	89
4.3 Test Specimens .....	95
4.4 Procedures .....	97
4.5 Operational Considerations .....	100
4.6 Error Analysis .....	103
<b>5.0 Experimental Results .....</b>	<b>106</b>
5.1 Twist Response .....	108
5.2 Axial Strain Response .....	137
5.3 Hoop Strain Response .....	164
5.4 Summary of Experimental Results .....	176
<b>6.0 Conclusions and Recommendations .....</b>	<b>177</b>
<b>References .....</b>	<b>182</b>
<b>Appendix A. Material Properties .....</b>	<b>184</b>
<b>Appendix B. Test Specimen Information .....</b>	<b>199</b>
<b>Appendix C. Program Listings .....</b>	<b>204</b>
<b>Vita .....</b>	<b>231</b>

## List of Illustrations

Figure 1. Coordinate System and Nomenclature .....	9
Figure 2. Fiber-Direction Compliances vs. Temperature .....	31
Figure 3. Transverse Direction and Shear Compliances vs. Temperature .....	32
Figure 4. Thermally-Induced Strain vs. Temperature .....	34
Figure 5. Axial Strain vs. Temperature .....	35
Figure 6. Twist Response vs. Temperature, Design 1 .....	36
Figure 7. Twist Response vs. Temperature, Design 2 .....	37
Figure 8. Fiber-Direction Stress vs. Temperature .....	38
Figure 9. Transverse Stress vs. Temperature .....	39
Figure 10. Radial Stress vs. Temperature .....	40
Figure 11. Shear Stress vs. Temperature .....	41
Figure 12. Fiber-Direction Stress Variation Through-The-Thickness .....	46
Figure 13. Transverse Stress Variation Through-The-Thickness .....	47
Figure 14. Radial Stress Variation Through-The-Thickness .....	48
Figure 15. Shear Stress Variation Through-The-Thickness .....	49
Figure 16. Axial Strain vs. Ply Orientation Angle, $\phi$ .....	51
Figure 17. Shear Strain vs. Ply Orientation Angle, $\phi$ , Design 1 .....	52
Figure 18. Shear Strain vs. Ply Orientation Angle, $\phi$ , Design 2 .....	53
Figure 19. Fiber-Direction Stress vs. Ply Orientation Angle, $\phi$ .....	54
Figure 20. Transverse Stress vs. Ply Orientation Angle, $\phi$ .....	55
Figure 21. Radial Stress vs. Ply Orientation Angle, $\phi$ .....	56

Figure 22. Shear Stress vs. Ply Orientation Angle, $\phi$ .....	57
Figure 23. Fiber-Direction Stress Variation Through-The-Thickness, with Coatings .....	62
Figure 24. Transverse Stress Variation Through-The-Thickness, with Coatings .....	63
Figure 25. Radial Stress Variation Through-The-Thickness, with Coatings .....	64
Figure 26. Shear Stress Variation Through-The-Thickness, with Coatings .....	65
Figure 27. Axial Strain vs. Ply Orientation Angle, $\phi$ , with Coatings .....	67
Figure 28. Shear Strain vs. Ply Orientation Angle, $\phi$ , Design 1, with Coatings .....	68
Figure 29. Shear Strain vs. Ply Orientation Angle, $\phi$ , Design 2, with Coatings .....	69
Figure 30. Fiber-Direction Stress vs. Ply Orientation Angle, $\phi$ , with Coatings .....	70
Figure 31. Transverse Stress vs. Ply Orientation Angle, $\phi$ , with Coatings .....	71
Figure 32. Radial Stress vs. Ply Orientation Angle, $\phi$ , with Coatings .....	72
Figure 33. Shear Stress vs. Ply Orientation Angle, $\phi$ , with Coatings .....	73
Figure 34. Maximum Principal Stress vs. Ply Orientation Angle, $\phi$ .....	75
Figure 35. Maximum Shear Stress vs. Ply Orientation Angle, $\phi$ .....	76
Figure 36. Configuration of Experimental Apparatus .....	79
Figure 37. Radial Arm Fitting Mounted on Specimen .....	83
Figure 38. Test Specimen Coordinate System .....	84
Figure 39. Thermocouple and Strain Gage Locations .....	87
Figure 40. Experimental Apparatus - Door Removed .....	90
Figure 41. Experimental Apparatus - Test Configuration .....	91
Figure 42. Schematic of Data Acquisition System .....	92
Figure 43. Typical Time-Temperature Response .....	99
Figure 44. Axial Temperature Distribution Model .....	102
Figure 45. Shear Strain vs. Temperature, Specimen 11 .....	109
Figure 46. Shear Strain vs. Temperature, Specimen 12 .....	111
Figure 47. Shear Strain vs. Temperature, Specimen 13 .....	112
Figure 48. Shear Strain vs. Temperature, Specimen 14 .....	113
Figure 49. Shear Strain vs. Temperature, Specimen 15 .....	115

Figure 50. Shear Strain vs. Temperature, Specimen 16 .....	116
Figure 51. Shear Strain vs. Temperature, Specimen 17 .....	117
Figure 52. Shear Strain vs. Temperature, Specimen 18 .....	118
Figure 53. Shear Strain vs. Temperature, Specimen 21 .....	119
Figure 54. Shear Strain vs. Temperature, Specimen 22 .....	120
Figure 55. Shear Strain vs. Temperature, Specimen 24 .....	121
Figure 56. Shear Strain vs. Temperature, Specimen 25 .....	122
Figure 57. Shear Strain vs. Temperature, Specimen 28 .....	123
Figure 58. Shear Strain vs. Temperature, Specimen 31 .....	125
Figure 59. Shear Strain vs. Temperature, Specimen 32 .....	126
Figure 60. Shear Strain vs. Temperature, Specimen 34 .....	127
Figure 61. Shear Strain vs. Temperature, Specimen 35 .....	128
Figure 62. Shear Strain vs. Temperature, Specimen 38 .....	129
Figure 63. Shear Strain vs. Ply Orientation Angle (Specimens 11 - 14) .....	130
Figure 64. Shear Strain vs. Ply Orientation Angle (Specimens 15 - 18) .....	131
Figure 65. Shear Strain vs. Ply Orientation Angle (Specimens 21, 22, and 24) .....	132
Figure 66. Shear Strain vs. Ply Orientation Angle (Specimens 25 and 28) .....	133
Figure 67. Shear Strain vs. Ply Orientation Angle (Specimens 31, 32, and 34) .....	134
Figure 68. Shear Strain vs. Ply Orientation Angle (Specimens 35 and 38) .....	135
Figure 69. Axial Strain vs. Temperature, Specimen 11 .....	138
Figure 70. Axial Strain vs. Temperature, Specimen 12 .....	139
Figure 71. Axial Strain vs. Temperature, Specimen 13 .....	140
Figure 72. Axial Strain vs. Temperature, Specimen 14 .....	141
Figure 73. Axial Strain vs. Temperature, Specimen 15 .....	142
Figure 74. Axial Strain vs. Temperature, Specimen 16 .....	143
Figure 75. Axial Strain vs. Temperature, Specimen 17 .....	144
Figure 76. Axial Strain vs. Temperature, Specimen 18 .....	145
Figure 77. Axial Strain vs. Temperature, Specimen 21 .....	146

Figure 78. Axial Strain vs. Temperature, Specimen 22	147
Figure 79. Axial Strain vs. Temperature, Specimen 24	148
Figure 80. Axial Strain vs. Temperature, Specimen 25	149
Figure 81. Axial Strain vs. Temperature, Specimen 28	150
Figure 82. Axial Strain vs. Temperature, Specimen 31	151
Figure 83. Axial Strain vs. Temperature, Specimen 32	152
Figure 84. Axial Strain vs. Temperature, Specimen 34	153
Figure 85. Axial Strain vs. Temperature, Specimen 35	154
Figure 86. Axial Strain vs. Temperature, Specimen 38	155
Figure 87. Axial Strain vs. Ply Orientation Angle (Specimens 11 - 14)	156
Figure 88. Axial Strain vs. Ply Orientation Angle (Specimens 15 - 18)	157
Figure 89. Axial Strain vs. Ply Orientation Angle (Specimens 21, 22, and 24)	158
Figure 90. Axial Strain vs. Ply Orientation Angle (Specimens 25 and 28)	159
Figure 91. Axial Strain vs. Ply Orientation Angle (Specimens 31, 32, and 34)	160
Figure 92. Axial Strain vs. Ply Orientation Angle (Specimens 35 and 38)	161
Figure 93. Hoop Strain vs. Temperature, Specimen 11	165
Figure 94. Hoop Strain vs. Temperature, Specimen 12	166
Figure 95. Hoop Strain vs. Temperature, Specimen 13	167
Figure 96. Hoop Strain vs. Temperature, Specimen 14	168
Figure 97. Hoop Strain vs. Temperature, Specimen 15	169
Figure 98. Hoop Strain vs. Temperature, Specimen 16	170
Figure 99. Hoop Strain vs. Temperature, Specimen 17	171
Figure 100. Hoop Strain vs. Temperature, Specimen 18	172
Figure 101. Hoop Strain vs. Temperature, Specimen 35	173
Figure 102. Hoop Strain vs. Ply Orientation Angle (Specimens 11 - 14)	174
Figure 103. Hoop Strain vs. Ply Orientation Angle (Specimens 15 - 18)	175

## List of Tables

Table 1. Tube Designs for Numerical Analysis	28
Table 2. Radial Locations of Stresses Illustrated in Figures	45
Table 3. LVDT Numbering Sequence and Coordinates	85
Table 4. Test Specimen Description	96
Table A.1. General Form of Temperature-Dependent Material Properties	188
Table A.2. Temperature-Independent Material Properties for T300-934	189
Table A.3. Temperature-Independent Material Properties for P75S-ERLX1962A	190
Table A.4. Temperature-Independent Material Properties for T300-ERLX1962A	191
Table A.5. Temperature-Independent Material Properties for AS4-976	192
Table A.6. Temperature-Independent Material Properties for 6061 Aluminum	193
Table A.7. Temperature-Independent Material Properties for Epoxy Adhesive	194
Table A.8. Temperature-Dependent Material Properties for T300-934	195
Table A.9. Temperature-Dependent Material Properties for P75S-ERLX1962A	196
Table A.10. Temperature-Dependent Material Properties for AS4-976	197
Table A.11. Temperature-Dependent Material Properties for 6061 Aluminum	198
Table B.1. Test Specimen Dimensions	201

Table B.2. Test Sequence and Miscellaneous Notes .....	202
Table B.3. Strain Gage Specifications .....	203

# 1.0 Introduction

## 1.1 Introduction

The US/International Space Station is currently planned for initial deployment in the mid 1990's. The backbone of the station will be an erectable truss structure. The structure will be fabricated from tubular elements. Because of the ability to tailor mechanical and thermal expansion properties, tubes fabricated from composite materials are a reasonable choice for the structure. Specifically, because of the low cost when compared to other types of composite materials, and because of the ease of fabrication, graphite-epoxy is a reasonable choice among composite materials. Although space structures typically experience small mechanical forces, they are subjected to severe environmental effects. In low earth orbit a structure must endure a temperature range of 116 K to 366 K. The material in the structure must be able to withstand these temperatures. In addition, some protection from the radiation and free atomic oxygen attachment found in low earth orbit (LEO) must be provided if a polymeric composite material is used. A metallic coating would provide protection against radiation, be a free atomic oxygen barrier, and would reduce, by heat conduction, the temperature gradient that the structure may experience in the space environment.

Current space station design calls for tubular truss elements 50 mm in diameter, and 5 to 7 meters long, made of graphite-epoxy composite material. An important design criteria for these tubes is axial stiffness<sup>1</sup>. Ideally, tubes with all their fibers oriented axially could be used. Unfortunately, such tubes are highly susceptible to crushing and impact damage and therefore, some off-axis fibers are necessary. The off-axis fibers contribute to thermally-induced stresses, particularly when one considers that graphite-epoxy is fabricated at temperatures in the range of 400 - 450 K and may have to operate at 144 K. Therefore, in addition to stiffness as a design parameter, minimizing, or at least accurately controlling thermally-induced stresses is an important factor. This implies that the thermally-induced stresses can be accurately predicted. This study addresses this particular issue, namely, the prediction of thermally-induced stresses. In addition, the deformations of the tube are of interest. The former issue is addressed analytically, while the latter is addressed both analytically and experimentally. An important point addressed in this study is the effect on the predicted stresses of including temperature-dependent material properties in the analysis. Often times thermal analyses are conducted using material properties measured at a specific temperature. The issue immediately arises as to the inaccuracies incurred. Considerable effort is made in this study to compare the stress predictions from an analysis which uses temperature-dependent properties with an analysis which assumes the properties are independent of temperature. Also, since protective coatings may be used in the space station truss structure, the influence of these coatings on tube response is studied.

A second major effort in this study was the result of findings regarding the twist deformation of tubes with layers having the fibers oriented off-axis. As will be seen, even tubes with a standard balanced symmetric wall construction will twist under thermal load. This finding has serious ramifications regarding dimensional stability and, in the presence of repeated heating and cooling (as may be experienced in orbit), thermally-induced fatigue. This predicted twist phenomenon was felt to be so important that it dictated the direction of the remainder of the

study. More analyses were conducted and an experimental apparatus was designed and built which could be used to study the phenomenon in a series of tube designs.

## **1.2 Summary of Specific Study Objectives**

The specific study objectives were:

1. To develop an analytical methodology to study the stresses and deformations in tubes of circular cross-section and which consisted of layers of anisotropic material. The loading was primarily thermal and temperature-dependent material properties were included in the methodology. Only axisymmetric tube responses were considered.
2. To use the analysis to study the effect, on predicted stresses and deformations, of including the temperature dependence of material properties.
3. To use the analysis to study the effect, on the predicted stresses and deformations, of metallic coatings.
4. To develop an experimental apparatus for measuring thermally-induced deformations in uniformly heated and cooled angle-ply composite tubes, particularly the phenomenon of thermally induced twist.
5. To measure the thermally-induced deformations in a series of tubes to validate the findings of the analysis, and to correlate the experimental results with the analytical results.

Objectives 1-3 were met by developing an analysis based on elasticity theory. The analysis was developed from first principles, the inclusion of temperature-dependent properties being relatively straightforward with this approach. An elasticity solution was used, as opposed to a shell-like theory, to account for any through-the-thickness effects that may prevail. As it turned out, one of these prevailing effects was thermally-induced twist. A shell-like approach would not have revealed this phenomenon.

Objectives 4 and 5 required the design and fabrication of a test apparatus. The twist phenomenon was felt to be so fundamental, and for some situations so pronounced, that the apparatus did not have to employ sophisticated thermal equipment or high resolution techniques. Thus, electromechanical transducers and a slightly modified standard environmental chamber were the basis for the design. The specimens used were similar in design to those being considered for use on the space station. The specimens included three types of graphite-epoxy material and eight lamination sequences.

### ***1.3 Overview of the Thesis***

In Ch. 2, the elasticity solution is derived. A rationale for the use of this particular approach and a brief discussion of other methods is presented. The formulation in Ch. 2 includes temperature-dependent and temperature-independent material property cases. The physical assumptions and their influence on the mathematical development are outlined. In Ch. 3, analytical predictions for two generic tube designs are presented. The effect of including temperature-dependent material properties on the predicted stresses and deformations is discussed. Two specific tube designs from these generic designs are used as the basis for further discussions. The maximum stresses within the layers, and overall deformations in the two designs, as a function of temperature, are presented. The further discussion of these

specific designs centers on the through-the-thickness distribution of stresses and the variations, at a given temperature, in stress and strain for various off-axis ply orientation angles. Temperature-dependent and temperature-independent material properties are considered. Finally, the influence of coating the two specific designs with thin layers of aluminum is discussed. Stresses in the coatings, as well as in the tubes, are presented.

The experimental apparatus is explained in Ch. 4. Design rationale and construction details are considered. Details of the data acquisition system are included. Test specimen choice, testing procedures, data reduction, and error analysis are discussed. Finally, apparatus operational problems, and their solutions, are presented.

Chapter 5 presents the experimental results. Results which illustrate the character of the responses of the tubes are presented graphically. A comparison of experimental data and results predicted with the analysis is made. Additionally, the temperature dependency of the material systems used is illustrated.

Finally, Ch. 6 presents conclusions and recommendations for further investigation. Appendices include material properties used, notes on specific tests, and listings of the computer codes that were developed.

## 2.0 Theoretical Formulation

### 2.1 Literature Review

In this investigation, an exact planar elasticity solution is developed to study thermally-induced stresses and deformations in composite tubes. In previous work on the subject of thermal effects in composite tubes, Cohen and Hyer considered various analytical approaches<sup>2-3</sup>. The approaches considered included classical<sup>4</sup>, higher order<sup>5-6</sup>, and modified shell theories<sup>7</sup>, and various planar elasticity solutions<sup>8-10</sup>. For the thermal problem classical shell theories based on Donnell's kinematic assumptions do not consider through-the-thickness thermal effects. These effects can become significant for thick-walled cylinders (radius-to-thickness ratio  $< 10$ ). In addition, with the thermal expansion effects in the radial direction many times larger than thermal expansion effects parallel to the fibers, through-the-thickness deformations must be accounted for. Modified shell theories can account for these through-the-thickness effects; however, they are at least as cumbersome to formulate as an exact elasticity solution. For planar elasticity solutions in the plane transverse to the tube axis, plane stress, plane strain, and generalized plane strain were considered by Cohen and Hyer. Generalized plane strain was found to be the most appropriate. The generalized

solution allows for out-of-plane displacements, i.e., in the tube's axial direction, which makes this solution most desirable for the problem of free thermal expansion of tubes. In addition to the above mentioned approaches, some researchers<sup>11 12</sup> have used flat laminate classical lamination theory (CLT) for the analysis of composite tubes. Classical lamination theory is a plane stress elasticity solution formulated in the plane of the laminate; in tubes, this is the curved surface of the tube wall. While yielding reasonable results for some aspects of the problem, classical lamination theory, by the nature of its formulation, does not correctly model several important aspects of the behavior of anisotropic cylinders, the most important aspect being that the solution neglects the constraining effects of the tubular geometry.

Formulations of generalized plane strain elasticity problems applied to tubes have existed for some time. Lekhnitskii<sup>13</sup> has defined the problem in general terms for a variety of situations. More recently, Pagano formulated the problem of laminated tubes with multiple off-axis orthotropic layers subjected to mechanical loads<sup>14</sup>, and for a single orthotropic layer with a uniform temperature change<sup>15</sup>. Hyer and Cohen<sup>3</sup> considered the problem of a tube made of multiple on-axis orthotropic layers subjected to a uniform temperature change, and Hyer and Cooper<sup>16</sup> included a circumferentially varying thermal load for the same tube. Hyer and Rousseau<sup>17</sup> extended Cohen's work to include layers with off-axis ply orientations. In the following section this formulation will be briefly summarized. Although not used specifically in this investigation, terms for axial and torsional loads, and internal and external pressure will be included in this formulation. In addition, thermal strains will be used in a form compatible with the use of temperature-dependent material properties.

## 2.2 Derivation of Elasticity Solution

Figure 1 shows the coordinate system and nomenclature associated with the layered tube. The inner radius is denoted as  $r_i$ , the outer radius  $r_o$ , and the radii of the interfaces  $r_1, r_2$ , etc. The mean radius is denoted by  $R$ . The axial coordinate is  $x$  and the displacement in that direction is  $u$ . The circumferential coordinate is  $\theta$  and  $v$  denotes circumferential displacement. The radial displacement is  $w$  and  $r$  the radial coordinate. The ply orientation angle is  $\phi$ , and the 1-2-3, or material principal coordinate system, has the 1-axis aligned with the fiber direction, the 2-axis in the lamina plane and perpendicular to the fibers, and the 3-axis in the radial, or  $r$  direction. The usual notation is used to identify the components of stress and strain, i.e.,  $\sigma_r$  is the normal stress in the radial direction,  $\gamma_{x\theta}$  is the engineering shear strain in the  $x$ - $\theta$  plane, etc. The temperature of the tube is spatially uniform and is  $\Delta T$  above some reference temperature. Here, the reference temperature will be the cure temperature of the material and  $\Delta T$  will be negative. The net tensile and torsional loads acting on the tube are denoted by  $F_x$  and  $T_x$  respectively. The internal and external pressures are  $P_i$  and  $P_o$ , and they are assumed to be independent of circumferential location.

The equations governing a single isolated layer will be derived. The solution to the equations will be expressed in terms of unknown constants of integration and the lamina material properties. There will be one such solution for each layer. The constants associated with each layer will be determined by enforcing the applied pressure boundary conditions on the inner and outer surface,  $r_i$  and  $r_o$ , and by enforcing certain interface conditions at  $r_1, r_2$ , etc. In addition, because of the planar nature of the solution, certain integrated cross-sectional conditions will be used in the determination of the constants. The enforcement of all these conditions "ties" the layers together to form a tube.

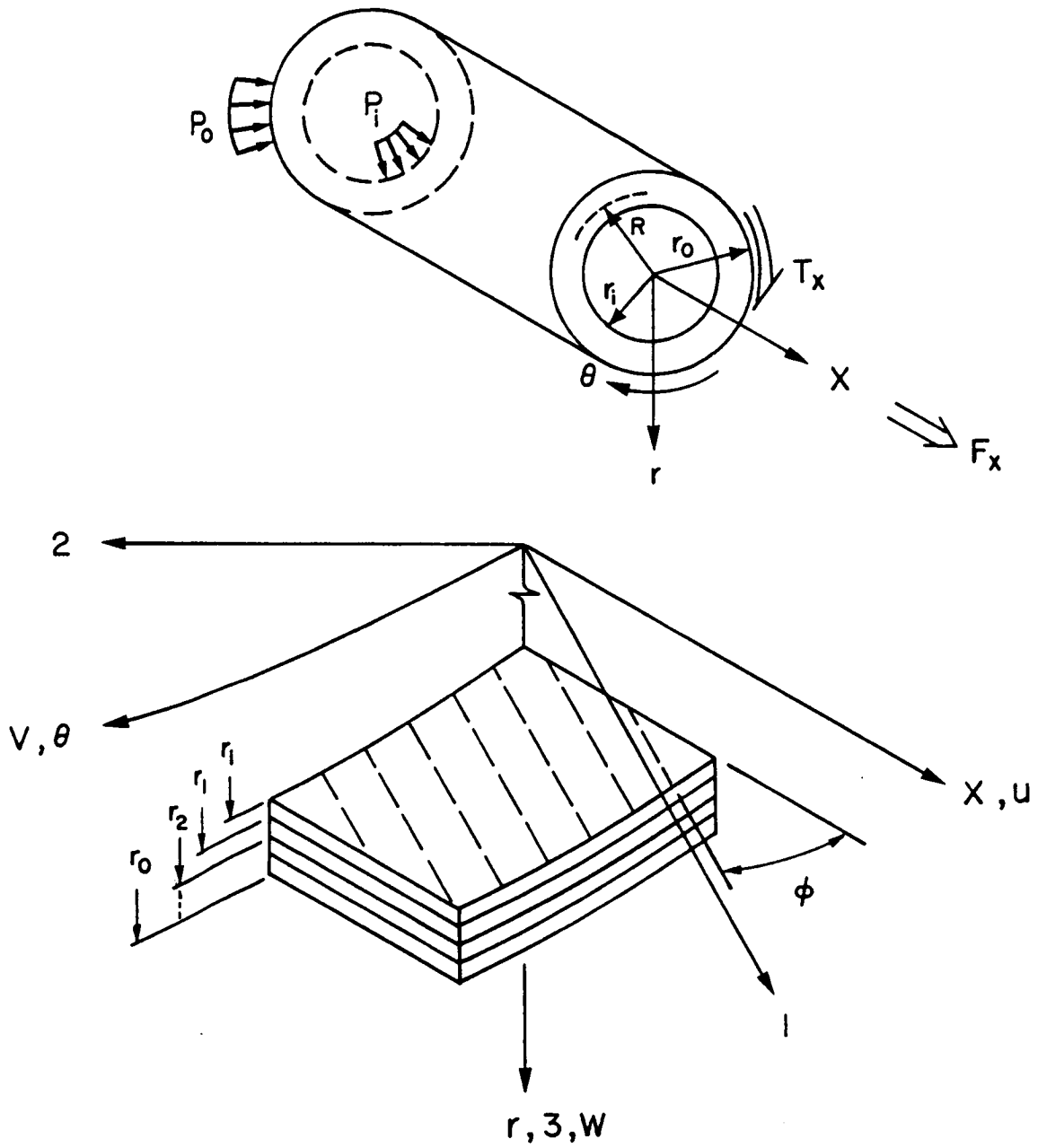


Figure 1. Coordinate System and Nomenclature

## 2.3 General Form of Solution for a Single Layer

In most general elasticity problems, the displacements are a function of  $x$ ,  $\theta$ , and  $r$ . For the tube problem considered here, the axial, circumferential, and radial displacements are given, respectively, by

$$u = u(x, \theta, r) \quad [1.a]$$

$$v = v(x, \theta, r) \quad [1.b]$$

$$w = w(x, \theta, r) \quad [1.c]$$

The strain-displacement relations in polar coordinates are

$$\epsilon_x = \frac{\partial u}{\partial x} \quad [2.a]$$

$$\epsilon_\theta = \frac{1}{r} \left( \frac{\partial v}{\partial \theta} + w \right) \quad [2.b]$$

$$\epsilon_r = \frac{\partial w}{\partial r} \quad [2.c]$$

$$\gamma_{\theta r} = \frac{1}{r} \left( \frac{\partial w}{\partial \theta} - v + r \frac{\partial v}{\partial r} \right) \quad [2.d]$$

$$\gamma_{xr} = \frac{\partial u}{\partial r} + \frac{\partial w}{\partial x} \quad [2.e]$$

$$\gamma_{x\theta} = \frac{\partial v}{\partial x} + \frac{1}{r} \frac{\partial u}{\partial \theta} \quad [2.f]$$

The stress-strain relation, within the 1-2-3 coordinate system, for a lamina with orthotropic material properties is given by

$$\begin{pmatrix} \sigma_1 \\ \sigma_2 \\ \sigma_3 \\ \tau_{23} \\ \tau_{13} \\ \tau_{12} \end{pmatrix} = \begin{bmatrix} C_{11} & C_{12} & C_{13} & 0 & 0 & 0 \\ C_{12} & C_{22} & C_{23} & 0 & 0 & 0 \\ C_{13} & C_{23} & C_{33} & 0 & 0 & 0 \\ 0 & 0 & 0 & C_{44} & 0 & 0 \\ 0 & 0 & 0 & 0 & C_{55} & 0 \\ 0 & 0 & 0 & 0 & 0 & C_{66} \end{bmatrix} \begin{pmatrix} \epsilon_1 - \epsilon_1^T \\ \epsilon_2 - \epsilon_2^T \\ \epsilon_3 - \epsilon_3^T \\ \gamma_{23} \\ \gamma_{13} \\ \gamma_{12} \end{pmatrix} \quad [3]$$

The  $C_{ij}$  are the elastic constants and the  $\epsilon_j^T$  are the thermal deformations of an unconstrained lamina. Most commonly, the  $\epsilon_j^T$  are simply the coefficients of thermal expansion,  $\alpha_j$ , multiplied by the temperature change relative to some reference. This results in the  $\epsilon_j^T$  being linear functions of temperature, i.e.

$$\epsilon_j^T = \alpha_j \Delta T \quad [4]$$

Here, the  $\epsilon_j^T$  will be considered more general, but known, functions of temperature. This reflects the often observed fact that the thermal deformations of an unstrained lamina are generally not linear functions of temperature. In addition, the  $C_{ij}$  will be considered to be temperature-dependent. Published data regarding the variation of engineering properties (i.e.,  $E_1$ ,  $E_2$ ,  $\nu_{12}$ , etc.) with temperature will be used to indirectly determine how the  $C_{ij}$  vary with temperature. More will be said of this shortly.

In the  $x$ - $\theta$ - $r$  system the stress-strain relation transforms to

$$\begin{Bmatrix} \sigma_x \\ \sigma_\theta \\ \sigma_r \\ \tau_{\theta r} \\ \tau_{xr} \\ \tau_{x\theta} \end{Bmatrix} = \begin{bmatrix} \bar{C}_{11} & \bar{C}_{12} & \bar{C}_{13} & 0 & 0 & \bar{C}_{16} \\ \bar{C}_{12} & \bar{C}_{22} & \bar{C}_{23} & 0 & 0 & \bar{C}_{26} \\ \bar{C}_{13} & \bar{C}_{23} & \bar{C}_{33} & 0 & 0 & \bar{C}_{36} \\ 0 & 0 & 0 & \bar{C}_{44} & \bar{C}_{45} & 0 \\ 0 & 0 & 0 & \bar{C}_{45} & \bar{C}_{55} & 0 \\ \bar{C}_{16} & \bar{C}_{26} & \bar{C}_{36} & 0 & 0 & \bar{C}_{66} \end{bmatrix} \begin{Bmatrix} \epsilon_x - \epsilon_x^T \\ \epsilon_\theta - \epsilon_\theta^T \\ \epsilon_r - \epsilon_r^T \\ \gamma_{\theta r} \\ \gamma_{xr} \\ \gamma_{x\theta} - \gamma_{x\theta}^T \end{Bmatrix} \quad [5]$$

The inverse of Equation 3 is

$$\begin{Bmatrix} \epsilon_1 - \epsilon_1^T \\ \epsilon_2 - \epsilon_2^T \\ \epsilon_3 - \epsilon_3^T \\ \gamma_{23} \\ \gamma_{13} \\ \gamma_{12} \end{Bmatrix} = \begin{bmatrix} S_{11} & S_{12} & S_{13} & 0 & 0 & 0 \\ S_{12} & S_{22} & S_{23} & 0 & 0 & 0 \\ S_{13} & S_{23} & S_{33} & 0 & 0 & 0 \\ 0 & 0 & 0 & S_{44} & 0 & 0 \\ 0 & 0 & 0 & 0 & S_{55} & 0 \\ 0 & 0 & 0 & 0 & 0 & S_{66} \end{bmatrix} \begin{Bmatrix} \sigma_1 \\ \sigma_2 \\ \sigma_3 \\ \tau_{23} \\ \tau_{13} \\ \tau_{12} \end{Bmatrix} \quad [6]$$

The  $S_{ij}$  are the compliances of the material and are, of course, the inverse of the  $C_{ij}$ . In the x- $\theta$ -r system the strain-stress relation is

$$\begin{Bmatrix} \epsilon_x - \epsilon_x^T \\ \epsilon_\theta - \epsilon_\theta^T \\ \epsilon_r - \epsilon_r^T \\ \gamma_{\theta r} \\ \gamma_{xr} \\ \gamma_{x\theta} - \gamma_{x\theta}^T \end{Bmatrix} = \begin{bmatrix} \bar{S}_{11} & \bar{S}_{12} & \bar{S}_{13} & 0 & 0 & \bar{S}_{16} \\ \bar{S}_{12} & \bar{S}_{22} & \bar{S}_{23} & 0 & 0 & \bar{S}_{26} \\ \bar{S}_{13} & \bar{S}_{23} & \bar{S}_{33} & 0 & 0 & \bar{S}_{36} \\ 0 & 0 & 0 & \bar{S}_{44} & \bar{S}_{45} & 0 \\ 0 & 0 & 0 & \bar{S}_{45} & \bar{S}_{55} & 0 \\ \bar{S}_{16} & \bar{S}_{26} & \bar{S}_{36} & 0 & 0 & \bar{S}_{66} \end{bmatrix} \begin{Bmatrix} \sigma_x \\ \sigma_\theta \\ \sigma_r \\ \tau_{\theta r} \\ \tau_{xr} \\ \tau_{x\theta} \end{Bmatrix} \quad [7]$$

The relations between the  $\bar{C}_{ij}$  and the  $C_{ij}$ , the  $C_{ij}$  relation to the  $S_{ij}$ , and the  $S_{ij}$  relation to engineering material properties can be found in Cohen, et al. <sup>2</sup>. It should be noted that the material properties for each layer are assumed to be different. From a computational standpoint, known temperature-dependent values of the engineering properties for the material will be used to write the compliances as functions of temperature. At a given temperature, then, the compliances are known and can be inverted to find the values of the  $C_{ij}$ .

The compatibility equations in polar coordinates are

$$\frac{\partial^2 \epsilon_r}{\partial x^2} + \frac{\partial^2 \epsilon_x}{\partial r^2} - \frac{\partial^2 \gamma_{x\theta}}{\partial x \partial r} = 0 \quad [8.a]$$

$$\frac{\partial^2 \epsilon_\theta}{\partial x^2} - \frac{1}{r} \frac{\partial^2 \gamma_{x\theta}}{\partial x \partial \theta} + \frac{1}{r^2} \frac{\partial^2 \epsilon_x}{\partial \theta^2} + \frac{1}{r} \frac{\partial \epsilon_x}{\partial r} - \frac{1}{r} \frac{\partial \gamma_{xr}}{\partial x} = 0 \quad [8.b]$$

$$\frac{\partial^2 \epsilon_r}{\partial \theta^2} - r \frac{\partial \epsilon_r}{\partial r} - \frac{\partial^2 (r \gamma_{\theta r})}{\partial \theta \partial r} + \frac{\partial}{\partial r} \left( r^2 \frac{\partial \epsilon_\theta}{\partial r} \right) = 0 \quad [8.c]$$

$$\frac{\partial^2 \gamma_{\theta r}}{\partial x^2} - r \frac{\partial^2}{\partial x \partial r} \left( \frac{1}{r} \gamma_{x\theta} \right) - \frac{1}{r} \frac{\partial^2 \gamma_{xr}}{\partial x \partial \theta} + 2 \frac{\partial^2}{\partial \theta \partial r} \left( \frac{1}{r} \epsilon_x \right) = 0 \quad [8.d]$$

$$\frac{2}{r} \frac{\partial^2 \epsilon_r}{\partial x^2 \partial \theta} - \frac{\partial^2}{\partial \theta \partial r} \left( \frac{1}{r} \gamma_{xr} \right) + \frac{\partial}{\partial r} \left[ \frac{1}{r} \frac{\partial}{\partial r} (r \gamma_{x\theta}) \right] - \frac{1}{r^2} \frac{\partial^2}{\partial x \partial r} (r^2 \gamma_{\theta r}) = 0 \quad [8.e]$$

$$\begin{aligned} \frac{\partial \gamma_{xr}}{\partial \theta^2} - 2r \frac{\partial \epsilon_r}{\partial x} - \frac{\partial^2}{\partial \theta \partial r} (r \gamma_{x\theta}) \\ + 2r \frac{\partial^2}{\partial x \partial r} (r \epsilon_{\theta}) - \frac{\partial^2}{\partial x \partial \theta} (r \gamma_{\theta r}) = 0 \end{aligned} \quad [8.f]$$

The general form of the equations of equilibrium can be written

$$\frac{\partial \sigma_r}{\partial r} + \frac{1}{r} (\sigma_r - \sigma_{\theta}) + \frac{1}{r} \frac{\partial \tau_{\theta r}}{\partial \theta} + \frac{\partial \tau_{xr}}{\partial x} + R_r = 0 \quad [9.a]$$

$$\frac{\partial \tau_{\theta r}}{\partial r} + \frac{1}{r} \frac{\partial \sigma_{\theta}}{\partial \theta} + \frac{\partial \tau_{x\theta}}{\partial x} + \frac{2}{r} \tau_{\theta r} + R_{\theta} = 0 \quad [9.b]$$

$$\frac{\partial \tau_{xr}}{\partial r} + \frac{1}{r} \frac{\partial \tau_{x\theta}}{\partial \theta} + \frac{\partial \sigma_x}{\partial x} + \frac{1}{r} \tau_{xr} + R_x = 0, \quad [9.c]$$

where  $R_r$ ,  $R_x$ , and  $R_{\theta}$  are the body forces.

## 2.4 Axisymmetric Solution

Since the temperature of the tube is spatially uniform, and the internal and external pressures are independent of  $\theta$ , the problem is axisymmetric. None of the components of displacement depend on the circumferential coordinate, and

$$\frac{\partial}{\partial \theta} ( ) = 0 \quad [10.a]$$

( ) being any stress, strain, or displacement. In addition, in the portion of the tube away from the ends, the stresses and, through Hooke's Law, the strains are assumed to be independent of  $x$ . That is,

$$\frac{\partial}{\partial x}(\text{stress}) = 0, \quad \frac{\partial}{\partial x}(\text{strain}) = 0 \quad [10.b]$$

This is the plane deformation assumption. Finally, away from the ends, the radial displacement is a function only of the radial coordinate. With these assumptions, the displacements in each layer take the form:

$$u = u(x,r) \quad [11.a]$$

$$v = v(x,r) \quad [11.b]$$

$$w = w(r) . \quad [11.c]$$

The strain-displacement relations, eq. 2, then simplify to

$$\epsilon_x = \frac{\partial u}{\partial x} \quad [12.a]$$

$$\epsilon_\theta = \frac{w}{r} \quad [12.b]$$

$$\epsilon_r = \frac{dw}{dr} \quad [12.c]$$

$$\gamma_{\theta r} = \frac{\partial v}{\partial r} - \frac{v}{r} \quad [12.d]$$

$$\gamma_{xr} = \frac{\partial u}{\partial r} \quad [12.e]$$

$$\gamma_{x\theta} = \frac{\partial v}{\partial x} \quad [12.f]$$

Hooke's Law for each layer remains the same as eqs. 3, 5, 6, and 7. Using the simplified strain-displacement relations, eq. 12, the six compatibility equations simplify and three are automatically satisfied. The remaining three are:

$$\frac{d^2 \epsilon_x}{dr^2} = 0 \quad [13.a]$$

$$\frac{1}{r} \frac{d\epsilon_x}{dr} = 0 \quad [13.b]$$

$$\frac{1}{2} \frac{d}{dr} \left[ \frac{1}{r} \frac{d}{dr} (r \gamma_{x\theta}) \right] = 0 \quad [13.c]$$

Integrating eq. 13.a leads to

$$\epsilon_x(r) = Ar + B \quad [14]$$

A and B being constants. Equation 13.b requires A to be zero. Redefining B to be  $\epsilon^\circ$ ,

$$\epsilon_x(r) = \epsilon^\circ \quad [15]$$

and it is seen that the axial strain in a layer is not a function of any of the coordinate variables.

Integrating eq. 13.c yields

$$\gamma_{x\theta} = Cr + D/r \quad [16]$$

in which C and D are constants.

Using eq. 15 and integrating eq. 12.a, the axial displacement can be written

$$u(x,r) = \epsilon^\circ x + f(r), \quad [17]$$

f(r) being an arbitrary function of r.

Using eq. 16 and integrating eq. 12.f yields an expression for circumferential displacement, namely

$$v(x,r) = (Cr + D/r)x + g(r), \quad [18]$$

where  $g(r)$  is an arbitrary function of  $r$ .

The simplified form of the equilibrium equations may be written (for the case of no body forces)

$$\frac{d\sigma_r}{dr} + \frac{\sigma_r - \sigma_\theta}{r} = 0 \quad [19.a]$$

$$\frac{d\tau_{\theta r}}{dr} + \frac{2\tau_{\theta r}}{r} = 0 \quad [19.b]$$

$$\frac{d\tau_{xr}}{dr} + \frac{\tau_{xr}}{r} = 0 \quad [19.c]$$

Integrating eqs. 19.b and c results directly in

$$\tau_{\theta r} = E/(r^2) \quad [20]$$

$$\tau_{xr} = F/r, \quad [21]$$

$E$  and  $F$  being constants.

The arbitrary function  $f(r)$  may now be determined by using eqs. 7, 12, 17, 20, and 21 such that

$$\gamma_{xr} = \frac{\partial u}{\partial r} = \frac{df}{dr} = \bar{S}_{45} \tau_{\theta r} + \bar{S}_{55} \tau_{xr} = \frac{1}{r^2} \bar{S}_{45} E + \frac{1}{r} \bar{S}_{55} F \quad [22]$$

or, integrating eq. 22,

$$f(r) = -\frac{1}{r} \bar{S}_{45} E + \bar{S}_{55} F \ln r + F_1, \quad [23]$$

where the constant of integration,  $F_1$ , represents axial rigid body translation. Similarly  $g(r)$  is determined by

$$\gamma_{\theta r} = \frac{\partial v}{\partial r} - \frac{v}{r} = \frac{dg}{dr} - \frac{g}{r} - \frac{2Dx}{r^2} = \quad [24]$$

$$\bar{S}_{44} \tau_{\theta r} + \bar{S}_{45} \tau_{xr} = \frac{1}{r^2} \bar{S}_{44} E + \frac{1}{r} \bar{S}_{45} F$$

or

$$\frac{dg}{dr} - \frac{g}{r} = \frac{1}{r^2} \bar{S}_{44} E + \frac{1}{r} \bar{S}_{45} F + \frac{2}{r^2} Dx. \quad [25]$$

Since  $g(r)$  is a function of  $r$  only,

$$D = 0. \quad [26]$$

Solving eq. 25 for  $g(r)$  yields

$$g(r) = -\frac{1}{2r} \bar{S}_{44} E - \bar{S}_{45} F + G_1 r, \quad [27]$$

where  $G_1$  represents rigid body rotation about the tube axis. The axial and circumferential displacements may now be written

$$u(x,r) = \varepsilon^0 x - \bar{S}_{45} E \frac{1}{r} + \bar{S}_{55} F \ln r + F_1 \quad [28]$$

$$v(x,r) = \gamma^0 x r - \bar{S}_{44} E \frac{1}{2r} - \bar{S}_{45} F + G_1 r, \quad [29]$$

where the constant,  $C$ , has been redefined as

$$C = \gamma^0. \quad [30]$$

The quantity  $\gamma^0$  has the physical interpretation of radians of twist per unit length of tube.

By writing the stresses in terms of the displacements, the first equilibrium equation leads to a differential equation for the remaining component of displacement,  $w(r)$ , namely

$$\frac{d^2 w}{dr^2} + \frac{1}{r} \frac{dw}{dr} - \frac{\bar{C}_{22}}{\bar{C}_{33}} \frac{1}{r^2} w = \quad [31]$$

$$\frac{1}{\bar{C}_{33}} \left[ \frac{(\bar{C}_{12} - \bar{C}_{13})\varepsilon^0 + \bar{\Sigma}}{r} + (\bar{C}_{26} - 2\bar{C}_{36})\gamma^0 \right].$$

Equation 31 may be solved for  $w(r)$ :

$$w(r) = A_1 r^\lambda + A_2 r^{-\lambda} + \left( \frac{\bar{C}_{12} - \bar{C}_{13}}{\bar{C}_{33} - \bar{C}_{22}} \right) \varepsilon^0 r + \left( \frac{\bar{C}_{26} - 2\bar{C}_{36}}{4\bar{C}_{33} - \bar{C}_{22}} \right) \gamma^0 r^2 \quad [32]$$

$$+ \left( \frac{\bar{\Sigma}}{\bar{C}_{33} - \bar{C}_{22}} \right) r ,$$

where

$$\lambda = \sqrt{\bar{C}_{22}/\bar{C}_{33}} , \quad [33.a]$$

$$\bar{\Sigma} = (\bar{C}_{13} - \bar{C}_{12}) \varepsilon_x^T + (\bar{C}_{23} - \bar{C}_{22}) \varepsilon_\theta^T \quad [33.b]$$

$$+ (\bar{C}_{33} - \bar{C}_{23}) \varepsilon_r^T + (\bar{C}_{36} - \bar{C}_{26}) \gamma_{x\theta}^T ,$$

and  $A_1$  and  $A_2$  are constants. The complete solution is now available for application to either a single-layer problem or to a multiple-layer problem.

## 2.5 Boundary Conditions

For multiple layers, the solutions for  $\tau_{\theta r}(r)$ ,  $\tau_{xr}(r)$ ,  $u(x,r)$ ,  $v(x,r)$ , and  $w(r)$  in eqs. 20, 21, 28, 29, and 32 require a different set of constants for each layer. Because the material constants for each layer can be different, the value of  $\lambda$  will be different for each layer. For the  $k^{\text{th}}$  layer,

$$\tau_{\theta r}^{(k)} = E^{(k)}/r^2 \quad [34]$$

$$\tau_{xr}^{(k)} = F^{(k)}/r \quad [35]$$

$$u^{(k)}(x,r) = \varepsilon^{o(k)} x - \bar{S}_{45}^{(k)} E^{(k)} \frac{1}{r} + \bar{S}_{55}^{(k)} F^{(k)} \ln r + F_1^{(k)} \quad [36]$$

$$v^{(k)}(x,r) = \gamma^{o(k)} xr - \bar{S}_{44}^{(k)} E^{(k)} \frac{1}{2r} - \bar{S}_{45}^{(k)} F^{(k)} + G_1^{(k)} r \quad [37]$$

and

$$w^{(k)}(r) = A_1^{(k)} r^{\lambda^{(k)}} + A_2^{(k)} r^{-\lambda^{(k)}} + \left[ \frac{\bar{C}_{12}^{(k)} - \bar{C}_{13}^{(k)}}{\bar{C}_{33}^{(k)} - \bar{C}_{22}^{(k)}} \right] \varepsilon^{o(k)} r \quad [38]$$

$$+ \left[ \frac{\bar{C}_{26}^{(k)} - 2\bar{C}_{36}^{(k)}}{4\bar{C}_{33}^{(k)} - \bar{C}_{22}^{(k)}} \right] \gamma^{o(k)} r^2 + \left[ \frac{\bar{\Sigma}^{(k)}}{\bar{C}_{33}^{(k)} - \bar{C}_{22}^{(k)}} \right] r,$$

where

$$\bar{\Sigma}^{(k)} = (\bar{C}_{13}^{(k)} - \bar{C}_{12}^{(k)}) \varepsilon_x^{T(k)} + (\bar{C}_{23}^{(k)} - \bar{C}_{22}^{(k)}) \varepsilon_{\theta}^{T(k)} \quad [39]$$

$$+ (\bar{C}_{33}^{(k)} - \bar{C}_{23}^{(k)}) \varepsilon_r^{T(k)} + (\bar{C}_{36}^{(k)} - \bar{C}_{26}^{(k)}) \gamma_{x\theta}^{T(k)}$$

and

$$\lambda^{(k)} = \sqrt{\frac{\bar{C}_{22}^{(k)}}{\bar{C}_{33}^{(k)}}} \quad [40]$$

For  $N$  layers, there are  $N$   $\varepsilon^{\circ}$ 's,  $N$   $\gamma^{\circ}$ 's,  $N$   $E$ 's,  $N$   $F$ 's,  $N$   $F_1$ 's,  $N$   $G_1$ 's,  $N$   $A_1$ 's and  $N$   $A_2$ 's, or  $8N$  unknown constants. These constants are determined by satisfying the boundary conditions on the inner and outer radii, satisfying continuity of tractions at each interface, satisfying continuity of displacements at each interface, suppressing rigid body motion, and by applying two integrated conditions on the cross-sectional area. These are explained below.

Since layer 1 is the inner layer and layer  $N$  is the outer layer, the boundary conditions at the inner and outer radii are

$$\sigma_r^{(1)}(r_i) = -P_i \quad [41.a]$$

$$\tau_{\theta r}^{(1)}(r_i) = 0 \quad [41.b]$$

$$\tau_{xr}^{(1)}(r_i) = 0 \quad [41.c]$$

$$\sigma_r^{(N)}(r_o) = -P_o \quad [41.d]$$

$$\tau_{\theta r}^{(N)}(r_o) = 0 \quad [41.e]$$

$$\tau_{xr}^{(N)}(r_o) = 0 \quad [41.f]$$

Here  $P_i$  and  $P_o$  are known pressures and there are no surface shear tractions. Eqs. 41.b, c, e, and f lead to, from eqs. 34 and 35,

$$E^{(1)} = E^{(N)} = 0 \quad [42]$$

and

$$F^{(1)} = F^{(N)} = 0 \quad [43]$$

Continuity of the interface tractions between the  $k^{\text{th}}$  and  $(k + 1)^{\text{st}}$  layers can be expressed as

$$\sigma_r^{(k)}(r_k) = \sigma_r^{(k+1)}(r_k) \quad [44.a]$$

$$\tau_{\theta r}^{(k)}(r_k) = \tau_{\theta r}^{(k+1)}(r_k) \quad [44.b]$$

$$\tau_{xr}^{(k)}(r_k) = \tau_{xr}^{(k+1)}(r_k) \quad [44.c]$$

$$k = 1, 2, \dots, N - 1.$$

Eqs. 44.b and c, along with eqs. 42 and 43 lead to the conclusions that

$$E^{(k)} = 0 \quad k = 1, N \quad [45]$$

and

$$F^{(k)} = 0 \quad k = 1, N. \quad [46]$$

Continuity of the interface displacements can be written as

$$u^{(k)}(x, r_k) = u^{(k+1)}(x, r_k) \quad [47.a]$$

$$v^{(k)}(x, r_k) = v^{(k+1)}(x, r_k) \quad [47.b]$$

$$w^{(k)}(r_k) = w^{(k+1)}(r_k) \quad [47.c]$$

$$k = 1, 2, \dots, N - 1.$$

Substituting from eq. 36, and using eqs. 45, 46, and 47.a results in

$$\varepsilon^{o(k)} x + F_1^{(k)} = \varepsilon^{o(k+1)} x + F_1^{(k+1)} \quad k = 1, 2, \dots, N - 1. \quad [48]$$

This equation leads to the conclusion that the constant axial strain for each layer is the same for all layers and so the tube-as-a-whole has strain  $\varepsilon^o$ . This strain is given by

$$\varepsilon^{o(k)} = \varepsilon^o \quad k = 1, N \quad [49]$$

Also from eq. 48, all  $F_1^{(k)}$  must be equal and, if axial rigid body translation is eliminated,

$$F_1^{(k)} = 0 \quad k = 1, N. \quad [50]$$

Similarly, from eqs. 37, 45, 46, and 47.b,

$$\gamma^{o(k)} x r + G_1^{(k)} r = \gamma^{o(k+1)} x r + G_1^{(k+1)} r \quad k = 1, 2, \dots, N-1. \quad [51]$$

This equation leads to the conclusion that the shear strain,  $\gamma_{x\theta}$ , which varies linearly with  $r$  for each layer, varies in a similar, and continuous, manner for all layers and so the tube-as-a-whole has shear strain  $\gamma^o r$ . From this,

$$\gamma^{o(k)} = \gamma^o \quad k = 1, N, \quad [52]$$

Eliminating rigid body rotation about the tube axis leads to

$$G_1^{(k)} = 0 \quad k = 1, N. \quad [53]$$

At this point,

$$u^{(k)}(x, r) = \varepsilon^o x, \quad [54]$$

$$v^{(k)}(x, r) = \gamma^o x r, \quad [55]$$

and

$$w^{(k)}(r) = A_1^{(k)} r^{\lambda(k)} + A_2 r^{-\lambda(k)} + \left[ \frac{\bar{C}_{12}^{(k)} - \bar{C}_{13}^{(k)}}{\bar{C}_{33}^{(k)} - \bar{C}_{22}^{(k)}} \right] \varepsilon^o r \quad [56]$$

$$+ \left[ \frac{\bar{C}_{26}^{(k)} - 2\bar{C}_{36}^{(k)}}{4\bar{C}_{33}^{(k)} - \bar{C}_{22}^{(k)}} \right] \gamma^o r^2 + \left[ \frac{\bar{\Sigma}^{(k)}}{\bar{C}_{37}^{(k)} - \bar{C}_{22}^{(k)}} \right] r.$$

These expressions for  $u$ ,  $v$ , and  $w$  involve  $\epsilon^\circ$ ,  $\gamma^\circ$ ,  $N A_1$ 's and  $N A_2$ 's, or  $2N + 2$  unknowns. Eqs. 41.a and d, 44.a, and 47.c provide  $2N$  equations. The remaining two necessary equations are determined by the integral conditions that net axial force and net torsion acting on the cross section of the tube are known constants, i.e.

$$\int_A \sigma_x r d\theta dr = F_x \quad [57]$$

and

$$\int_A \tau_{x\theta} r^2 d\theta dr = T_x, \quad [58]$$

where  $A$  is the annular area of all  $N$  layers,  $F_x$  is a known applied axial force and  $T_x$  is a known applied torque. Specifically these conditions are written as

$$2\pi \sum_{k=1}^N \int_{r_{k-1}}^{r_k} \sigma_x^{(k)}(r) r dr = F_x \quad [59]$$

and

$$2\pi \sum_{k=1}^N \int_{r_{k-1}}^{r_k} \tau_{x\theta}^{(k)}(r) r^2 dr = T_x. \quad [60]$$

The complete solution for the displacements, and hence the stresses, for the  $N$  layers is now available. This process can be easily automated for an arbitrary number of layers, each with material properties that are arbitrary but orthotropic in the 1-2-3 system.

## 2.6 Temperature-Dependent Material Properties

The previous development is valid for either temperature-independent or temperature-dependent material properties. This study uses both formulations and compares predicted

tube response. When temperature-dependent material properties are used, the compliances are assumed to behave in the following manner with temperature,

$$S_{ij}(T) = S_{ij}^0 + S_{ij}^1 T + S_{ij}^2 T^2, \quad [61]$$

where temperature,  $T$ , is the absolute temperature (as opposed to relative temperature,  $\Delta T$ ) in degrees Celsius. The thermally-induced strain is assumed to behave as

$$\varepsilon_i^T(T) = e_i^0 + e_i^1 T + e_i^2 T^2 + e_i^3 T^3. \quad [62]$$

The value of  $e_i^0$  is such that when  $T$  is the cure temperature,  $\varepsilon_i^T = 0$ . For a given temperature, the compliances and thermal strains for each layer are calculated. The constitutive equations are then written in terms of known constants.

For temperature-independent material properties, the compliances and thermally-induced strain assume the form

$$S_{ij} = S_{ij}^0 \quad [63.a]$$

$$\varepsilon_i^T(T) = e_i^0 + e_i^1 T, \quad [63.b]$$

where  $e_i^1$  is the coefficient of thermal expansion,  $\alpha_i$ , of the material.

For the temperature-dependent properties the polynomial forms of compliance and thermally induced strain are derived from existing temperature-dependent engineering properties. It should be noted that when  $\bar{C}_{33} = \bar{C}_{22}$ , the solution for  $w(r)$  of eq. 32 is not valid. Resolving eq. 31 for this case leads to the proper solution for  $w(r)$ . Since material properties are not known with certainty, rather than resolving eq. 31 for  $\bar{C}_{33} = \bar{C}_{22}$ , here the values of  $E_2$  and  $E_3$  are adjusted slightly so that  $\bar{C}_{33} \neq \bar{C}_{22}$  for any problem studied. A detailed explanation of the specific temperature-dependent material properties used in this investigation is given in the following chapter and in Appendix A.

The development just presented will be used to calculate numerical values of stresses and deformations. The influence of including or not including temperature-dependent material properties on tube response will be assessed. The next chapter presents these results.

### 3.0 Analytical Predictions

In this chapter, analytical predictions obtained from the elasticity analysis are presented. Two issues are examined with the analysis. First, the influence on predicted tube response of including temperature-dependent material properties is studied. Second, the effects on tube response of an inner and outer coating of aluminum on graphite-epoxy tubes are discussed. Stresses in the coatings and the differences in overall tube behavior with and without the coatings are discussed. In all cases, the cure temperature is assumed to be the stress- and deformation-free state.

The tube geometries and nomenclature for the numerical analysis in this chapter are given in Table 1 and Figure 1. Specifically, the designs considered in this chapter are 14 layer tubes designated as follows:

$$\text{Design 1 : } [ - \varphi / \varphi / 0_{10} / \varphi / - \varphi ]$$

$$\text{Design 2 : } [ - \varphi_2 / 0_{10} / \varphi_2 ],$$

where  $\varphi$  is off-axis ply orientation angle. These designs were chosen as being similar to those being considered for use on the space station. Design considerations for the space station include high axial stiffness (hence, the large percentage of axially oriented fibers) and ease of fabrication. The off-axis plies provide enough hoop strength for ease of fabrication and durability for handling.

**Table 1. Tube Designs for Numerical Analysis**

**UNCOATED**

Inner radius,  $r_i = 25.4$  mm and  $t_{ply} = 0.127$  mm

Design 1 : [  $-\phi / \phi / O_{10} / \phi / -\phi$  ]

Design 2 : [  $-\phi_2 / O_{10} / \phi_2$  ]

**COATED**

Inner radius,  $r_i = 25.4$  mm

For the graphite-epoxy,  $t_{ply} = 0.127$  mm

The coatings consist of aluminum (Al) with  $t = 0.051$  mm, and adhesive (Ad) with  $t = 0.076$  mm.

Design 1 : [ Al / Ad /  $-\phi / \phi / O_{10} / \phi / -\phi$  / Ad / Al ]

Design 2 : [ Al / Ad /  $-\phi_2 / O_{10} / \phi_2$  / Ad / Al ]

Both designs considered in this analysis exhibit balanced lamination sequences. Design 1 is symmetric as well as balanced. These two designs were chosen to illustrate some important characteristics of tube response, and to demonstrate the ability of the elasticity solution to predict differences in the responses of the two designs. The material systems considered are T300/934 graphite-epoxy for the tubes themselves, and for the coatings, 6061 aluminum. As seen in Table 1, for the coated tubes, an adhesive layer between the graphite-epoxy and the aluminum is also modelled. All of the results are based on assuming that the tube is subjected to a temperature change of 334 K relative to the cure state. As mentioned previously, it is assumed that the tube is stress and deformation free at the cure temperature of T300/934, namely 450 K. The 334 K temperature drop represents the cold extreme of the orbital environment.

### ***3.1 Temperature Dependency of Material Properties***

An examination of the theory reveals that nine elastic properties and three thermal expansion properties are needed for a complete description of the material. There is little published information on how these 12 material properties vary with temperature over a wide temperature range. There are studies which present information on the in-plane properties at selected temperatures. The in-plane properties at other temperatures can be determined by interpolation. This was done by Milkovich, et al.<sup>18</sup> for T300/934. These in-plane data are used as the basis for this study. The out-of-plane properties (e.g.  $S_{33}$  and  $\epsilon_3^T$ ) are estimated, using the in-plane properties as a basis. Since it is highly likely that  $S_{22}$  and  $S_{33}$ , and  $\alpha_2$  and  $\alpha_3$  are similar, the approach has justification. The only material property which cannot be estimated from in-plane properties is  $\nu_{23}$  (and therefore  $S_{23}$ ). A value of 0.49 has been measured<sup>19</sup> for  $\nu_{23}$  in graphite-epoxy at room temperature. If it is assumed that  $\nu_{23}$  is invariant with temperature,

then a temperature-dependent expression for  $S_{23}$  may be found using the temperature-dependent expression for  $E_2$ . That is what is done here.

The material properties used in this study, and their referenced sources, may be found in Appendix A. Table A.2 and Table A.8 present the temperature-independent and temperature-dependent properties, respectively, for T300/934. The properties for the 6061 aluminum are shown in Table A.6 and Table A.11. For the adhesive layer, material properties for a typical aerospace epoxy adhesive are used. No temperature-dependent data were available for the adhesive, however, the temperature-independent properties are indicated in Table A.7.

To illustrate the character of the temperature dependence of the compliances, the polynomial representations of T300/934 from Table A.8 are plotted in Figure 2 and Figure 3. Due to the negligible effect of temperature on  $E_1$ ,  $S_{11}$  is assumed to be independent of temperature for the entire range considered here, and is thus a horizontal line in Figure 2. Since  $\nu_{12}$  was observed to vary with temperature,  $S_{12}$  varies with temperature. From Figure 3, it is clear that  $S_{22}$ ,  $S_{23}$ ,  $S_{33}$ , and  $S_{66}$  change by varying degrees with temperature. Indicated as circles on these figures are the room-temperature values as reported by Milkovich, et al. <sup>18</sup>. The room-temperature values do not coincide with the values indicated by the polynomials for the following reasons; i) The polynomials illustrated in the figures are least-squares fits to data taken at  $-157^{\circ}\text{C}$ ,  $21^{\circ}\text{C}$ , and  $121^{\circ}\text{C}$  <sup>18</sup>. At each temperature, there were repeated measurements made. The least-squares fit is influenced by all data and so the value of compliance at room temperature, as derived from the least-squares fit, is influenced by data at other temperatures. ii) The data used for the temperature-independent values are simply averages of repeated measurements at room temperature. This averaging gives different estimates of the room-temperature compliances than the value derived from the least-squares fit to all the data at all the temperatures. In general, the temperature-dependent and the temperature-independent values of compliance are close, the exception being  $S_{66}$ .

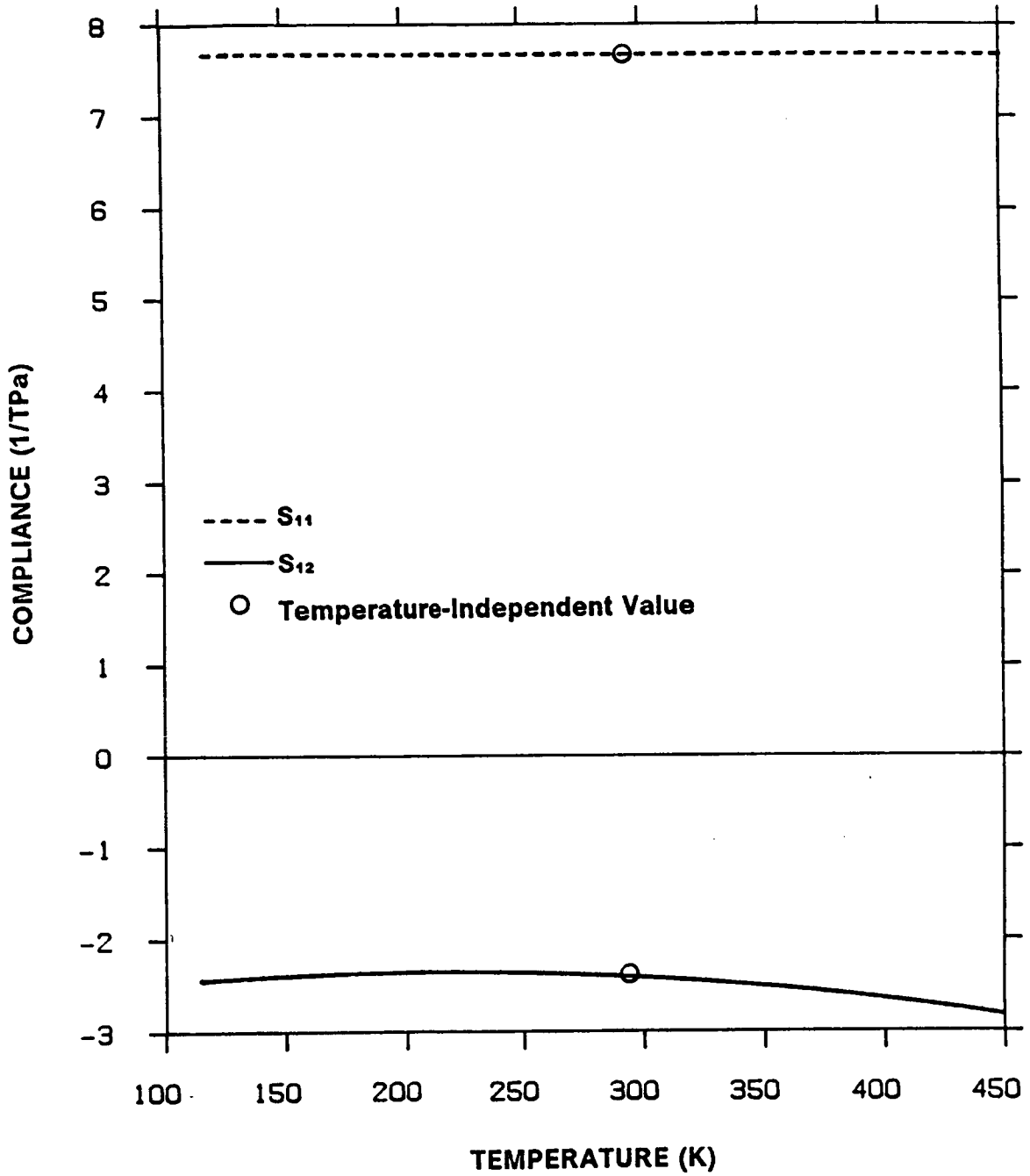


Figure 2. Fiber-Direction Compliances vs. Temperature:  $S_{11}$  and  $S_{12}$ , T300/934 Temperature-dependent and temperature-independent material property data.

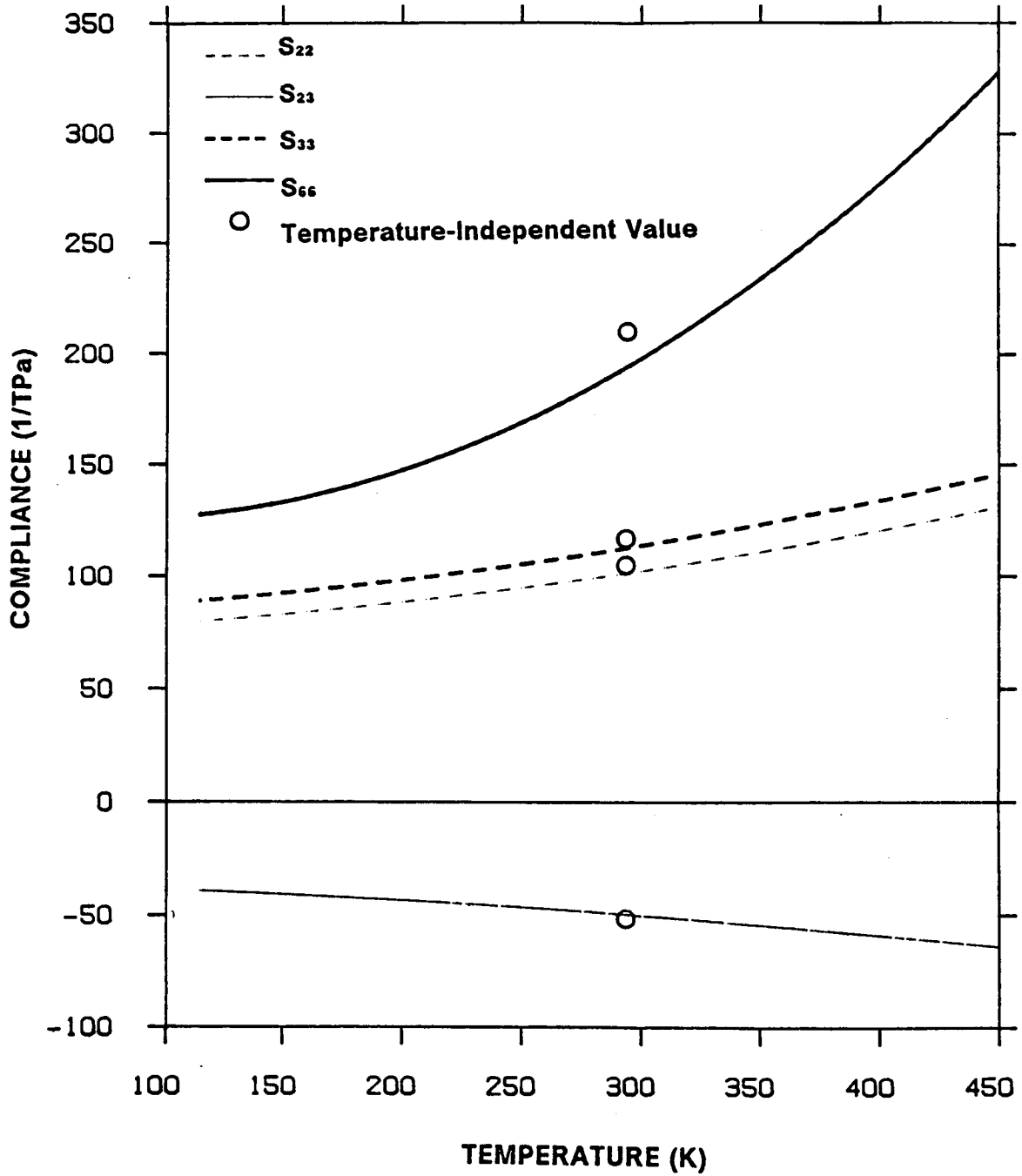


Figure 3. Transverse Direction and Shear Compliances vs. Temperature:  $S_{22}$ ,  $S_{23}$ ,  $S_{33}$ , and  $S_{66}$ . T300/934 Temperature-dependent and temperature-independent material property data.

Often the thermal expansion properties of a material are represented by the slope of the thermal strain vs. temperature relation. However, as seen in the analytical development of Ch. 2, the thermally-induced strain is a more fundamental quantity. In fact, thermal strain is the quantity that is measured in experiments designed to study thermal expansion. For graphite-epoxies, the thermal strain perpendicular to the fiber direction, and in the plane of the lamina,  $\epsilon_2^T$ , the so-called transverse thermal strain, is easy to measure. It is a large enough quantity that strain gages can be used with sufficient accuracy. It is often assumed that the thermal strain perpendicular to the plane of the lamina,  $\epsilon_3^T$ , is similar to the transverse thermal strain,  $\epsilon_2^T$ . The thermal strain parallel to the fibers,  $\epsilon_1^T$ , is much more difficult to measure. It is difficult because it is a very small quantity and, it appears that it may be a strong function of temperature and the particular type of graphite fiber used. Since it is a small quantity, there are often uncertainties in its measurement. Because of the magnitude of  $\epsilon_1^T$  relative to  $\epsilon_2^T$  and  $\epsilon_3^T$ , and because of uncertainties in the available data, here it will be assumed that  $\epsilon_1^T = 0$  for all temperatures. The character of  $\epsilon_2^T$  with temperature for T300/934 is illustrated in Figure 4. Also, shown is the behavior if it is assumed that the thermal expansion is linear with temperature, the slope of the relation being equal to the room-temperature value of the coefficient of thermal expansion,  $\alpha_2$ . As can be seen, for T300/934 graphite-epoxy, inclusion of nonlinear temperature-dependent expansion is not dramatically different than the linear assumption. Other graphite-epoxies may show a more serious nonlinear trend.

### **3.2 Tube Response**

Figure 5 - Figure 11 illustrate the temperature dependence of the various components of stress and strain in tube Designs 1 and 2, for an off-axis ply orientation angle,  $\phi$ , of  $20^\circ$ .

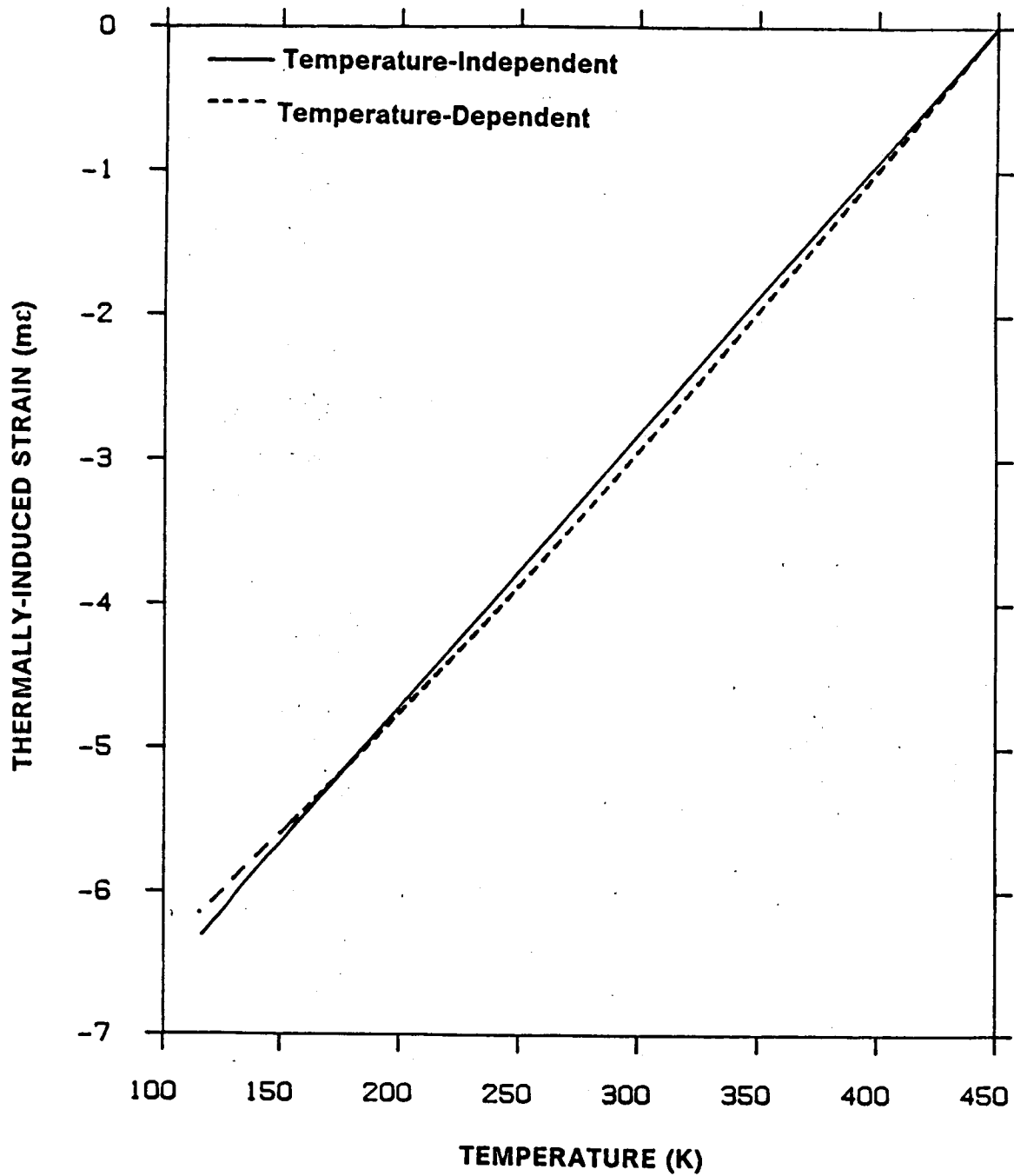


Figure 4. Thermally-Induced Strain vs. Temperature: T300/934, transverse direction ( $\epsilon_2^T$ ), temperature-dependent and temperature-independent material property data.

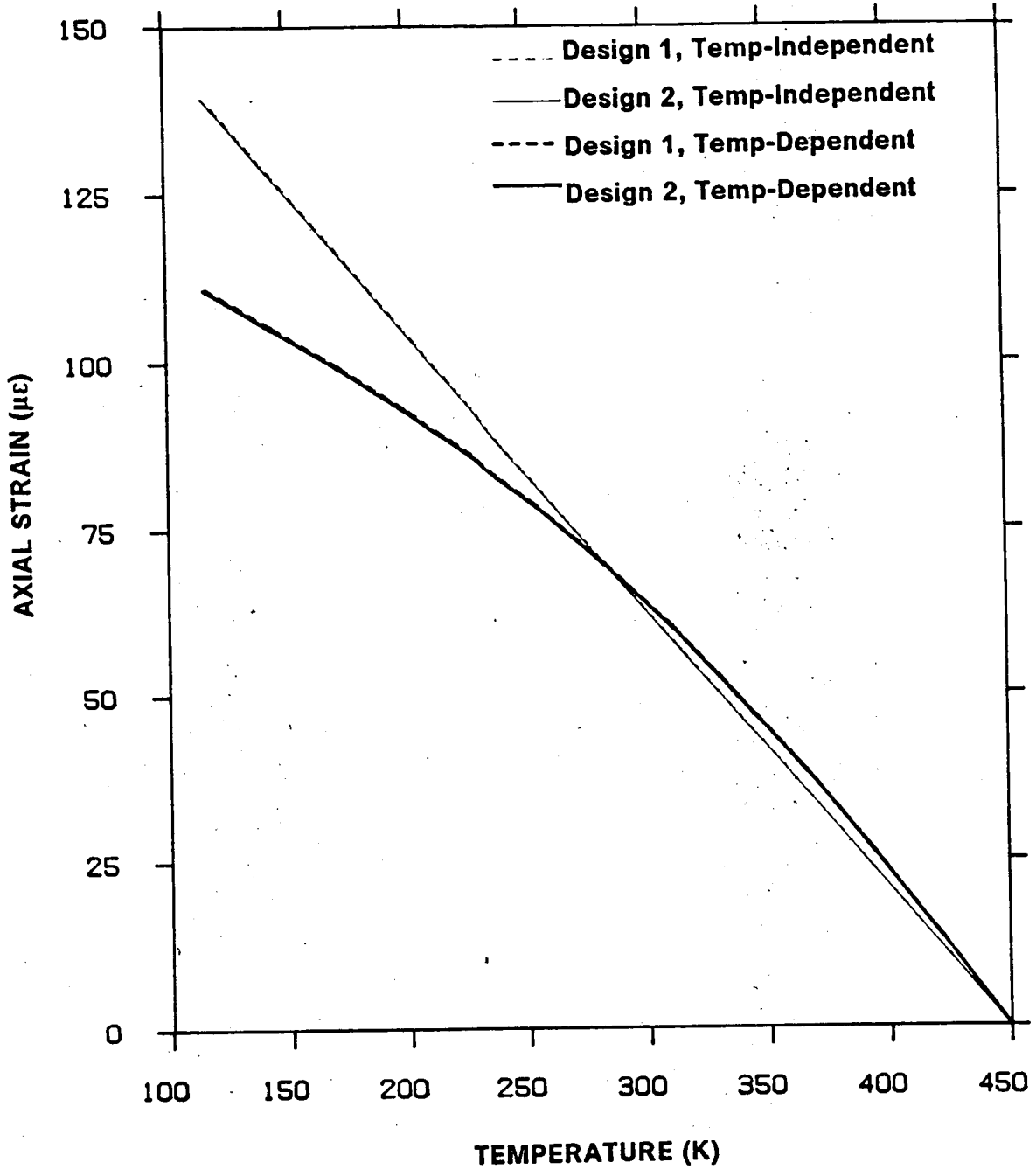


Figure 5. Axial Strain vs. Temperature: Temperature-dependent and temperature-independent material properties, Designs 1 and 2,  $\phi = 20^\circ$ .

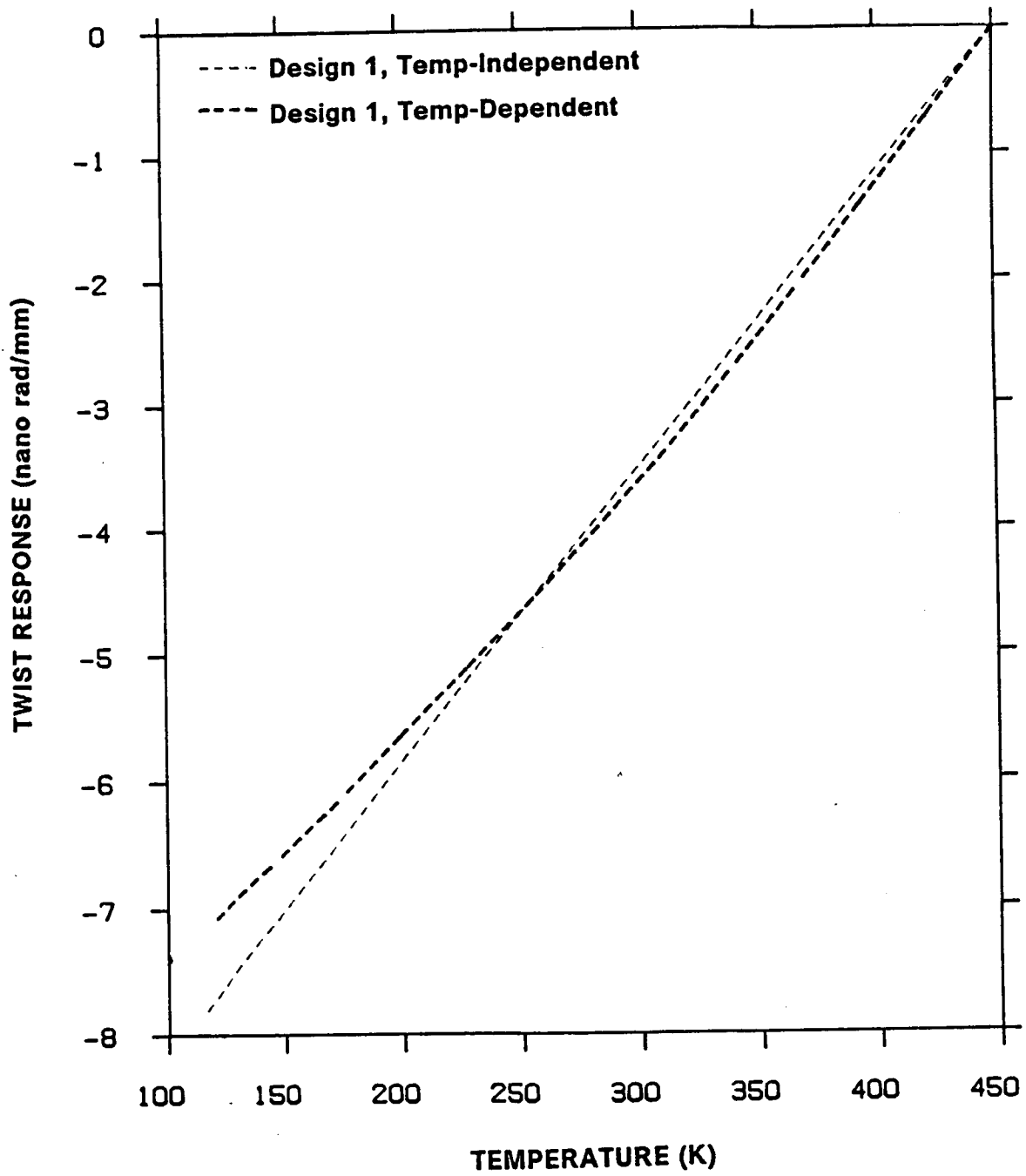


Figure 6. Twist Response vs. Temperature, Design 1: Temperature-dependent and temperature-independent material properties,  $\phi = 20^\circ$ .

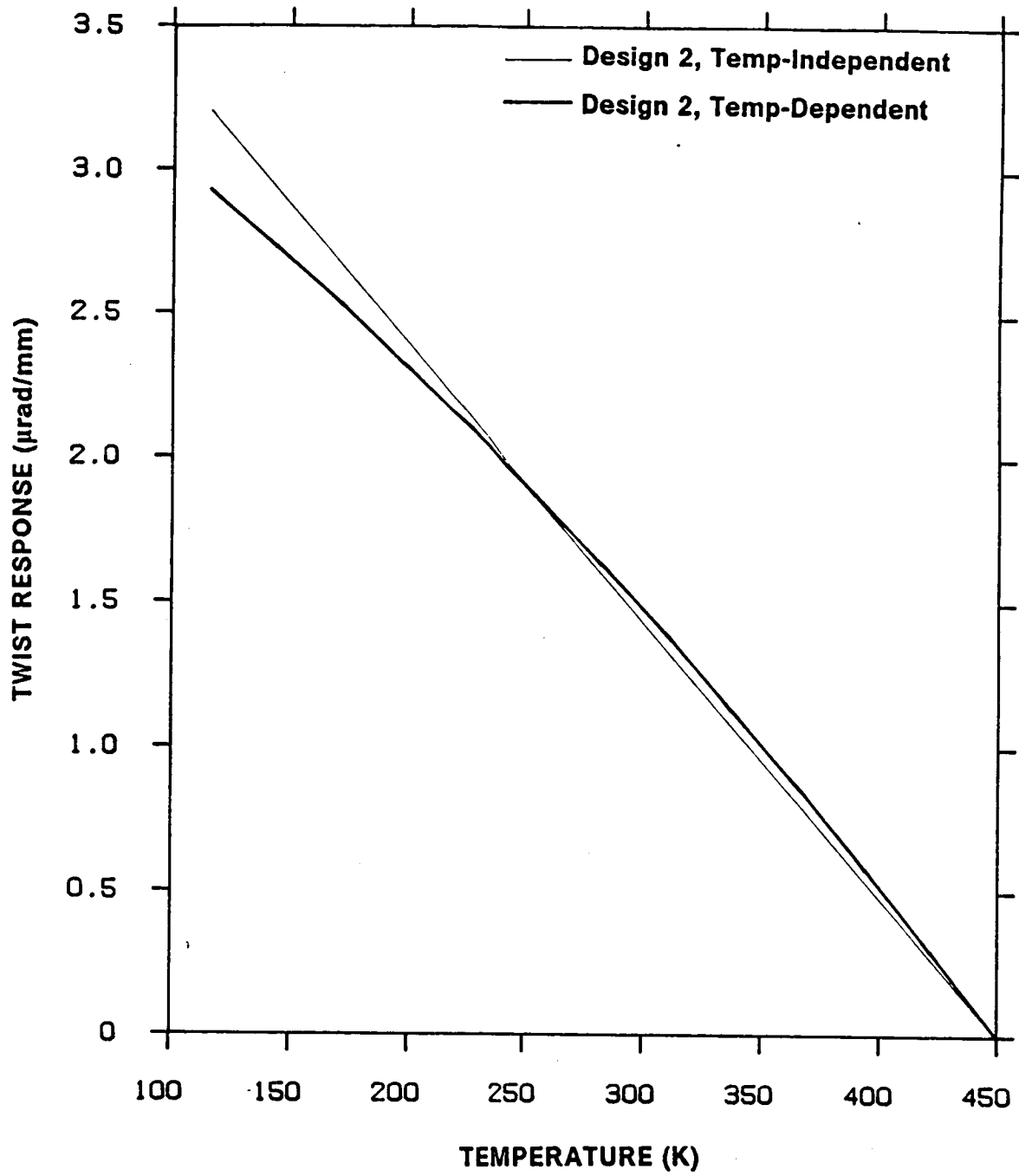


Figure 7. Twist Response vs. Temperature, Design 2: Temperature-dependent and temperature-independent material properties,  $\phi = 20^\circ$ .

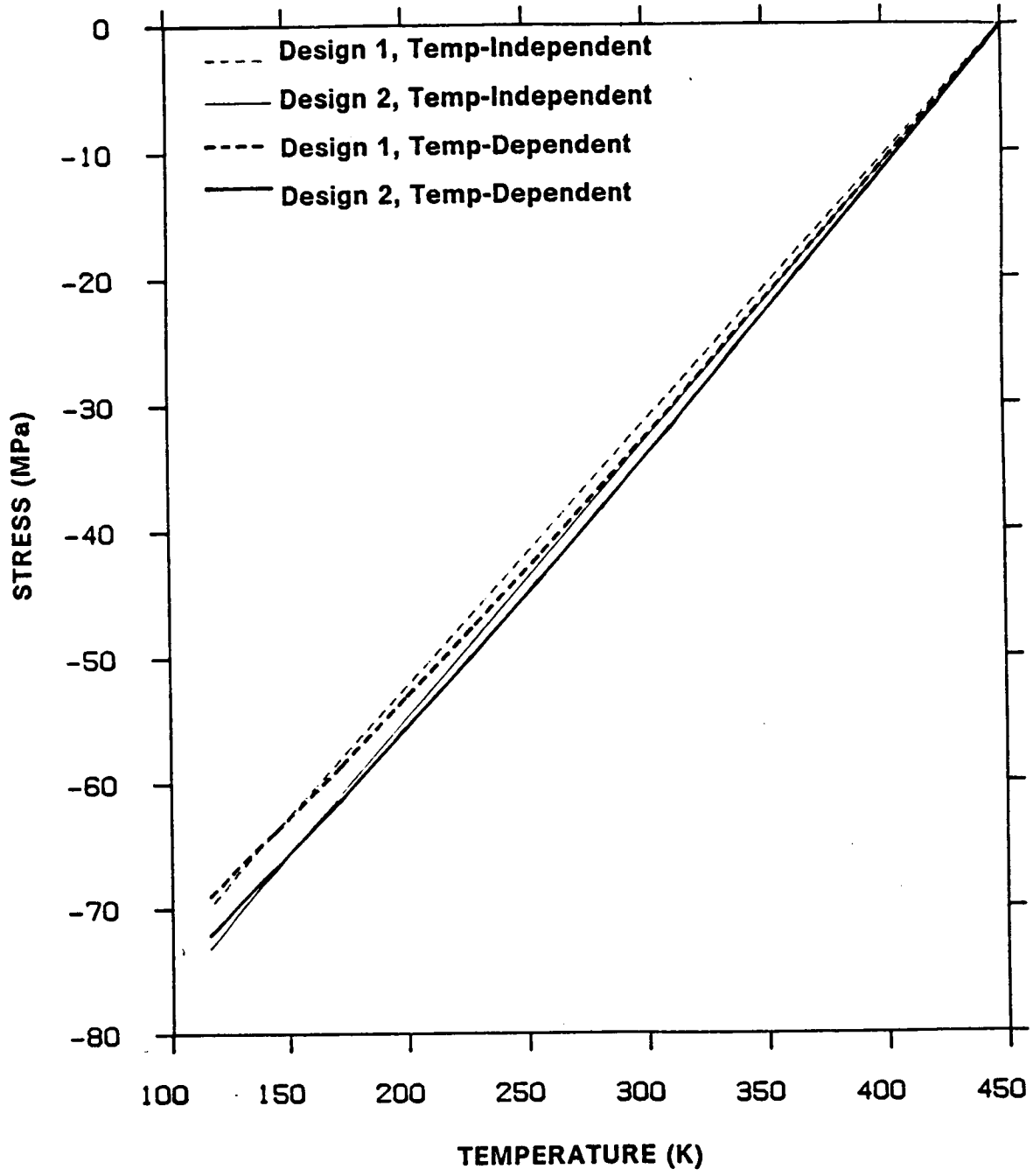


Figure 8. Fiber-Direction Stress vs. Temperature: Temperature-dependent and temperature-independent material properties, Designs 1 and 2,  $\phi = 20^\circ$ , Stress at inner radius.

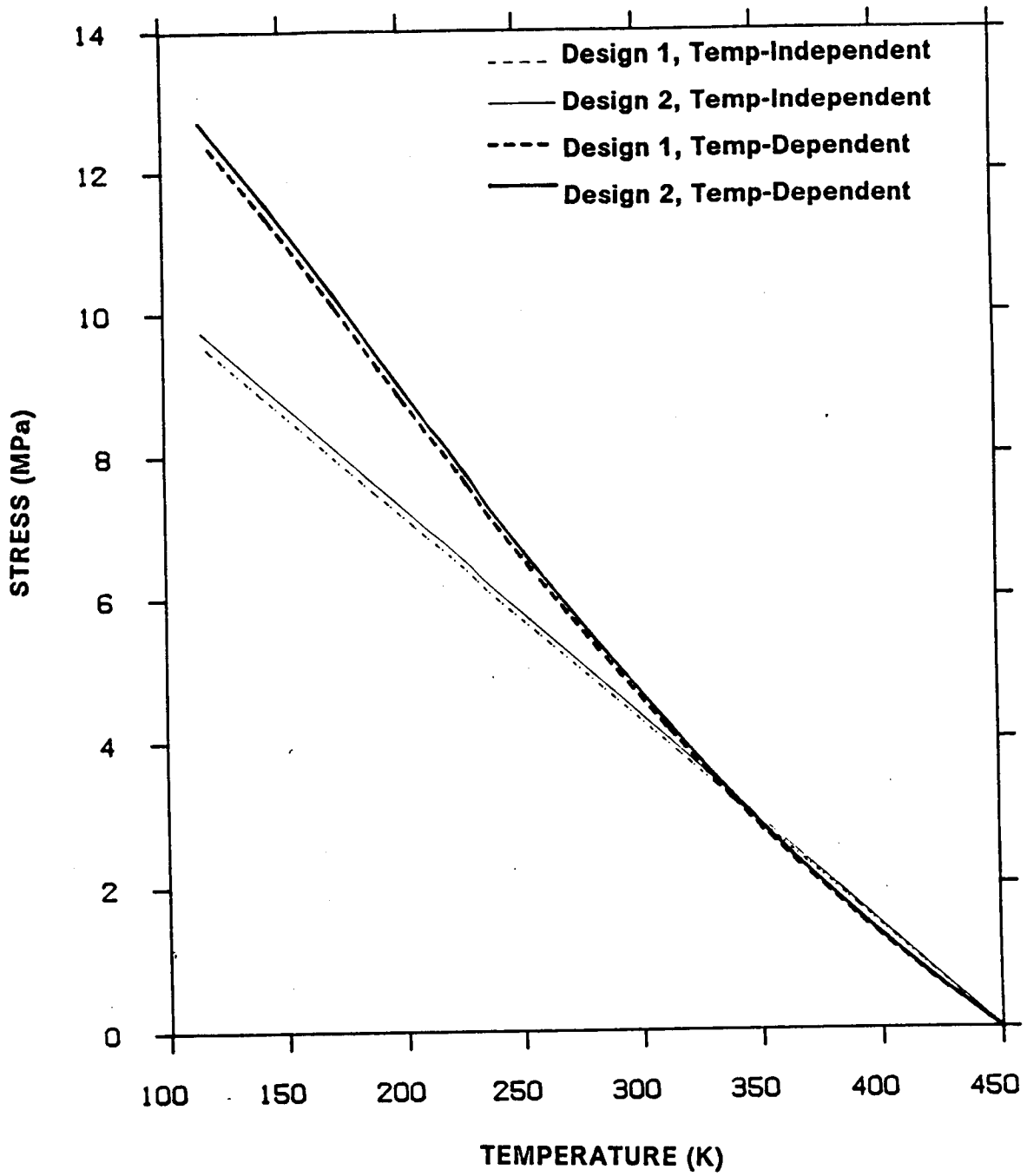


Figure 9. Transverse Stress vs. Temperature: Temperature-dependent and temperature-independent material properties, Designs 1 and 2,  $\phi = 20^\circ$ , Stress at inner radius.

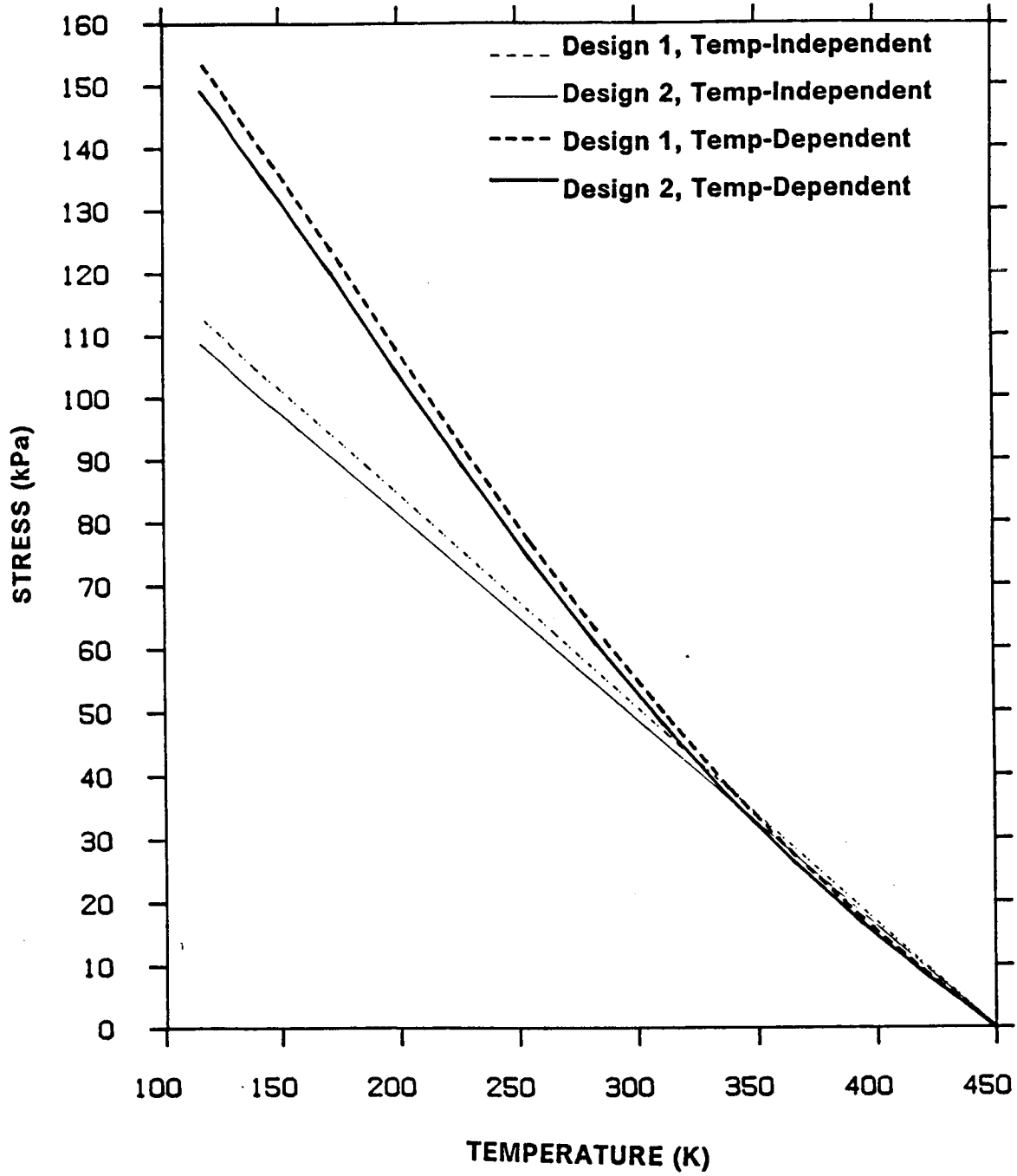


Figure 10. Radial Stress vs. Temperature: Temperature-dependent and temperature-independent material properties, Designs 1 and 2,  $\phi = 20^\circ$ , Stress at  $0/+20^\circ$  interface.

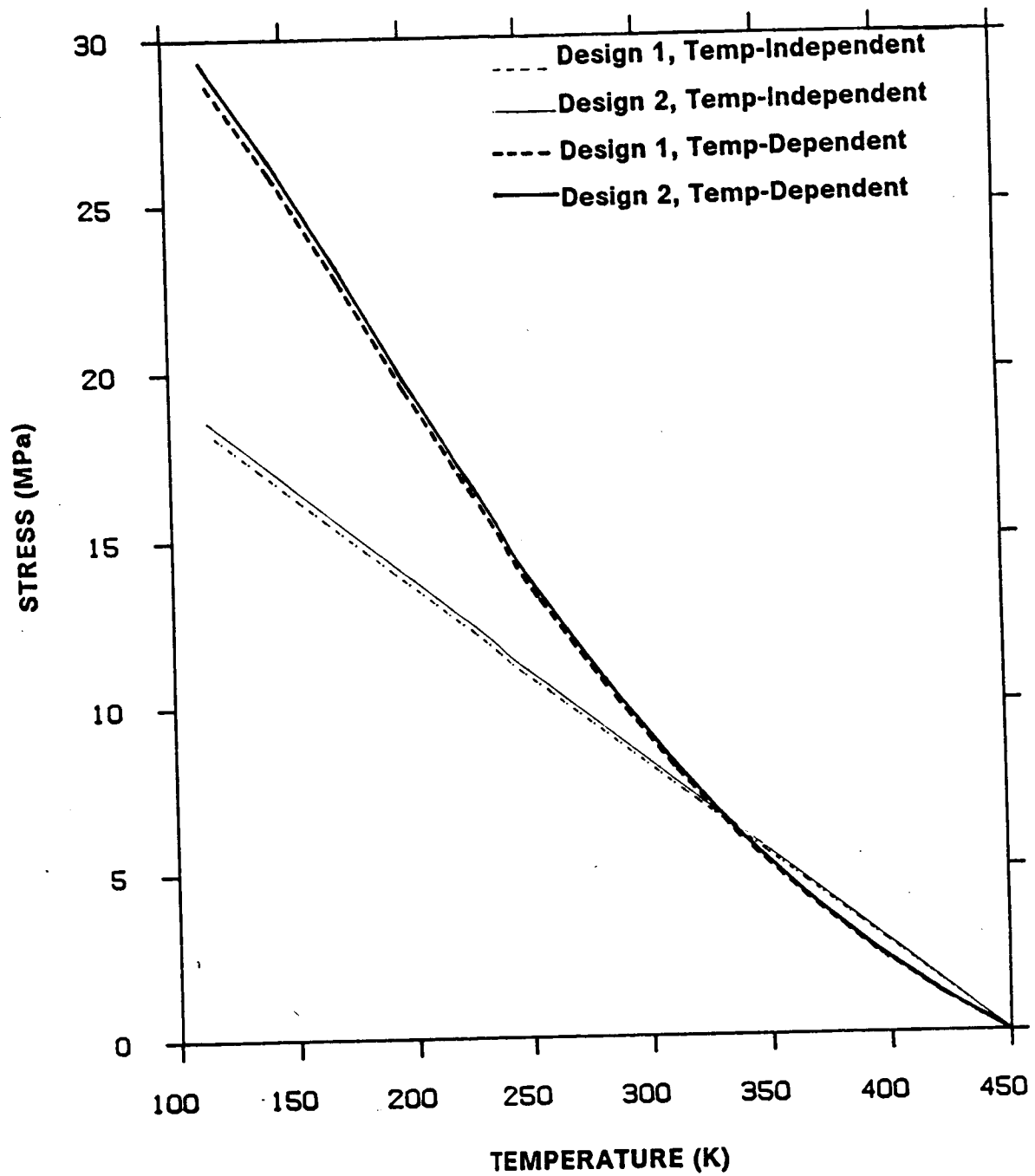


Figure 11. Shear Stress vs. Temperature: Temperature-dependent and temperature-independent material properties, Designs 1 and 2,  $\phi = 20^\circ$ . Stress at inner radius.

Twenty degrees is a realistic angle for use in the space station truss structure tubes. In other words, the tubes considered in the following figures can be designated as

Design 1 : [- 20 / 20 / 0<sub>10</sub> / 20 / -20]

Design 2 : [-20<sub>2</sub> / 0<sub>10</sub> / 20<sub>2</sub>].

In these figures the temperature is on the horizontal axis and the tube response is on the vertical axis. The cure temperature is the right end of the horizontal axis.

Figure 5, Figure 6, and Figure 7 illustrate the axial expansion and twist response ( $\epsilon^\circ$  and  $\gamma^\circ$ ) of the two designs as a function of temperature, using temperature-dependent and temperature-independent material properties. As mentioned in Ch. 2,  $\epsilon^\circ$  is a measure of the axial strain for the tube-as-a-whole. It represents the axial strain in each layer and is a constant through the tube wall thickness. The quantity  $\gamma^\circ$  is a measure of twist for the tube-as-a-whole. The shear strain at any radial location,  $r$ , can be determined by multiplying  $\gamma^\circ$  by  $r$ . Recall that  $\epsilon^\circ$  and  $\gamma^\circ$  are two responses that are solved for directly in the elasticity solution. As can be seen, there is no difference between the axial strain response of the two designs. On the other hand, the inclusion of temperature-dependent properties influences the magnitude of the predicted axial strain. For example, at 116 K, the axial strain using temperature-independent material properties is at least 25 % higher than the axial strain predicted using temperature-dependent material properties. The effect is felt to be due primarily to the variation in compliance with temperature.

Figure 6 and Figure 7 reveal a unexpected but very important finding in the analysis. Both designs represent balanced laminates, a construction that is generally felt to be free of shear deformations that might be induced by axial strains or a temperature change. However, Figure 6 and Figure 7 indicate that both tube designs will exhibit twist under thermal load. This can be a serious problem for the application to an orbital environment, where the temperature may change periodically. The twisting of the tubes represents a loss of dimensional stability for the structure that they are a part of. On the other hand, if the tubes are firmly attached to other structures at each end, the tendencies illustrated in Figure 6 and Figure 7 will lead to

thermally-induced torsional loads in the tubes. If the temperature change is cyclic, the thermally-induced loads will be cyclic, leading to possible fatigue problems. It is important to realize that the results of Figure 6 and Figure 7 are for two very specific tube designs. The twist magnitudes are not alarmingly high. However, the point to be made is that balanced laminates exhibit twist. The tendency to twist is due to the radial difference in location of the off-axis plies. This effect is physically real and not accounted for in any shell or flat-plate forms of analysis. Such analyses lump stiffnesses of all layers at the mean radius and differences in the radial positions of the layers are not accounted for. For this reason, the elasticity solution presented in this investigation is uniquely suited to analyze the thermally-loaded anisotropic cylinder problem. The difference in the sign of the twist between Design 1 and Design 2 is due to the fact that the angle of the outermost off-axis ply in Designs 1 and 2 are opposite in sign. The twist tendency of the outermost ply generally determines the twist tendency of the tube. A realistic example of the twist tendency may be shown using the data in Figure 7. A tube ten meters in length, with the geometry, lay-up, and material system of Design 2 would have to operate at a temperature of 116 K in the cold of space. Measuring the unconstrained thermally-induced twist relative to cure (450 K), the twist of one end of the 10 m tube relative to the other would be approximately 0.029 rad, or 1.7°.

As can be seen in Figure 6 and Figure 7, the inclusion of temperature-dependent properties reduces the magnitude of the predicted twist at lower temperatures, the reduction being roughly 5-10 %.

Figure 8 - Figure 11 present the variations in four components of stress with temperature and illustrate the differences in predicted stresses due to temperature dependence of material properties. The four components of stress illustrated are the only stresses predicted by the elasticity solution to be nonzero. The other components of stress are predicted to be zero. Since they are more meaningful than the stresses in the  $x-\theta-r$  coordinate system, the stresses in the principle material coordinate system (1-2-3) are shown in the figures. In these figures the values of stress for the in-plane components  $\sigma_1$ ,  $\sigma_2$ , and  $\tau_{12}$ , calculated at the inner surface

of the tubes are reported. The radial component ( $\sigma_3$ ) reported is the value at the 0/+20° interface. These locations are shown in Table 2. The radial locations used for each component yield a magnitude for the stress that is the maximum, or close to the maximum, for that component, through the entire wall thickness. Note that in the figure for radial stress, Figure 10, the units are kPa while the other figures are in MPa. This will be the situation for the radial stresses in all subsequent figures.

In Figure 8 it is seen that, as expected, in the fiber direction the stress is fairly linear with respect to temperature. There is little difference in the two designs and the predictions of the temperature-independent theory are close to the predictions of temperature-dependent theory. Also note that for the temperature range considered, the magnitudes are well below the ultimate failure stress of 1.0 GPa for graphite-epoxy. On the otherhand, the stresses illustrated in Figure 9 - Figure 11 show a noticeable dependence on whether or not temperature-dependent material properties are used. For the tube designs and the off-axis ply orientation angle considered here, the use of temperature-independent material properties results in an underprediction of  $\sigma_2$ ,  $\sigma_3$ , and  $\tau_{12}$  stress levels below room temperature (294 K). The normal stresses  $\sigma_2$  and  $\sigma_3$  are underpredicted by 25 %, whereas the shear stress  $\tau_{12}$  is underpredicted by 30 %. It should be emphasized that the above-mentioned trends are design- and material-dependent, rather than general characteristics of temperature-dependent tube behavior.

Figure 12 - Figure 15 show the through-the-thickness variations of the four components of stress, using both the temperature-dependent and temperature-independent material properties discussed above. The stresses shown are those calculated at 334 K below cure, i.e. at a temperature of 116 K. The independent variable in the following figures,  $\rho$ , is defined as

$$\rho = \frac{r - r_i}{r_o - r_i}$$

**Table 2. Radial Locations of Stresses Illustrated in Figures**

For Figure 8 - Figure 11, and Figure 19 - Figure 22.  
Uncoated Tubes

	<i>Design 1</i>	<i>Design 2</i>
$\sigma_1$	inner radius ( $\rho = 0$ )	inner radius ( $\rho = 0$ )
$\sigma_2$	inner radius ( $\rho = 0$ )	inner radius ( $\rho = 0$ )
$\sigma_3$	O/ + $\phi$ interface ( $\rho = 0.86$ )	O/ + $\phi$ interface ( $\rho = 0.86$ )
$\tau_{12}$	inner radius ( $\rho = 0$ )	inner radius ( $\rho = 0$ )

For Figure 30 - Figure 33. Coated Tubes

	<i>Design 1</i>	<i>Design 2</i>
$\sigma_1$	adhesive/- $\phi$ interface ( $\rho = 0.06$ )	adhesive/- $\phi$ interface ( $\rho = 0.06$ )
$\sigma_2$	adhesive/- $\phi$ interface ( $\rho = 0.06$ )	adhesive/- $\phi$ interface ( $\rho = 0.06$ )
$\sigma_3$	O/ + $\phi$ interface ( $\rho = 0.81$ )	O/ + $\phi$ interface ( $\rho = 0.81$ )
$\tau_{12}$	adhesive/- $\phi$ interface ( $\rho = 0.06$ )	adhesive/- $\phi$ interface ( $\rho = 0.06$ )

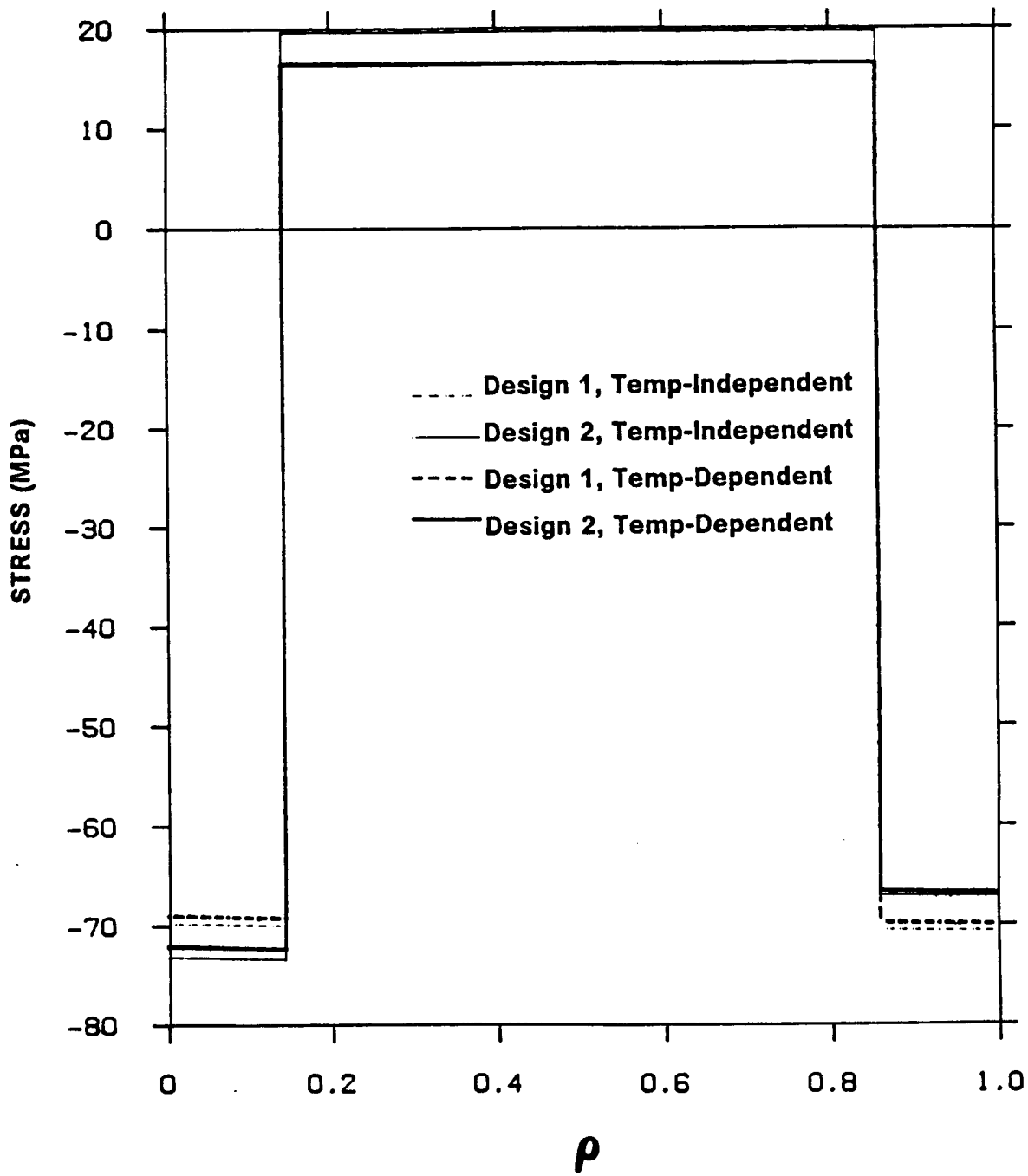


Figure 12. Fiber-Direction Stress Variation Through-The-Thickness: Temperature-dependent and temperature-independent material properties, Designs 1 and 2,  $\phi = 20^\circ$ ,  $T = 116$  K.

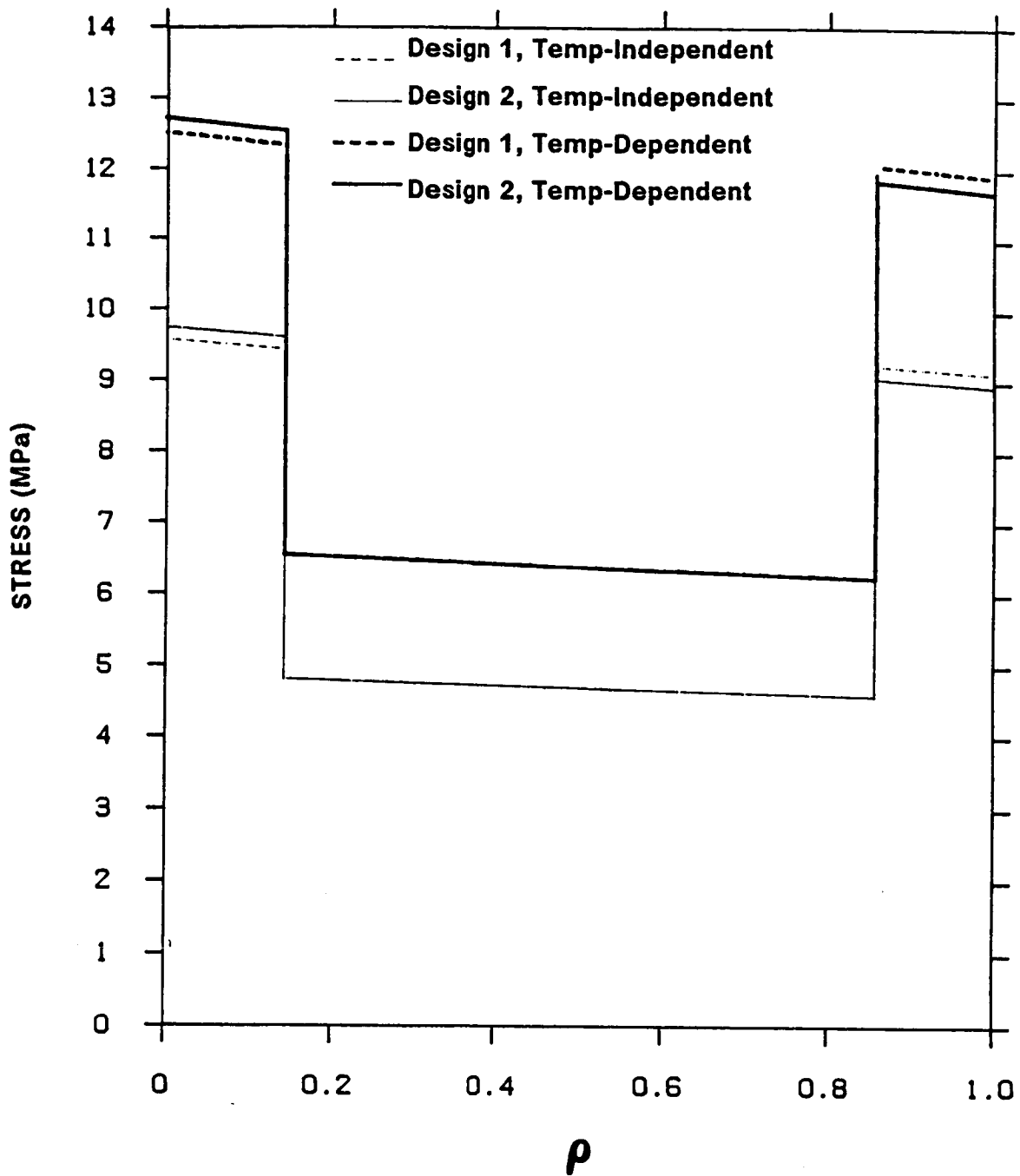


Figure 13. Transverse Stress Variation Through-The-Thickness: Temperature-dependent and temperature-independent material properties, Designs 1 and 2,  $\phi = 20^\circ$ ,  $T = 116$  K.

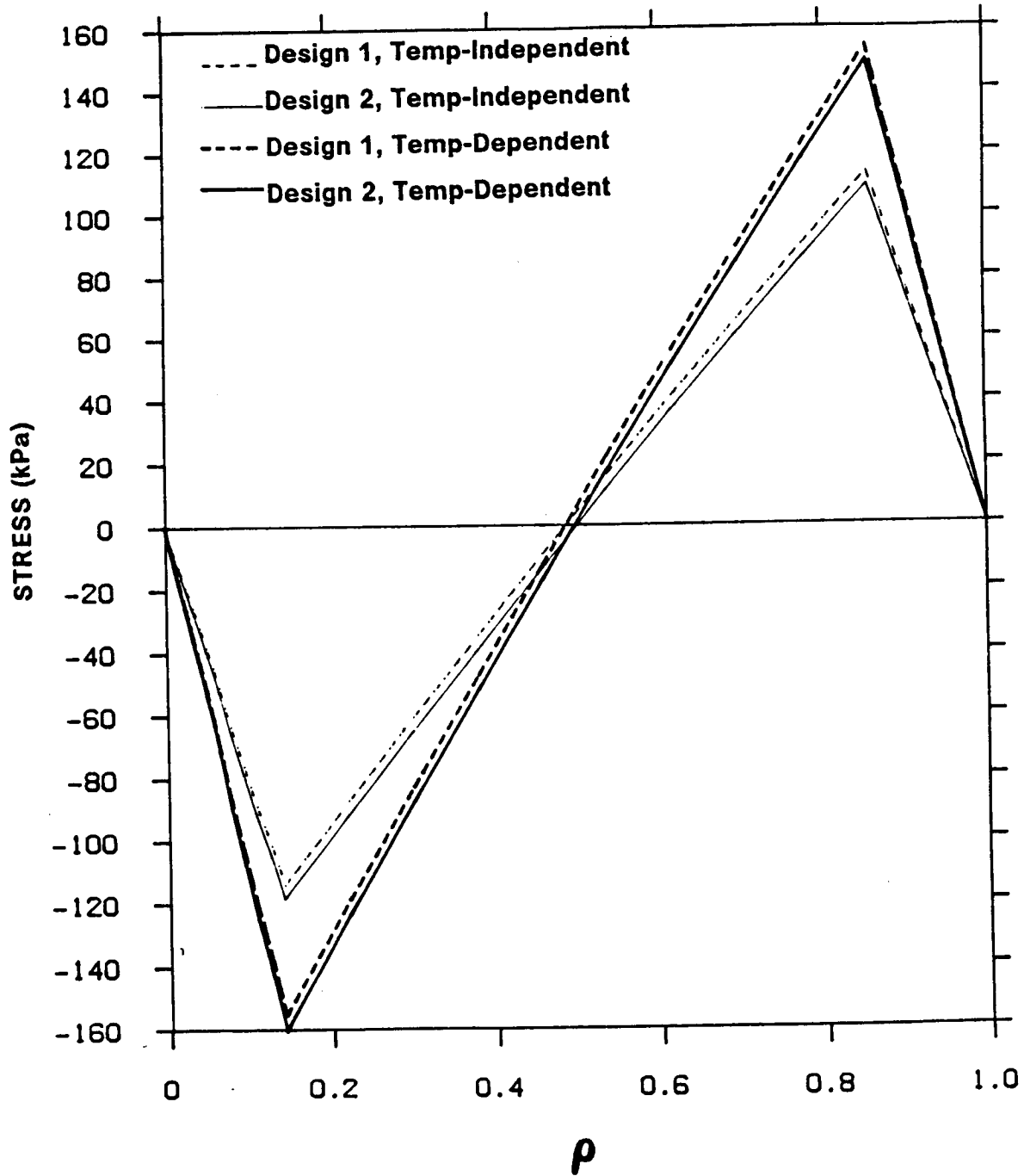


Figure 14. Radial Stress Variation Through-The-Thickness: Temperature-dependent and temperature-independent material properties, Designs 1 and 2,  $\phi = 20^\circ$ ,  $T = 116$  K.

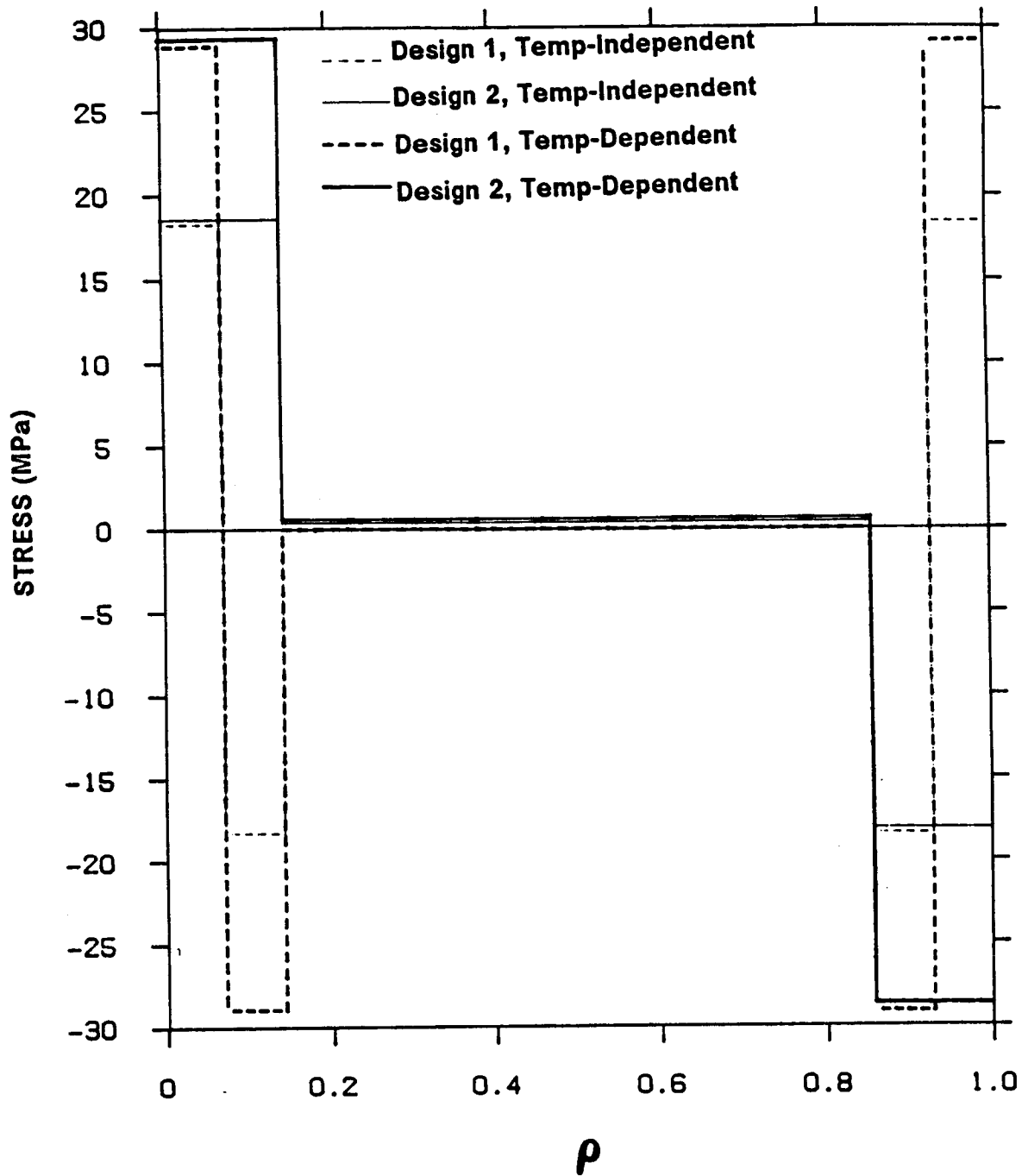


Figure 15. Shear Stress Variation Through-The-Thickness: Temperature-dependent and temperature-independent material properties, Designs 1 and 2,  $\phi = 20^\circ$ ,  $T = 116$  K.

and is a non-dimensional expression for the radial location through the tube wall thickness. At the inner radius  $\rho$  is 0.0 while  $\rho$  is 1.0 at the outer surface. The results for both tube designs are presented. As can be seen in Figure 12, Figure 13, and Figure 15, the in-plane stresses are highest in the off-axis plies ( $0 < \rho < 0.14$ ,  $0.86 < \rho < 1.0$ ). The variation of the stresses through-the-thickness of the individual layers is apparent in the figures, and it is clear why the radial locations of Table 2 were used in the earlier figures. Figure 12, Figure 13, and Figure 15 illustrate that  $\sigma_1$ ,  $\sigma_2$ , and  $\tau_{12}$  components of stress are largest at the inner radius (or are at least nearly as large as anywhere else), while Figure 14 shows that the radial stress is largest at the  $0/\varphi$  interface. It should also be noted that the magnitudes of the radial stress at the inner and outer ply interfaces are not quite equal,  $\sigma_3$  at the outer interface being slightly smaller. As required by the boundary conditions in the elasticity solution,  $\sigma_3$  is zero at the inner and outer surfaces.

As was shown in Figure 8 - Figure 11, the use of temperature-dependent material properties has a negligible effect on the predicted values of  $\sigma_1$  but makes a significant difference in the predicted values of  $\sigma_2$ ,  $\sigma_3$ , and  $\tau_{12}$ . These effects are evident in all of the figures. Figure 13 - Figure 15 show a 20 - 40 % increase in  $\sigma_2$ ,  $\sigma_3$  and  $\tau_{12}$  at 116 K, using temperature-dependent properties.

Figure 16 - Figure 22 illustrate the variations of stress and deformations in the two designs for variable ply orientation angle,  $\varphi$ . The range of  $\varphi$  considered is  $0^\circ \leq \varphi \leq 90^\circ$ . Temperature-dependent and temperature-independent material property responses are compared. With a variable  $\varphi$  Designs 1 and 2 now represent two families of laminates, rather than single lay-ups. As before, the operating temperature is 116 K.

Figure 16 illustrates the character of the axial strain,  $\epsilon^\circ$  as a function of off-axis angle. For axial strain there is virtually no difference between Designs 1 and 2 over the entire range of  $\varphi$ . The difference between the predictions using temperature-dependent and temperature-independent material properties is the greatest at  $\varphi = 90^\circ$ . This difference is because the

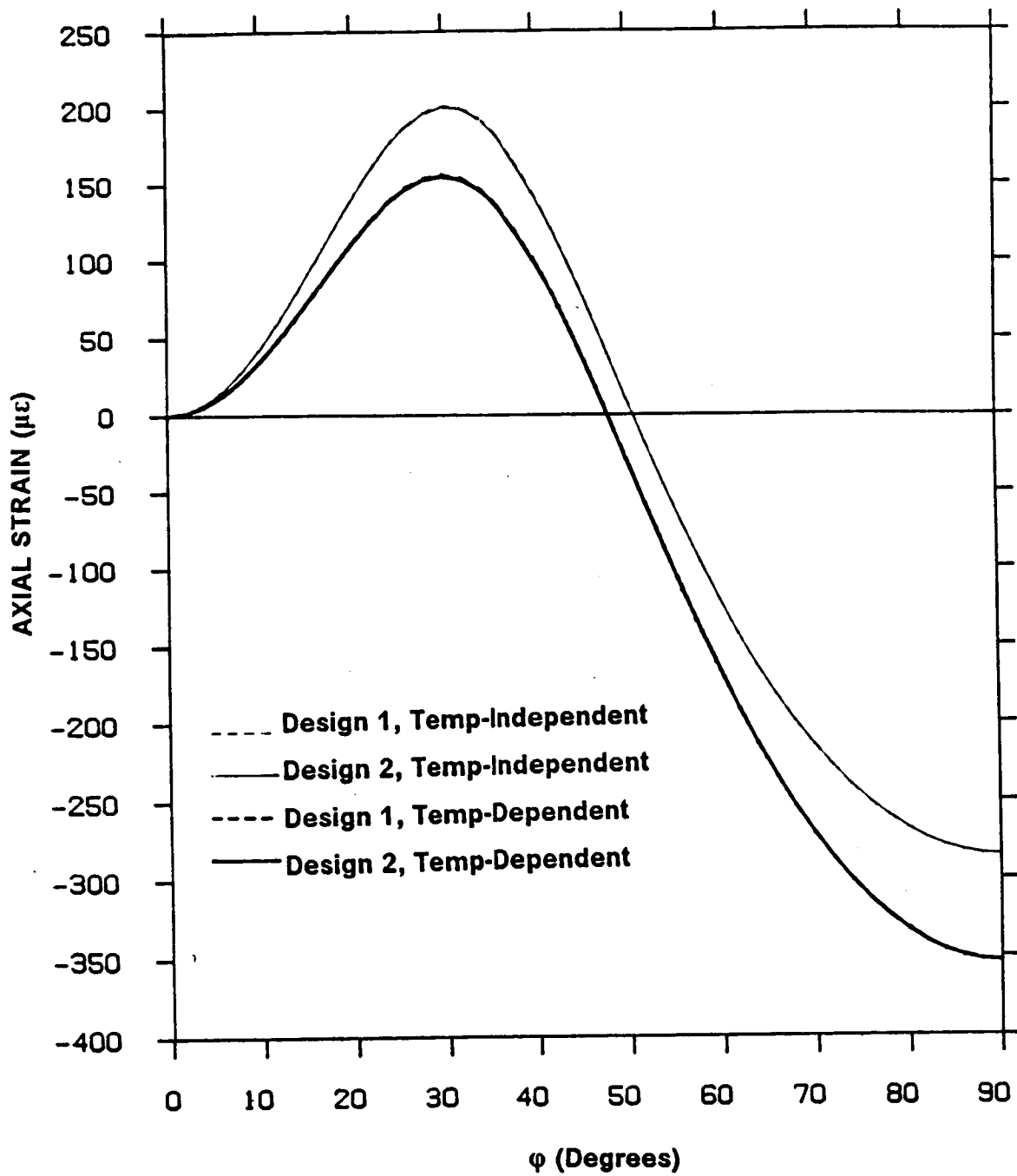


Figure 16. Axial Strain vs. Ply Orientation Angle,  $\phi$ : Temperature-dependent and temperature-independent material properties, Designs 1 and 2,  $T = 116$  K.

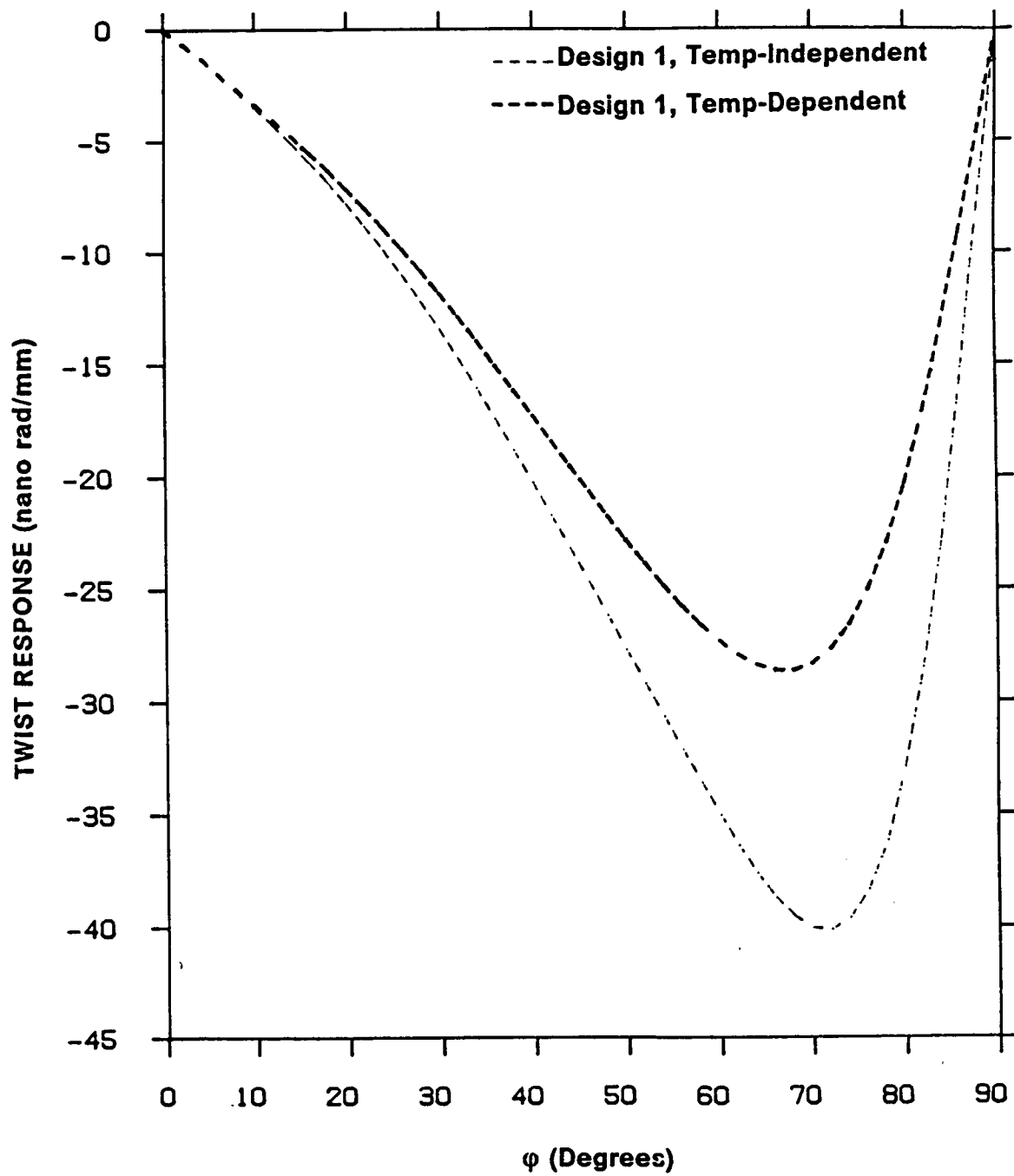


Figure 17. Shear Strain vs. Ply Orientation Angle,  $\phi$ , Design 1: Temperature-dependent and temperature-independent material properties,  $T = 116$  K.

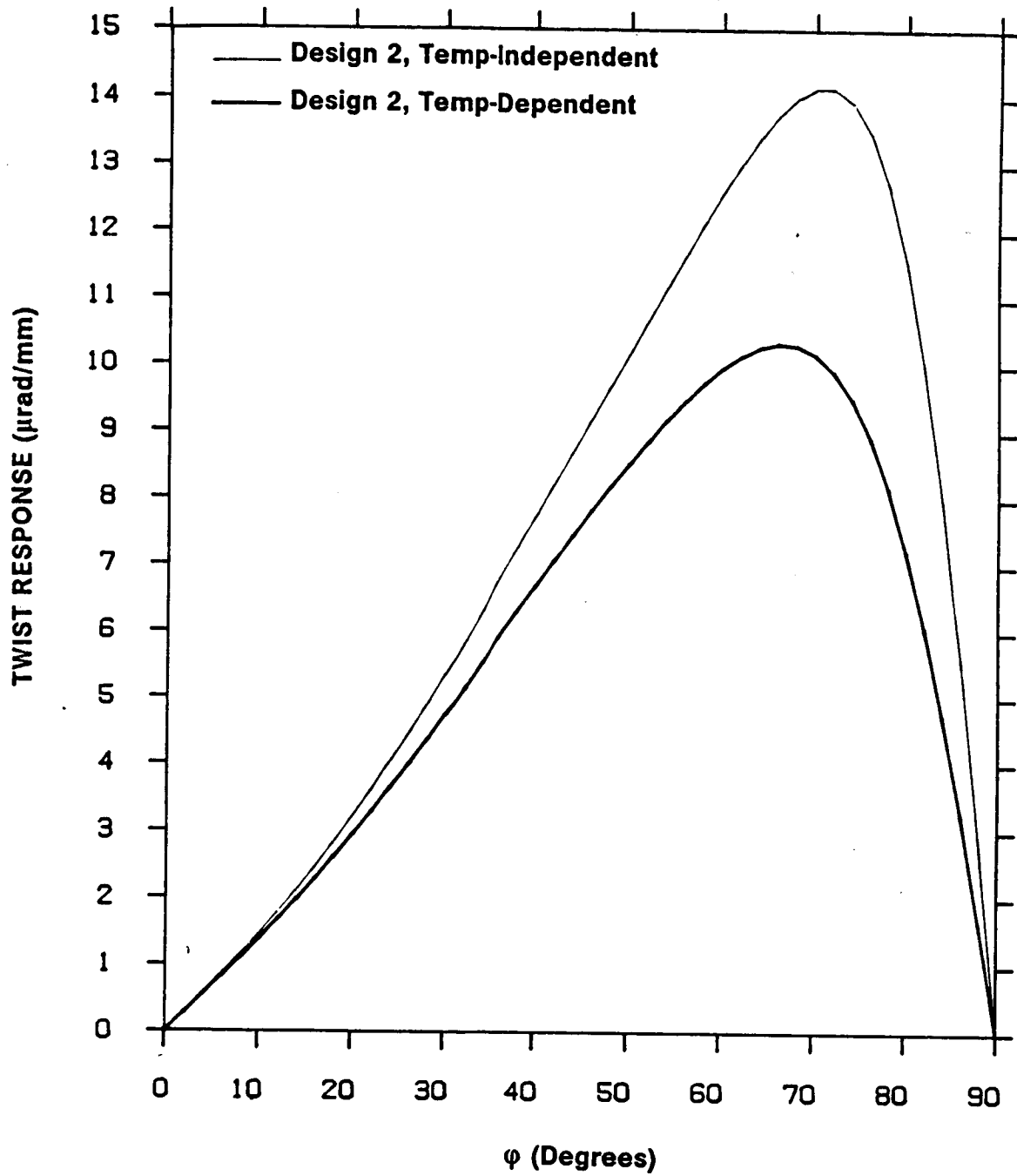


Figure 18. Shear Strain vs. Ply Orientation Angle,  $\phi$ , Design 2: Temperature-dependent and temperature-independent material properties,  $T = 116$  K.

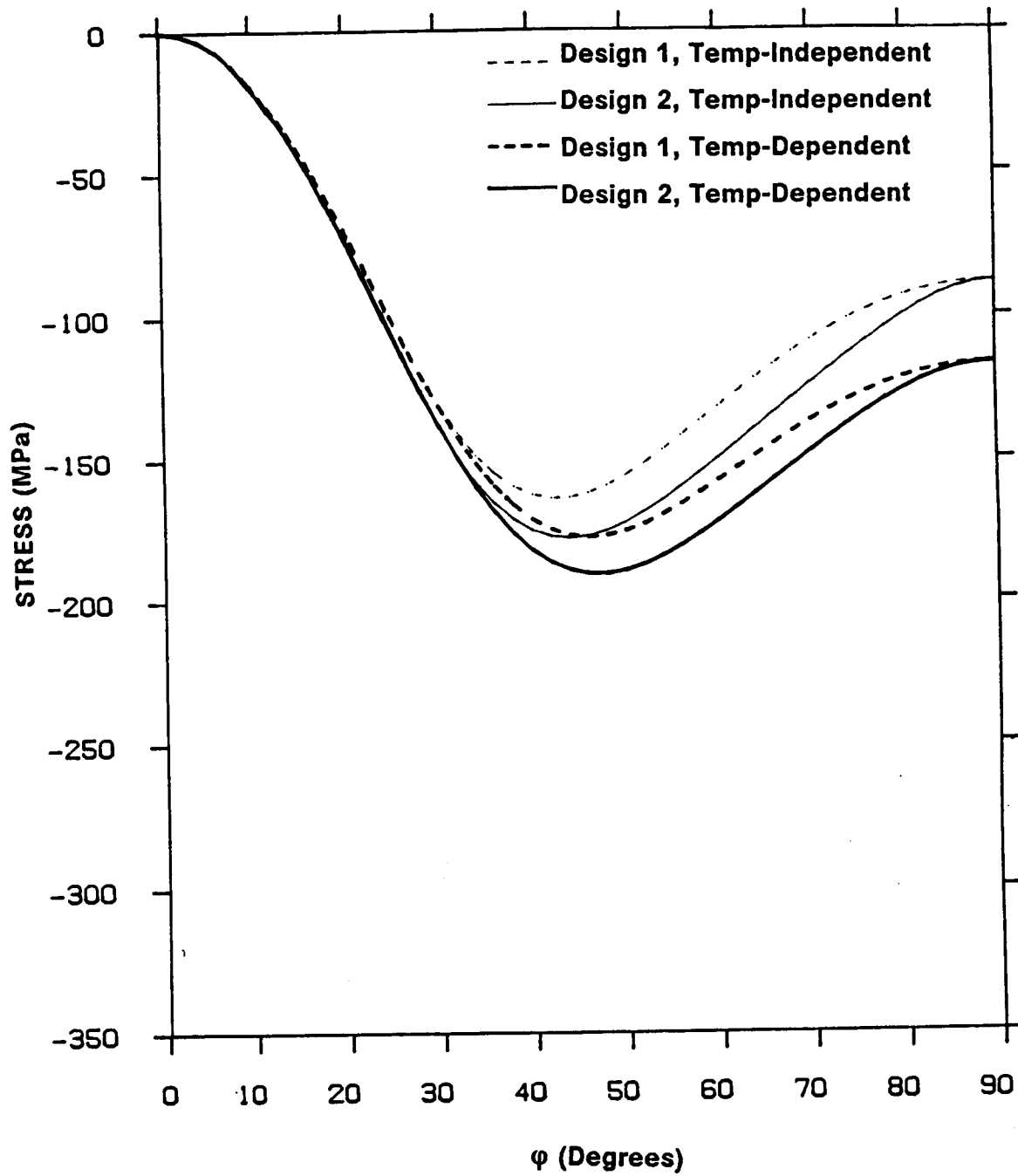


Figure 19. Fiber-Direction Stress vs. Ply Orientation Angle,  $\phi$ : Temperature-dependent and temperature-independent material properties, Designs 1 and 2,  $T = 116$  K, Stress at inner radius.

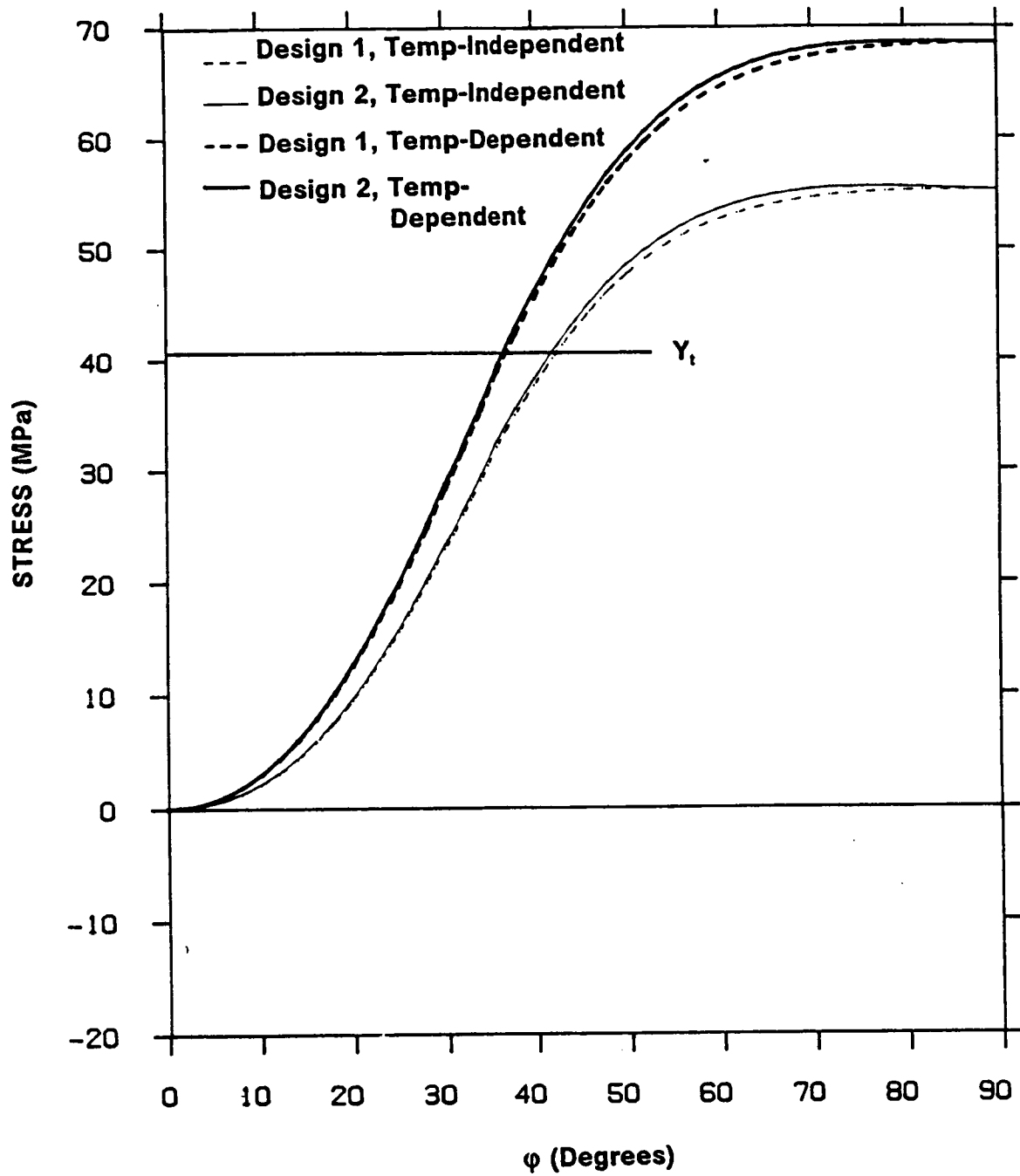


Figure 20. Transverse Stress vs. Ply Orientation Angle,  $\phi$ : Temperature-dependent and temperature-independent material properties, Designs 1 and 2,  $T = 116$  K, Stress at inner radius.

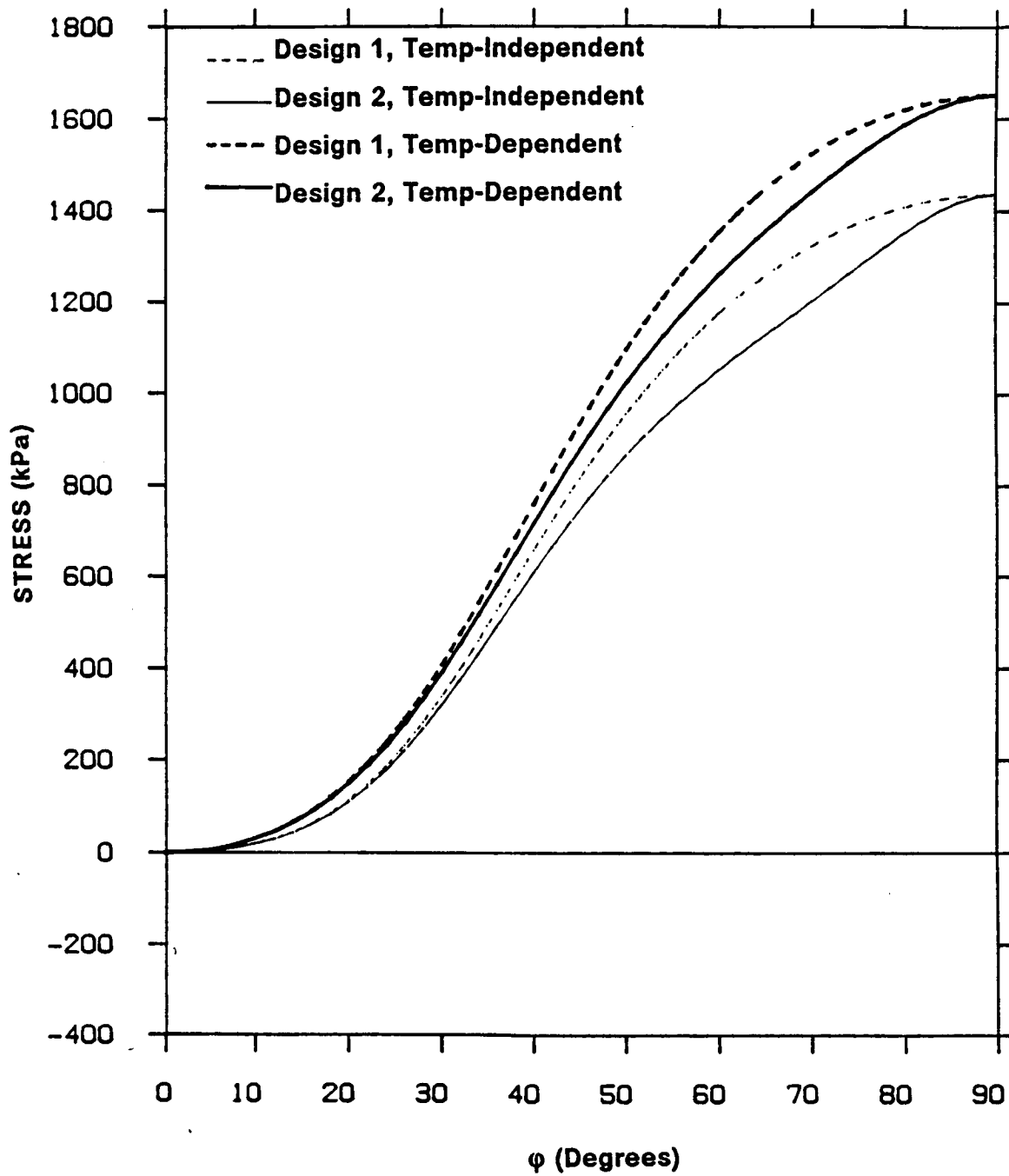


Figure 21. Radial Stress vs. Ply Orientation Angle,  $\phi$ : Temperature-dependent and temperature-independent material properties, Designs 1 and 2,  $T = 116$  K, Stress at  $0/\phi$  interface.

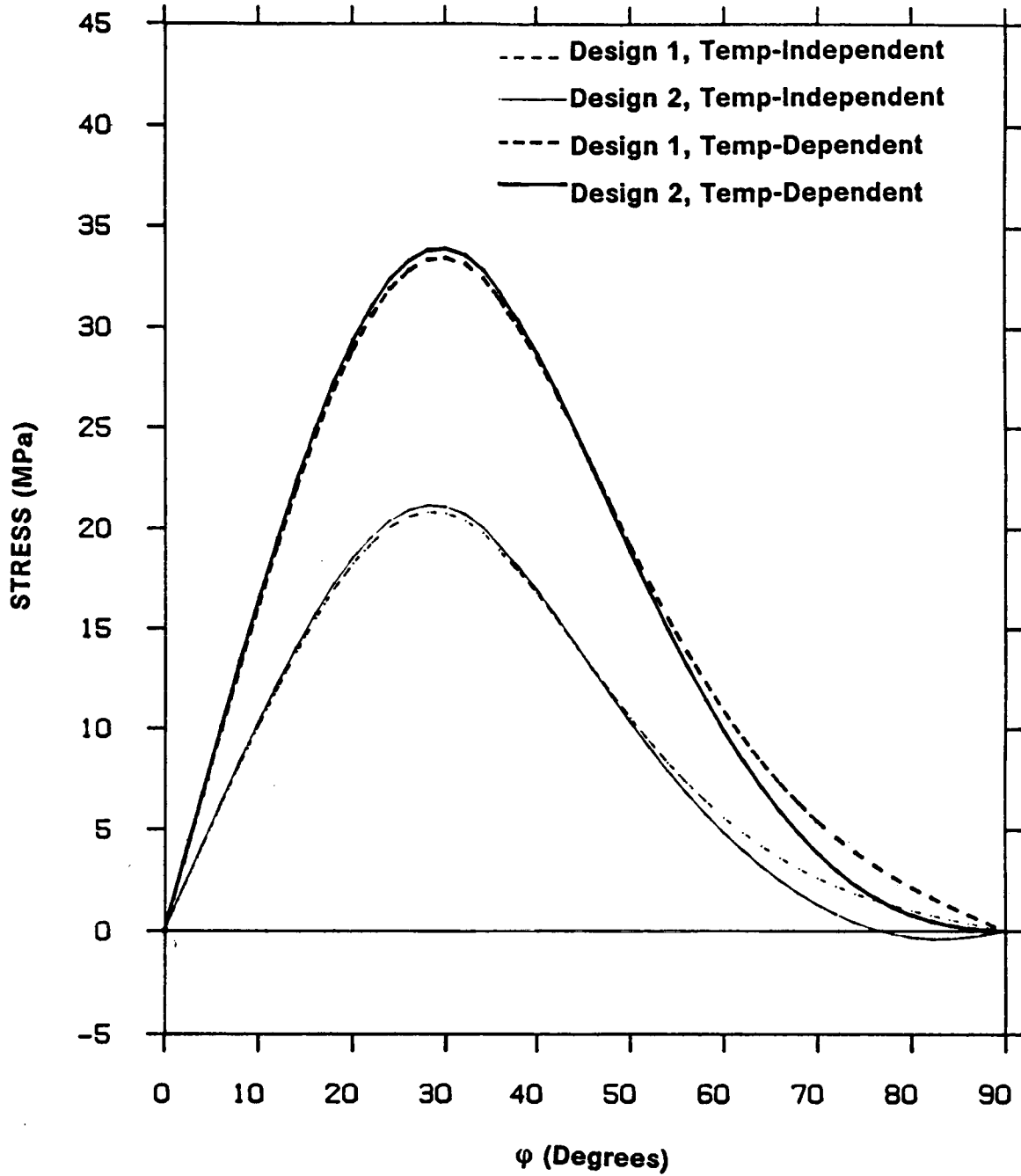


Figure 22. Shear Stress vs. Ply Orientation Angle,  $\phi$ : Temperature-dependent and temperature-independent material properties, Designs 1 and 2,  $T = 116$  K, Stress at inner radius.

transverse properties in the off-axis plies dominate axial response at that angle and it is the transverse properties that are most influenced by temperature. For  $\phi = 0^\circ$  (unidirectional  $0^\circ$  tube), axial strain is zero since  $\epsilon_1^T$  is assumed to be zero for both types of material properties. It is interesting to note that the tubes expand for off-axis angles less than  $50^\circ$  and contract for off-axis angles greater than  $50^\circ$ . This is due to the interaction between fiber direction and transverse direction properties in the off-axis and axial layers.

Figure 17 and Figure 18 show the effect on the twist parameter  $\gamma^\circ$  of varying ply orientation angle. For both designs the twist parameter is a maximum at approximately  $\phi = 70^\circ$ . The use of temperature-dependent material properties not only results in a lower value of  $\gamma^\circ$ , but it also shifts the point of maximum  $\gamma^\circ$  from  $\phi = 72^\circ$  to  $\phi = 65^\circ$ . The twist is, of course, exactly zero at  $\phi = 0^\circ$  and  $90^\circ$ .

Figure 19 - Figure 22 illustrate the dependence of the four components of stress on the off-axis angle for the two designs. The radial locations of the stresses are, again, those shown in Table 2. It can be seen that in all cases, over the entire range of  $\phi$ , the use of temperature-dependent material properties results in higher predicted stresses. This phenomenon is design dependent and with other laminates or other materials, the temperature dependency of the material might lower, rather than increase, the magnitudes of the stresses. It is worthwhile to note in Figure 22 that the maximum shear stress occurs at approximately  $\phi = 30^\circ$ . The shear stresses are zero at  $\phi = 0$ . Thus, for the low off-axis angles being considered for the space station tubes, a small change in  $\phi$  can result in a relatively large change in  $\tau_{12}$ .

Finally, for the balanced-unsymmetric tube (Design 2), the use of temperature-independent material properties indicates a change of sign for  $\tau_{12}$  at high off-axis angles that is not seen when temperature-dependent properties are used. This change in sign is even more evident for other unsymmetric designs. With one exception, none of the stresses reported in Figure 19 - Figure 22 exceed typical graphite-epoxy failure strengths, although the interaction

of all four components might produce a combined loading case that exceeds initial failure limits. The one exception to this statement is the transverse component,  $\sigma_2$ . As is noted in Figure 20, the transverse tensile failure strength for graphite-epoxy,  $Y_t$  is approximately 40 MPa<sup>20</sup>. This value is exceeded by the designs considered here in the range of  $\phi > 35^\circ$ . This means that even for relatively low ( $35^\circ$ ) values of  $\phi$ , matrix cracking will occur in the off-axis plies of these designs, at an operating temperature of 116 K. From this fact the conclusion can be drawn that for the space station application, the most critical design considerations should involve minimizing transverse tensile stress in the off-axis plies, and maximizing the transverse tensile strength of the graphite-epoxy material system chosen.

This concludes the analysis of the significance of including temperature dependent material properties in an analysis. It can be concluded that inclusion of the effect is important. In addition, ply orientation angle and tube design can play an important role in determining tube response. It is clear, however, that composite materials provide enough parameters to vary that a satisfactory design can be achieved.

### ***3.3 Comparison of Coated and Uncoated Tubes***

As stated earlier, aluminum coatings on composite tubes would protect the epoxy matrix from degradation due to the free atomic oxygen encountered in the orbital environment. In addition, because of the high thermal conductivity of aluminum, an aluminum coating would tend to prevent large thermal gradients from developing either axially or circumferentially within the tube. A major question is the influence of the coating on the response of the tube... and the influence of the tube on the aluminum coating. Excessive stresses in the coating may cause it to tear. Excessive stresses between the coating and the tube itself could cause the coating to separate from the tube. Both situations are undesirable. In this section the effect

of an aluminum coating on the predicted tube behavior will be presented. The stresses and deformations predicted in the tube with a coating will be compared to the stresses and deformations predicted in the uncoated tubes. The stresses and deformations in the uncoated tubes have just been presented. However, for comparative purposes, they will be presented again, plotted with the predictions of the responses of the coated tubes. With the presentation to follow, the stresses in the coatings themselves will also be illustrated.

The word "coating" is somewhat of a misnomer. It is envisioned that the aluminum would be added to the inner and outer tube surfaces by wrapping a foil, in the form of a tape, on the tube surfaces. The foil would be attached to the tube with a layer of epoxy adhesive. Experience has shown that inclusion of this adhesive layer in numerical analyses has a significant effect on predicted stresses and deformations. Here, it will be assumed that the foil is 6061 aluminum and is 0.051 mm thick. It will be assumed that the adhesive layer is 0.076 mm thick. The inner and outer surfaces of the tube are wrapped with foil. Unfortunately, no temperature-dependent material properties are available for the epoxy adhesive. Therefore, temperature-independent material properties will be used. For continuity, the format of the following figures is identical to the format previously used. When possible, the same scaling of the figures is used.

Figure 23 - Figure 26, illustrate the through-the-thickness variations of the four components of stress. The stresses illustrated in Figure 23 are the fiber-direction stresses,  $\sigma_1$ , in the graphite-epoxy tube and the axial stress,  $\sigma_x$ , in the isotropic coating. In Figure 24 the stresses are the matrix direction stress,  $\sigma_2$ , in the graphite-epoxy, and the hoop stress,  $\sigma_\theta$ , in the coating. In Figure 26, the stresses are, respectively,  $\tau_{12}$  and  $\tau_{x\theta}$ . Later figures will illustrate the principal stresses and the maximum shear stresses in the aluminum. When examining the figures it should be noted that the uncoated tubes have a smaller wall thickness. The non-dimensional wall thickness parameter,  $\rho$ , has been scaled to the coated tubes. Thus, the inner and outer radii of the uncoated tubes are located at  $\rho = 0.0625$  and  $\rho = 0.9375$  respectively. The inner and outer radii of the uncoated tubes are indicated on the figures.

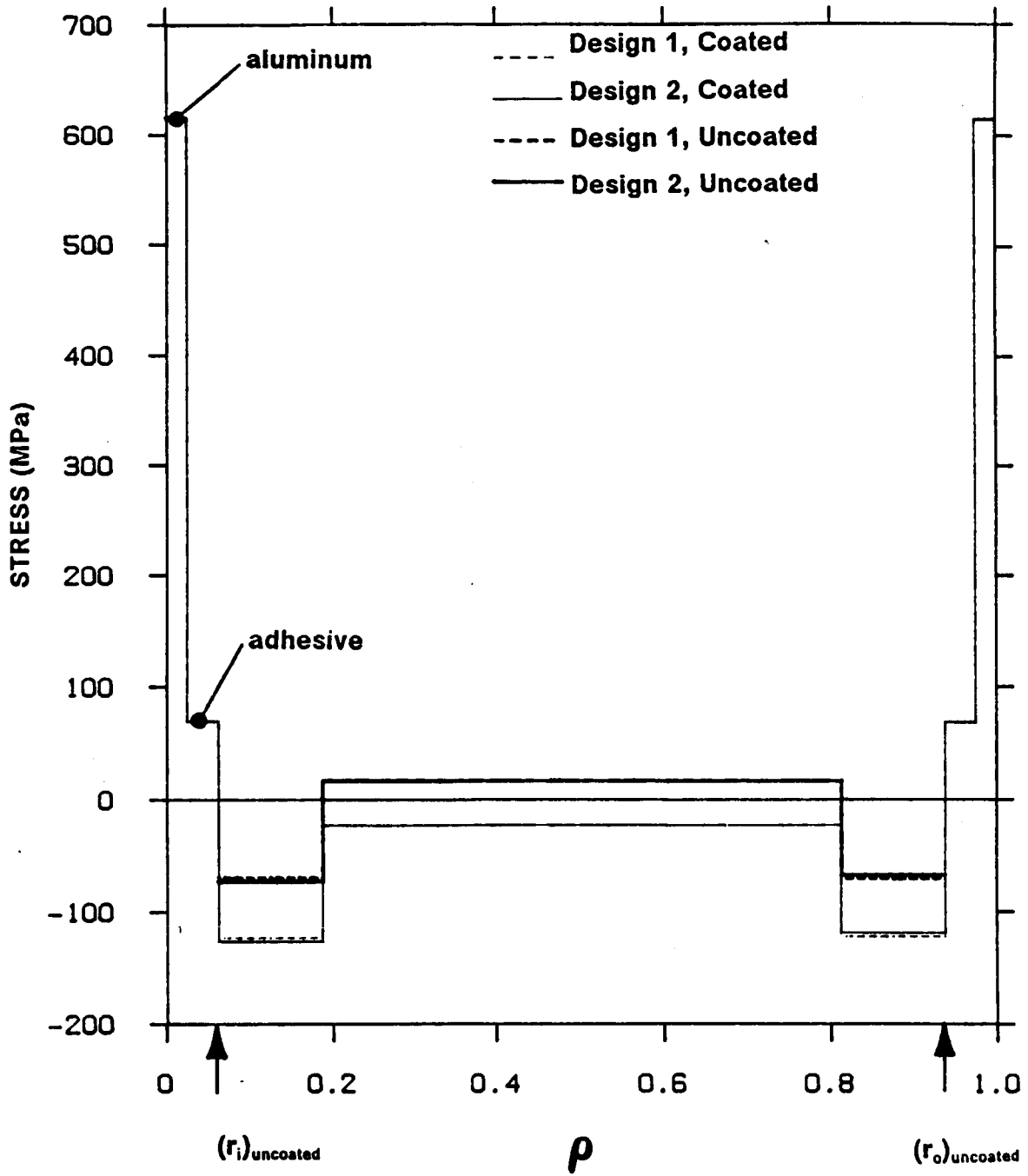


Figure 23. Fiber-Direction Stress Variation Through-The-Thickness, with Coatings: Temperature-dependent material properties, Designs 1 and 2,  $\varphi = 20^\circ$ ,  $T = 116$  K.

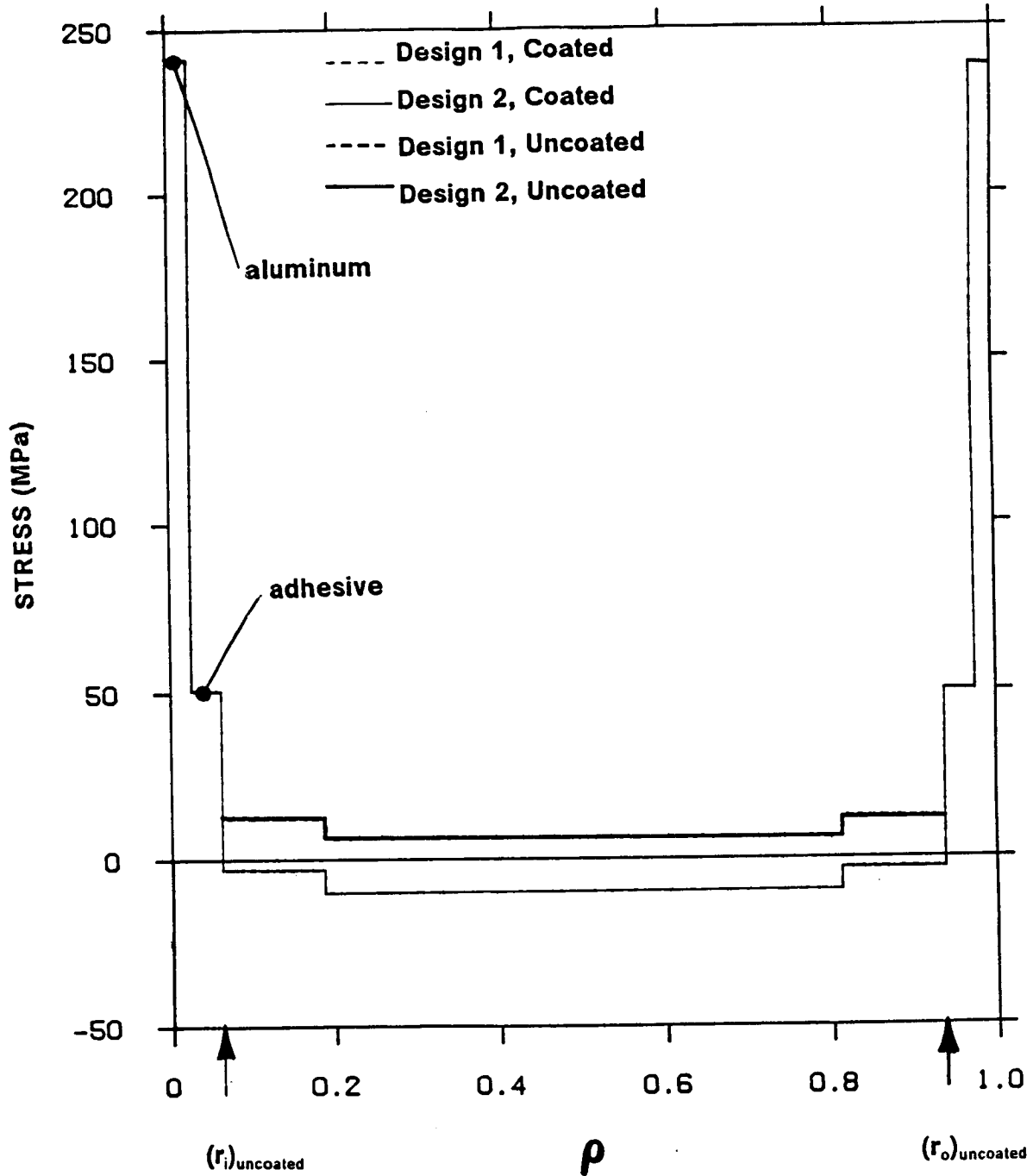


Figure 24. Transverse Stress Variation Through-The-Thickness, with Coatings: Temperature-dependent material properties, Designs 1 and 2,  $\phi = 20^\circ$ ,  $T = 116$  K.

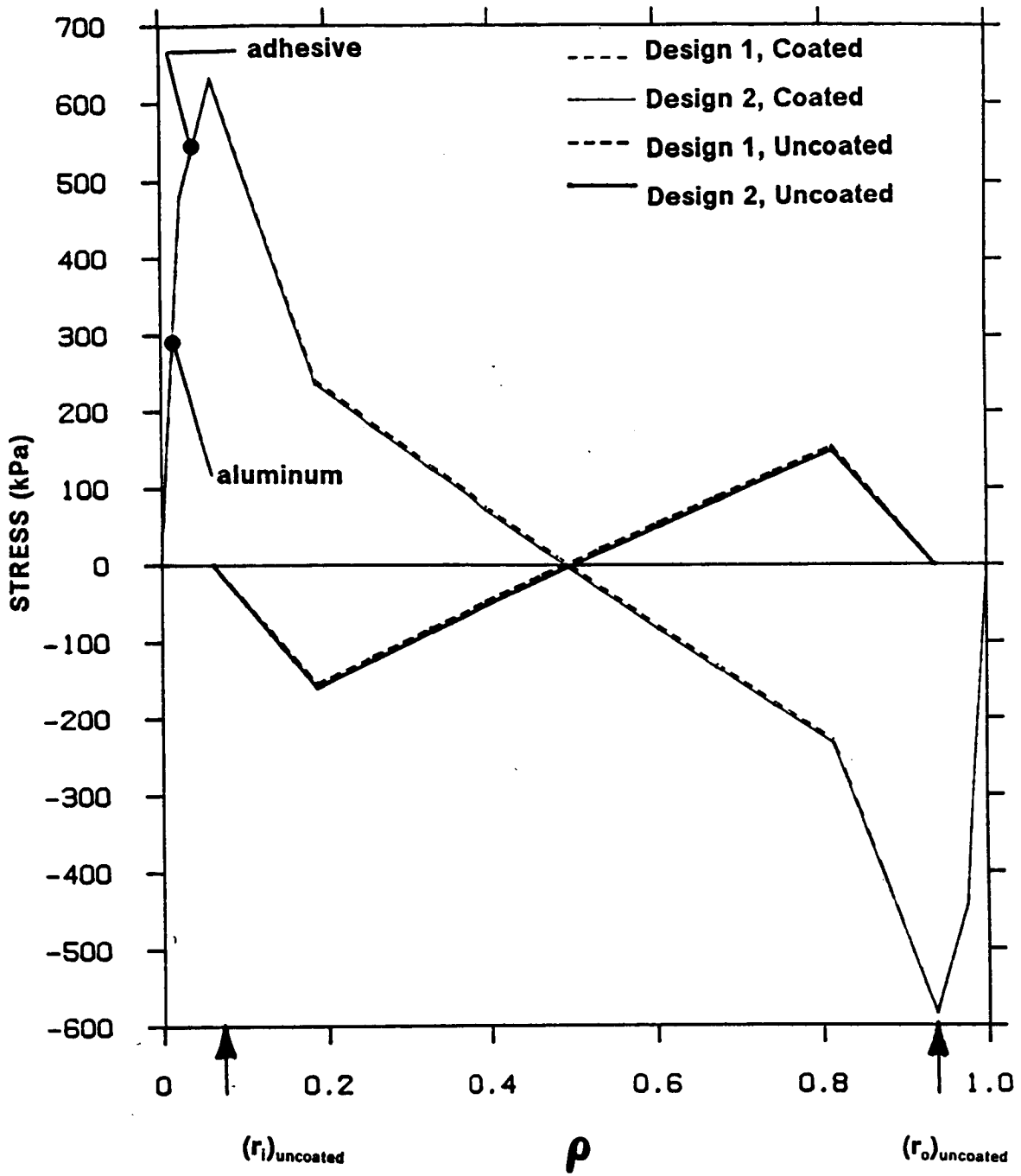


Figure 25. Radial Stress Variation Through-The-Thickness, with Coatings: Temperature-dependent material properties, Designs 1 and 2,  $\phi = 20^\circ$ ,  $T = 116$  K.

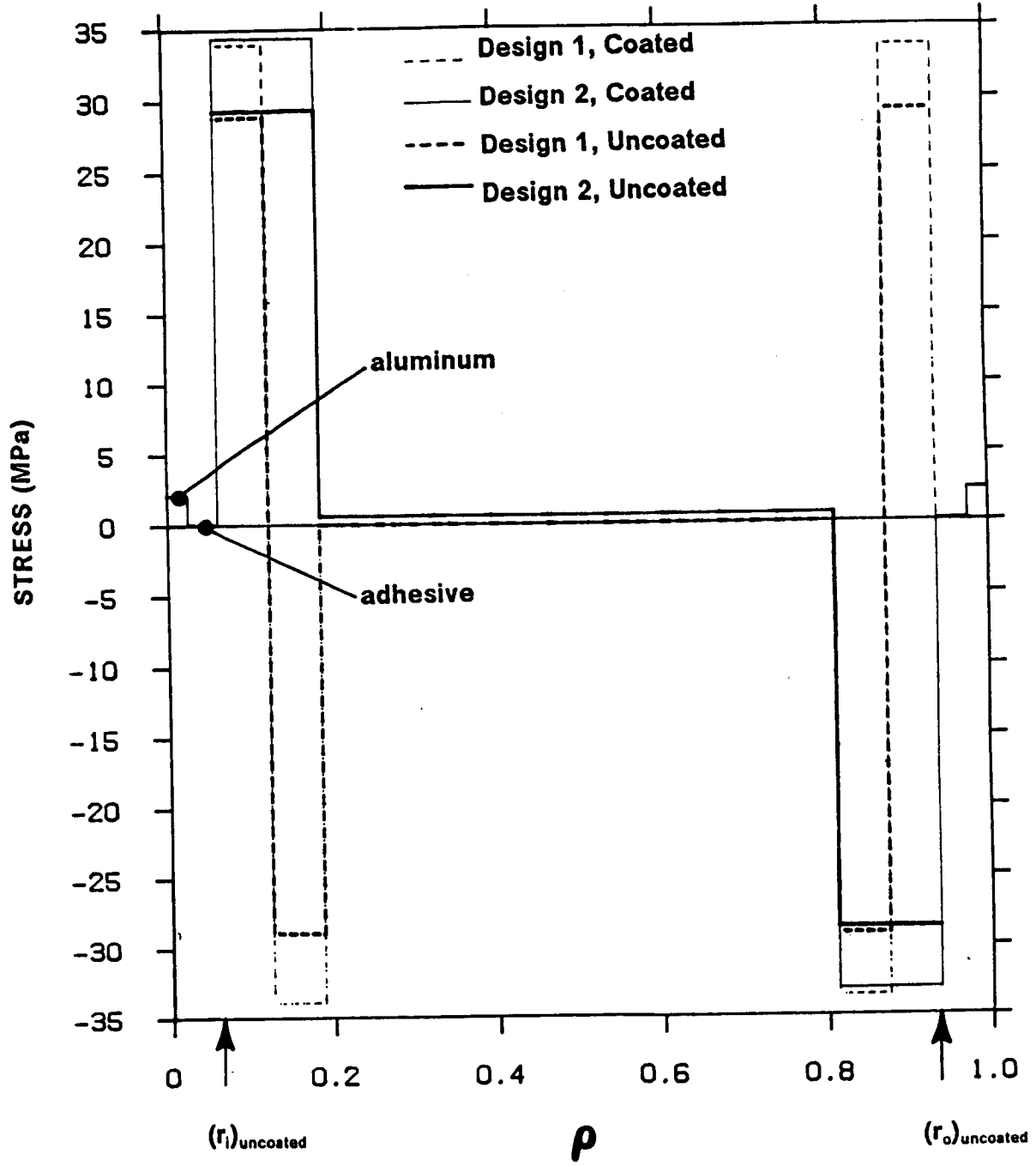


Figure 26. Shear Stress Variation Through-The-Thickness, with Coatings: Temperature-dependent material properties, Designs 1 and 2,  $\varphi = 20^\circ$ ,  $T = 116$  K.

The most obvious characteristic of Figure 23 and Figure 24 is the high stress level in the aluminum coating. It should be noted that axial and hoop stresses,  $\sigma_x$  and  $\sigma_\theta$ , are not necessarily maximum principal stresses, nor is  $\tau_{12}$  maximum shear stress. It is therefore incorrect to draw conclusions about maximum coating stresses from Figure 23, Figure 24, or Figure 26. A following section will discuss coating stresses in detail, however it is useful to note at this point how high the predicted coating stresses are. It is assumed that 6061 aluminum yields at  $\sim 75$  MPa, and it is therefore clear that the aluminum is considerably past yield and the stress calculations are in error. On the other hand, other aluminums have a higher yield stress and the cryogenic temperature may raise the yield to an even higher stress level. In this case, the linear elastic results of these figures would be a good first approximation to reality.

Although the aluminum and adhesive coatings comprise only a small amount of the cross sectional area of the tubes, and despite the fact that the aluminum and adhesive materials are much more compliant than graphite-epoxy in the fiber direction, the coatings have a noticeable effect on the stresses in the graphite-epoxy. For example, as can be seen in Figure 23, the fiber direction stress  $\sigma_1$  in the coated tube is opposite in sign in the  $0^\circ$  plies, when compared to the uncoated case, and 70 % higher in magnitude in the off-axis plies. Fortunately, these stress levels are quite low and so the effect of the coatings is of little consequence on  $\sigma_1$ . As can be seen in Figure 24, with a coating the stress component  $\sigma_2$  is compressive throughout the wall thickness. This could suppress matrix cracking, a beneficial effect. The most radically influenced stress is the radial stress component,  $\sigma_3$ , as seen in Figure 25. With a coating the radial stress component completely changes character, including a sign change. In the inner and outer graphite-epoxy layers the stress magnitude also changes. The most telling effect of the coating is evident in Figure 25. The radial stress in the adhesive is compressive for the outer foil and tensile for the inner foil. This means that the outer foil is contracting due to the temperature drop, and is squeezing the tube in the radial direction. The inner foil is also contracting, and is trying to pull away from the inner

surface of the graphite-epoxy. This means that the outer coating will not peel off, while the inner one may. Detailed information regarding the tendency of a coating to peel off is an advantage of an elasticity approach. Peel tendencies could be implied from a shell-like analysis by examining the hoop strains in the aluminum and the tube. However, the elasticity approach is more direct and gives the magnitude of the peel stress. Figure 26 indicates that the shear stress,  $\tau_{12}$ , is not significantly altered, and that the shear stress in the foil is quite small. The shear stress in the relatively compliant adhesive is negligible.

The influence of the coating on the axial strain and the twist response is illustrated in Figure 27 - Figure 29. Figure 27 shows that the coatings have an influence on the tube's axial deformation. This is an important finding if dimensional stability considerations are important. Figure 28 and Figure 29 indicate a small (1 %) change in the tube's shear deformation due to the presence of the coatings. Due to the isotropic nature of the coatings, this inertness to influencing the twist could be expected.

Figure 30 - Figure 33 indicate the influence of the coating on the maximum stresses in the tubes as a function of ply orientation angle. The radial locations of the stresses in Figure 30 - Figure 33 are those shown in Table 2. From Figure 30, it is seen that the coatings increase the fiber-direction stress,  $\sigma_1$ , by as much as 100 %. This is because the axial contraction of the aluminum forces the fibers into compression. The 100 % increase is not a problem because relative to the fiber failure stress, the stress levels are quite low. Figure 31 indicates that the matrix direction stress,  $\sigma_2$ , is influenced in sign at the low off-axis angles and in magnitude at the higher values of  $\phi$ . At the lower off-axis angles the coating forces  $\sigma_2$  to be compressive. At the high off-axis angles, the values of  $\sigma_2$  exceed the failure stress levels of  $Y_t = 40$  MPa. As seen in Figure 32, the radial stress is also influenced by the coating. With or without the coating, the radial stress levels are so low that they are not an issue, except with respect to possible delamination propagation. In that regard, the effect of the coating is beneficial in that it lowers the maximum tensile radial stresses in the tubes. In fact, for low values of  $\phi$ , the radial stress is compressive. The shear stress,  $\tau_{12}$ , shown in Figure 33, is

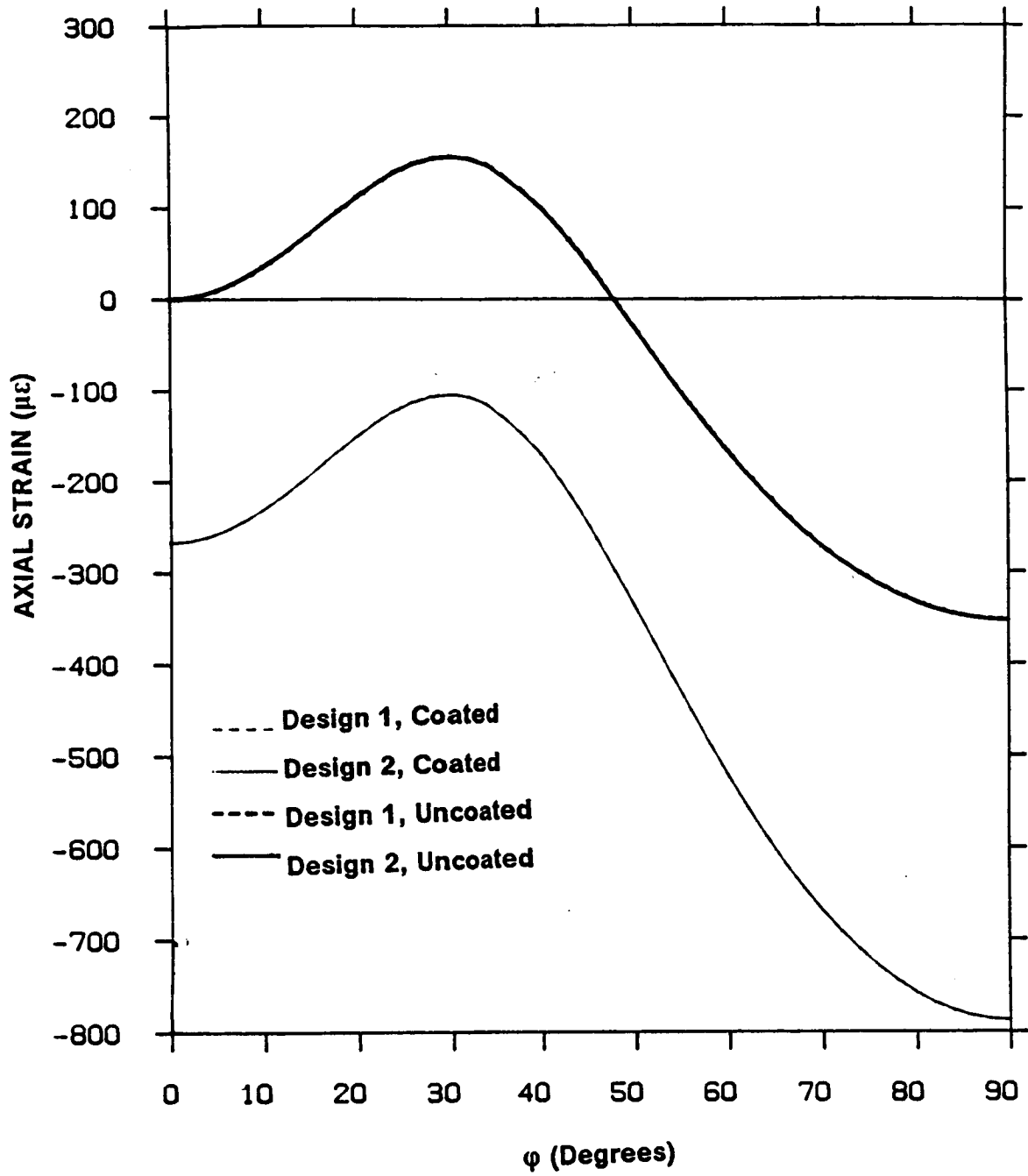


Figure 27. Axial Strain vs. Ply Orientation Angle,  $\phi$ , with Coatings: Temperature-dependent material properties, Designs 1 and 2,  $T = 116$  K.

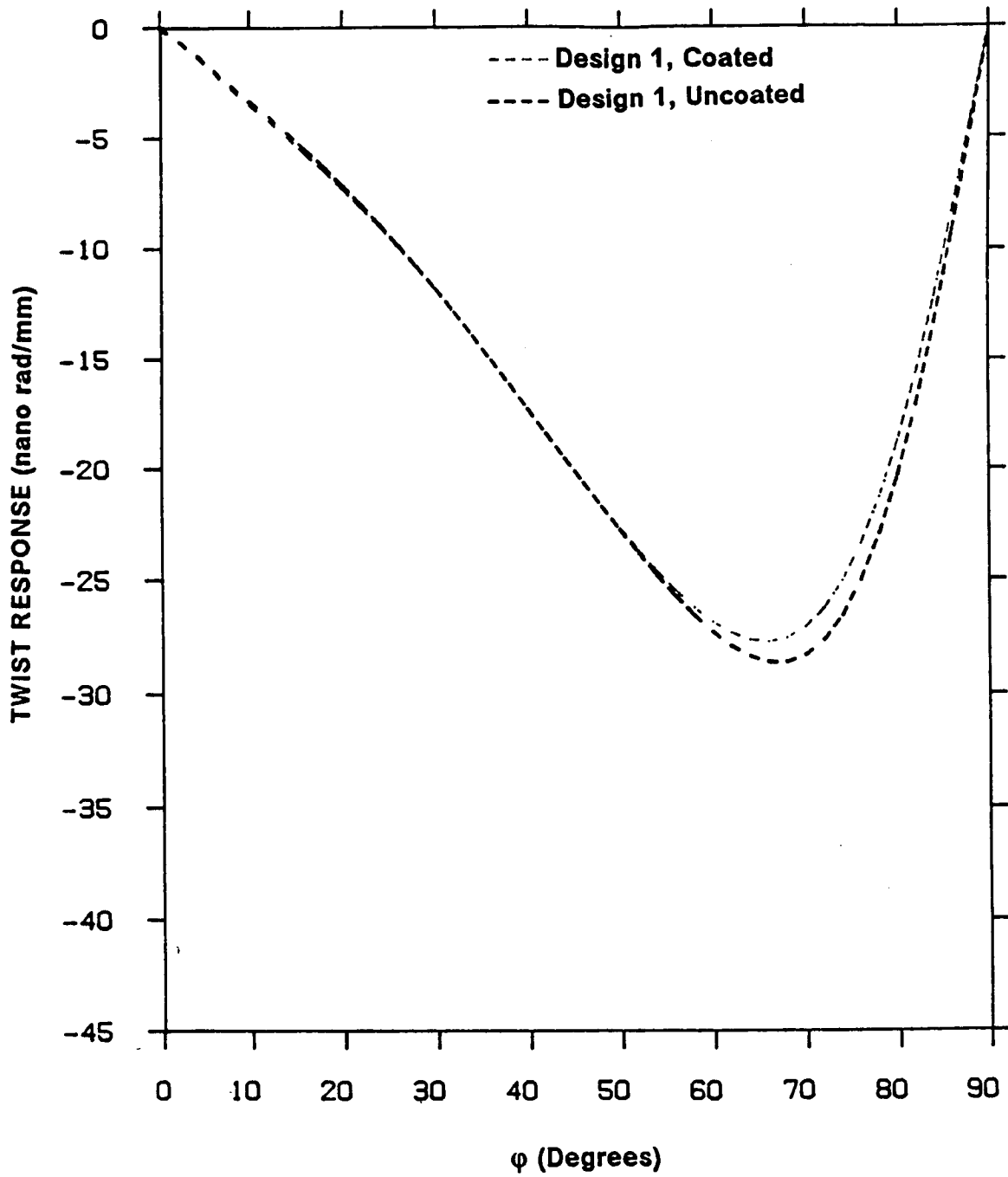


Figure 28. Shear Strain vs. Ply Orientation Angle,  $\phi$ , Design 1, with Coatings: Temperature-dependent material properties,  $T = 116$  K.

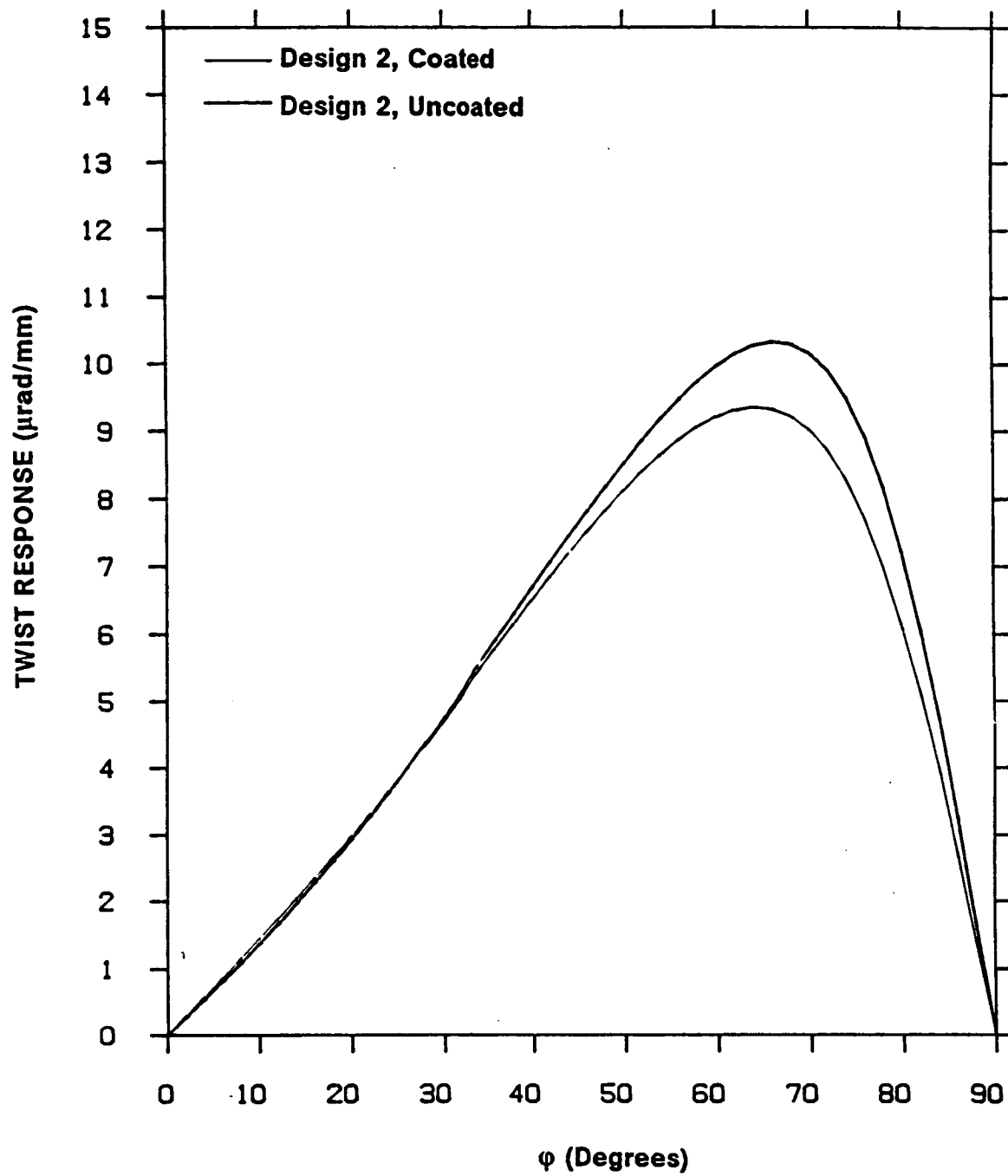


Figure 29. Shear Strain vs. Ply Orientation Angle,  $\phi$ , Design 2, with Coatings: Temperature-dependent material properties,  $T = 116$  K.

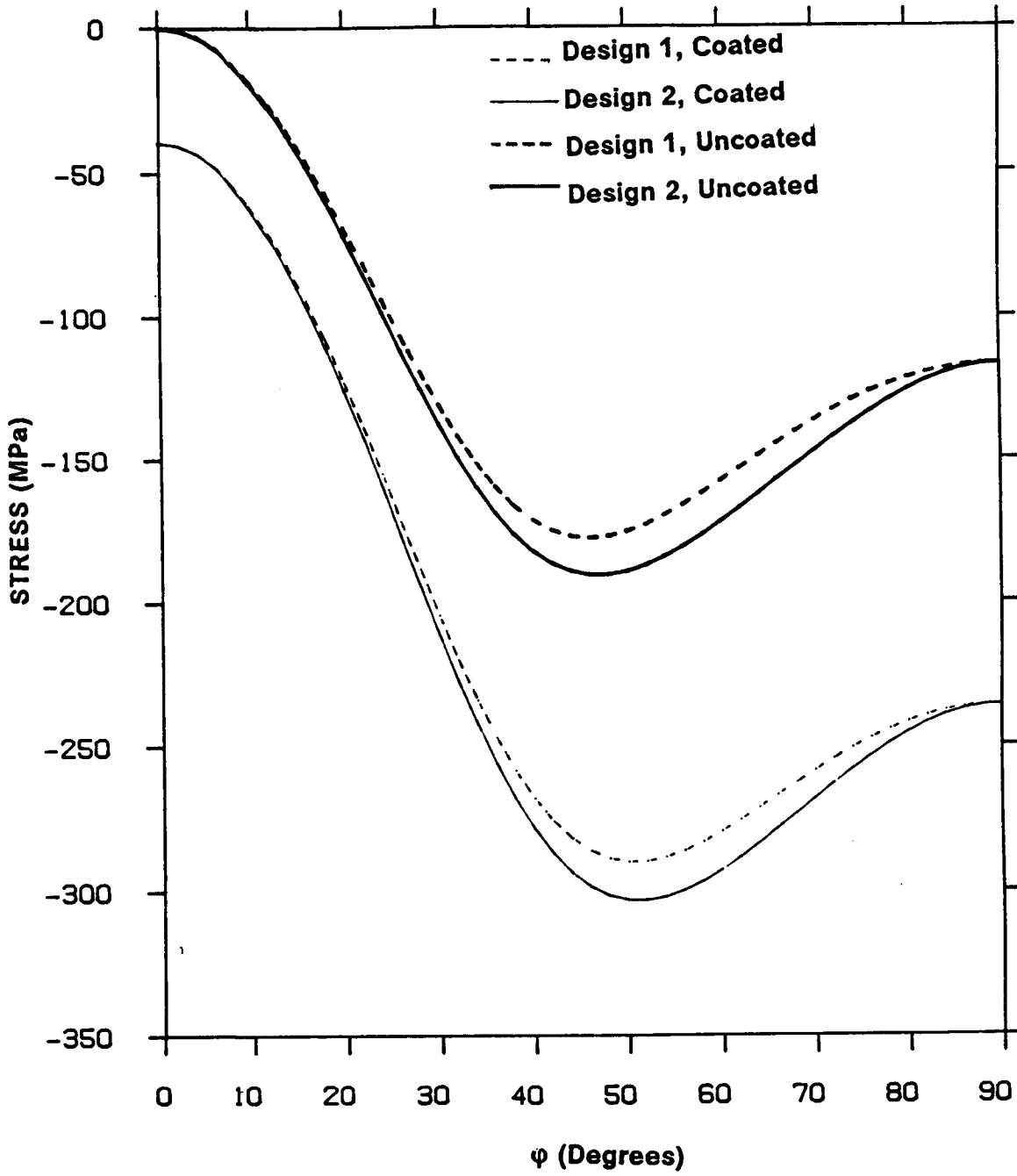


Figure 30. Fiber-Direction Stress vs. Ply Orientation Angle,  $\phi$ , with Coatings: Temperature-dependent material properties, Designs 1 and 2,  $T = 116$  K, Stress at inner radius.

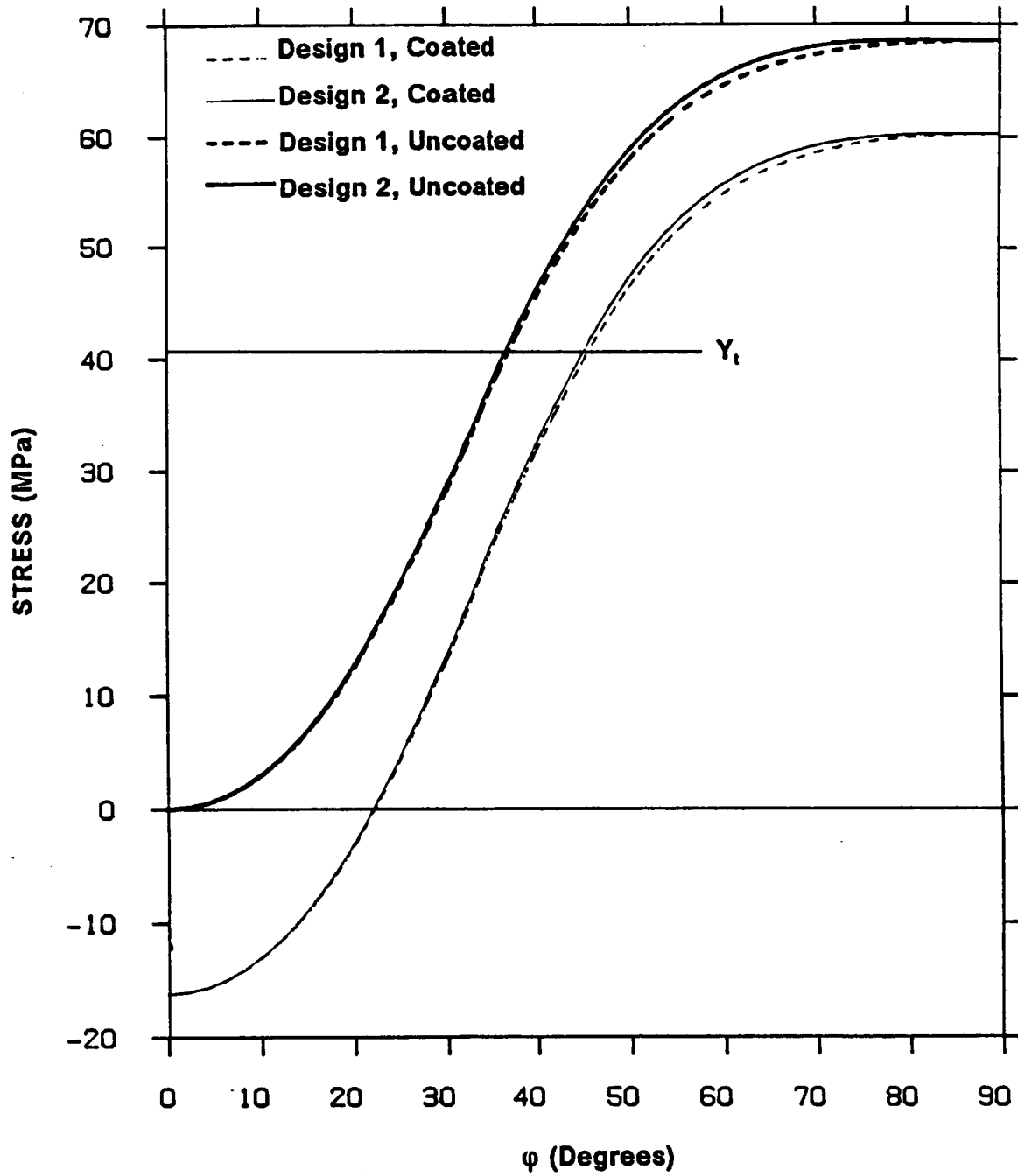


Figure 31. Transverse Stress vs. Ply Orientation Angle,  $\phi$ , with Coatings: Temperature-dependent material properties, Designs 1 and 2,  $T = 116$  K, Stress at inner radius.

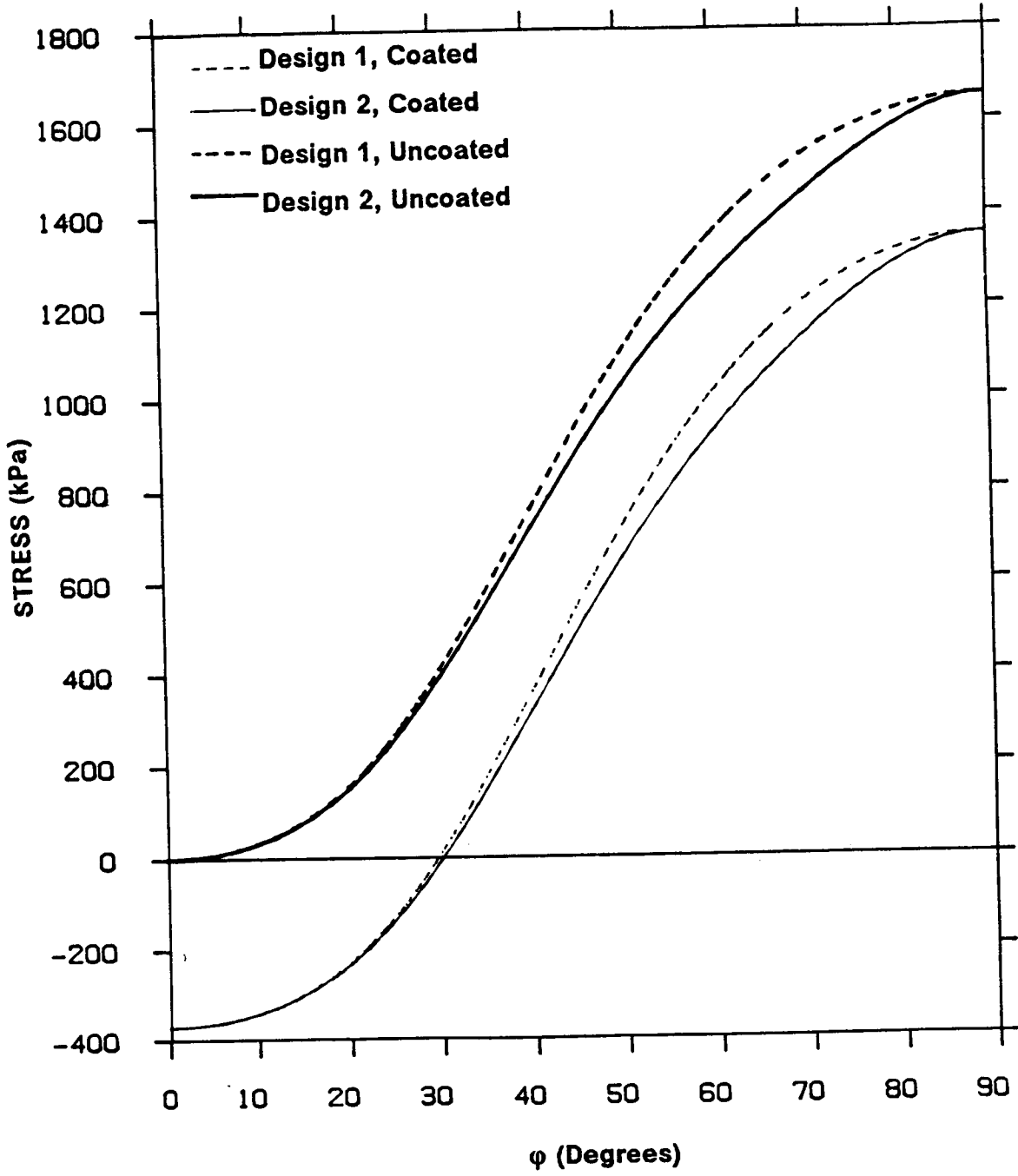


Figure 32. Radial Stress vs. Ply Orientation Angle,  $\phi$ , with Coatings: Temperature-dependent material properties, Designs 1 and 2,  $T = 116$  K, Stress at  $0/\phi$  interface.

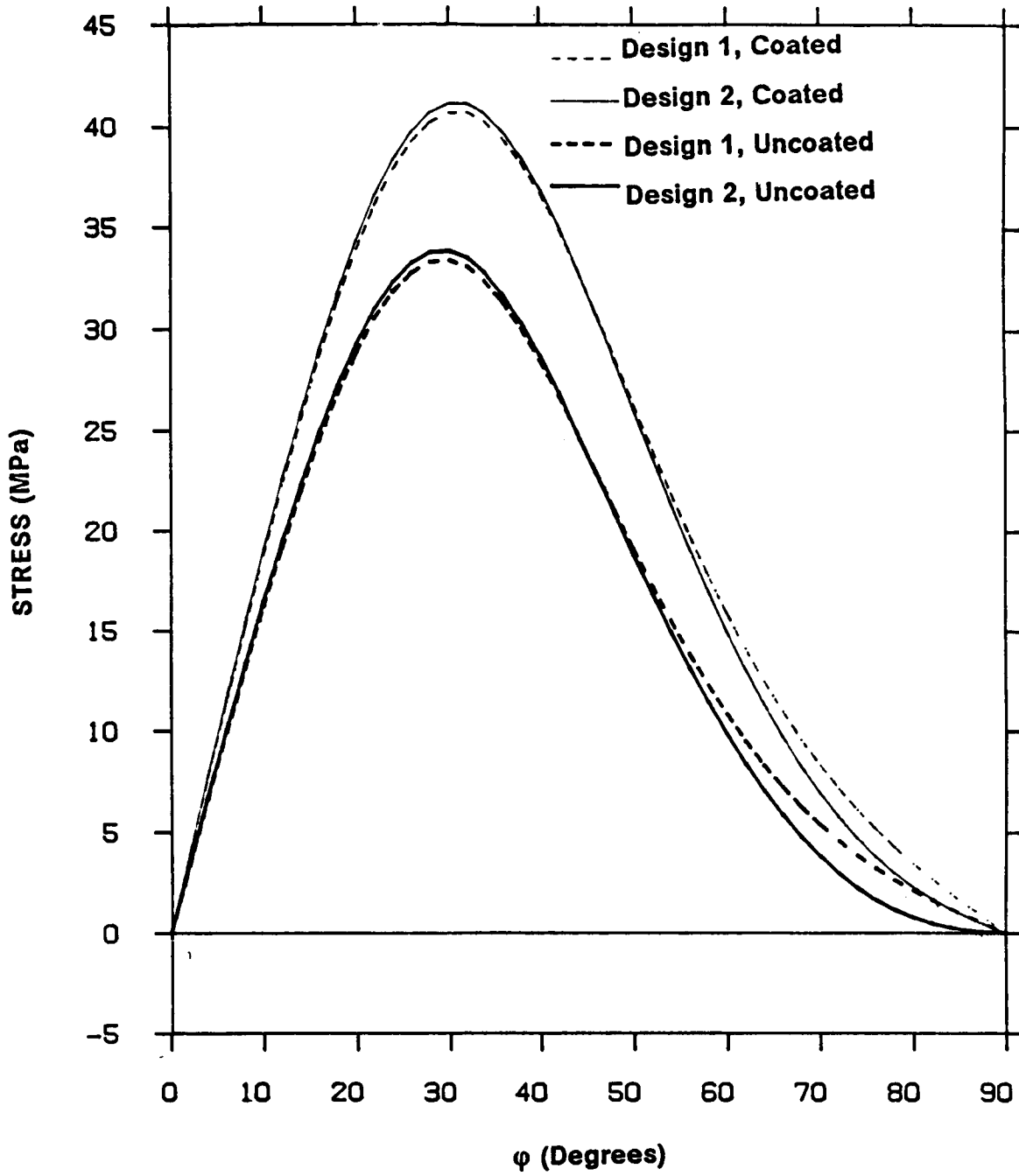


Figure 33. Shear Stress vs. Ply Orientation Angle,  $\phi$ , with Coatings: Temperature-dependent material properties, Designs 1 and 2,  $T = 116$  K, Stress at inner radius.

increased by the presence of the coating. At an off-axis angle of about  $30^\circ$ , the coating increases the shear stress by 20 %. Whereas this by itself is detrimental, the coating decreased the transverse stress  $\sigma_2$ . At this particular off-axis angle, the net influence of the coating is not perfectly clear. However, at lower off-axis angles, the coating may actually provide a more favorable stress state in the tube (see Figure 24 and the associated discussion).

### **3.4 Stresses in the Coatings**

In the previous section, Figure 23 - Figure 26 indicated that the predicted stresses in the aluminum coating were quite high (greater than the yield stress of aluminum). The deformations of the coatings are due mainly to the overall response of the graphite-epoxy tube, and it is this induced deformation that is the primary cause of the high stresses in the coatings, i.e. the large mismatch in material properties induces high stresses. For the isotropic aluminum, in order to accurately evaluate the stress state in the coatings, the maximum principal stress and the maximum shear stress should be considered. The stresses in the outer coating are greater and therefore they will be evaluated. Figure 34 and Figure 35 illustrate the maximum principal stress and the maximum shear stress in the coating as a function of off-axis ply angle in the graphite-epoxy. The stresses reported are those calculated at the adhesive/aluminum interface. At this location, the stresses in the aluminum are greatest. The most obvious feature of Figure 34 and Figure 35 is that the normal and shear stresses both exceed 6061 yield strengths (110 MPa and 55 MPa, respectively) by large margins. Since the scope of this investigation does not include a plasticity analysis of the coatings, suffice it to say that failure of the coating is predicted. However, in a qualitative sense, these results are useful in noting the effect of the overall tube response on the coating. It is seen in both figures that at high values of  $\phi$ , where the twist deformations of the two designs are noticeably different, the max-

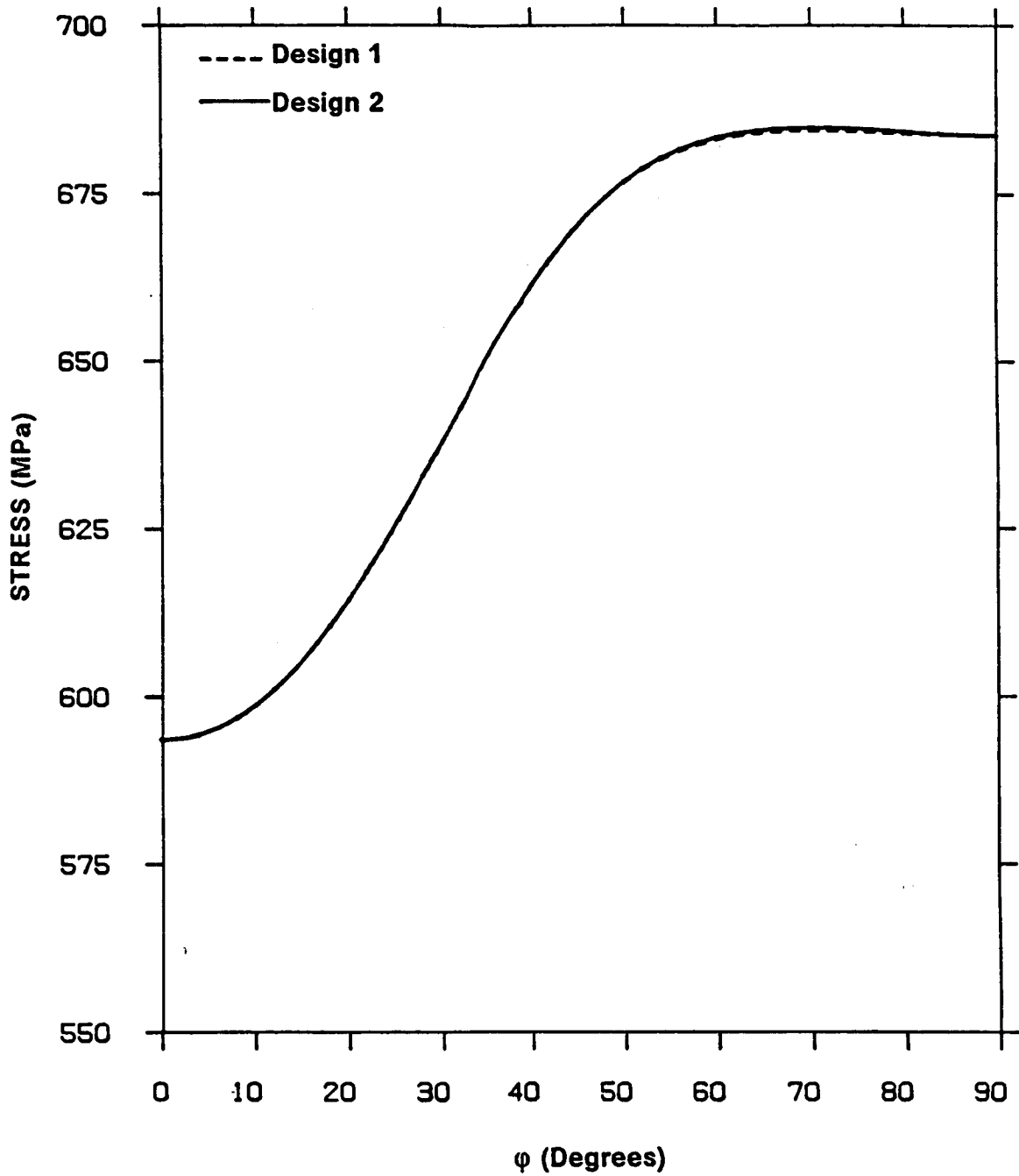


Figure 34. Maximum Principal Stress vs. Ply Orientation Angle,  $\phi$ : Temperature-dependent material properties, Designs 1 and 2,  $T = 116$  K, Stress at adhesive/aluminum interface.

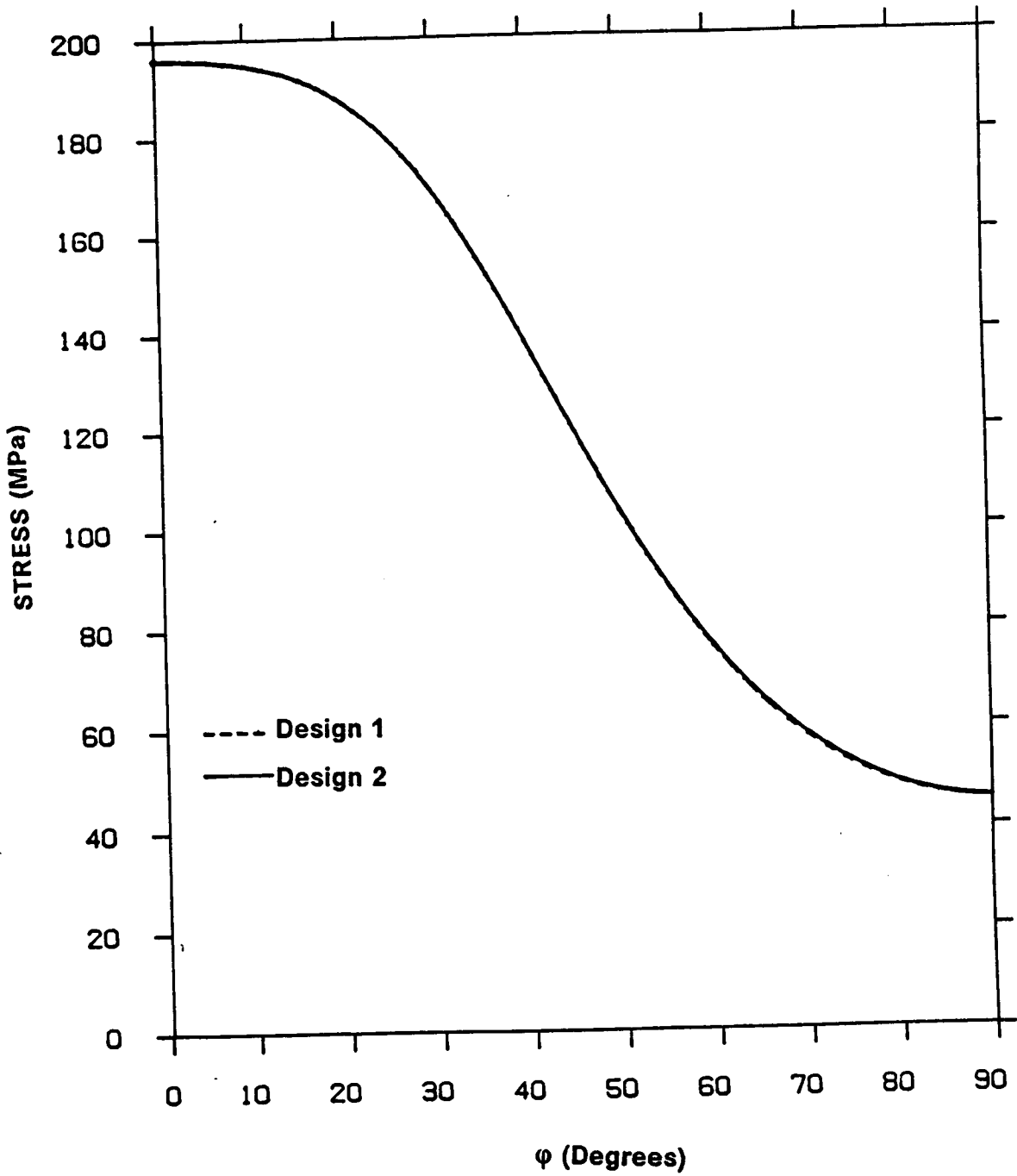


Figure 35. Maximum Shear Stress vs. Ply Orientation Angle,  $\phi$ : Temperature-dependent material properties, Designs 1 and 2,  $T = 116$  K, Stress at adhesive/aluminum interface.

imum shear stress induced in the coatings is virtually the same. It is thus apparent that the twist of the tube does not influence the stress in the coating. Rather, the coating stresses are due to axial and hoop deformations of the tube. It should be mentioned that these results are valid only for these tube designs and extension of the conclusions to other tube designs should be verified.

This concludes the section on coating stresses and this chapter of analytical predictions. In the following chapters experimental results will be presented and compared with predictions of the elasticity solution used to generate the numerical analysis in this chapter. It should be noted that two of the material systems used in the following experimental investigation are similar to the T300/934 graphite-epoxy presented in this chapter. Additionally, one of the test specimen lamination sequences is a specific case of the uncoated Design 2 seen in this chapter. Therefore, the results from two of the tests in the following experimental investigation may be compared directly to the data presented in this chapter.

## 4.0 Experimental Apparatus

It was felt that the twist phenomenon in the tubes was such a basic response that off-the-shelf equipment and transducers, modified for the particular application, could be used. The primary considerations in designing the experimental set-up were: (1) a method to change the temperature of the tube in a known and controllable fashion, (2) a method to measure the twist of one end of the tube relative to the other, and (3) accurate and automatic recording of the data. Secondary issues were the producing of a significant temperature change so that the twist response was measurable, and keeping the test set-up time and actual test time to a reasonable number of hours. With this latter issue resolved, a number of test specimens could be studied within the scope of this investigation. The design of the apparatus and consideration of other experimental aspects are discussed in this chapter.

### 4.1 Design

Figure 36 is a diagram of the apparatus configuration chosen. The major components of the apparatus were:

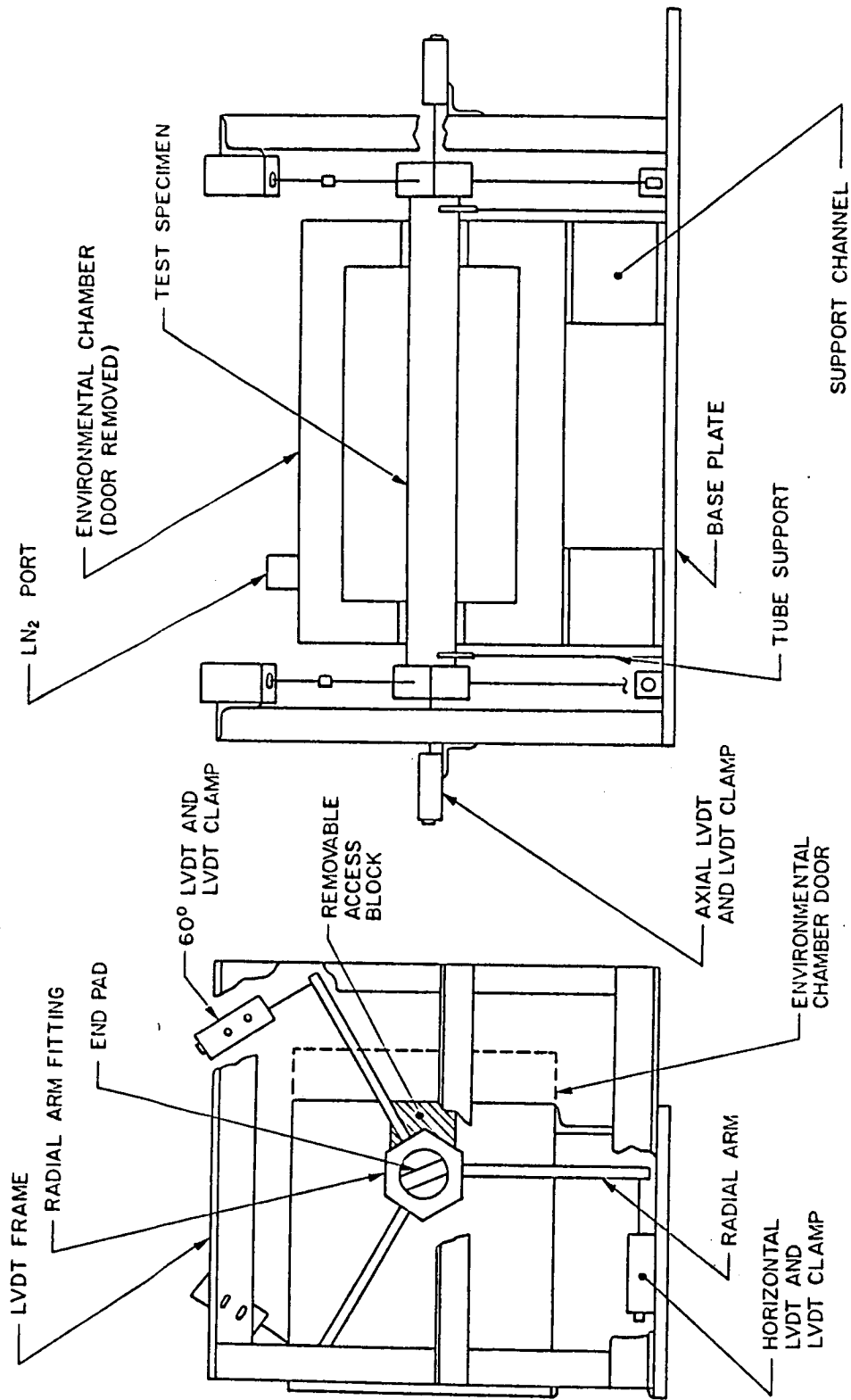


Figure 36. Configuration of Experimental Apparatus

- An Applied Test Systems (ATS) Series 2911 environmental chamber.
- A 12.7 mm thick aluminum base plate.
- Three steel support channels which supported the oven 120 mm above the base plate.
- Aluminum LVDT frames, located at each end of the chamber, on which the linearly variable displacement transducers (LVDT's) were mounted. These frames were constructed from 38 mm and 51 mm angles and were bolted together.
- Eight LVDT clamps, two of which were mounted on the base plate and six that were on the LVDT frames. The clamps were machined out of aluminum blocks.
- Eight LVDT's. At each end of the apparatus, three of the LVDT's measured tangential displacement, and the other measured axial displacement. One of the tangential LVDT's was mounted horizontally on the base plate, and the other two were oriented 60° from the horizontal and supported by the LVDT frame. The axial transducer was aligned with the tube axis and was also mounted on the LVDT frame.
- Two Y-shaped tube supports that were used to support the tubular test specimen. The supports were located just outside the oven, one at each end. They were threaded into the base plate and could be used to adjust the vertical position of the tube.
- Two hexagonal radial arm fittings that clamped on each end of the tube. Each fitting had three radial arms attached. An LVDT measured the tangential motion of the tip of each radial arm. The fittings were machined out of aluminum.
- Two zero-expansion glass end pads that fit into the the ends of the tube and provided a point for the axially oriented LVDT's to measure the displacement. The end pads were machined from Zerodur<sup>21</sup> glass.

The environmental chamber was used to control the temperature of the tube. The tube was cooled by venting liquid nitrogen (LN<sub>2</sub>) into the chamber and was heated by using the electrical resistance heater that was part of the chamber. The chamber was chosen because of its availability and size, the chamber and the apparatus being small enough to result in a table-top experiment. To conform to the dimensions of the environmental chamber, a test specimen length of 0.61 meters was chosen. A tube inside diameter of 50.8 mm and wall thickness of 1.78 mm were chosen in order to conform to current specifications for a space station truss structure. To support the test specimen and to measure the twist, the specimen protruded from the ends of the chamber. A horizontal test specimen orientation was chosen in order to eliminate any thermal "chimney effect" in the hollow specimen. The off-the-shelf chamber was modified by boring 57 mm diameter holes in each end to allow the specimen to protrude. To be able to move the tubular specimens in and out of the chamber conveniently, two slots were cut into the ends of the chamber. The portions of the chamber walls that were cut away to make the slots were put back into place when the tube was in position for testing. These are the access blocks referred to in Figure 36. This method for installing the tube in the oven was preferred over simply sliding it through the two holes (with no access slots). This method allowed the radial arm fittings to be clamped onto the tube and aligned with one another before the specimen was installed in the chamber. Additionally, this method of installation was preferred because the axial LVDT's did not have to be moved in order to install the test specimen. The ATS chamber was designed for operation with its major dimension in the vertical direction, however it was found to function adequately in the horizontal configuration.

A simple Y-shaped tube support at each end of the specimen cradled the tube and allowed it to freely expand and contract, conforming to the theoretical model developed earlier. The Y-shaped tube supports were wrapped with teflon tape in order to minimize friction on the test specimen.

At each end of the tube, the four transducers were used to measure the displacements. One of the transducers measured axial motion. The other three LVDT's measured the tangential displacements of the three arms that extended radially from the hexagonal fitting. Figure 37 illustrates the three radial arms extending from the fitting, and test specimen on which they are clamped. The radial arm fitting was a hexagonal shaped aluminum fitting. It was clamped to the tube to provide a base for the radial arms to attach to. The coordinate system used to describe the apparatus is shown in Figure 38. The coordinate  $x$  measures the axial location along the tube while  $\theta$  measures the circumferential location around the tube,  $\theta = 0^\circ$  is the bottom of the tube. Table 3 lists the numbering sequence and coordinates of the tips of the eight LVDT's, the points at which the test specimen displacements were measured. From Figure 36, Figure 38, and Table 3, it should be apparent that axial displacement was measured at each end of the test specimen, along the centerline of the tube. Tangential displacements at each end were measured at three equally spaced points around the circumference of the specimen, at a radial distance of 254 mm from the center of the tube, and 19 mm from each end of the 610 mm long specimen (resulting in a 572 mm effective gage length). It should be emphasized at this point that in the ideal situation the ends of the radial arms would move tangentially only because of the thermally-induced twist in the tube. In reality, the ends of the radial arms moved tangentially for other reasons. The additional movement was due primarily to the fact that the tube would experience bending deformations. These bending deformations would cause additional tangential displacement. The bending was due to a lack of a perfectly uniform circumferential temperature distribution, uniform material properties and geometric dimensions, and a slight amount of bending in the 210 mm long radial moment arms. Fortunately, given three separate measures of circumferential motion, the extraneous displacements could be determined and subsequently eliminated from the data so that the actual rotation of the end of the tube could be determined.

To measure the axial displacement of the tube, a glass bar (referred to as a glass end pad) was inserted into each end of the test specimen, perpendicular to the axis of the tube (see

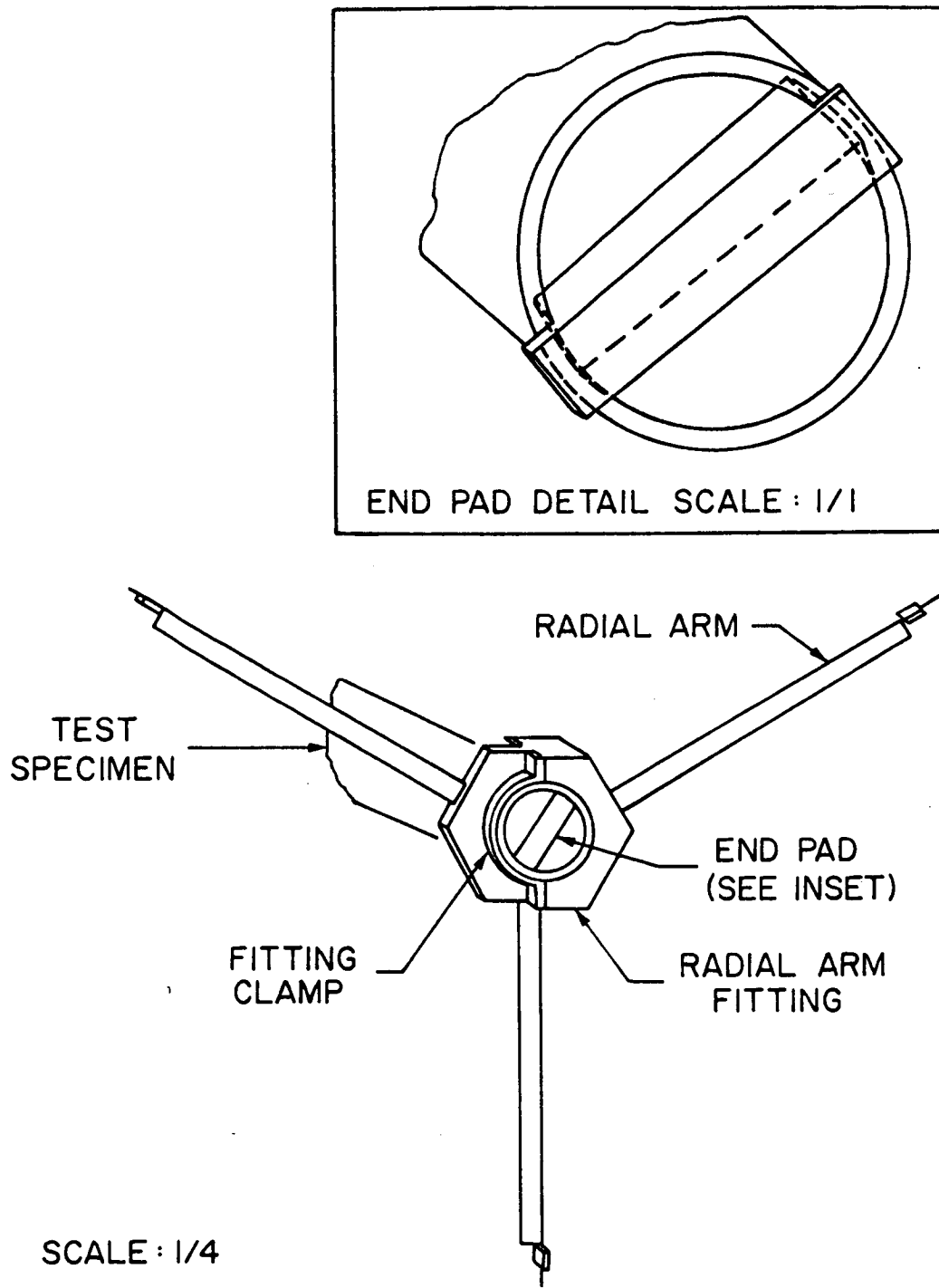


Figure 37. Radial Arm Fitting Mounted on Specimen: The glass end pad is shown in the inset.

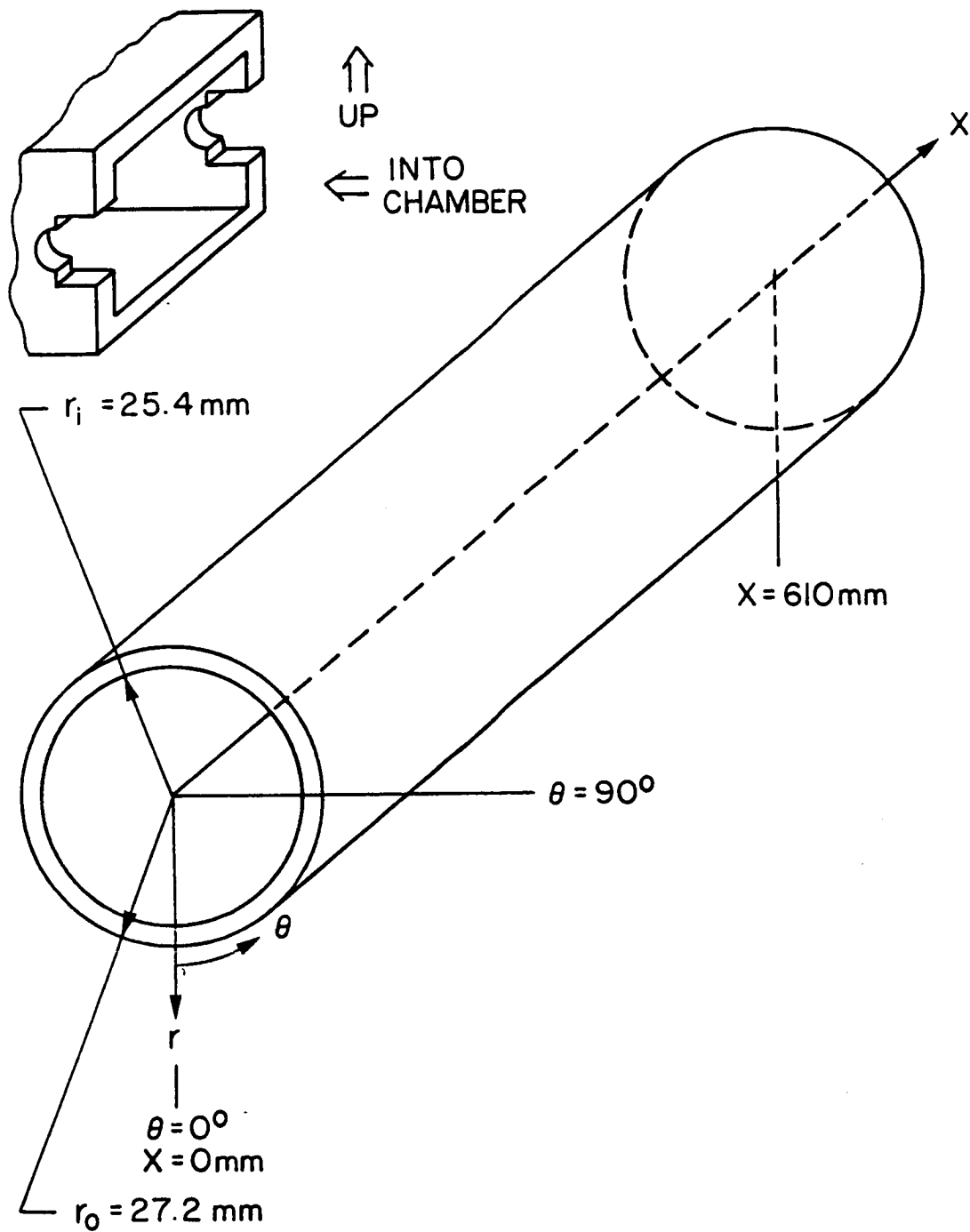


Figure 38. Test Specimen Coordinate System

**Table 3. LVDT Numbering Sequence and Coordinates**

<b>LVDT</b>	<b><i>x (mm)</i></b>	<b><math>\theta</math></b>	<b><i>r (mm)</i></b>
1	19	0°	254
2	19	120°	254
3	19	240°	254
4	591	0°	254
5	591	120°	254
6	591	240°	254
7	0	-	0
8	610	-	0

inset of Figure 37). The bar extended across the diameter of the tube and the axially oriented displacement transducers measured the axial motion of the glass bars. Zero-expansion glass was used so that any temperature change at the end of the tube would not cause any errors in the measured axial displacement. The outside of the environmental chamber was insulated with a variety of insulation in order to protect the support structure and LVDT's from large temperature gradients. Insulation was also inserted in the ends of the tube to shield the axial transducers.

In addition to the displacement measurements, which to a large degree dictated the design of the apparatus, temperature and strain measurements were also made. The temperature of the tube was measured, using K-type thermocouples, at a number of locations on each tube. Figure 39 indicates the locations of some of the thermocouples. In all, 14 thermocouples were used to measure the temperature at various locations in and around the environmental chamber. Thermocouples 4, 6, and 7 were used, on all specimens, to calculate the average temperature of the tube. Thermocouples 2, 3, and 4 or 5 were located coincident with the three strain gage rosettes, on the specimens which were gaged. Thermocouple 1 was located on a Zerodur glass reference material which was used for compensation of the strain gages for thermal effects. Thermocouples 8-14 were located in various positions outside the environmental chamber. These were used to monitor any temperature gradients on sensitive parts of the test apparatus, such as LVDT clamps and the radial arm fittings.

The thermally-induced twist and axial elongation were actually manifestations of thermally-induced strains. Both of these more global quantities could be related to the local values of shear and axial strain measured at any arbitrary point on the tube. Since, in theory, the tube response was spatially uniform, assuming a spatially uniform temperature, the strains at any location could be correlated with the twist and elongation. However, there were spatial non-uniformities in the temperature of the tube. These non-uniformities were due to convective and conductive heat fluxes in the oven, the spatial locations of the heating elements and the LN<sub>2</sub> ports, and material and geometric non-uniformities of the test specimens. Hence, the

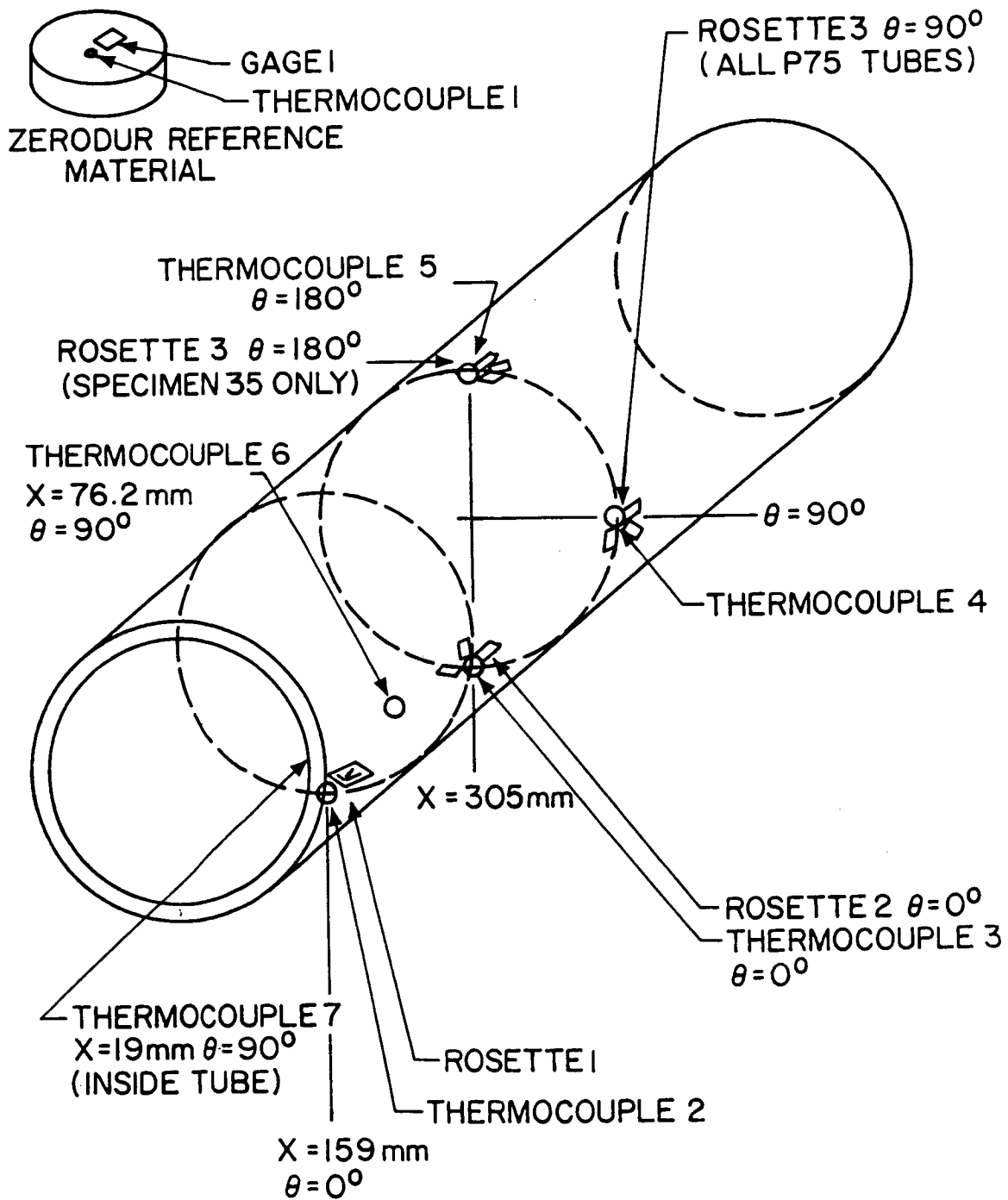


Figure 39. Thermocouple and Strain Gage Locations

thermally-induced strains at any one location may not have correlated closely with the overall twist and elongation responses. Therefore, gages at multiple locations were used to measure the test specimen strains. Figure 39 shows the strain gage locations. Three three-gage 45° rosettes were used. Referring to the coordinate system shown in Figure 38, two rosettes were located at the  $\theta = 0^\circ$  circumferential location, i.e., on the bottom of the tube as it was mounted in the chamber. One of these rosettes was located at roughly the 25 % point along the tube axis, i.e., at  $x = 159$  mm. The second rosette on the bottom of the tube was located at the axial midpoint of the test specimen,  $x = 305$  mm. Finally, the third rosette was located at  $x = 305$  mm and  $\theta = 90^\circ$  ( $180^\circ$  for one specimen). All gages had a gage length of 3.175 mm and were high temperature gages. On all gaged specimens the rosette located at  $x = 159$  mm was a manufactured 45° rosette. The gage specification was Micro Measurements WK-00-125RA-350. The other two rosettes were built up (but not stacked) from three single gages. The single gages were Micro Measurements WK-00-125AD-350 type. Gage factors and transverse sensitivities for all gages used are shown in Appendix B. These gage types and configuration were chosen due to the availability of the gages. Since the resistance of strain gages is a function of temperature, a temperature-change alone (with no actual strain) will result in an apparent strain. The simplest way to compensate for this characteristic of strain gage response is to bond a gage to a material with known thermal expansion characteristics and subject this material to the same thermal environment as the test specimen on which the gages of interest are mounted. This compensation gage should be identical to the ones mounted on the test specimen. If it is identical, the actual strain in the specimen is the difference in specimen and known material strain responses. This was the approach taken in this study, the reference material being a disk of Zerodur glass with a WK-00-125AD-350 gage mounted on it.

Figure 40 is a photograph of the apparatus with the door of the environmental chamber removed. The strain gage and thermocouple wiring may be seen leading out the open door. The Zerodur reference material is hidden behind the tube. It is positioned on a short piece

of aluminum angle, close to the test specimen. The access blocks are removed and are sitting on top of the oven. The insulated tube leading to the top of the chamber is the LN<sub>2</sub> line. The two glass end pads may be seen inside the chamber, in the lower right-hand corner. Figure 41 shows the complete apparatus during a test. Adhesive tape was used to close any gaps in the insulation and was of considerable help in minimizing the temperature gradients present in the external fixtures. The specimen temperature at the time of this photograph was approximately 144 K. Clearly visible is the external frost buildup on the fixture. The equipment rack containing the data acquisition and control hardware is just out of the picture to the left. The box with the digital voltmeter on top of it (just above the keyboard on the left) is the manual switching unit for the LVDT's. The controller for the environmental chamber can be seen under the table. The tank of LN<sub>2</sub> is in the right foreground.

## **4.2 Data Acquisition**

Figure 42 is a schematic of the data acquisition system. The LVDT's used were a product of Automatic Systems Laboratories (ASL), the transducers being Model 1083A Super Linear Variable Capacitive (SLVC) displacement transducers. This model was theoretically capable of 0.00254 mm accuracy and resolution. The operational theory of capacitive transducers may be found in Wolfendale<sup>22</sup>. An ASL Model 22 signal conditioner powered by a Datel Intersil BCM-15/200 power supply was used with the displacement transducers. In this application the eight transducers were coupled to a single signal conditioner through a manual switching unit. A Kiethly Model 191 Digital Multimeter was used to continuously read transducer voltages in order to facilitate manual switching. The output of the transducer signal conditioner was a 0-10 volt signal calibrated to a 0-25.4 mm full scale displacement. A HP3497A Data Acquisition/Control Unit with a 44422A thermocouple card and a 44427B strain gage card was

ORIGINAL PAGE IS  
OF POOR QUALITY

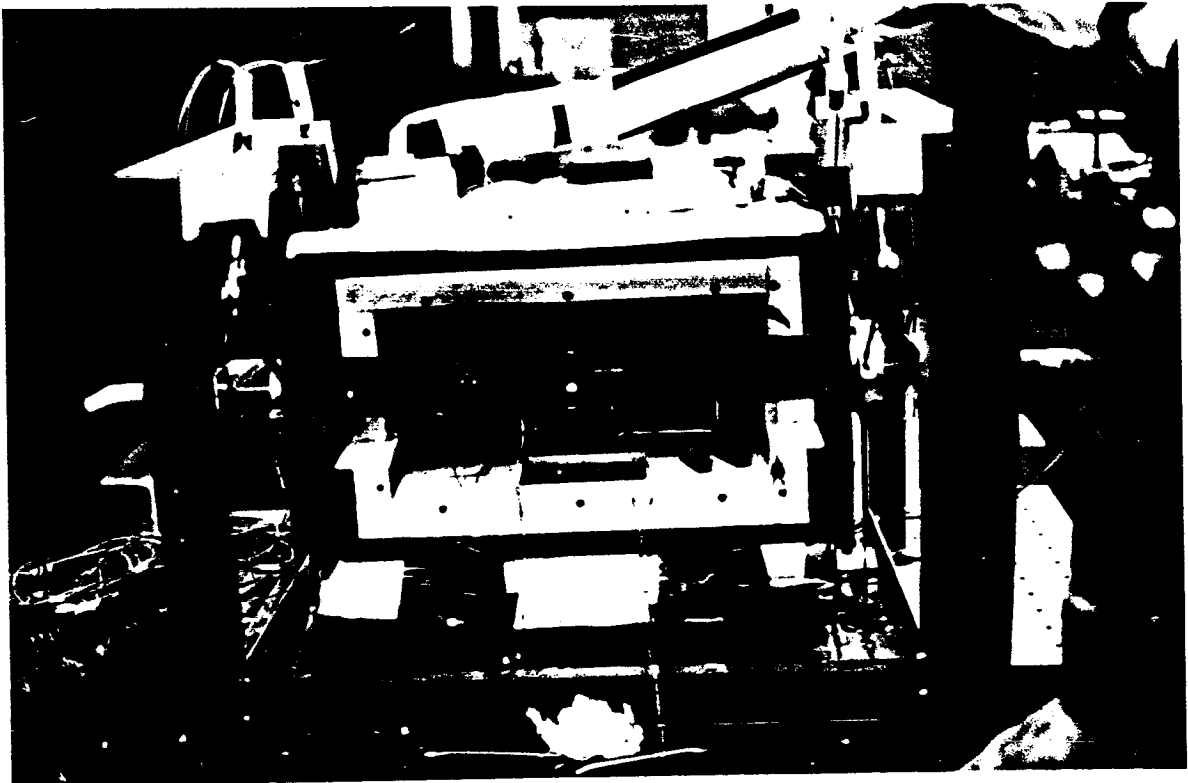


Figure 40. Experimental Apparatus - Door Removed

ORIGINAL PAGE IS  
OF POOR QUALITY

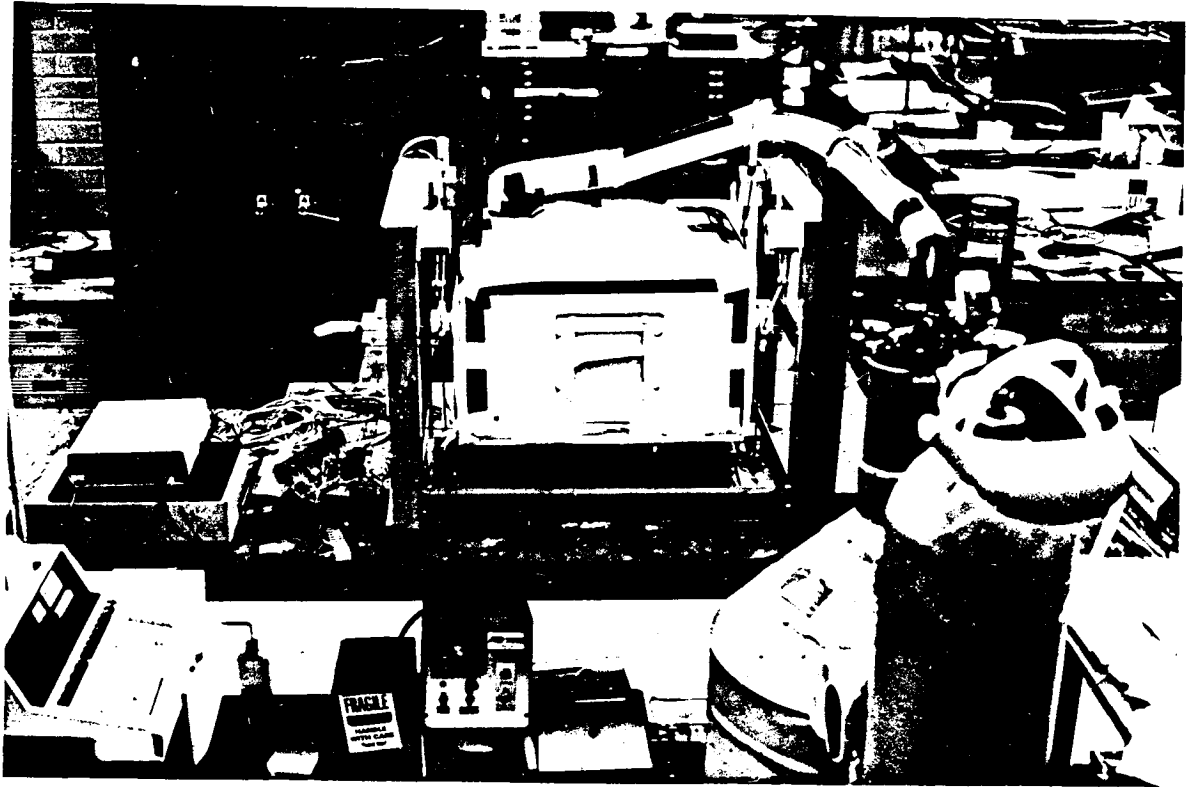


Figure 41. Experimental Apparatus - Test Configuration

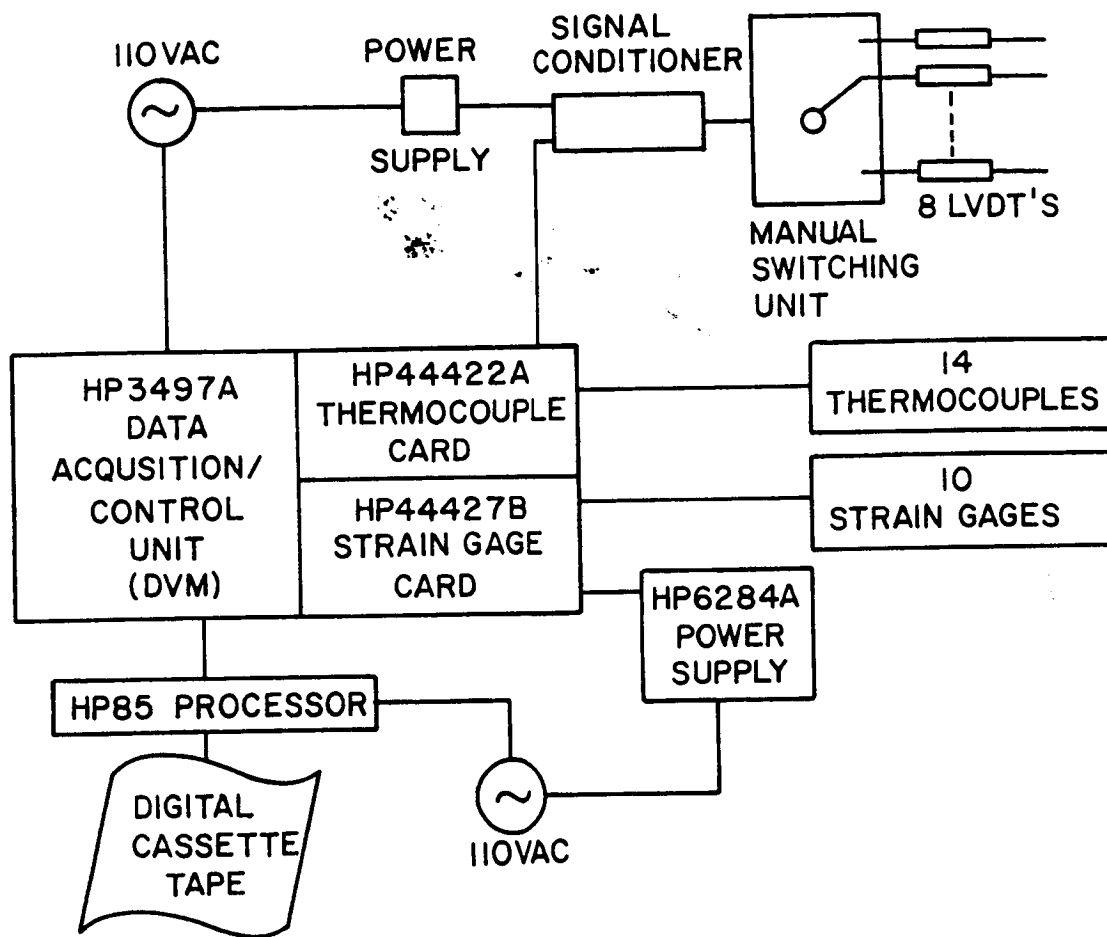


Figure 42. Schematic of Data Acquisition System

used to acquire up to 18 thermocouple voltages, the transducer signal conditioner voltage (through the 44422A), and up to 10 strain gages...each of which was wired in a quarter bridge configuration. The strain gages were powered by a HP6284A DC Power Supply, wired through the 44427B strain gage card. The HP3497A had 5 1/2 decimal place accuracy. For the tests conducted in this investigation, 14 thermocouple channels were acquired. A HP85 processor was used to process the voltages acquired through the HP3497A. The K-type thermocouples were compensated relative to a reference temperature in the HP85 software. Conversion of transducer voltages was accomplished in the software using the following equation

$$X = M (V_0 - V) \quad [64]$$

where M is the transducer calibration factor (nominally 2.54 mm/volt),  $V_0$  the initial voltage reading at the start of the test, and V the reading of the specific scan. Ten strain gages were used. As was seen in Figure 39, gage 1 was mounted on a Zerodur glass reference material having a known thermal expansion coefficient<sup>21</sup> of  $\alpha = 0.108 \times 10^{-6}$  mm/mm°C. Gages 2-10 were mounted on the specimen. True strains were calculated in the HP85 software using the following process;

$$E2 = E1 / V \quad [65]$$

$$E3 = E2 - E0 \quad [66]$$

$$E4 = - 4 E3 / (F2 (1 + 2 E3)) \quad [67]$$

$$E5 = E4 - E4(\text{Zerodur}) + E6 \quad [68]$$

where F2 was a temperature-dependent function of gage factor, GF, of the form

$$F2 = GF (1.0023076 - 3.076923 \times 10^{-5} T) . \quad [69]$$

The term E1 is the gage voltage, V is source voltage, E2 the normalized gage voltage, E0 the normalized initial voltage, E3 the difference in strained and unstrained voltage, E4 the total

strain, E4(Zerodur) the total strain of the reference material, and E5 strain corrected for temperature, i.e., true strain. The term E6 is the calculated thermal strain of the reference material, calculated using the above value of  $\alpha$  and the temperature change. The temperatures used in eq. 69 are measured by thermocouples adjacent to each rosette. The true strains are corrected for transverse sensitivity and 45° rosette transformations are made in the post-test data reduction. The gage factors and transverse sensitivities for the actual gages used on each test specimen may be found in Appendix B. The relations used to correct for transverse sensitivity in the post-test data reduction may be found in Measurements Group, Inc. literature<sup>23</sup>. The 45° rosette transformations made in reducing the strain data were

$$\epsilon_x = \epsilon_1 \quad [70.a]$$

$$\epsilon_\theta = \epsilon_3 \quad [70.b]$$

$$\gamma_{x\theta} = \epsilon_1 + \epsilon_3 - 2\epsilon_2, \quad [70.c]$$

where  $\epsilon_1$ ,  $\epsilon_2$ , and  $\epsilon_3$  were the true strains, corrected for transverse sensitivity, recorded by the axial, hoop, and 45° gages respectively. It should be noted that the sign of eq. 70.c is opposite from that of conventional shear transformations. This was because, in the coordinate system used for the tube, the rosettes were oriented such that the 45° gages were at - 45°. For each scan, the HP85 software stored scan number, elapsed time, 14 thermocouple temperatures, eight transducer displacements, and ten strains on digital cassette tape.

### 4.3 Test Specimens

Eighteen tubular specimens were tested in the apparatus described above. Table 4 presents the test specimens' nominal geometry, the material systems, and the lamination sequences.

Due to the many anomalies associated with the fabrication of composite tubes, deviations from a perfectly uniform wall thickness, perfect straightness, and perfect roundness were expected. Appendix B contains the details of each specimens' actual geometry, weight before and after testing, and a discussion of the effect of each test specimen's peculiarities on the test results. As can be seen from Table 4, the 18 specimens may be grouped by material system, and divided into two families. The families were:

Family 1:  $[-10_2/0_{10}/\phi_2]$

Family 2:  $[-10/0_3/\phi_2/0_3/-10]$ .

These laminates were chosen since, for  $\phi = 10^\circ$ , they approximate designs being considered for use on the space station. The other values of  $\phi$  were chosen in order to provide a range of different values of thermally-induced twist. Only values of  $\phi < 20^\circ$  were chosen since they are within the practical range of design consideration for the space station, and because larger  $\phi$ 's would have led to stress levels that could have caused damage over the range of temperatures that were used in the testing. Specimens 21, 22, 24, 25, and 28 were not strain gaged. Specimens 31, 32, 34, and 38 were gaged, however, due to a hardware problem in the data acquisition system, no usable strains were obtained.

## **4.4 Procedures**

The general procedure for measuring the thermally-induced responses of a test specimen was as follows: First, the thermocouples were bonded to the test specimen. The same thermocouples were used repeatedly, and therefore had to be removed from the previous test specimen prior to setting up the following test. Next, the radial arm fittings were clamped onto the test specimen. A coordinate system having already been marked on each test specimen, it was possible to align the fittings on the tubes in an identical fashion on all test specimens. Also at this point insulation was inserted into each end of the test specimen (inside the end

**Table 4. Test Specimen Description**

geometry :  $L = 610 \text{ mm}$   $r_i = 25.4 \text{ mm}$   $t_{ply} = 0.127 \text{ mm}$

<i>specimen</i>	<i>material system</i>	<i>lamination sequence</i>
11	P75S/ERLX1962A	$[-10_2 / 0_{12}]$
12	P75S/ERLX1962A	$[-10_2 / 0_{10} / 10_2]$
13	P75S/ERLX1962A	$[-10_2 / 0_{10} / 15_2]$
14	P75S/ERLX1962A	$[-10_2 / 0_{10} / 20_2]$
15	P75S/ERLX1962A	$[-10 / 0_{12} / -10]$
16	P75S/ERLX1962A	$[-10 / 0_5 / 10_2 / 0_5 / -10]$
17	P75S/ERLX1962A	$[-10 / 0_5 / 15_2 / 0_5 / -10]$
18	P75S/ERLX1962A	$[-10 / 0_5 / 20_2 / 0_5 / -10]$
21	T300/ERLX1962A	$[-10_2 / 0_{12}]$
22	T300/ERLX1962A	$[-10_2 / 0_{10} / 10_2]$
24	T300/ERLX1962A	$[-10_2 / 0_{10} / 20_2]$
25	T300/ERLX1962A	$[-10 / 0_{12} / -10]$
28	T300/ERLX1962A	$[-10 / 0_5 / 20_2 / 0_5 / -10]$
31	AS4/976	$[-10_2 / 0_{12}]$
32	AS4/976	$[-10_2 / 0_{10} / 10_2]$
34	AS4/976	$[-10_2 / 0_{10} / 20_2]$
35	AS4/976	$[-10 / 0_{12} / -10]$
38	AS4/976	$[-10 / 0_5 / 20_2 / 0_5 / -10]$

pads) in order to shield the axial transducers from the temperature extremes that the inside of the tube would experience. The specimen was now ready to be installed in the chamber. The specimen slid horizontally through the access slots cut in the chamber walls, into the holes through which the specimen protruded. With the specimen aligned on the tube supports, the supports were adjusted vertically, until the specimen did not contact the chamber in any way. The removable access blocks were then installed. At this point, the glass end pads were inserted in the tube ends, and the strain gage and thermocouple wiring was connected (the LVDT's remained permanently mounted on the test fixture and connected to the data acquisition system). Thermocouple polarity and continuity of all data acquisition channels was checked. Once these checks were complete, the oven door was mounted and closed, and external tape and insulation were added in order to shield the test fixture from temperature variations as much as possible. Once fine adjustments were made to insure that all LVDT's were initially close to mid-range, and that the test specimen was free to move, the test apparatus was allowed to sit untouched for a period of time to allow all transient electrical signals induced in the data acquisition system to dissipate. Afterwards, the data acquisition system was started, an initial data scan taken, and the environmental chamber then turned on. The initial data scan was considered to be the zero scan and was taken at time  $t = 0$ . These strain and displacement values were subtracted from all subsequent data.

After the  $t = 0$  data scan, the test temperature was first decreased to 144 K. The decision to go first to the low temperature, and to do so as rapidly as possible, was made in order to make most efficient use of time. It turned out that the cooling process with liquid nitrogen ( $LN_2$ ) was slower than the heating cycle, therefore, the cooling portion was done first.

The data acquisition software automatically acquired data every 15 minutes (however, the LVDT's had to be switched manually from one transducer to the next for each scan). The oven temperature was also controlled manually. At 144 K, the temperature was allowed to stabilize, then the temperature was increased. From 144 K to 366 K, the temperature was increased in roughly 28°C or 56°C increments. At the end of a 15 to 45 minute dwell after each

temperature increment, the dwell being necessary in order for temperature gradients and other transient responses to decrease, the scan number was noted. This scan number was then identified as having data recorded at thermal equilibrium. The temperature was ultimately increased to approximately 366 K, the temperature allowed to stabilize, and data recorded. Following the 366 K peak, the temperature was allowed to return to the initial temperature (room temperature). Data acquisition was terminated when room temperature was reached. It should be noted that since the chamber was manually controlled, the times to reach thermal equilibrium were all slightly different, and the temperature increments between equilibrium states were not all the same, for each test. Figure 43 illustrates a typical time-temperature relation. At time  $t = 0$ , the temperature started at room temperature. About three to three-and-a-half hours later, point A, the  $\text{LN}_2$  had lowered the temperature to 144 K. The temperature was then increased to approximately 172 K and conditions stabilized. The incrementing of temperature continued until, seven to seven-and-a-half hours into the test, the maximum temperature of 366 K was reached, point B in Figure 43. Eight hours after the test began, the temperature had returned to room conditions.

Finally, it should also be noted that the specimens were too large to be kept in drying chambers. The specimens were weighed before and after testing and the moisture loss or gain,  $\Delta M$ , was calculated. It was found that  $\Delta M < 0.2\%$  in all tests and therefore the effects of moisture absorption-desorption were neglected.

## **4.5 Operational Considerations**

Several initial difficulties were encountered with the test apparatus and these will now be considered. The initial LVDT configuration consisted of eight transducers, eight separate signal conditioners, and three power supplies. Although the capacitive-type transducers the-

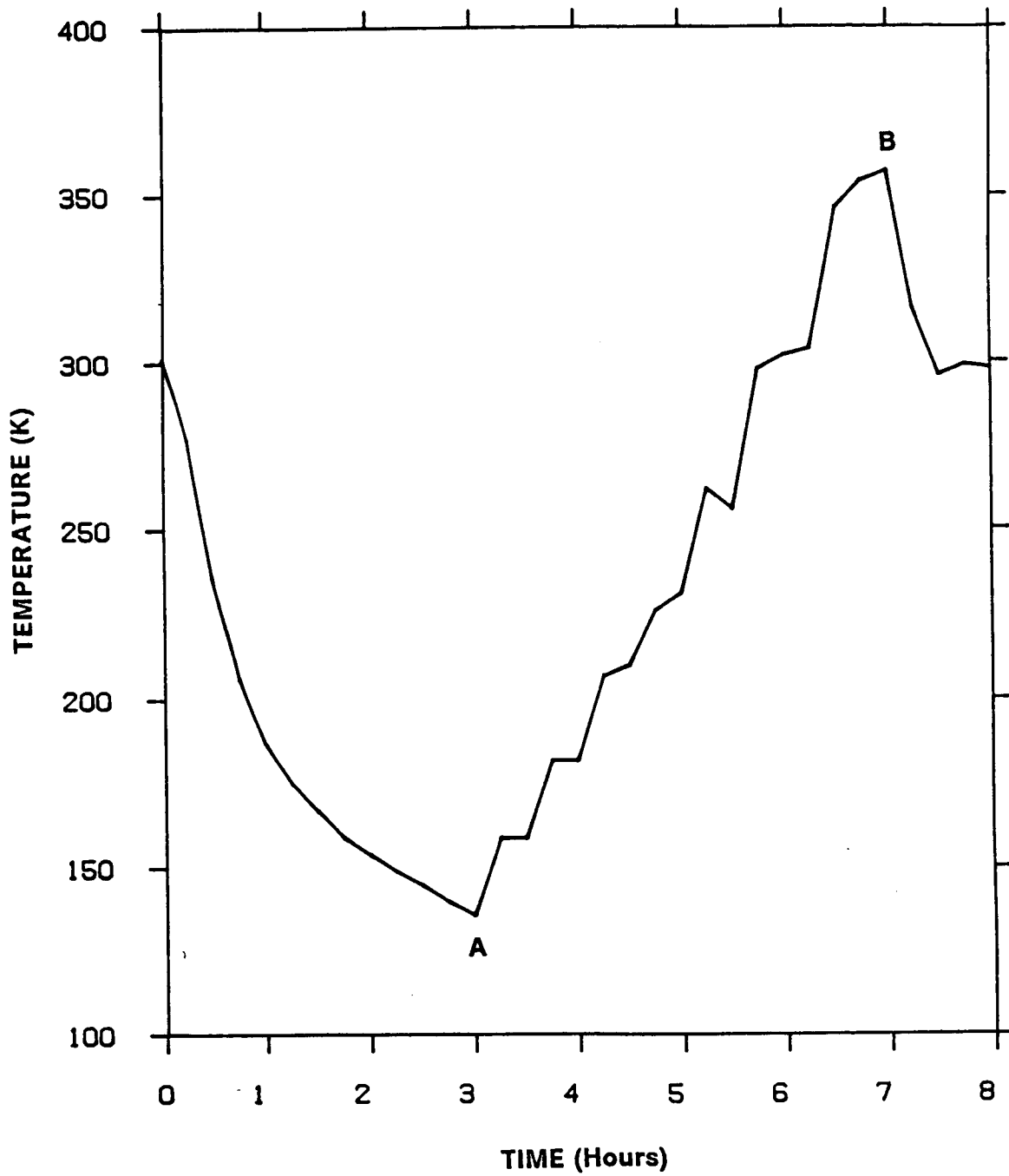


Figure 43. Typical Time-Temperature Response

oretically possessed zero signal drift, in practice, this was not found to be so. Transducer drift was found to be one to two orders of magnitude larger ( $\pm 0.127$  mm) than the published accuracy of the LVDT's. The switch to a single signal conditioner lessened, but did not eliminate this problem. In order to quantify the drift problem, numerous tests were conducted with no temperature change. In the final analysis it was concluded that the drift was small enough not to mask the real displacement measurements.

Another factor affecting the measure of displacements was the fact that, due to temperature gradients around the circumference of the test specimens, and due to tube fabrication anomalies, the specimens exhibited bending during some portions of the tests. It was for this reason that three displacement transducers were used to measure tangential displacement. With three measures of tangential displacement at each end of the test specimens, it was possible to solve for the two degrees of end translation, as well as the twist, at each end. As it turned out, the twist was directly related to the average of the three tangential displacement measurements.

The fact that the LVDT's exerted small forces on the points that they bore against affected the performance of the apparatus. These forces varied with the spring-loaded LVDT plunger displacement. For the torsional transducers, the 254 mm radial arms behaved as cantilevered beams with a variable point force on the end. The radial arms were stiffened as much as was practical, so that the error due to radial arm bending was observed to be negligible. Another effect of the LVDT spring force was important. LVDT's 1, 3, 4, and 6 caused the tube to rotate (as a rigid body) in one direction about the centerline axis while LVDT's 2 and 5 caused the tube to rotate the other direction. There were twice as many LVDT's causing rotation one way as the other. Therefore, the spring compression, and hence plunger position of each LVDT had to be adjusted so that the tube was in static equilibrium (in rotation), yet the plungers needed to be somewhere near mid-range of their stroke. Finally, some LVDT plungers had more frictional resistance than others. This had a significant effect on the behavior of the tests. Due to a plunger, or plungers, sticking, one end of the tube would not rotate and all of

the rotation would be measured at the other end of a test specimen. Due to the nature in which the end displacement data was reduced, a plunger sticking would, nominally, affect no more than the calculated end translations; the measured twist and axial displacement would be unaffected. However, the increased force on a radial arm due to a sticking plunger increased the bending in the radial arm. This in turn caused increased error in the measured twist. Additionally, a sticking LVDT plunger often was observed to move in an intermittent manner, first sticking and not moving, then suddenly moving, reducing the force on the surface on which it was bearing. This phenomenon was the prime motivator of the practice used here, namely, to consider as usable only the data taken after a 15 to 45 minute dwell time at a given temperature. The temperature dwell allowed transient responses such as large temperature gradients and the mechanical effects of the LVDT's to dissipate.

Another aspect of these tests which had to be accounted for in any comparison with theory was the fact that the temperature of the test specimen varied along its length and that this variation changed during the course of the temperature cycle. By use of a number of thermocouples along the length of the tube - both inside and outside the oven - the axial temperature variation was modelled as shown in Figure 44. It was found to be piecewise linear along the length of the tube. The 19 mm of tube length at each end of the tube was neglected since each was clamped in the radial arm fitting and was considered to be ineffective in influencing the tube's response. Note also that the thermocouples used were located at  $\theta = 90^\circ$  (the side of the tube, see Figure 39), resulting in temperature readings that were averages of the extremes of the circumferential temperature gradient. The maximum and minimum temperatures at a given axial location on the tube were, in general, found at  $\theta = 180^\circ$  and  $0^\circ$ , respectively, i.e., the top and bottom of the tube. The average temperature over the length of the tube was found using the relation

$$T_{avg} = 0.100 T_7 + 0.233 T_6 + 0.667 T_4 \quad [71]$$

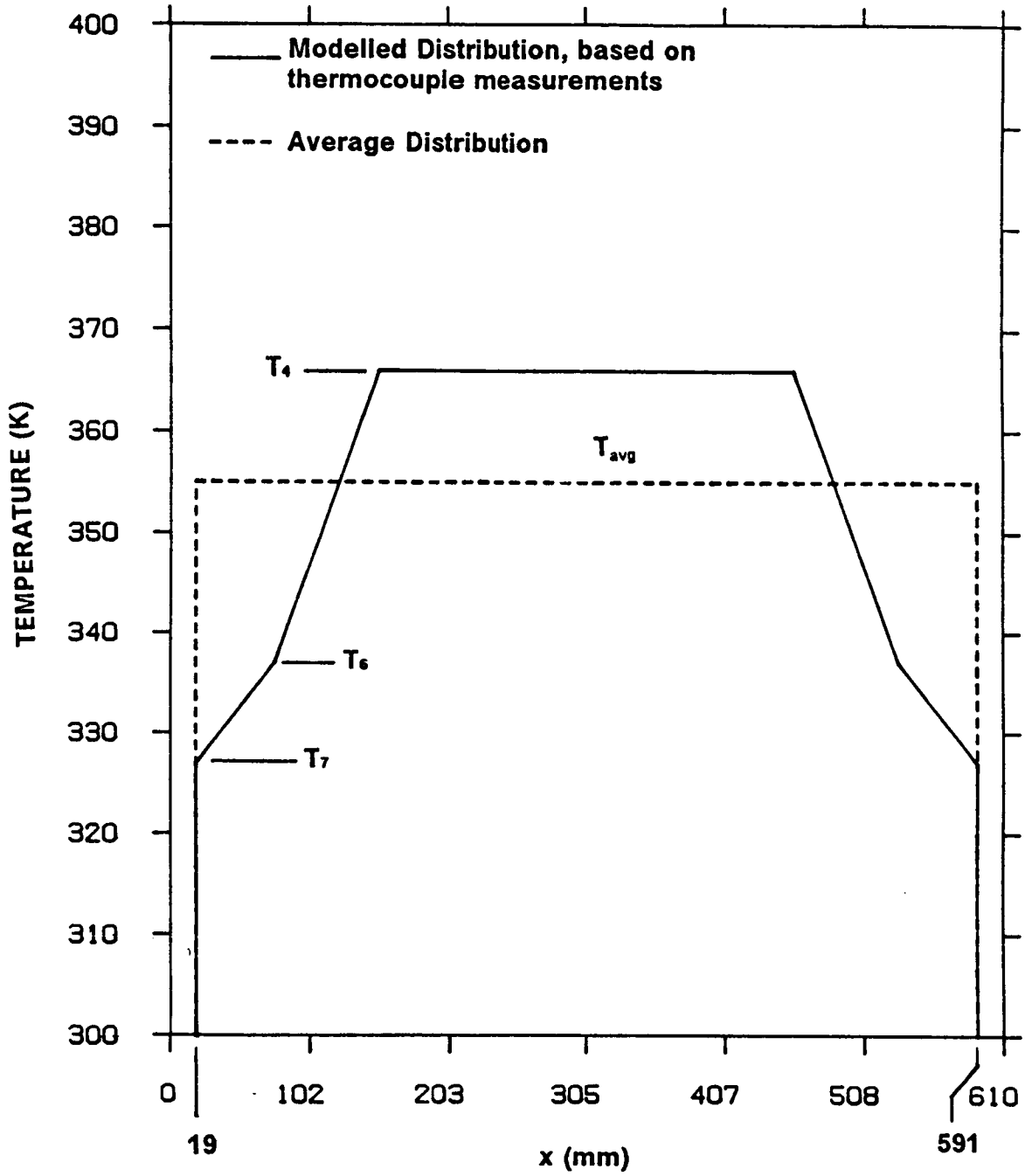


Figure 44. Axial Temperature Distribution Model:  $T_i$  are thermocouple readings, circumferentially located at  $\theta = 90^\circ$ . Nineteen millimeters at each end of the tube were neglected.

where  $T_7$ ,  $T_6$ , and  $T_4$  are temperature readings from thermocouples 7, 6, and 4 respectively. The above relation was determined by equating the area under the modelled distribution in Figure 44 to an average value of temperature over the whole effective length of the tube.

## 4.6 Error Analysis

As mentioned at several points in this chapter, there were errors involved in the experimental measurements. The sources of possible error were many and varied. Although they will be discussed in detail in this section, it was not possible to isolate and measure the individual sources of error. Rather, a series of controlled tests were conducted in which the overall experimental error was observed, and from these observations, conclusions concerning the magnitude of the experimental error were drawn. In this section, the possible sources of error will be categorized in general terms, and their effect on the experimental data discussed.

For the displacement transducers, the inherent accuracy of the transducer-signal conditioner-power supply set-up is  $\pm 0.00254$  mm<sup>22</sup>. A measurable amount of drift in the acquired signal was also observed. All displacement measurements were subtracted from an initial zero-reference point (taken at time,  $t=0$ , in the test) and assumed the form

$$X_i = X_i^{scan} - X_i^0 \quad [72]$$

where  $X_i^{scan}$  was the displacement at a given scan and  $X_i^0$  was the initial zero-reference. The error in  $X_i$  was assumed to be the above-mentioned instrument accuracy and acquisition system drift, as well as the following time-dependent effects:

1. rigid body motion of the test specimen,

2. thermally-induced bending of the test specimen,
3. specimen binding, in the test apparatus,
4. induced strains present in the specimen when initial displacement was recorded, but which were later relieved,
5. motion of the specimen within the radial arm fitting grip,
6. changes in the deflected shape of the radial arms (affecting only the circumferential LVDT's),
7. thermal expansion of the glass end pads (affecting only the axial LVDT's),
8. varying mechanically-induced strains in the end pads, due to tube expansion/contraction (affecting axial LVDT's only).

These effects were observed, or assumed to exist, and were accounted for by observing and quantifying the measurement error during a series of controlled tests, or by mathematically eliminating the effects in the data reduction. Effects (1) and (2) were eliminated in the calculations of average tangential displacement, and the axial displacement. Effects (7) and (8) were assumed to be negligible due to the small thermal expansion coefficient and high stiffness of the Zerodur glass. Effects (3) - (6) were accounted for by observation of a series of controlled tests of overall signal variation. From these tests, the conclusion was drawn that the measured displacements of tube response would always be at least an order of magnitude larger than the uncertainty due to experimental error. Recall that the apparatus configuration was chosen due to the fact that the expected tube responses were large enough not to be masked by the measurement error. Perhaps an even stronger argument in favor of neglecting the influences of Effects (3) - (6) may be found in considering the consistency and repeatability

that was observed in the actual tests. Effects (3) - (6) would be random in nature and would thus influence the test results in a random manner if they were significant.

The strain gage data were acquired through an unbalanced Wheatstone bridge circuit. By observing the initial bridge and power supply voltages, representative values of  $E_1 = 0.001$  V and  $V = 5.0$  V were chosen to be substituted into eqs. 65 - 68, resulting in an experimental error of  $\pm 8 \mu\epsilon$  for the three elements of each rosette. This then became the experimental error of the axial and hoop strain measurements, and considering the transformation eq. 70.c, the error for the shear strain became  $\pm 32 \mu\epsilon$ .

The next chapter presents data obtained from the test specimens shown in Table 4, subjected to a temperature-time history similar to that shown in Figure 43. Theoretical calculations of tube response, based on available material property data and the analysis of Ch. 2, are included and discussed.

## 5.0 Experimental Results

Since strain gages measure the strain at a specific location, local measures of shear strain, axial strain, and hoop strain in the tube could be obtained. In the experiments, the strains were measured directly as a function of the temperature of the tube. In addition to the strain gages, overall twist and axial deformation of the tube was measured using the displacement transducers. This chapter discusses both the local strain response and the more general displacement response. Fortunately, these measurements can be compared and, in fact, displayed on common axes. The overall axial strain of the tube can be determined from the axial displacement data by dividing the axial displacement,  $u$ , by the effective tube length,  $L$ , i.e.,

$$\varepsilon^o \text{ (in } \mu\varepsilon) = \frac{u}{L} = \frac{u \text{ (mm)}}{572 \text{ mm}} (10^6) \quad [73]$$

where  $u$  is the difference in displacement measured by the two axial transducers. This measure of axial strain should correlate with the axial strain measured by the strain gages.

Similarly, the twist response can be compared directly with the response as measured by the strain gage rosettes by noting that the shear strain on the surface of the tube ( $r = 27.2 \text{ mm}$ ) is related to the tangential displacement of the ends of the radial arms ( $r = 254 \text{ mm}$ ) by the relation

$$\gamma^{\circ} r \text{ (in } \mu\text{rad)} = \frac{v r_o}{L r_{arm}} = \frac{v \text{ (mm)} (27.2 \text{ mm})}{(572\text{mm})(254 \text{ mm})} (10^6) \quad [74]$$

where  $v$  is the average tangential displacement of the end of the radial arm, found using the six tangentially oriented LVDT's.

When comparing the strains measured by displacements with strains measured by strain gages, an important factor must be taken into account. Despite attempts to minimize temperature gradients, Figure 44 indicated that there were gradients along the length of the tube. In addition, there were gradients around the circumference of the tube. Whereas the strain gages measured the response of the tube at the local temperature, the displacement transducers measured the response of the tube to the average temperature. Figure 44 indicated how the average temperature of the tube compared with the actual axial temperature distribution and eq. 71 detailed the relation between the assumed average temperature and the temperature data from the various thermocouples. These details of the relation between overall tube response and local tube response, and the relation between local and average temperature are important for understanding the figures that follow. The following figures illustrate the variation with temperature of the strains of the various tubes tested. On all of the figures the strains, as determined by either eq. 73 or 74 are illustrated as solid circles and squares. For those specimens that were strain gaged, the strains measured by the gages are indicated by crosses, plusses, and open triangles. What is important to note is that the displacement-derived strains are plotted as a function of **average** temperature and the strains from the gages are plotted as a function of the temperature as measured by the thermocouple located in the immediate vicinity of the rosette. It should be noted that in general there is just one set of LVDT data per test specimen. However, specimens 34 and 35 were each tested twice, therefore there are two sets of displacement data for these two test specimens.

The experimental error present in these data were discussed in Ch. 4. The significant sources of error were discussed and a rationale for considering the data to be viable was presented.

At this point, it is re-emphasized that due to the complexities of the various sources of error and the inability to isolate and quantify them, no error bands for the experimental data are presented on the figures in this chapter. It was concluded through observation, that the trends and overall magnitudes seen in the experimental data were realistic tube responses.

The figures also include the theoretical prediction of the variation of strain with temperature and off-axis ply orientation angle,  $\phi$ . The theory of Ch. 2 in conjunction with the best available material property data, as presented in Appendix A, was used to calculate the theoretical values of strain. In the calculation of the following figures, temperature-**dependent** material properties were used for the figures showing strain vs. temperature, and temperature-**independent** data were used for the figures showing strain vs. ply orientation angle.

## **5.1 Twist Response**

Figure 45 illustrates the twist characteristics, in terms of shear strain, for specimen 11. Due to the construction of the tube, this tube was expected to show significant twist. The variation of twist with temperature is dictated by the orientation of the off-axis layers. It will be seen in the ensuing figures that if the twist is governed by fibers with negative off-axis angles (see Figure 1), then the slope of the twist vs. temperature relation is positive. In this and subsequent figures, the values of response are shown relative to room temperature values. Thus, at a temperature of 294 K, the twist response is identically zero. From Figure 45, it is seen that the twist as measured by the displacement transducers correlates well with the theoretical predictions. For temperatures both above and below room temperature the experimental data follow the theoretical prediction. On the other hand, the twist characteristics measured by the strain gages correlate poorly with the theoretical prediction. In addition, the twist as

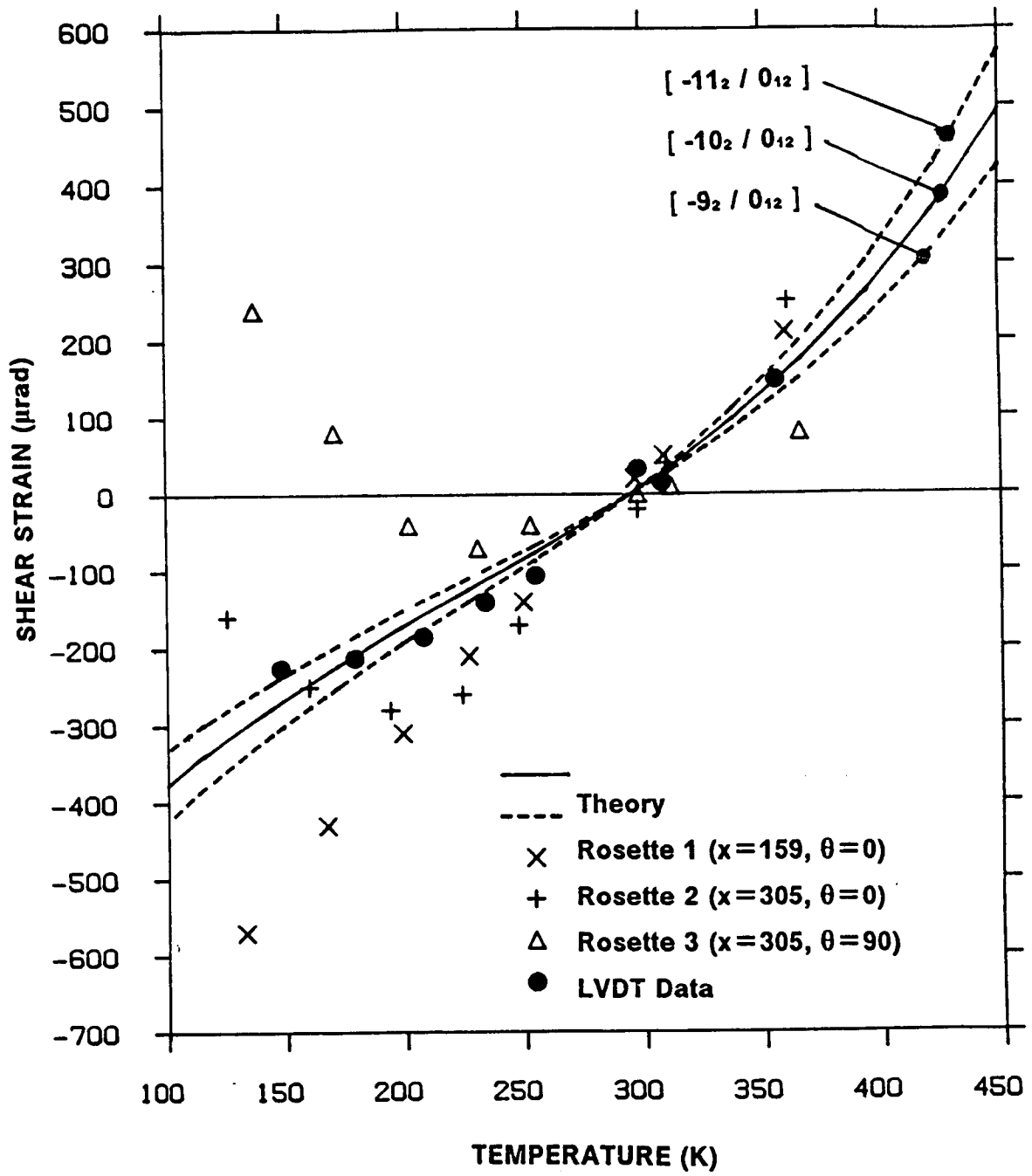


Figure 45. Shear Strain vs. Temperature, Specimen 11:  $[-10_2 / 0_{12}]$ . Experiment and Theory, Temperature-dependent material properties.

measured by the strain gages is not consistent. Below room temperature the twist as measured by the three rosettes does not agree in magnitude, sign, or slope. Though the rosettes were at different axial and circumferential locations, the temperature gradients alone could not have produced such different strain response at the different locations. A quick glance at those figures that include strain gage data (Figure 45 - Figure 52, and Figure 61) indicates that the erratic behavior of the shear strain response was common. It is worth noting that the displacement data is nonlinear with respect to temperature, the data exhibiting nearly the same temperature-dependent trends as that predicted by the temperature-dependent theory. Finally, the theoretical curves in Figure 45 illustrate an important point. It is not at all clear what the level of control was in maintaining the specified fiber angle when the tubes were fabricated. It is conceivable that orientation of the off-axis layers were only accurate to within one degree. How sensitive is the tube response to inaccuracies in the fiber angle? It clearly depends on the particular tube design. However, the dashed lines in Figure 45 illustrate the range of predicted response of the tube, given that the off-axis angle varies  $\pm 1^\circ$ . The solid line is the predicted response of a  $[-10_2/0_{12}]$  lay-up and the dashed lines represent the behavior of  $[-9_2/0_{12}]$  and  $[-11_2/0_{12}]$  tubes. For this particular tube it is clear that there is not a significant influence of possible inaccuracies in the off-axis angle. More will be said of this later, with regard to other test specimen lay-ups.

Figure 46 is the twist response of specimen 12 as a function of temperature. This specimen possesses a balanced lamination sequence and the twist is therefore quite small. Since the outermost ply has a positive off-axis angle, the slope of the twist response is negative. In a manner similar to the previous figure, the displacement data agree well with the theoretical predictions while the strain gage data are erratic.

Figure 47 and Figure 48 illustrate the twist response of specimens 13 and 14 respectively. These are the final two specimens in the  $[-10_2/0_{10}/\phi_2]$  family of P75S/ERLX1962A tubes. In the figures, the outer off-axis ply angle is increased to  $15^\circ$  and  $20^\circ$ . The slope of the twist response vs. temperature continues to become more negative in the two figures. The dis-

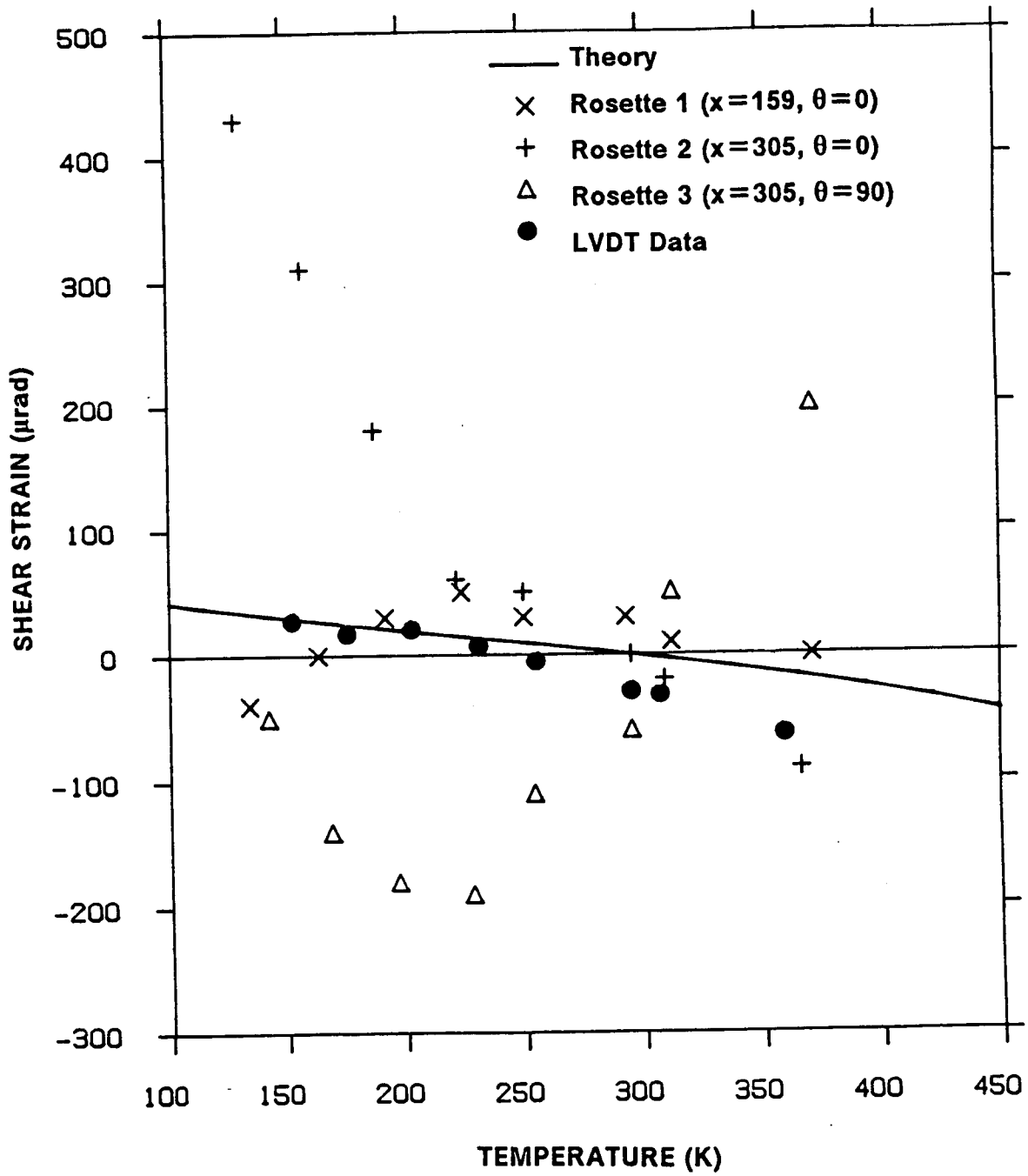


Figure 46. Shear Strain vs. Temperature, Specimen 12:  $[-10_2 / 0_{10} / 10_2]$ . Experiment and Theory, Temperature-dependent material properties.

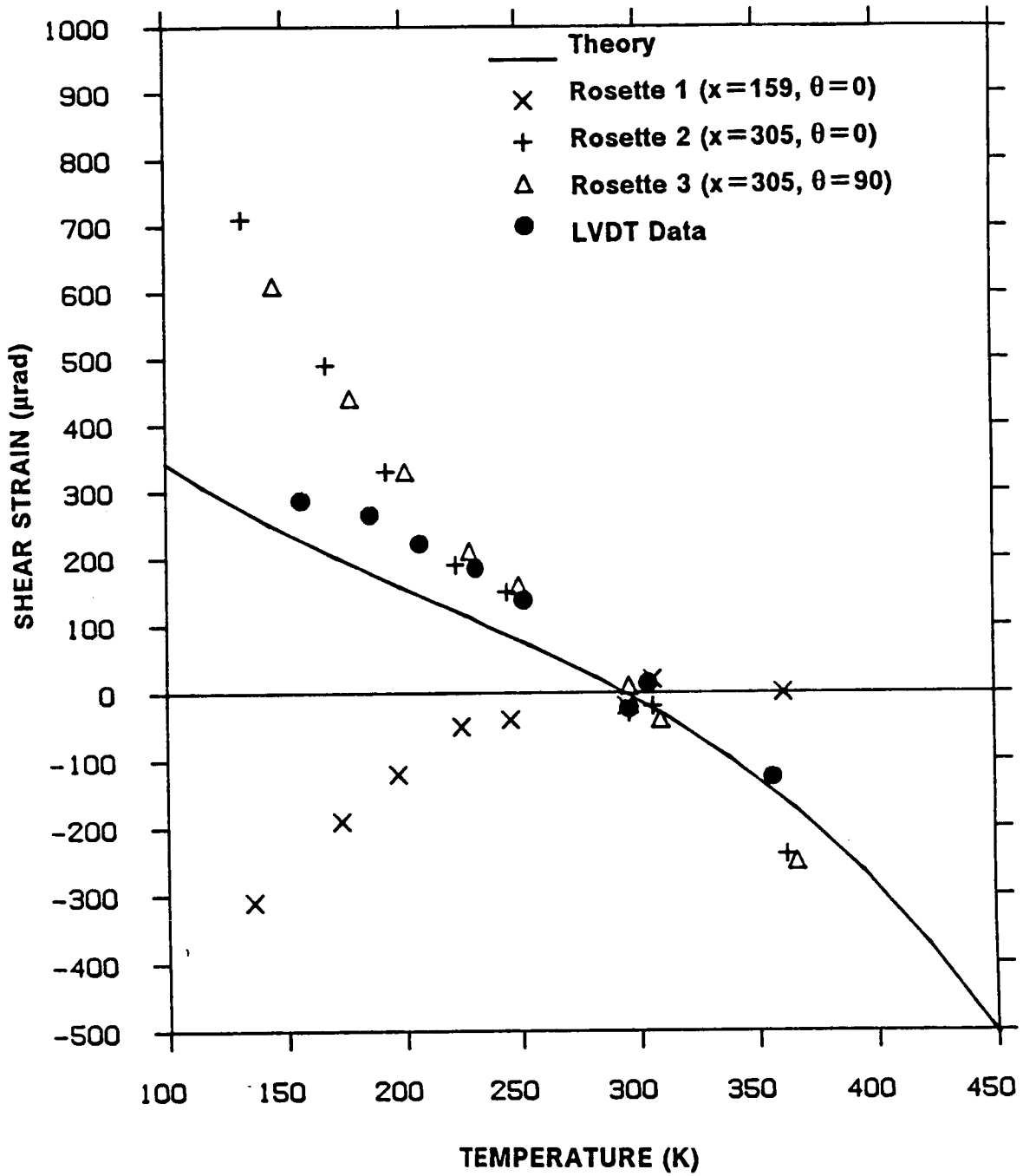


Figure 47. Shear Strain vs. Temperature, Specimen 13:  $[-10_2 / 0_{10} / 15_2]$ . Experiment and Theory, Temperature-dependent material properties.

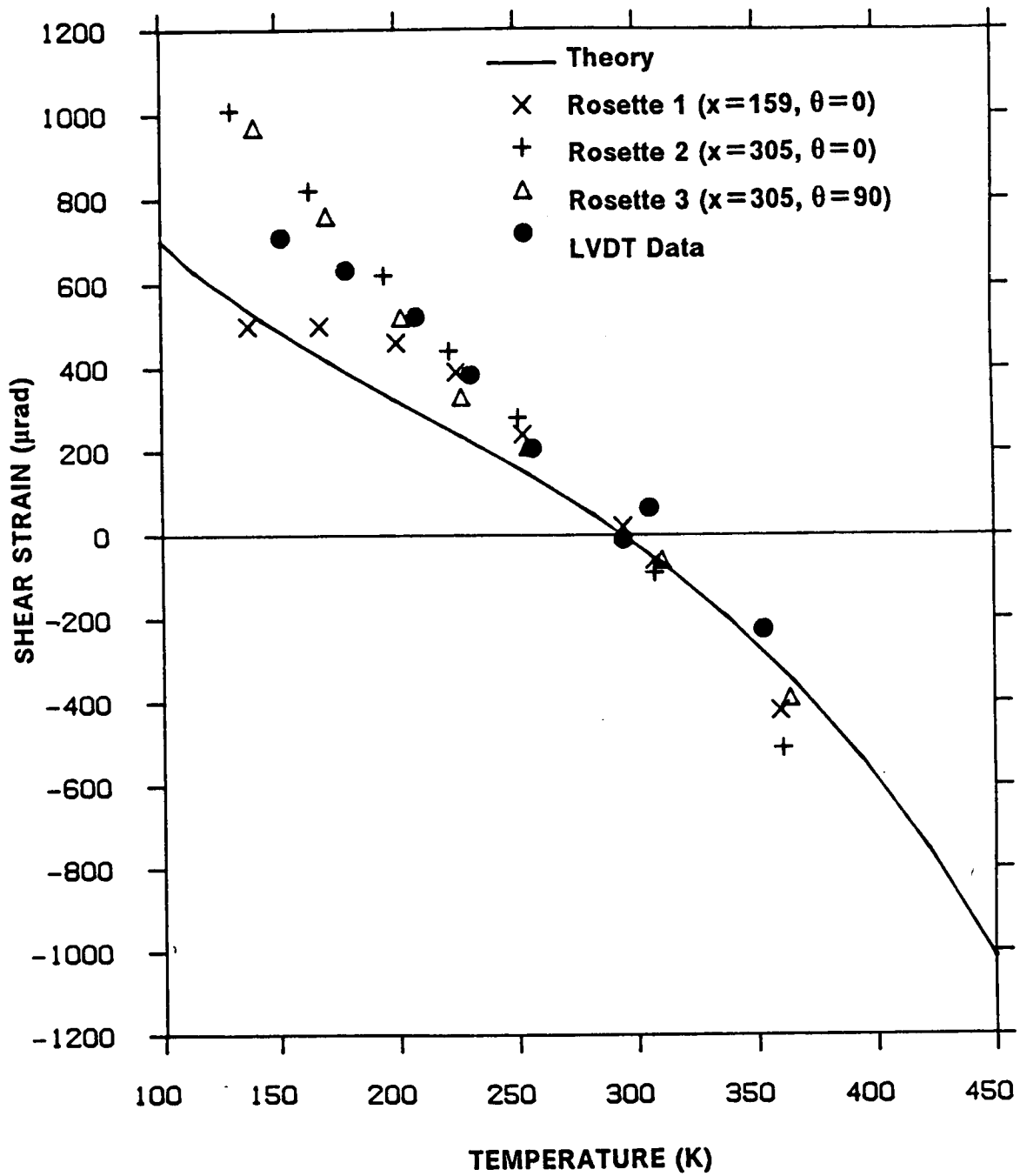


Figure 48. Shear Strain vs. Temperature, Specimen 14:  $[-10_2 / 0_{10} / 20_2]$ . Experiment and Theory, Temperature-dependent material properties.

placement data in Figure 47 again agrees well with theory while the strain gage data is erratic. It should be noted that in Figure 48, the strain gage data are more well behaved, and tend to follow the displacement data. For the tube in Figure 48, the shear strains are quite large. This indicates that the error levels in the shear measurements for the strain gages are comparable to the shear levels in the tubes of Figure 45 - Figure 47. The shear response of the tube in in Figure 48, on the otherhand, is large enough to overcome some of the error. Also note that the displacement data in Figure 48 seem to indicate that the tube twisted somewhat more than was predicted theoretically. This effect could be caused by the outermost off-axis ply actually being somewhat more than  $20^\circ$  (or the inner ply being less than  $-10^\circ$ ).

Figure 49 - Figure 52 illustrate the twist response of the four tubes in the  $[-10/0_3/\phi_2/0_5/-10]$  family of P75S/ERLX1962A tubes (specimens 15, 16, 17, and 18). In general these tubes behaved in a manner similar to the first four tubes, i.e., the displacement data agreed well with theory while the strain gage data was generally erratic. Figure 50 is significant in that it was a balanced symmetric lay-up, hence the predicted twist was virtually (though not exactly) zero. The experimental data for specimen 15 did not bear this prediction out however. The dashed line in Figure 50 represents the predicted twist for a  $[-10/0_5/+11_2/0_5/-10]$  tube. Assuming that the off-axis ply that was supposed to be  $10^\circ$  was, in fact  $11^\circ$ , results in good agreement between theory and displacement data. This is assumed to be the most reasonable explanation for this data, given that other specimens generally maintained good agreement between theory and experiment. Note should also be taken at this point that specimen 17 had an open circuit on one of the strain gages in rosette 2 and therefore no data was obtained for any of the strains at this location on this test specimen.

Figure 53 - Figure 57 present the twist response vs. temperature of the T300/ERLX1962A specimens (21, 22, 24, 25, and 28). These specimens were not strain gaged therefore only displacement data are indicated on the figures. Notice that with the lower modulus and lower expansion fiber, the magnitude of the twist response is less than that of the P75S tubes, even though the lamination sequences are identical (e.g. compare Figures 45 and 53). In general,

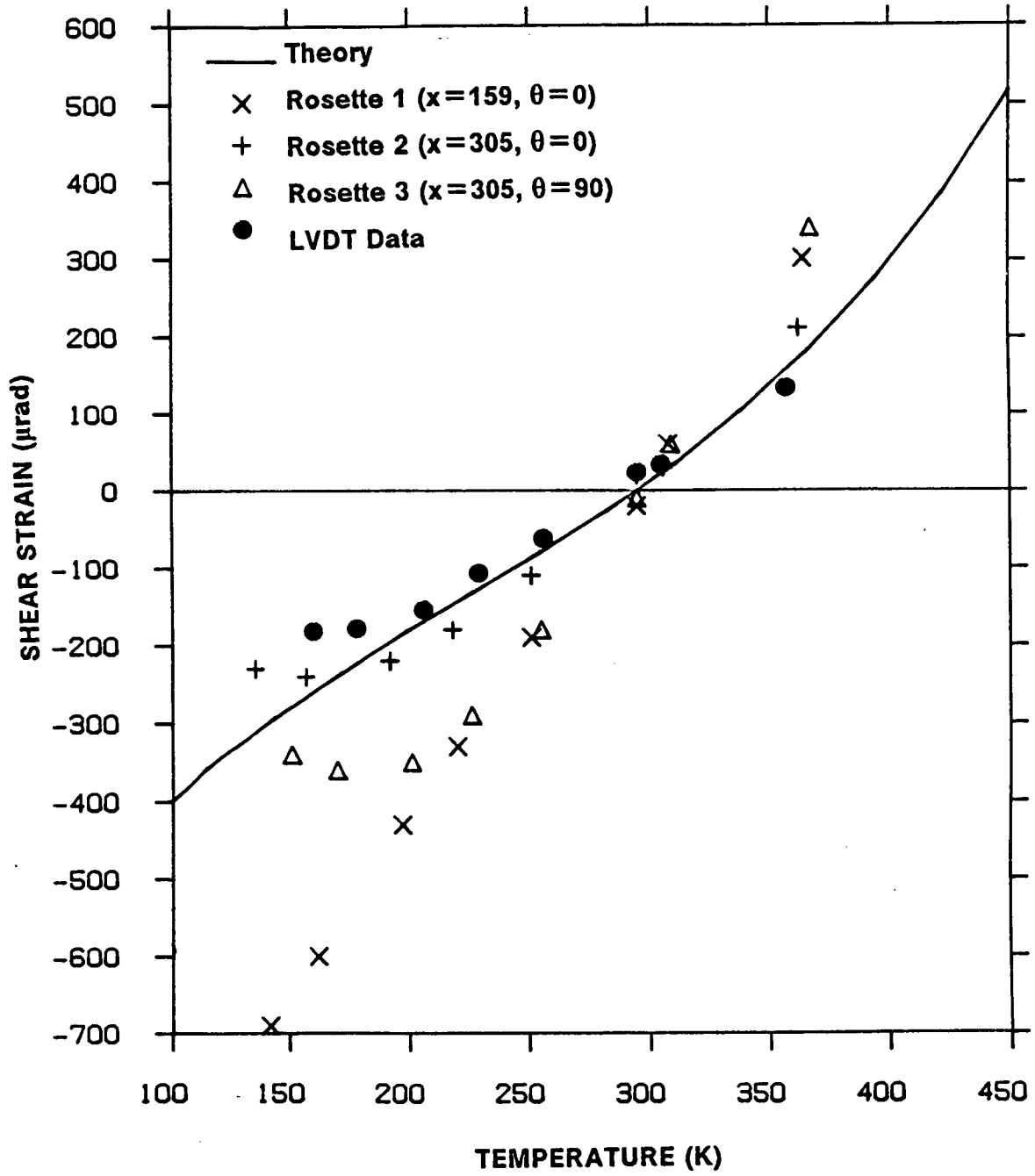


Figure 49. Shear Strain vs. Temperature, Specimen 15: [-10 / 0<sub>12</sub> / -10]. Experiment and Theory, Temperature-dependent material properties.

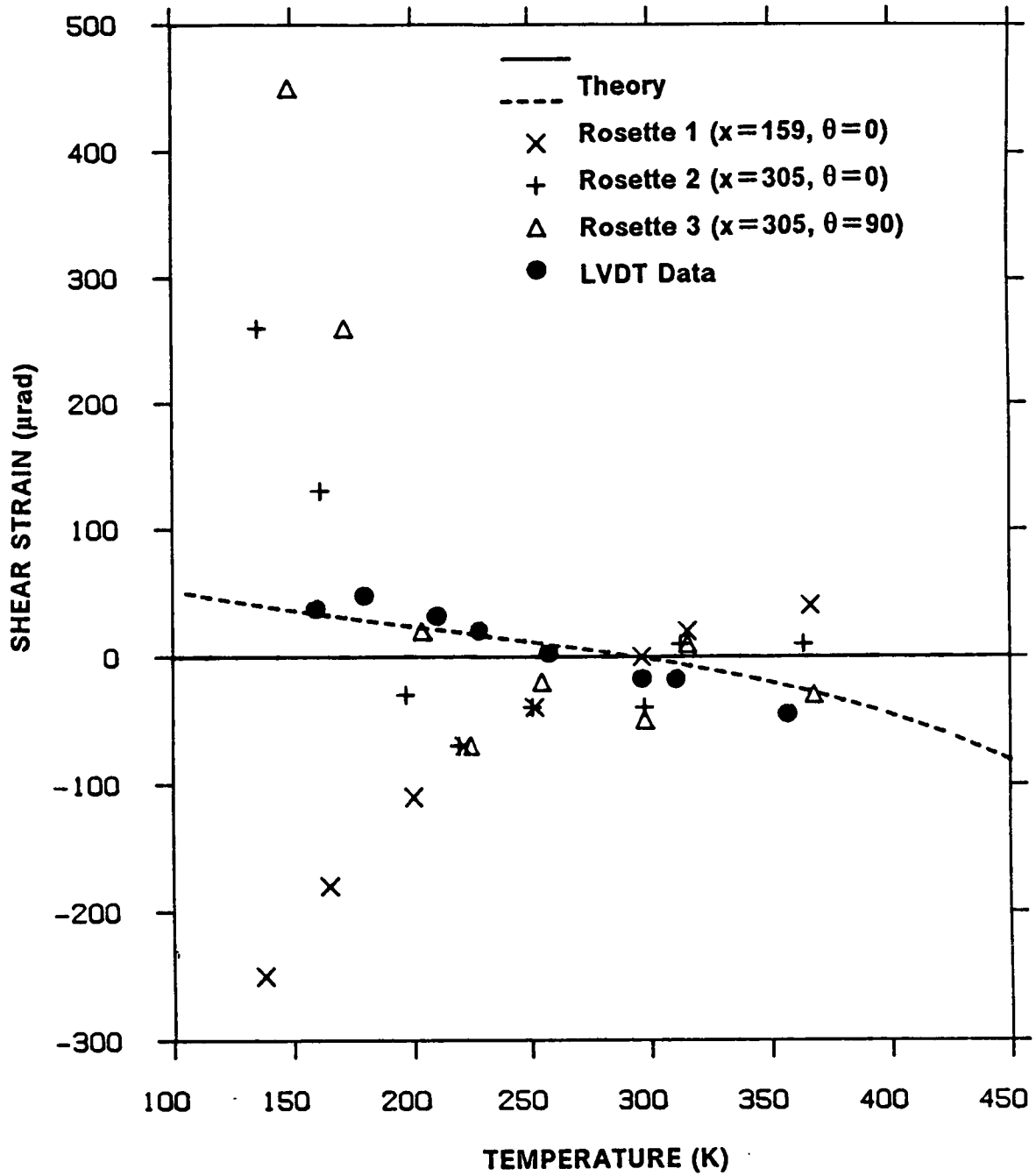


Figure 50. Shear Strain vs. Temperature, Specimen 16:  $[-10 / 0_s / 10_s / 0_s / -10]$ . Experiment and Theory, Temperature-dependent material properties.

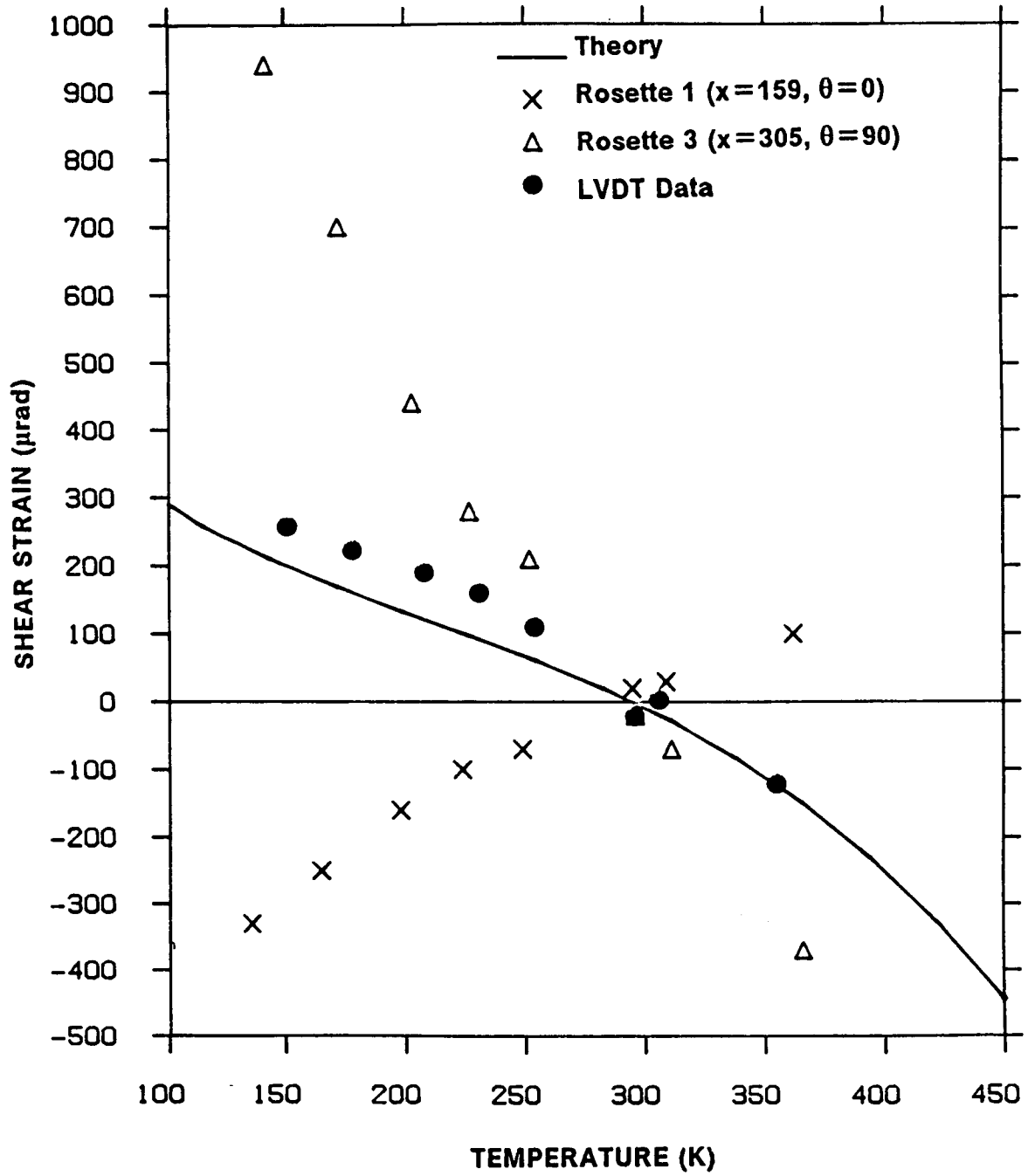


Figure 51. Shear Strain vs. Temperature, Specimen 17: [-10 / 0<sub>s</sub> / 15<sub>2</sub> / 0<sub>s</sub> / -10]. Experiment and Theory, Temperature-dependent material properties.

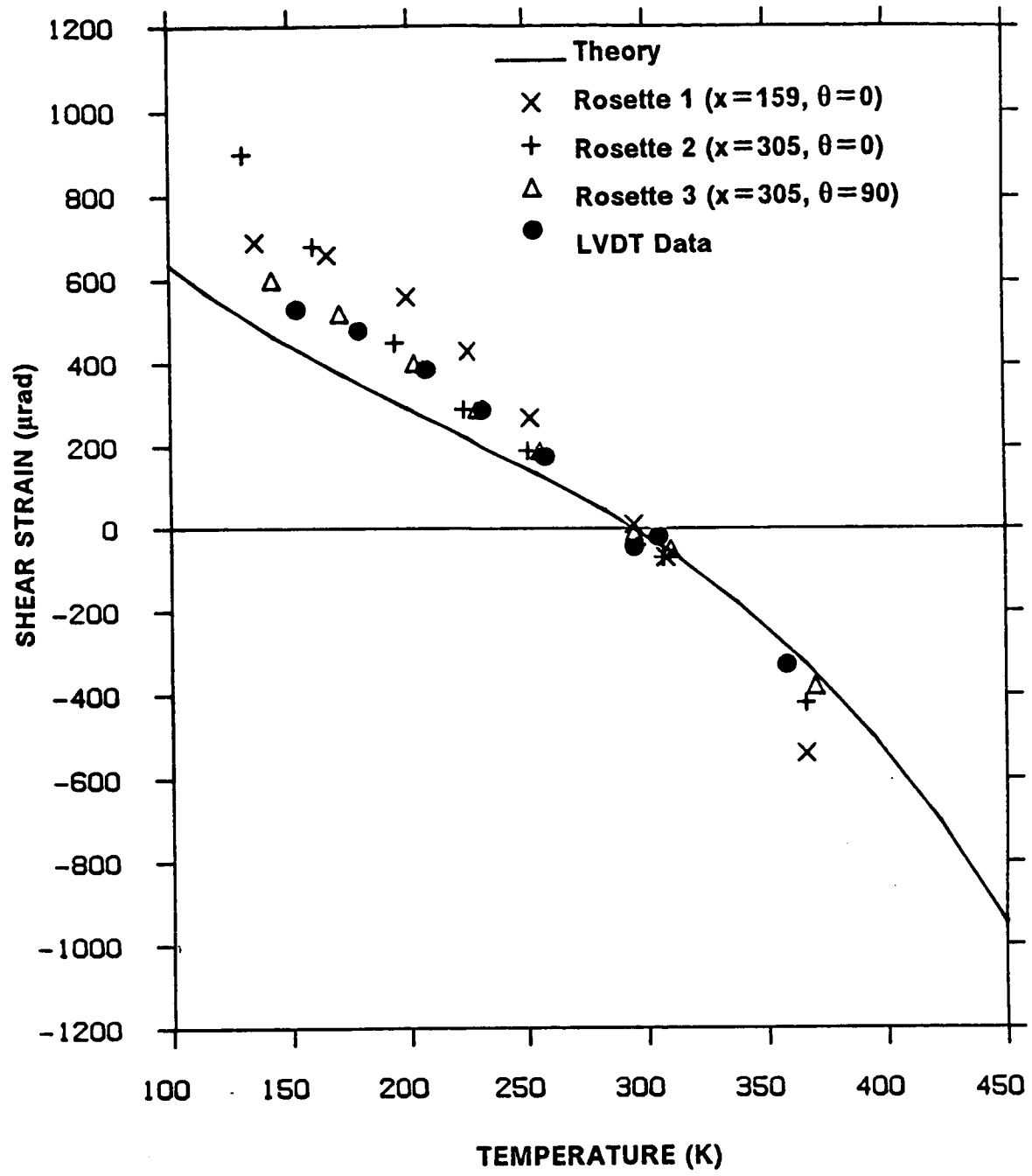


Figure 52. Shear Strain vs. Temperature, Specimen 18: [-10 / 0<sub>s</sub> / 20<sub>2</sub> / 0<sub>s</sub> / -10]. Experiment and Theory, Temperature-dependent material properties.

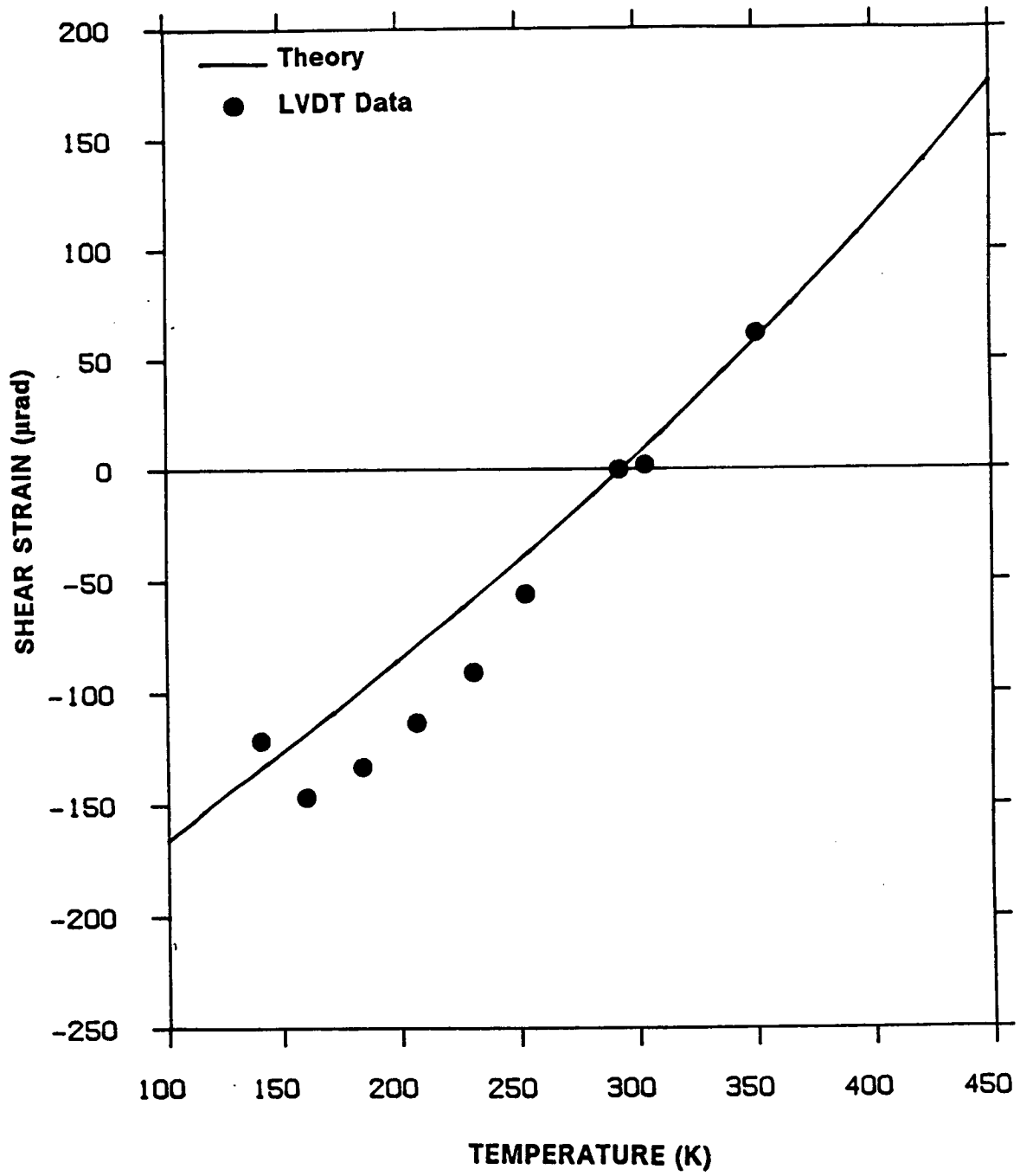


Figure 53. Shear Strain vs. Temperature, Specimen 21:  $[-10_2 / 0_{12}]$ . Experiment and Theory. Temperature-dependent material properties.

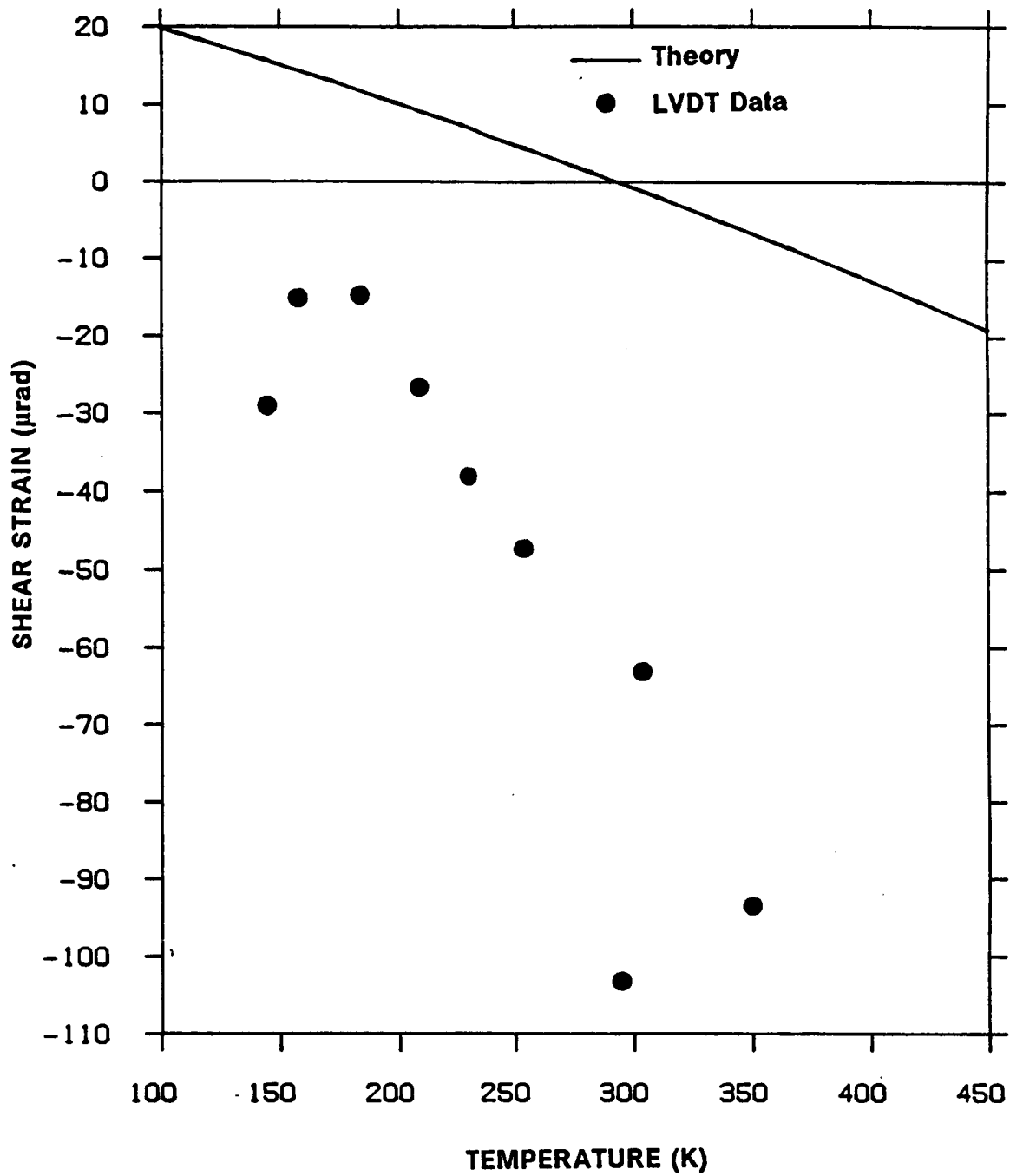


Figure 54. Shear Strain vs. Temperature, Specimen 22:  $[-10_2 / 0_{10} / 10_2]$ . Experiment and Theory, Temperature-dependent material properties.

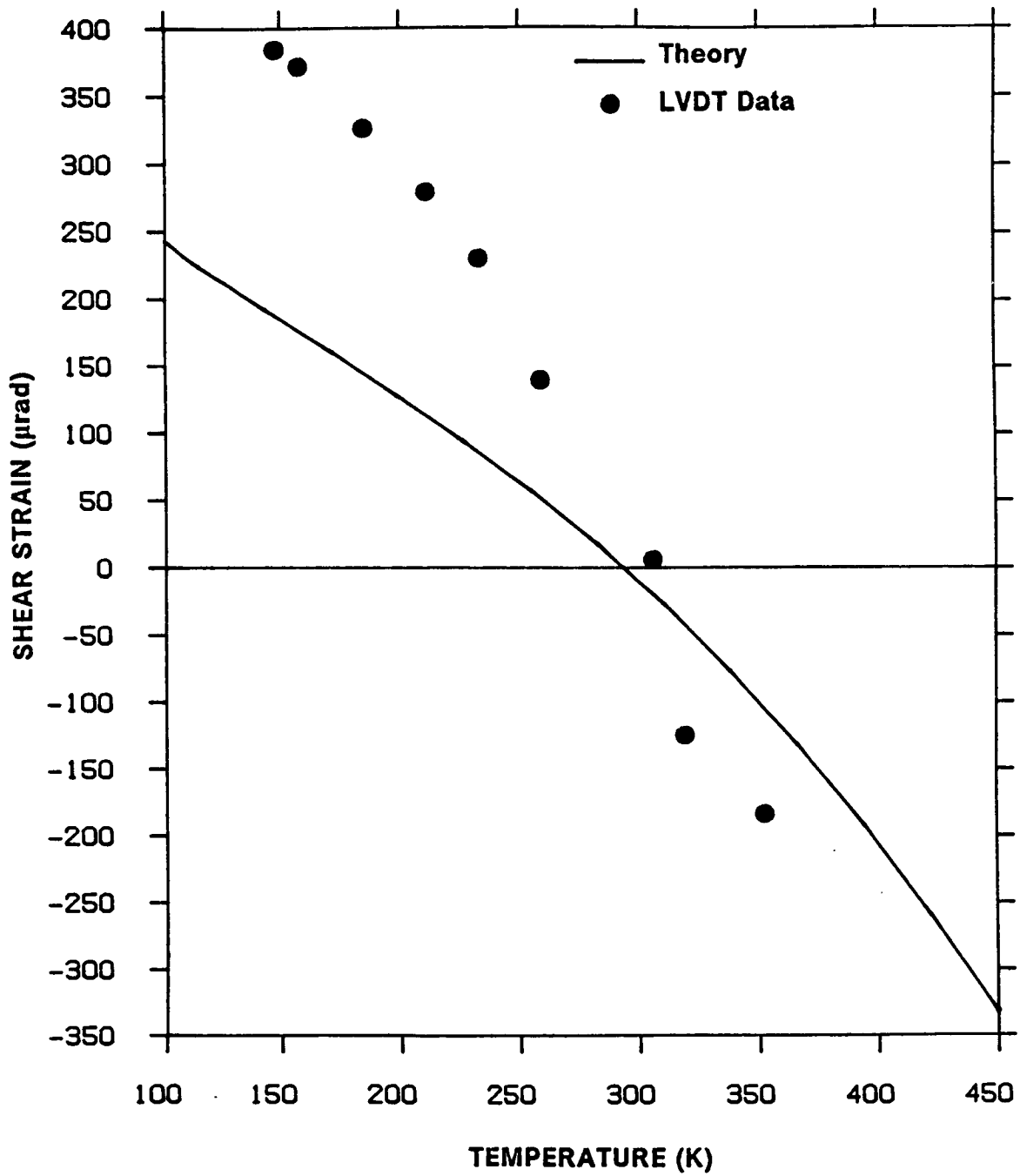


Figure 55. Shear Strain vs. Temperature, Specimen 24: [-10<sub>2</sub> / 0<sub>10</sub> / 20<sub>2</sub>]. Experiment and Theory, Temperature-dependent material properties.

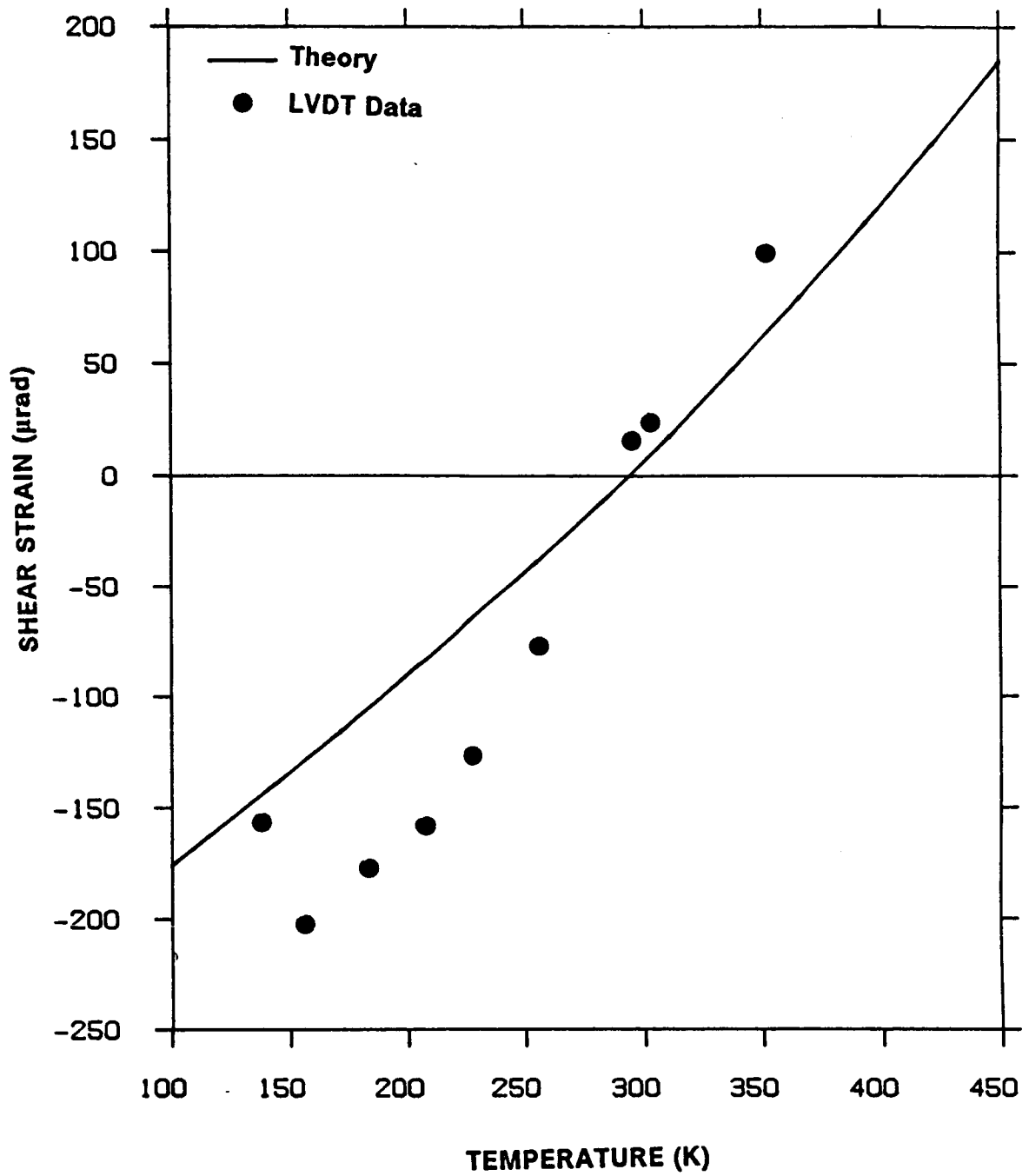


Figure 56. Shear Strain vs. Temperature, Specimen 25: [-10 / 0<sub>12</sub> / -10]. Experiment and Theory, Temperature-dependent material properties.

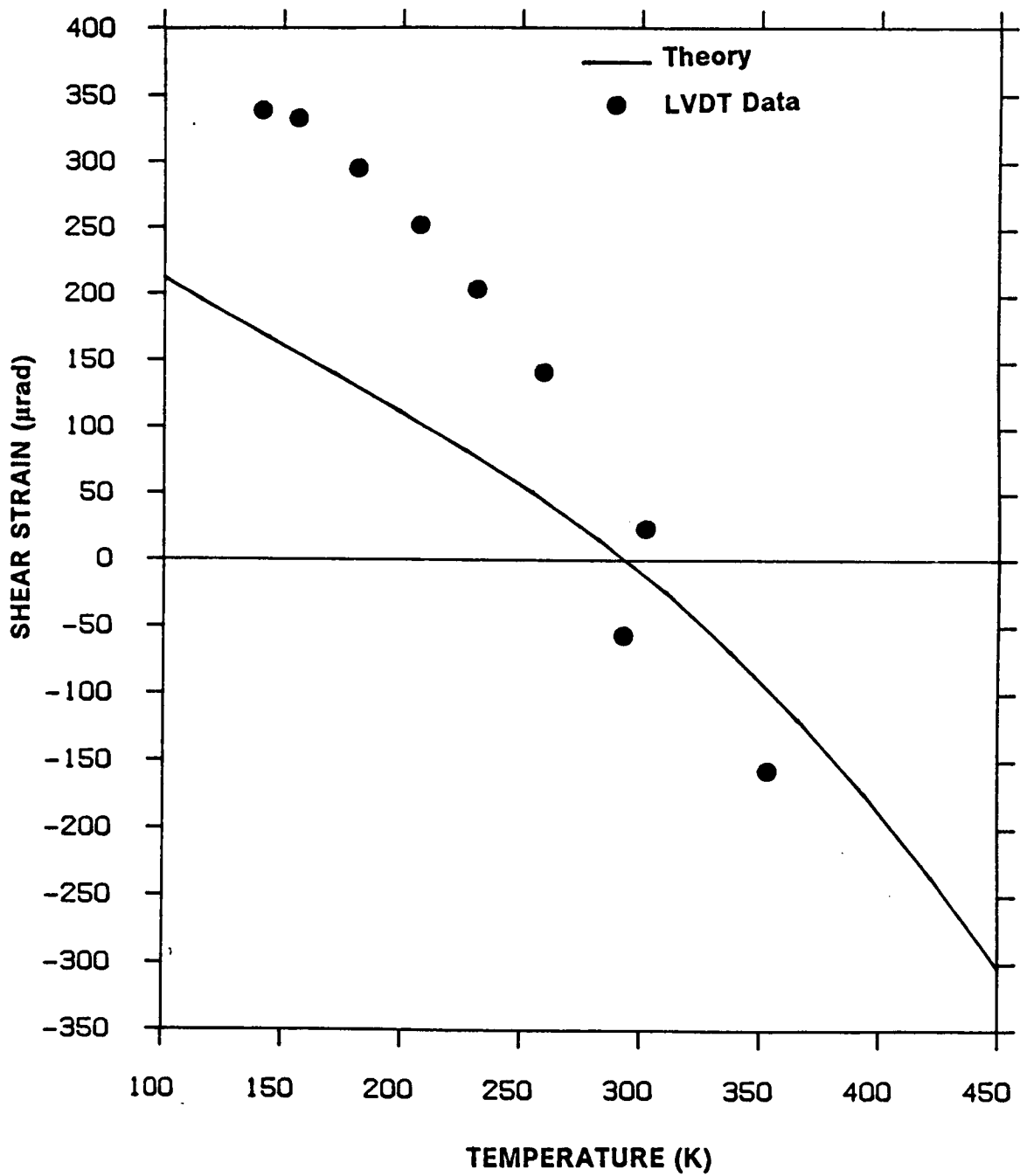


Figure 57. Shear Strain vs. Temperature, Specimen 28: [-10 / 0<sub>s</sub> / 20<sub>s</sub> / 0<sub>s</sub> / -10 ]. Experiment and Theory, Temperature-dependent material properties.

the agreement between theory and experiment for this material system is not as good as that of the other materials. In Figure 53 - Figure 57, the experimental results seem to yield consistently higher magnitudes of twist than predicted. As is explained in Appendix A, no actual material properties for T300/ERLX1962A were available. The lack of good material property data is suspected to be the reason for the poor agreement between theory and experiment here.

Figure 58 - Figure 62 illustrate the dependence of twist response on temperature for the AS4/976 tubes (specimens 31, 32, 34, 35, and 38). Specimens 34 and 35 were each tested twice, the first test being denoted as A and the second test denoted as B, and data from all tests are shown. Specimen 34 was subjected to two thermal cycles to determine if the test results were repeatable, or whether significant damage was induced in the first test and would therefore yield significantly different results. It is apparent in Figure 60 and Figure 61 that the results of the second test were essentially the same as those of the first test, indicating that no damage was induced that significantly effected twist response. Specimen 35 was tested a second time in order to check out changes in the strain gage acquisition hardware. Due to hardware problems, no useable strain gage data were obtained in tests 31, 32, 34A, 34B, 35A, and 38. The second test of specimen 35 yielded good strain gage data and it is presented in Figure 61. For the twist response of the AS4/976 material system, agreement between theory and the LVDT displacement data was generally good, with the strain gage data from the second test of specimen 35 being erratic.

The second group of figures, Figure 63 - Figure 68, illustrate another aspect of the thermally induced twist response of the tubes. In these figures, the dependence of twist per unit temperature change on fiber angle for the two lamination families and three material systems is shown. These figures show both the experimental data, as measured by the strain gage rosettes, and as derived from the tangential displacement transducer data. Also indicated on the figures are theoretical calculations. Both the experimental data and the theoretical predictions are approximations. The experimental data are approximations in the following sense:

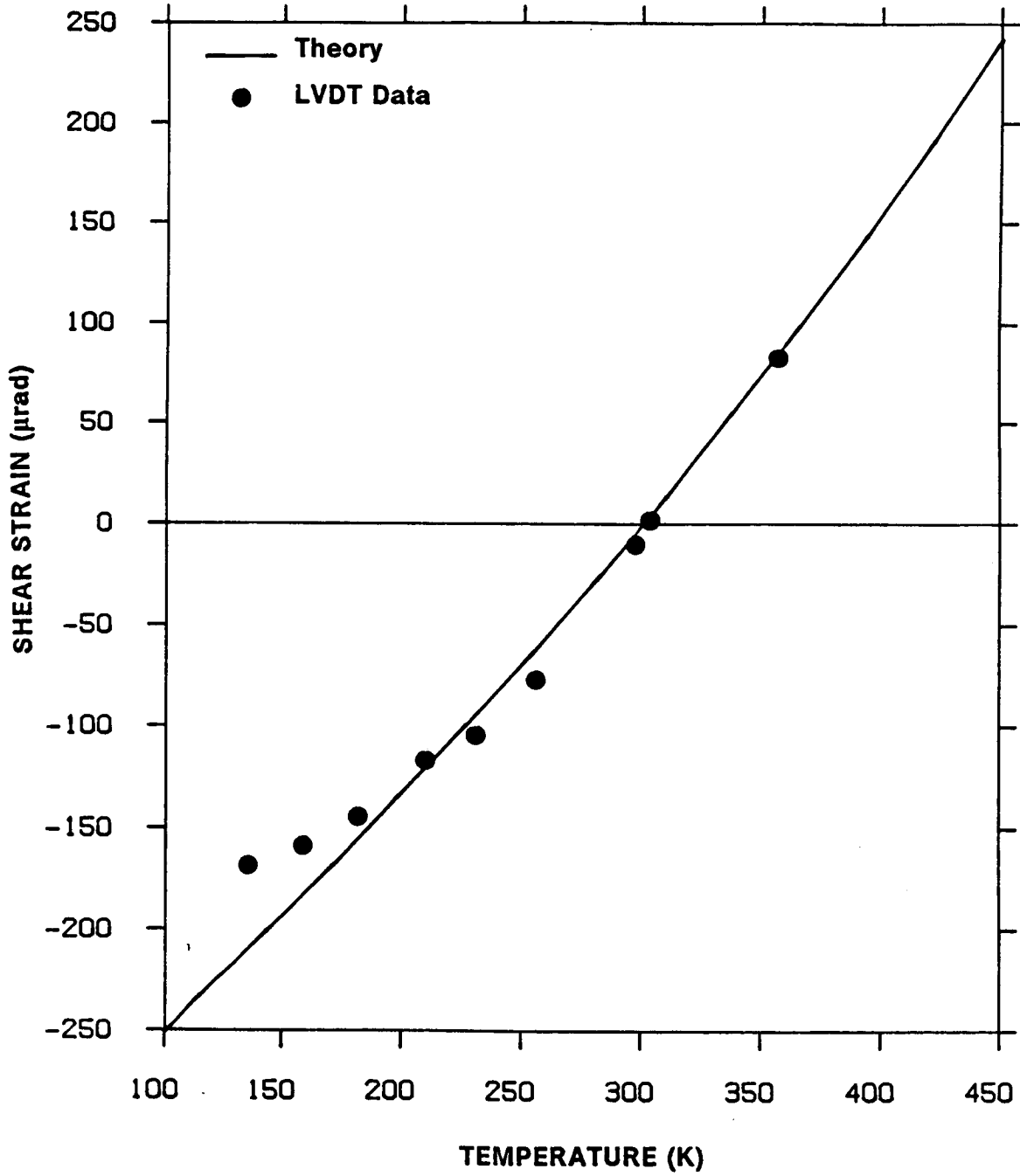


Figure 58. Shear Strain vs. Temperature, Specimen 31:  $[-10_2 / 0_{12}]$ . Experiment and Theory, Temperature-dependent material properties.

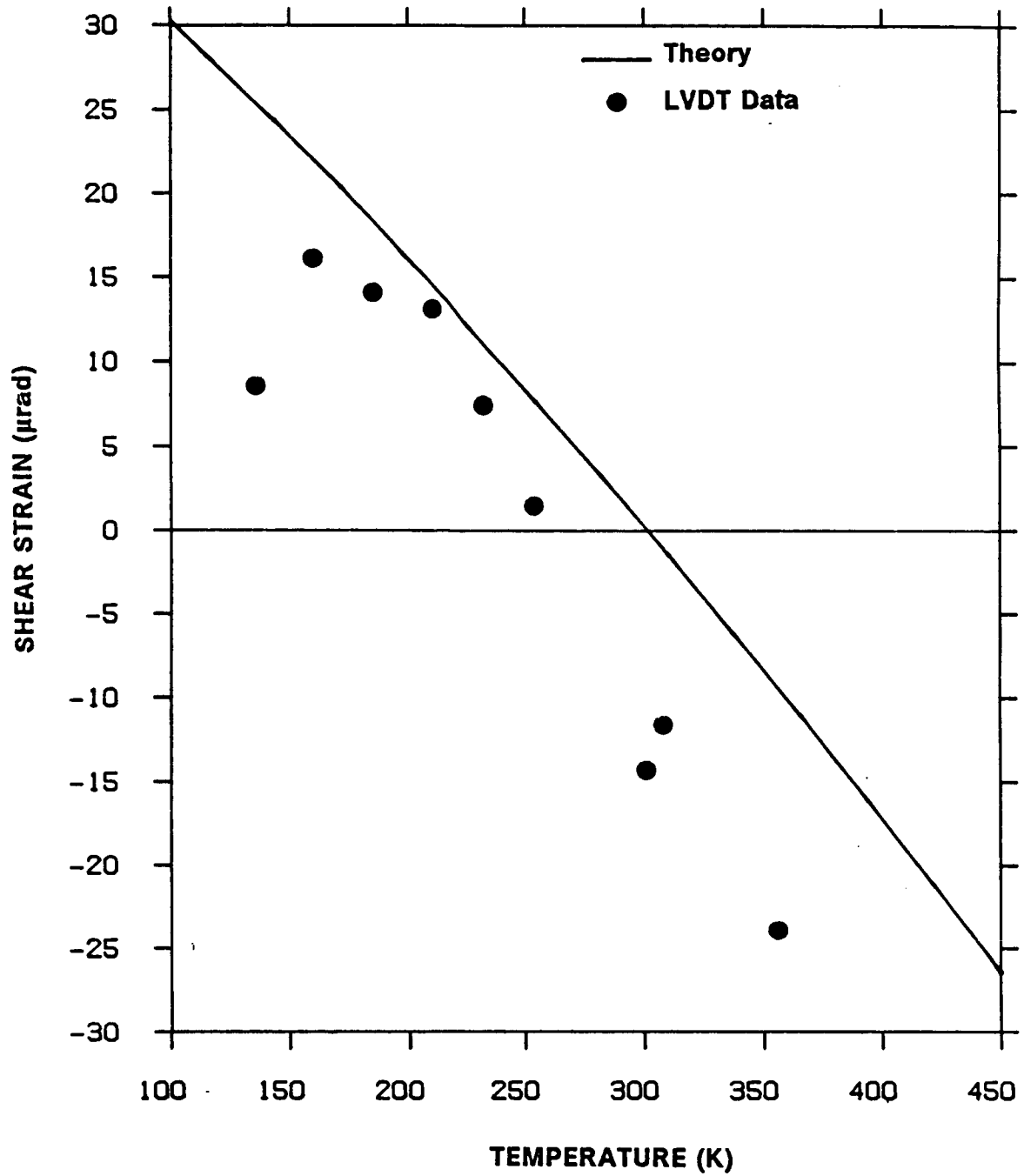


Figure 59. Shear Strain vs. Temperature, Specimen 32:  $[-10_2 / 0_{10} / 10_2]$ . Experiment and Theory, Temperature-dependent material properties.

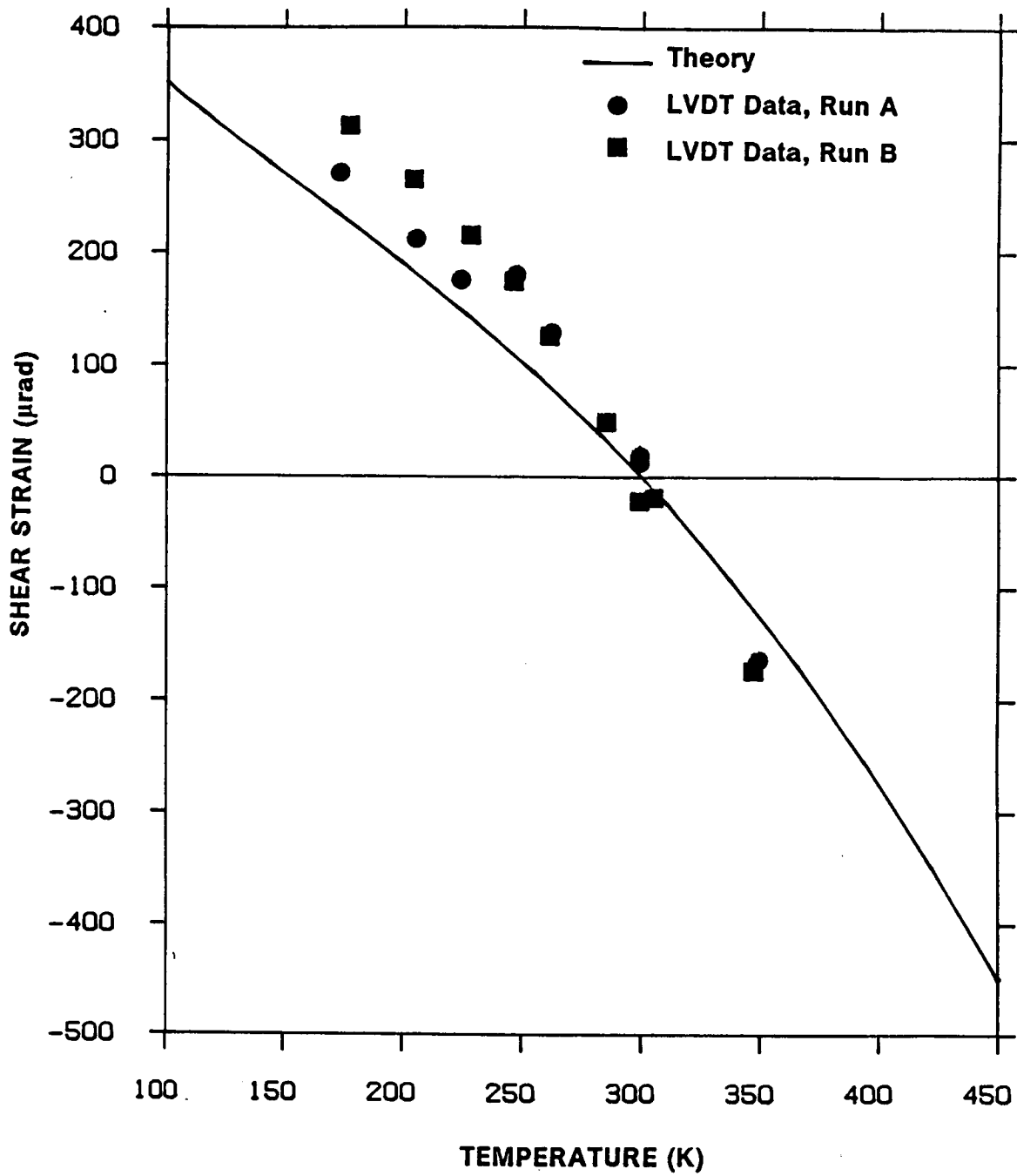


Figure 60. Shear Strain vs. Temperature, Specimen 34: [-10<sub>2</sub> / 0<sub>10</sub> / 20<sub>2</sub>]. Experiment and Theory, Temperature-dependent material properties. Data from two tests shown.

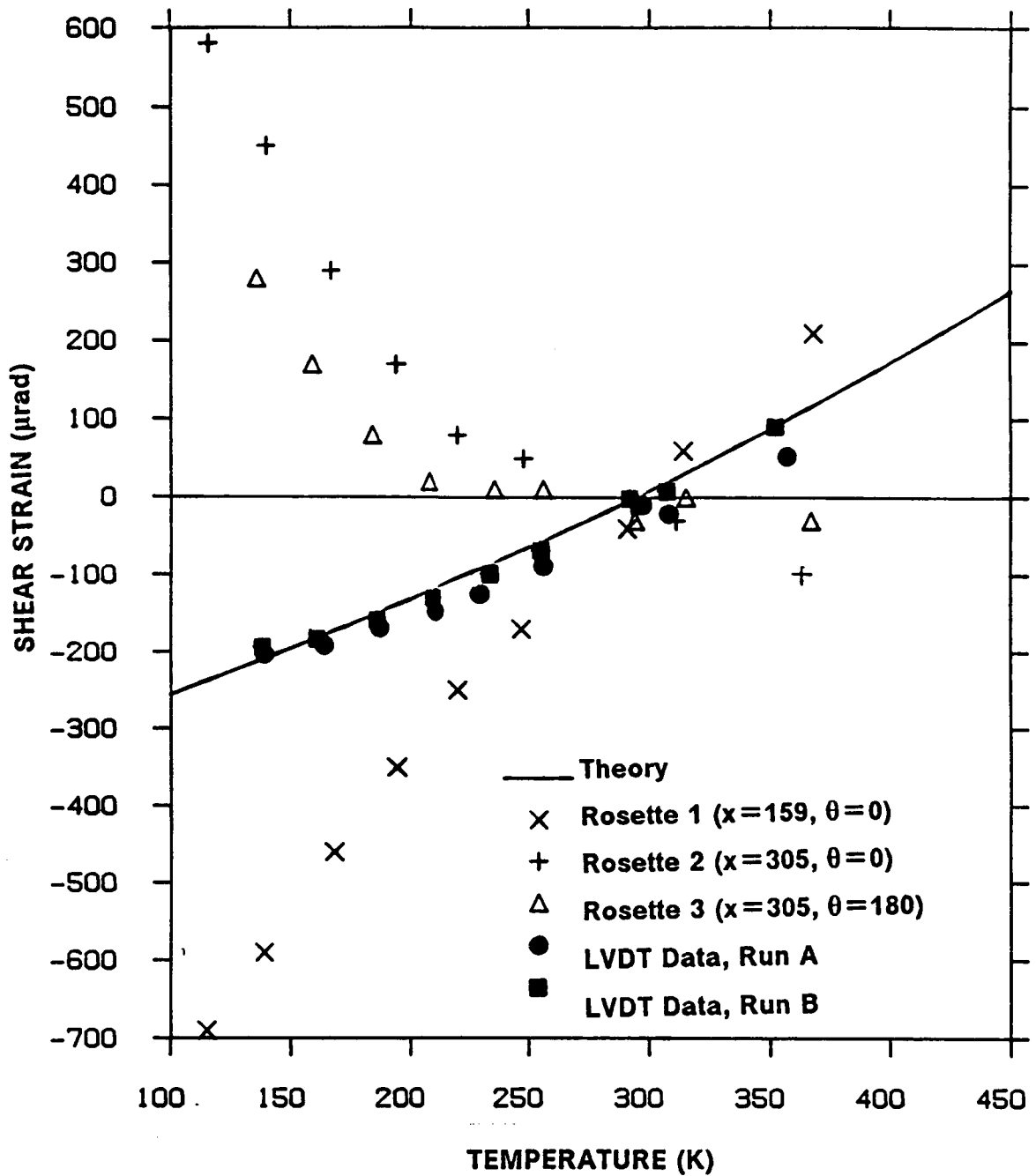


Figure 61. Shear Strain vs. Temperature, Specimen 35: [-10 / 0<sub>1,2</sub> / -10]. Experiment and Theory, Temperature-dependent material properties. Displacement data from two tests shown. Strain gage data from test 2 only.

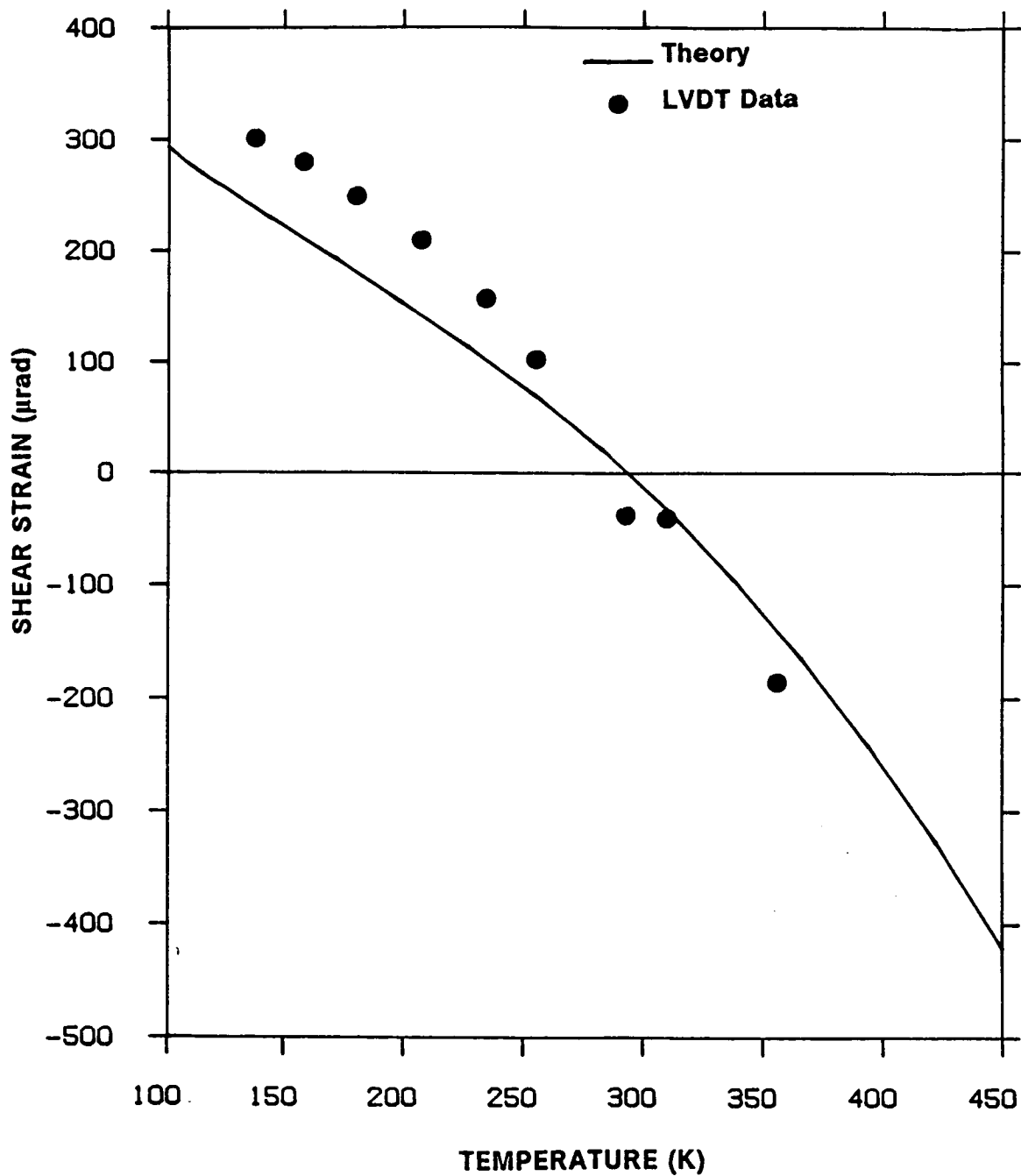


Figure 62. Shear Strain vs. Temperature, Specimen 38: [-10 / 0<sub>s</sub> / 20<sub>2</sub> / 0<sub>s</sub> / -10 ]. Experiment and Theory, Temperature-dependent material properties.

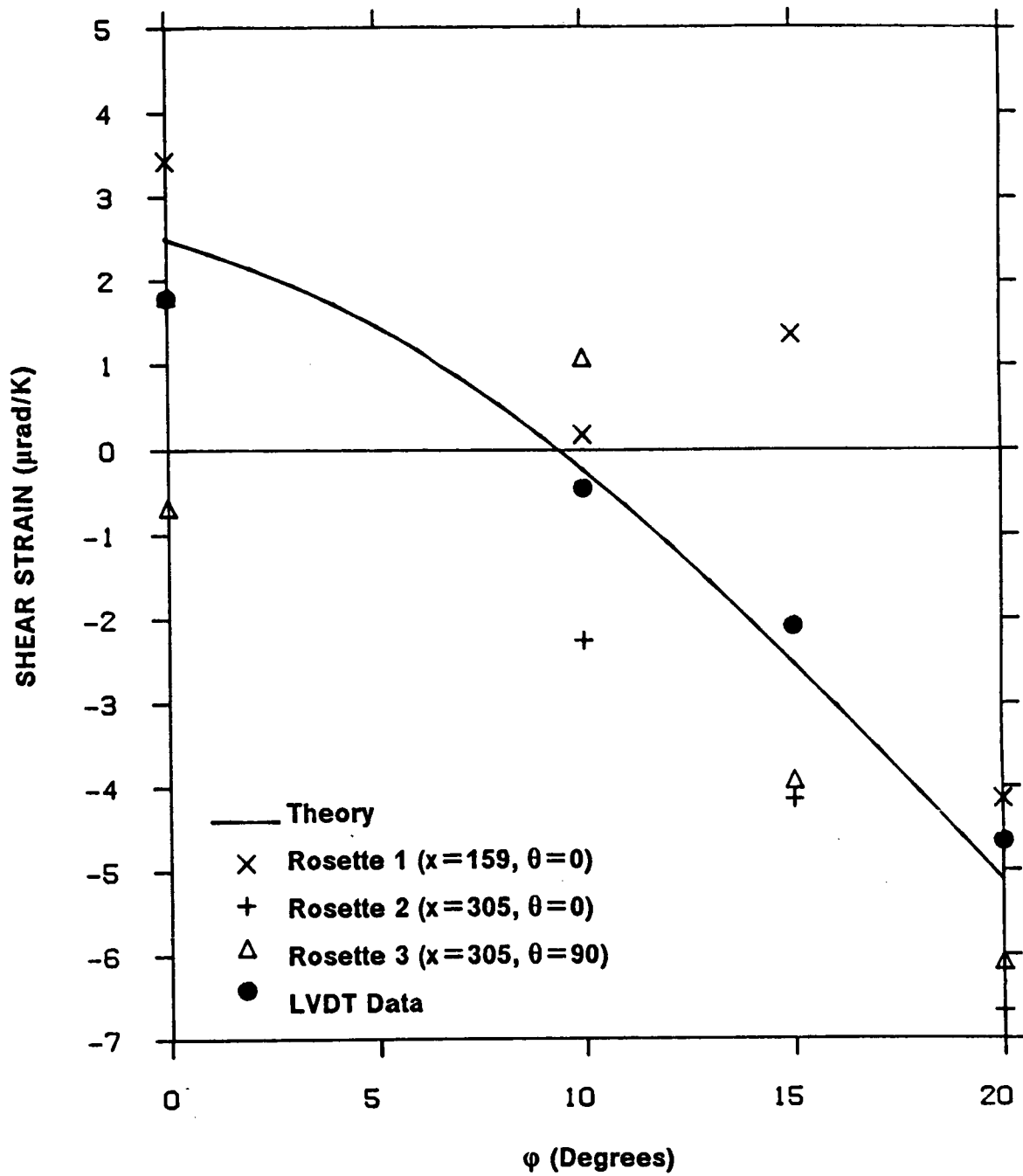


Figure 63. Shear Strain vs. Ply Orientation Angle (Specimens 11 - 14): Family 1 :  $[-10_2 / 0_{10} / \phi_2]$ . Experiment and Theory, Temperature-independent material properties. material system : P75S/ERLX1962A.

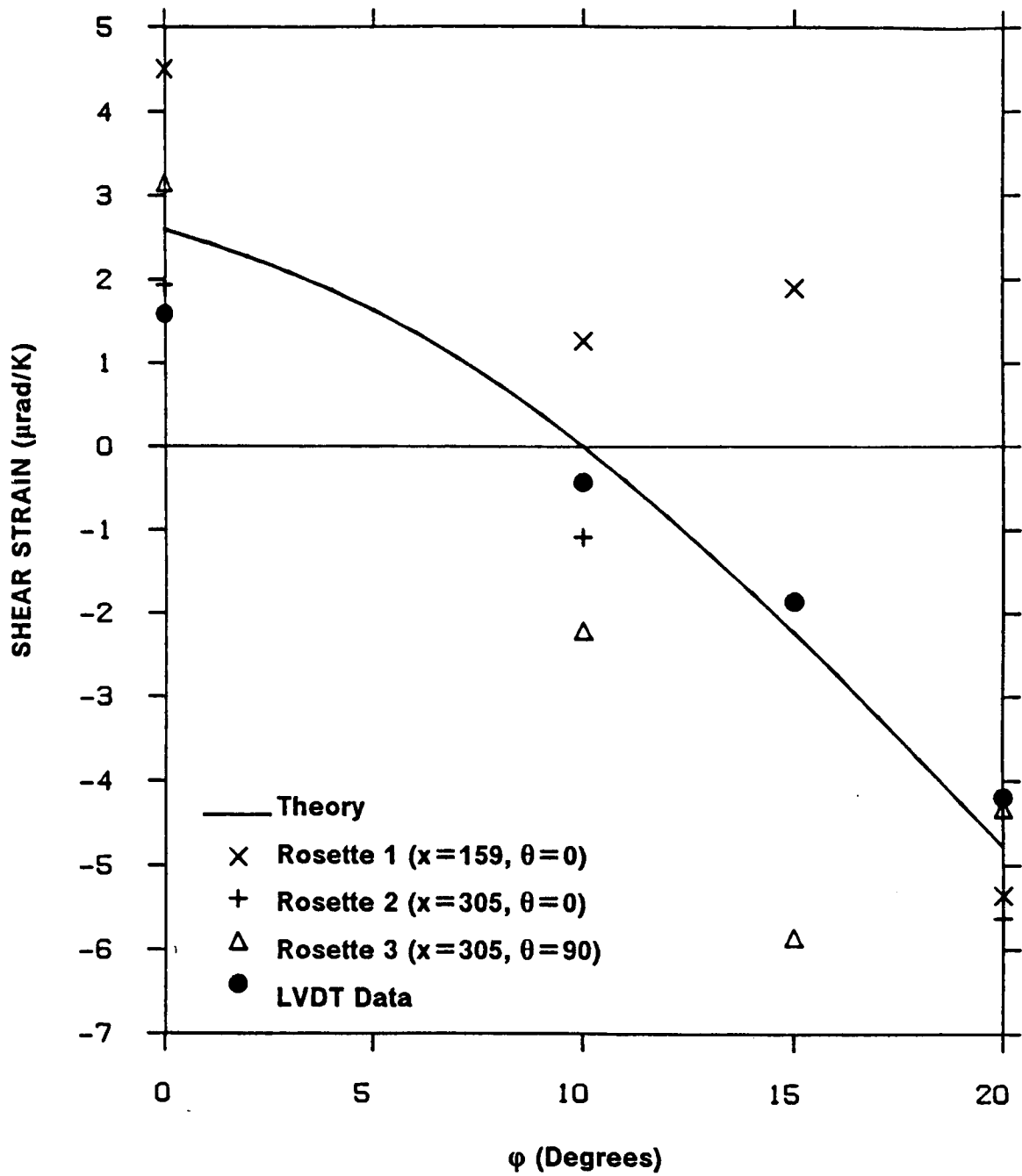


Figure 64. Shear Strain vs. Ply Orientation Angle (Specimens 15 - 18): Family 2 :  $[-10^\circ / 0_3 / \varphi_2 / 0_3 / -10^\circ]$ . Experiment and Theory, Temperature-independent material properties. material system : P75S/ERLX1962A.

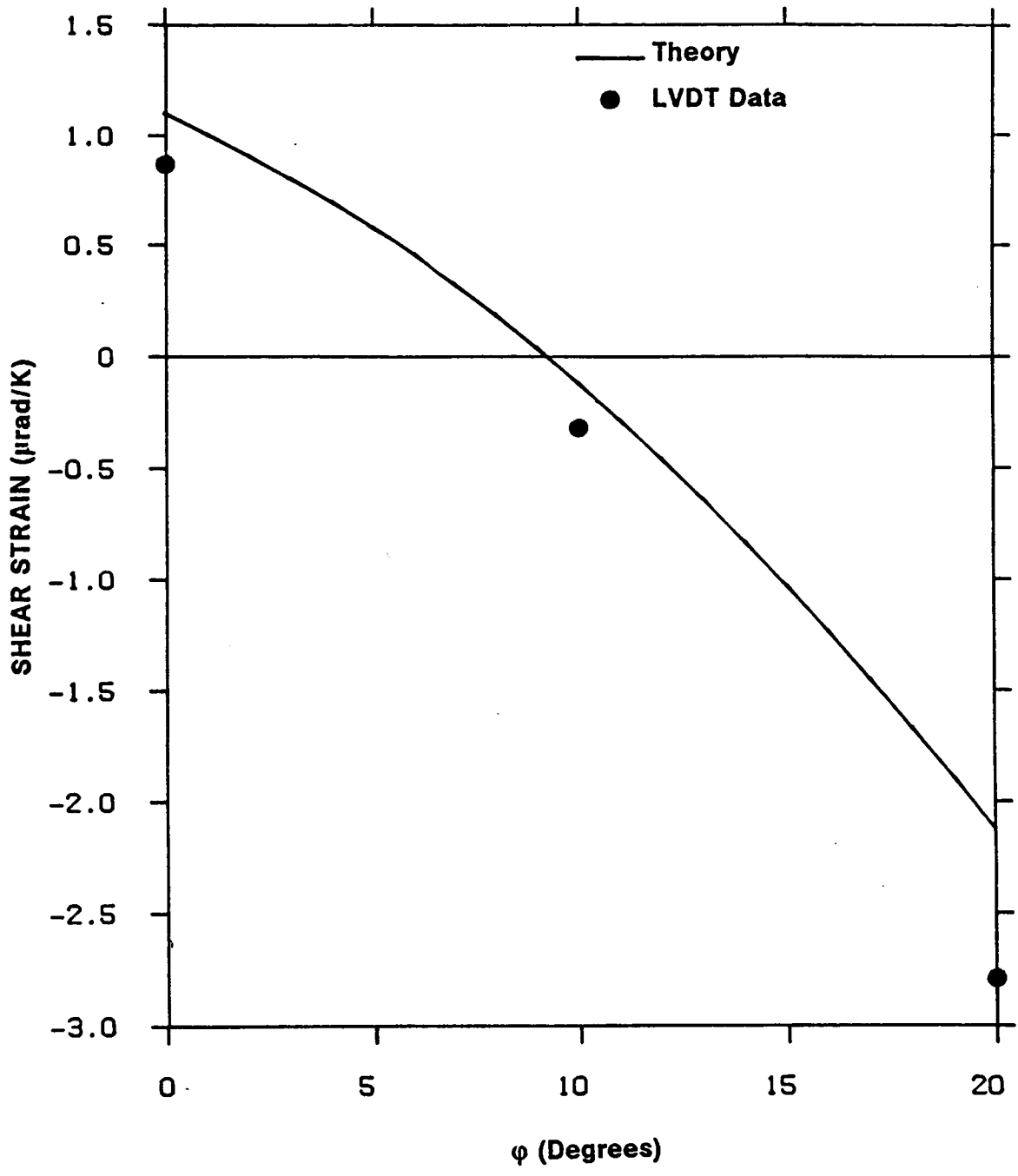


Figure 65. Shear Strain vs. Ply Orientation Angle (Specimens 21, 22, and 24): Family 1 : [-10<sub>2</sub> / 0<sub>10</sub> / φ<sub>2</sub>]. Experiment and Theory, Temperature-independent material properties. material system : T300/ERLX1962A.

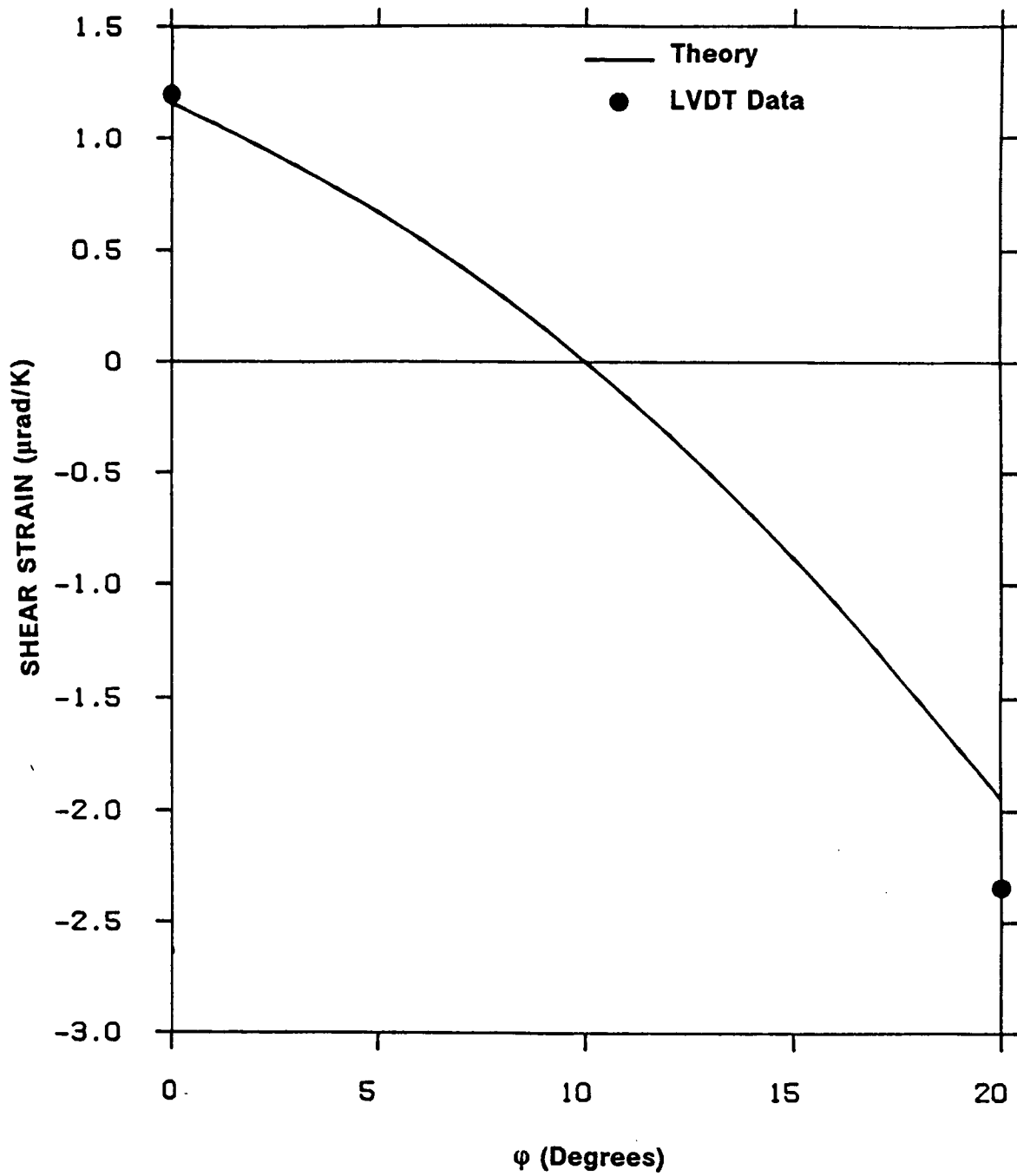


Figure 66. Shear Strain vs. Ply Orientation Angle (Specimens 25 and 28): Family 2 : [-10 / 0<sub>s</sub> / φ<sub>2</sub> / 0<sub>s</sub> / -10 ]. Experiment and Theory, Temperature-independent material properties. material system : T300/ERLX1962A.

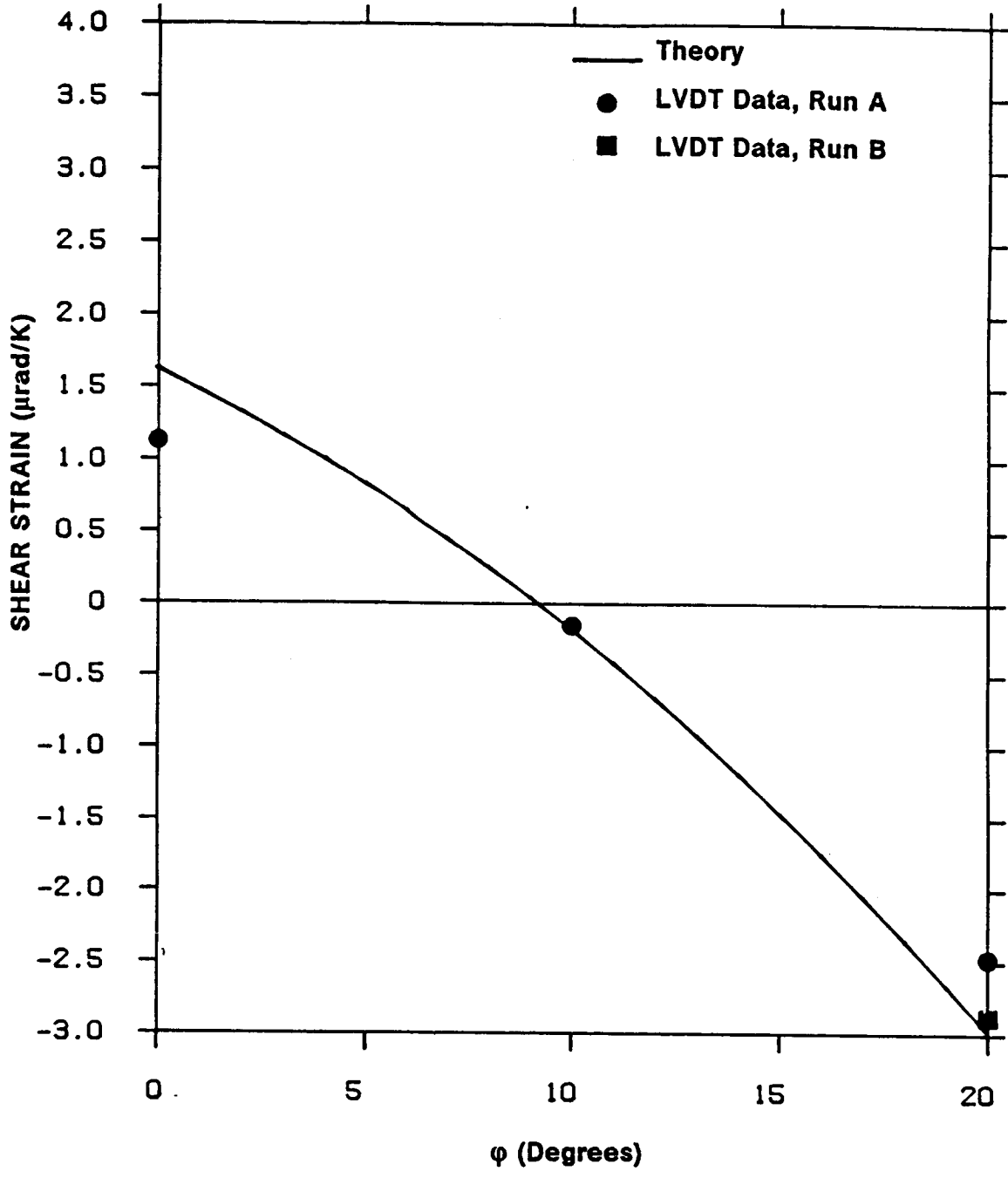


Figure 67. Shear Strain vs. Ply Orientation Angle (Specimens 31, 32, and 34): Family 1 :  $[-10_2 / 0_{10} / \phi_2]$ . Experiment and Theory, Temperature-independent material properties. material system : AS4/976.

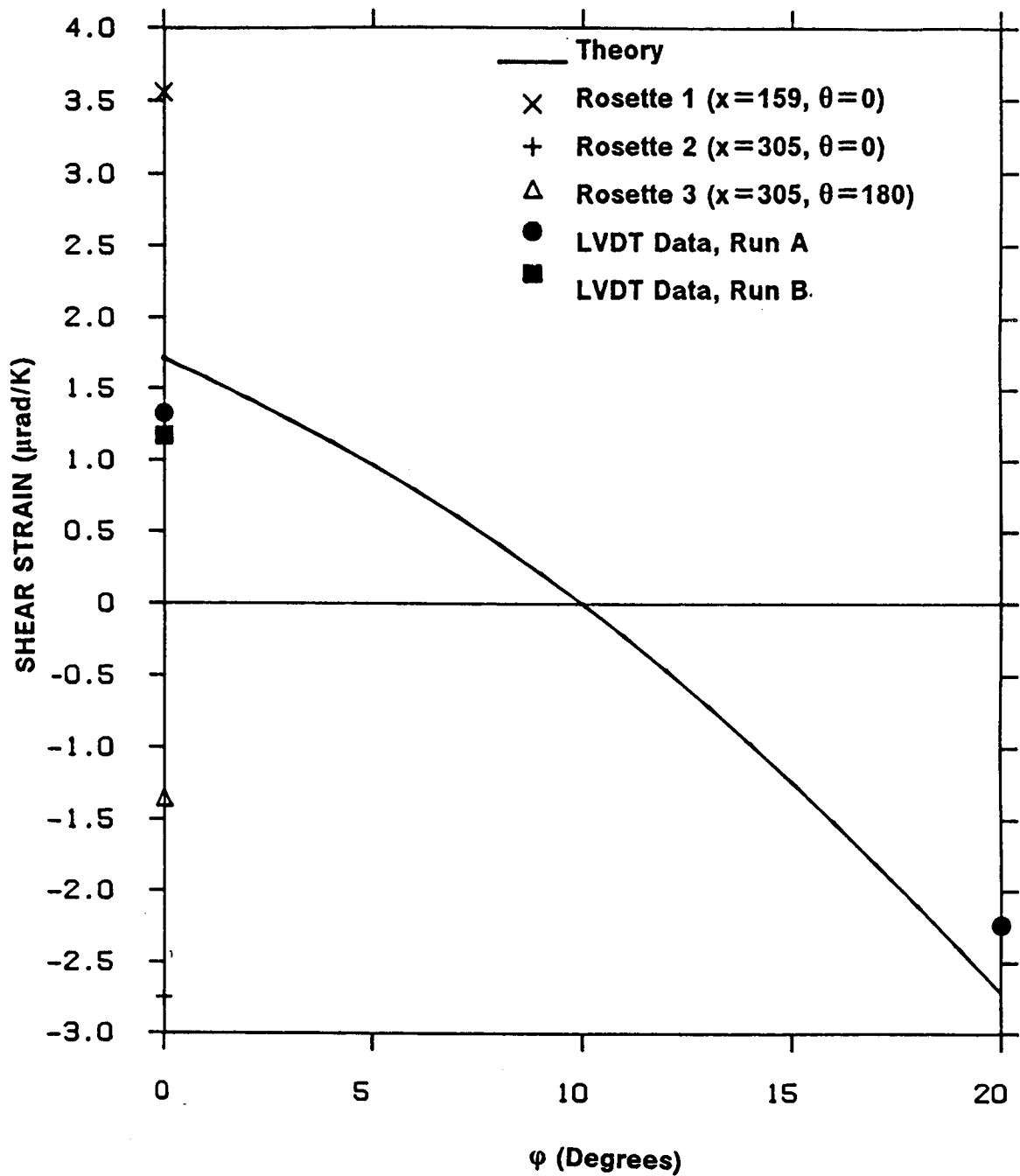


Figure 68. Shear Strain vs. Ply Orientation Angle (Specimens 35 and 38): Family 2 : [-10 / 0<sub>s</sub> /  $\phi_2$  / 0<sub>s</sub> / -10 ]. Experiment and Theory, Temperature-independent material properties. material system : AS4/976.

To obtain a particular data point in the figure, the twist response at the lowest temperature is subtracted from the twist response measured at the highest temperature. This difference is then divided by the difference in temperatures for that specific test, resulting in a differential shear strain per unit temperature change ( $\Delta\gamma^{\circ}/K$ ). This calculation smears out any nonlinear relations between shear strain and temperature that may occur over the temperature range. As seen in Figure 45 - Figure 62, nonlinearities exist but they are not so severe as to make this calculation meaningless. In effect, this linearization of the experimental data is equivalent to ignoring the influence of temperature-dependent material properties. Accordingly, the theoretical predictions are approximations in the following sense: As has been seen, the use of temperature-dependent material properties influences the predicted tube response. To properly discuss the response of the tube per unit temperature change, the temperature of the tube enters the calculation. If the theoretical response of the tube is computed using temperature-independent material properties, the temperature of the tube is not important. The response per unit temperature change is independent of temperature. The theoretical predictions in Figure 63 - Figure 68 are obtained using temperature-independent material properties. In a sense, then, the figures compare theoretical and experimental linearizations of tube response.

As can be seen in the figures, the comparison between theoretical predictions and the twist response measured with the displacement transducers (solid circles and squares) is good. The comparison with the strain gage-measured response, when strains were measured, is not so good. This would be expected, in light of the previous illustrations of strain gage data. It is important to note that for Family 1 (Figure 63), independent of material system, a twist is predicted even when  $\phi = 10^{\circ}$ , the condition of a balanced laminate. The twist is nonzero for this family because the two balanced off-axis plies are separated by the axial plies, and the laminate is not symmetric. On the other hand, for Family 2 (Figure 64),  $\phi = 10^{\circ}$ , a balanced symmetric laminate results, yielding a much lower (but still non-zero) predicted value of twist. Regarding another general trend seen in Figure 63 - Figure 68, the linear theory seems to

overpredict the magnitude of the twist, the exception being for Figure 65 and Figure 66, where (as mentioned earlier) there is reason to suspect the accuracy of the material properties used for T300/ERLX1962A.

## **5.2 Axial Strain Response**

Though compared to the shear strain, or twist response, not as much emphasis has been placed on it, the axial response of the tube to temperature changes is of importance. As with the shear strain response, the axial response as measured by the displacement transducers is illustrated in Figure 69 - Figure 92. For the specimens that were strain gaged, the axial strain gage data are also presented (crosses, plusses, and open triangles). In addition, the theoretical predictions are included. For the figures illustrating axial strain vs. temperature, temperature-dependent material properties were used in the analysis. For the figures illustrating axial strain vs. off-axis angle, temperature-independent material properties were used in the calculations.

Figure 69 illustrates that specimen 11 contracted when heated. The theoretical predictions indicated that this would happen and the experimental data confirmed this. However, the correlation between the magnitude predicted in the theory and value measured in the experiment is poor. The experimental data show that the axial contraction is much greater than predicted (by roughly a factor of three). For those specimens that were strain gaged, the strain gage data correlate well with the displacement transducer data, confirming that the contraction is, indeed, more than predicted.

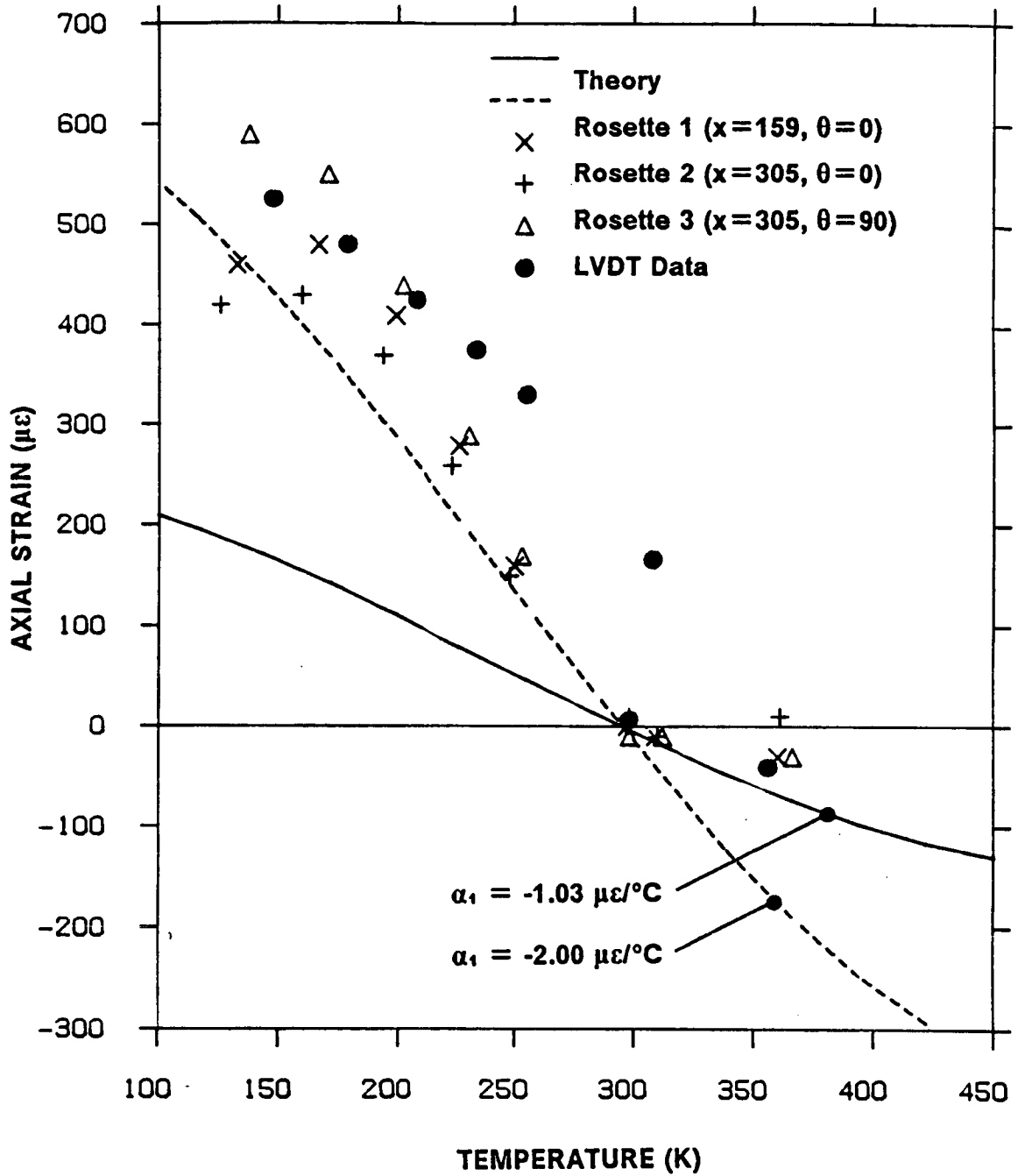


Figure 69. Axial Strain vs. Temperature, Specimen 11:  $[-10_2 / 0_{12}]$ . Experiment and Theory, Temperature-dependent material properties.

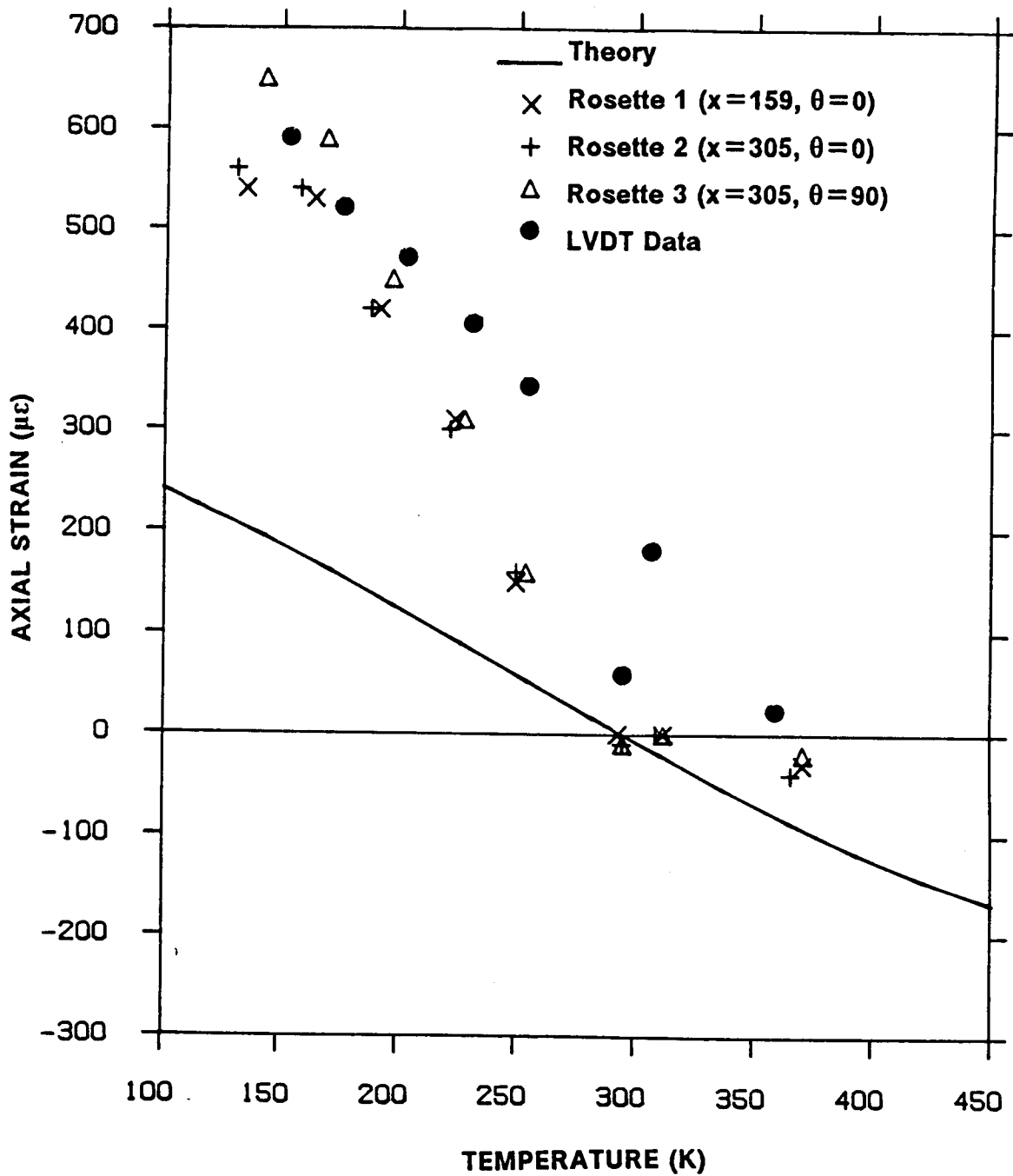


Figure 70. Axial Strain vs. Temperature, Specimen 12:  $[-10_2 / 0_{10} / 10_2]$ . Experiment and Theory. Temperature-dependent material properties.

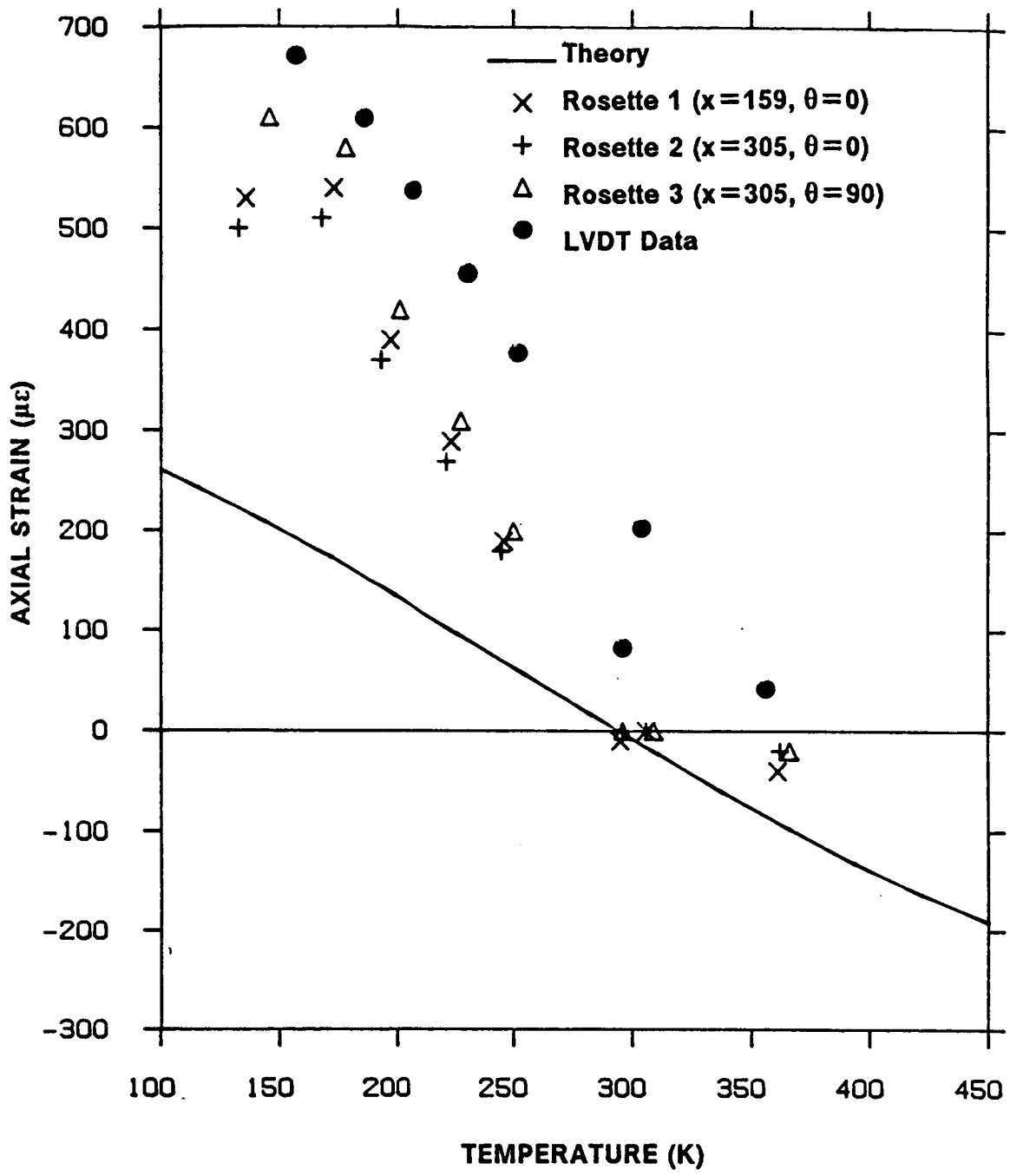


Figure 71. Axial Strain vs. Temperature, Specimen 13:  $[-10_2 / 0_{10} / 15_2]$ . Experiment and Theory, Temperature-dependent material properties.

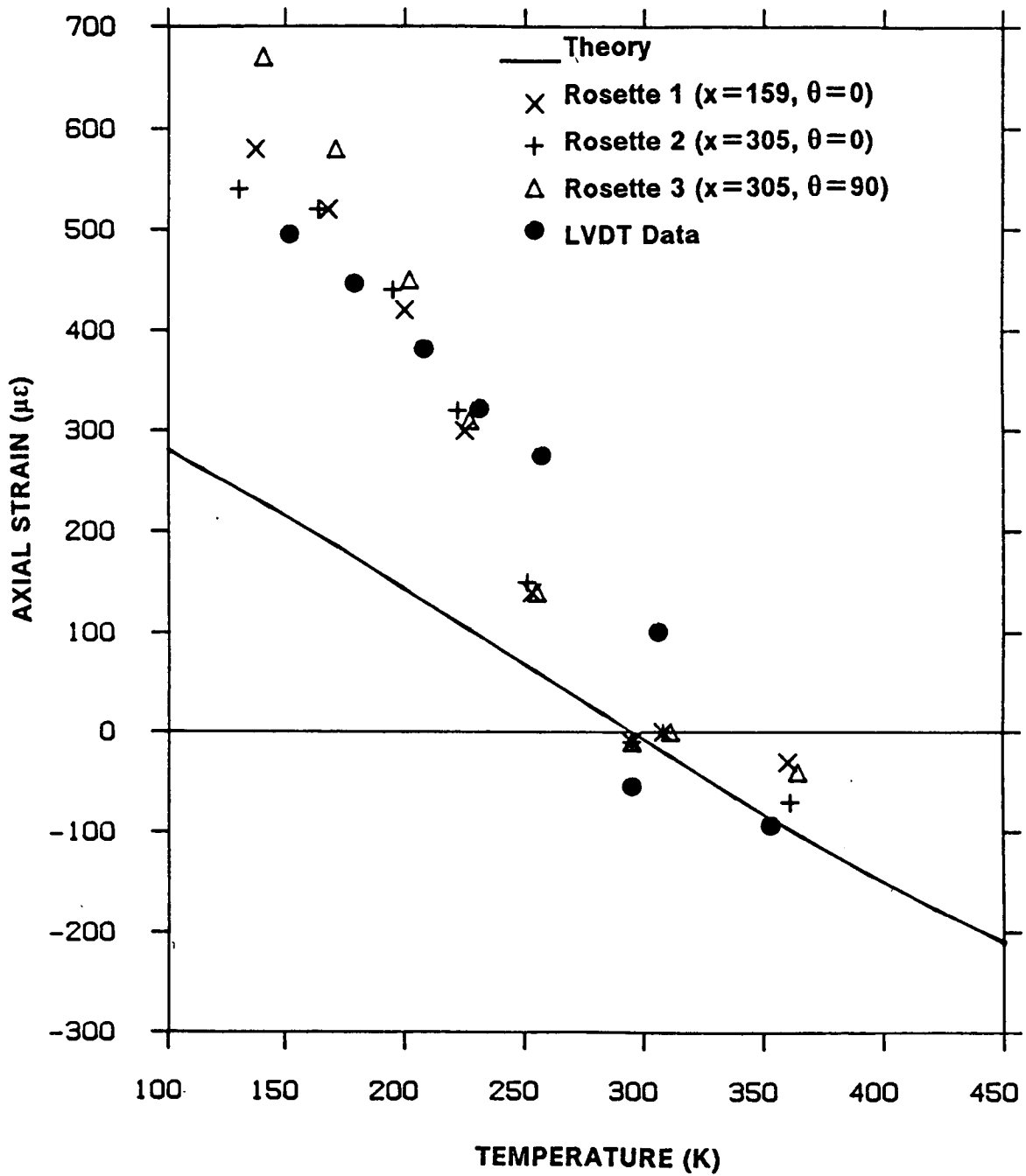


Figure 72. Axial Strain vs. Temperature, Specimen 14:  $[-10_2 / 0_{10} / 20_2]$ . Experiment and Theory, Temperature-dependent material properties.

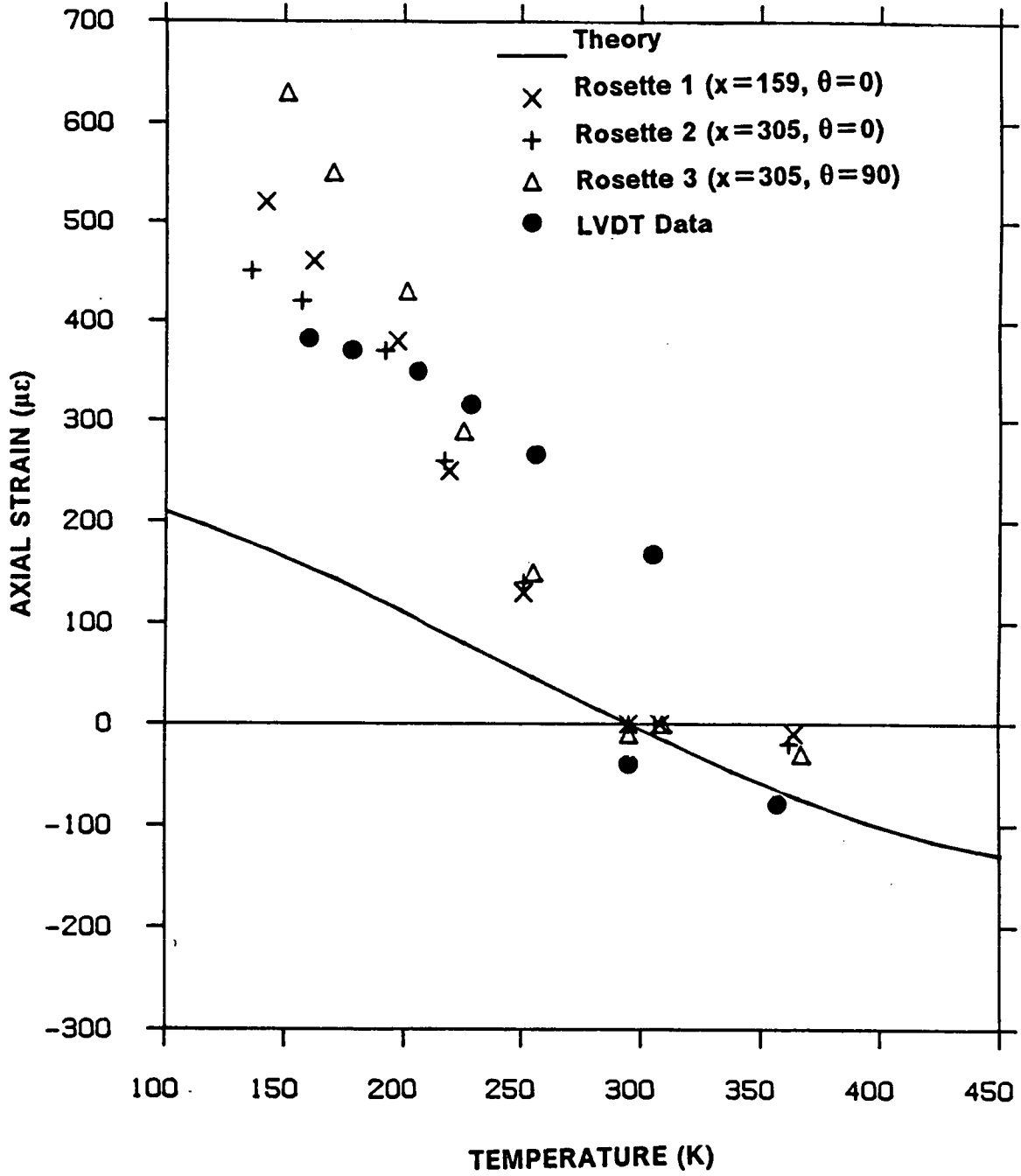


Figure 73. Axial Strain vs. Temperature, Specimen 15: [-10 / 0<sub>12</sub> / -10]. Experiment and Theory, Temperature-dependent material properties.

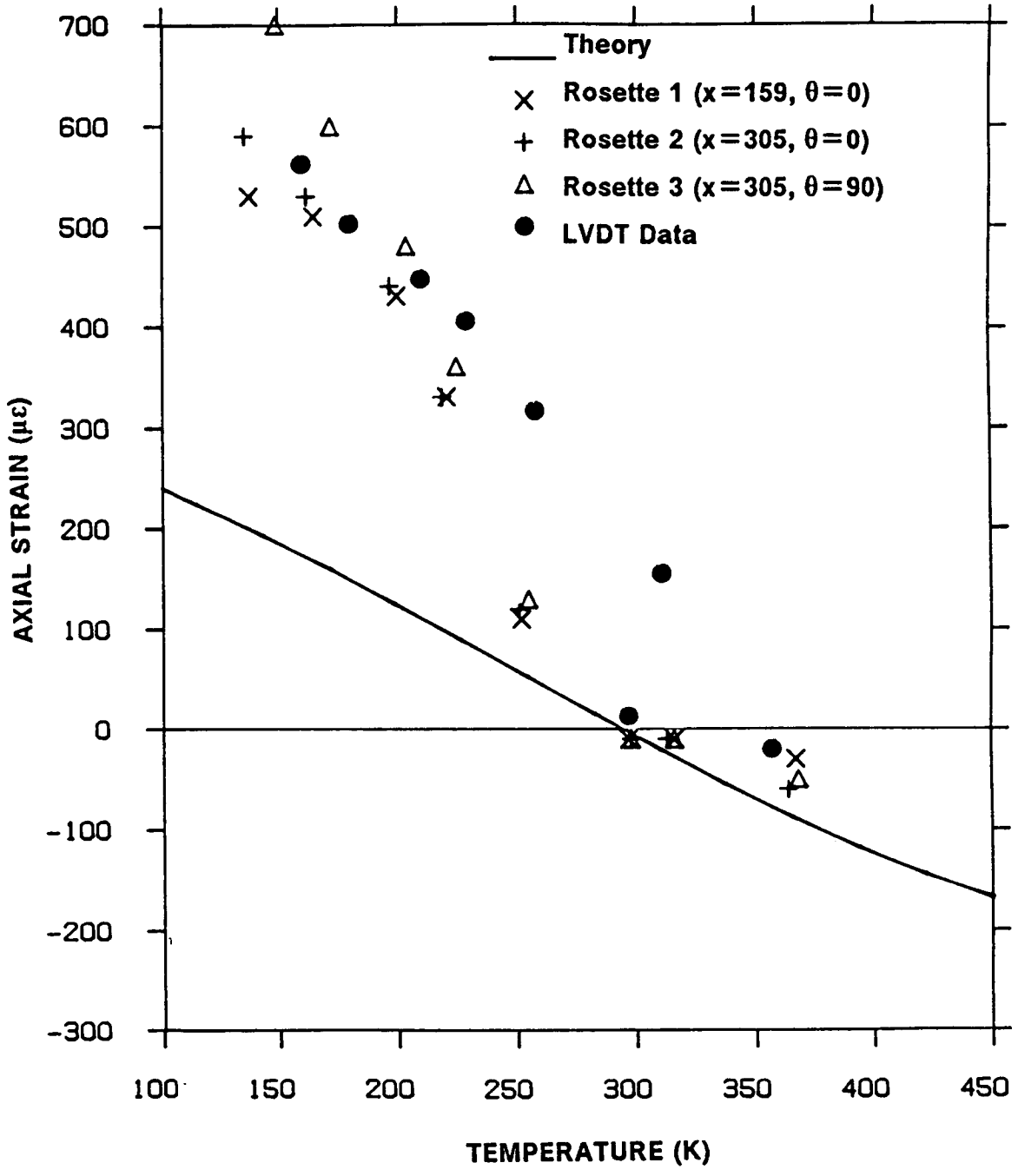


Figure 74. Axial Strain vs. Temperature, Specimen 16: [-10 / 0, / 10, / 0, / -10 ]. Experiment and Theory, Temperature-dependent material properties.

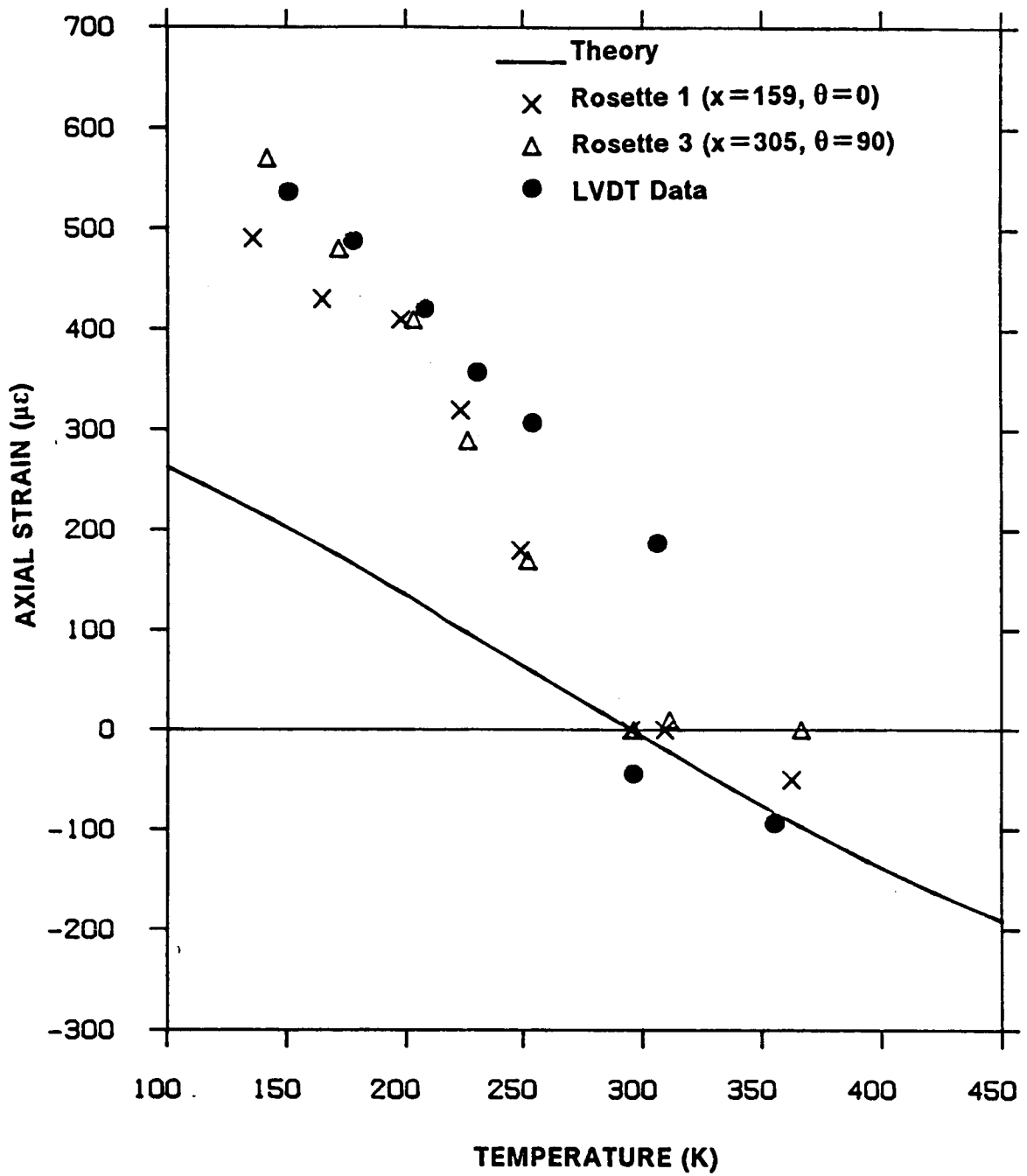


Figure 75. Axial Strain vs. Temperature, Specimen 17:  $[-10 / 0_s / 15_s / 0_s / -10]$ . Experiment and Theory, Temperature-dependent material properties.

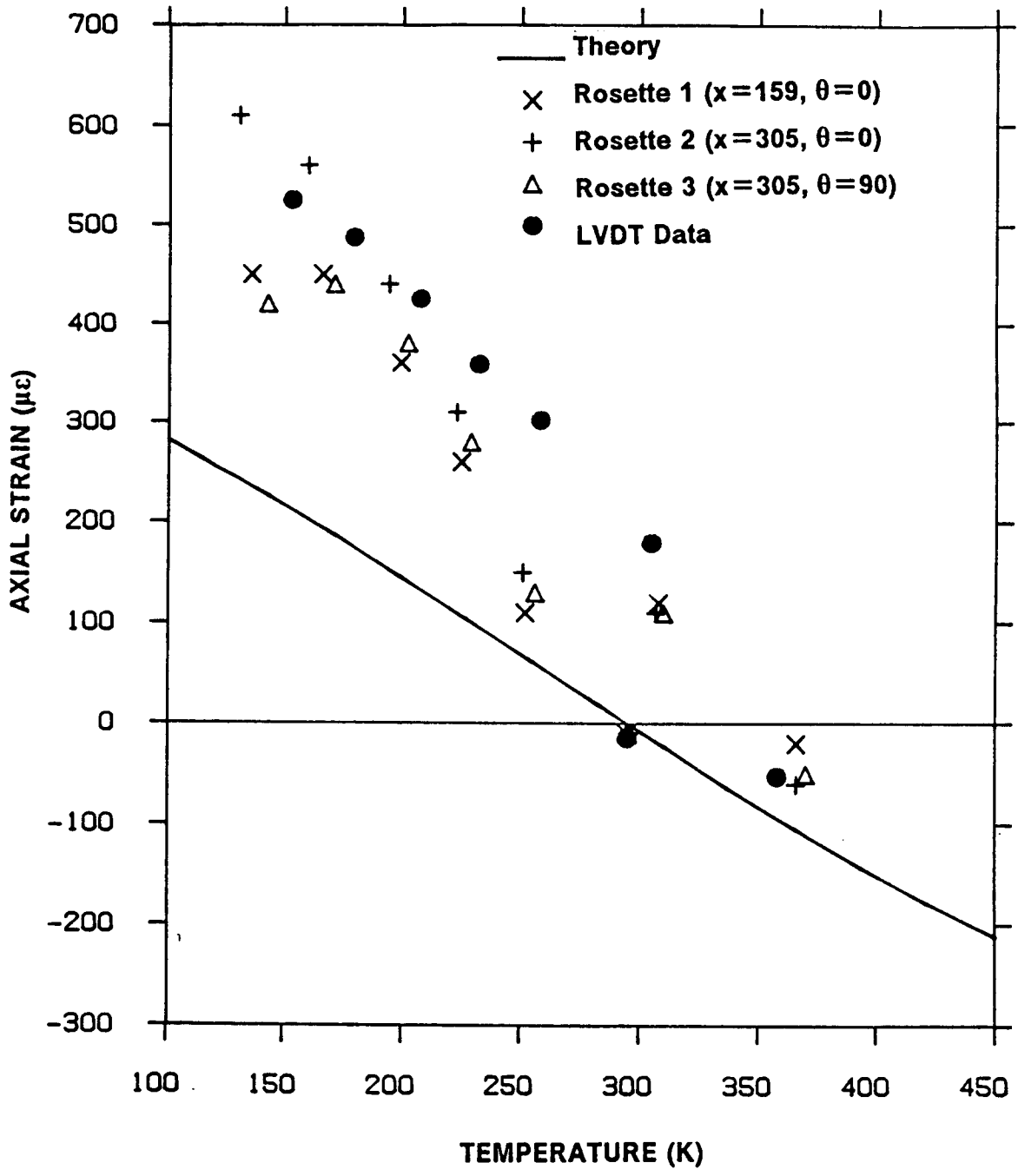


Figure 76. Axial Strain vs. Temperature, Specimen 18: [-10 / 0<sub>s</sub> / 20<sub>s</sub> / 0<sub>s</sub> / -10]. Experiment and Theory, Temperature-dependent material properties.

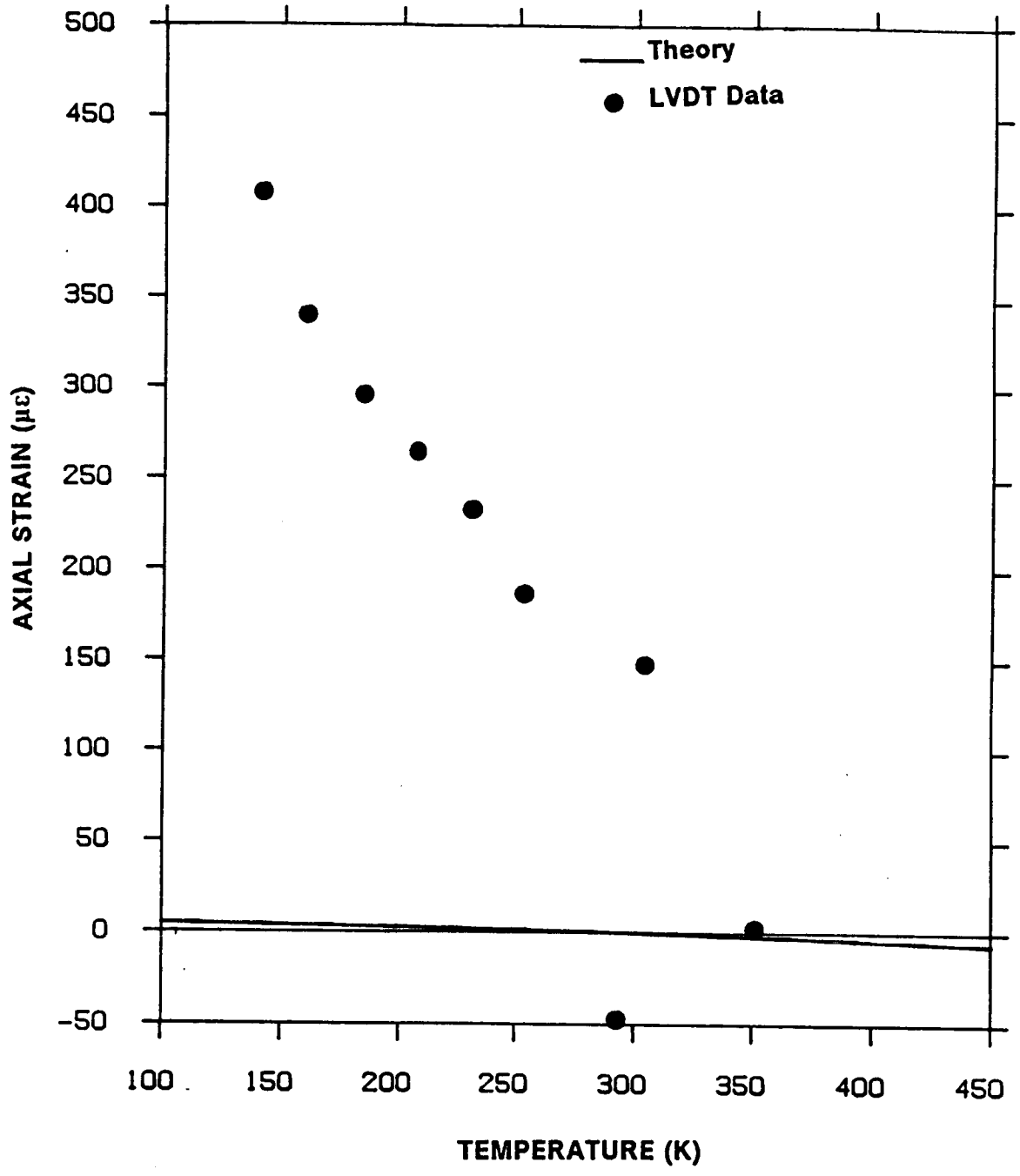


Figure 77. Axial Strain vs. Temperature, Specimen 21: [-10<sub>2</sub> / 0<sub>2</sub>]. Experiment and Theory, Temperature-dependent material properties.

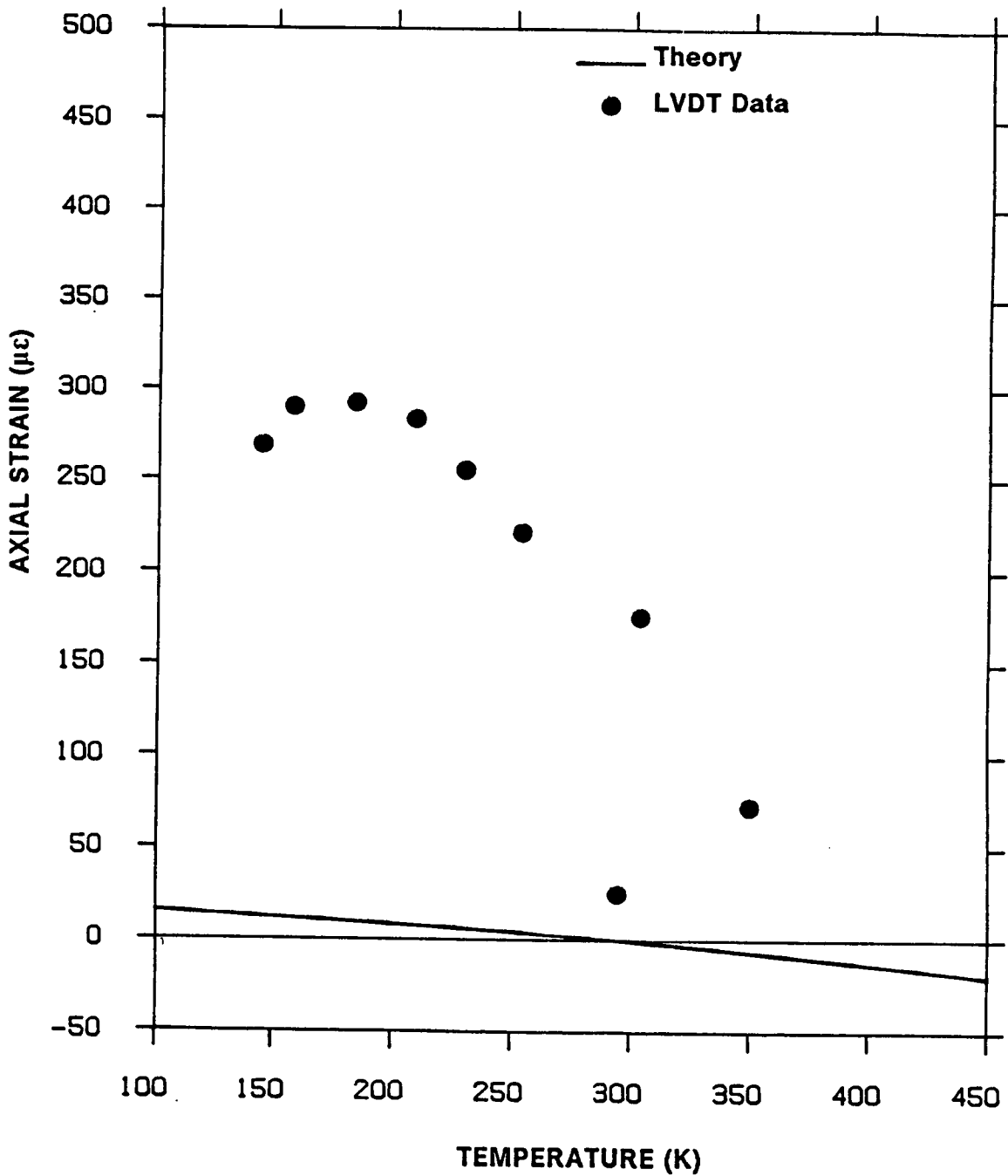


Figure 78. Axial Strain vs. Temperature, Specimen 22:  $[-10_2 / 0_{10} / 10_2]$ . Experiment and Theory, Temperature-dependent material properties.

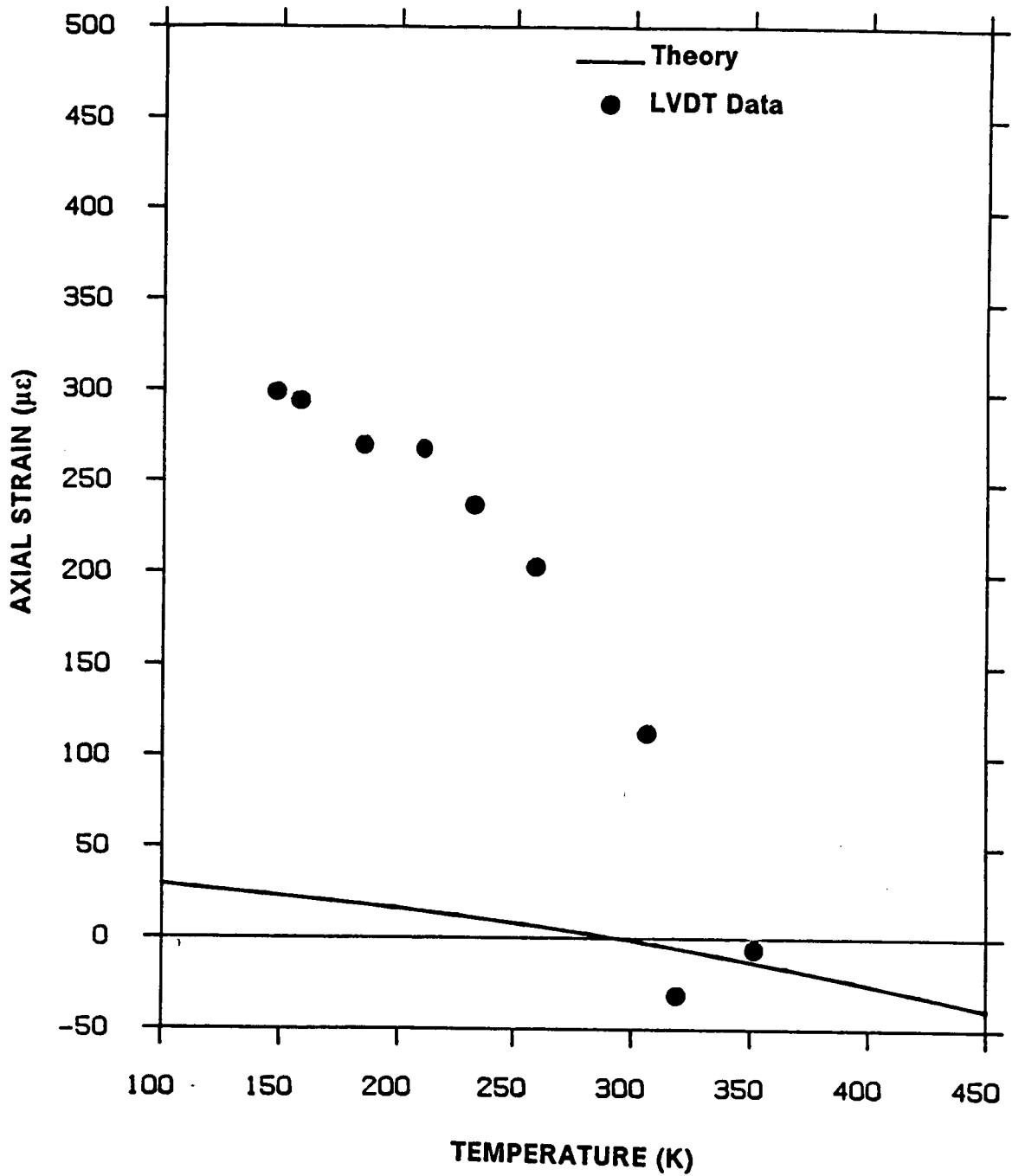


Figure 79. Axial Strain vs. Temperature, Specimen 24:  $[-10_2 / 0_{10} / 20_2]$ . Experiment and Theory, Temperature-dependent material properties.

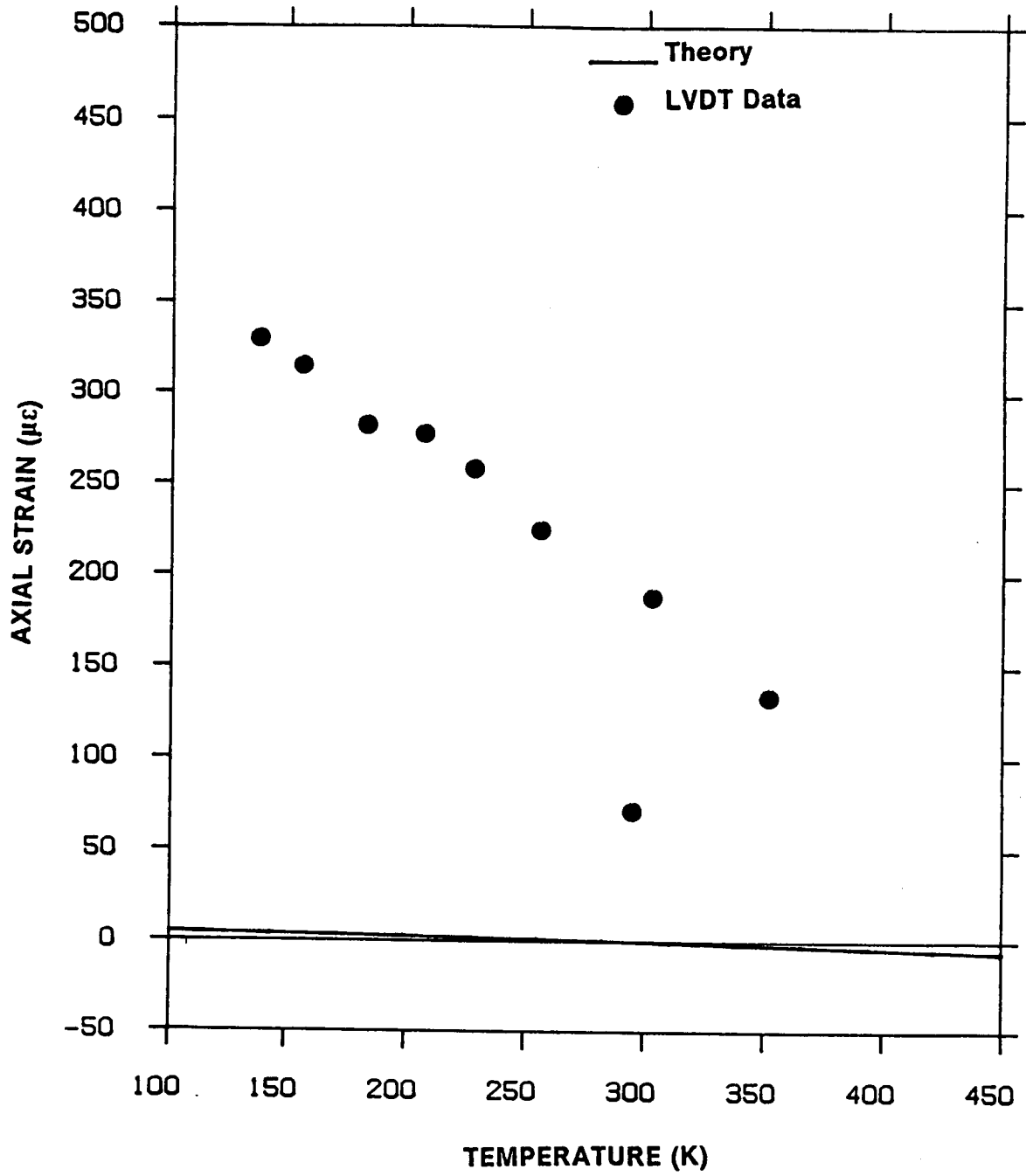


Figure 80. Axial Strain vs. Temperature, Specimen 25: [-10 / 0<sub>12</sub> / -10 ]. Experiment and Theory, Temperature-dependent material properties.

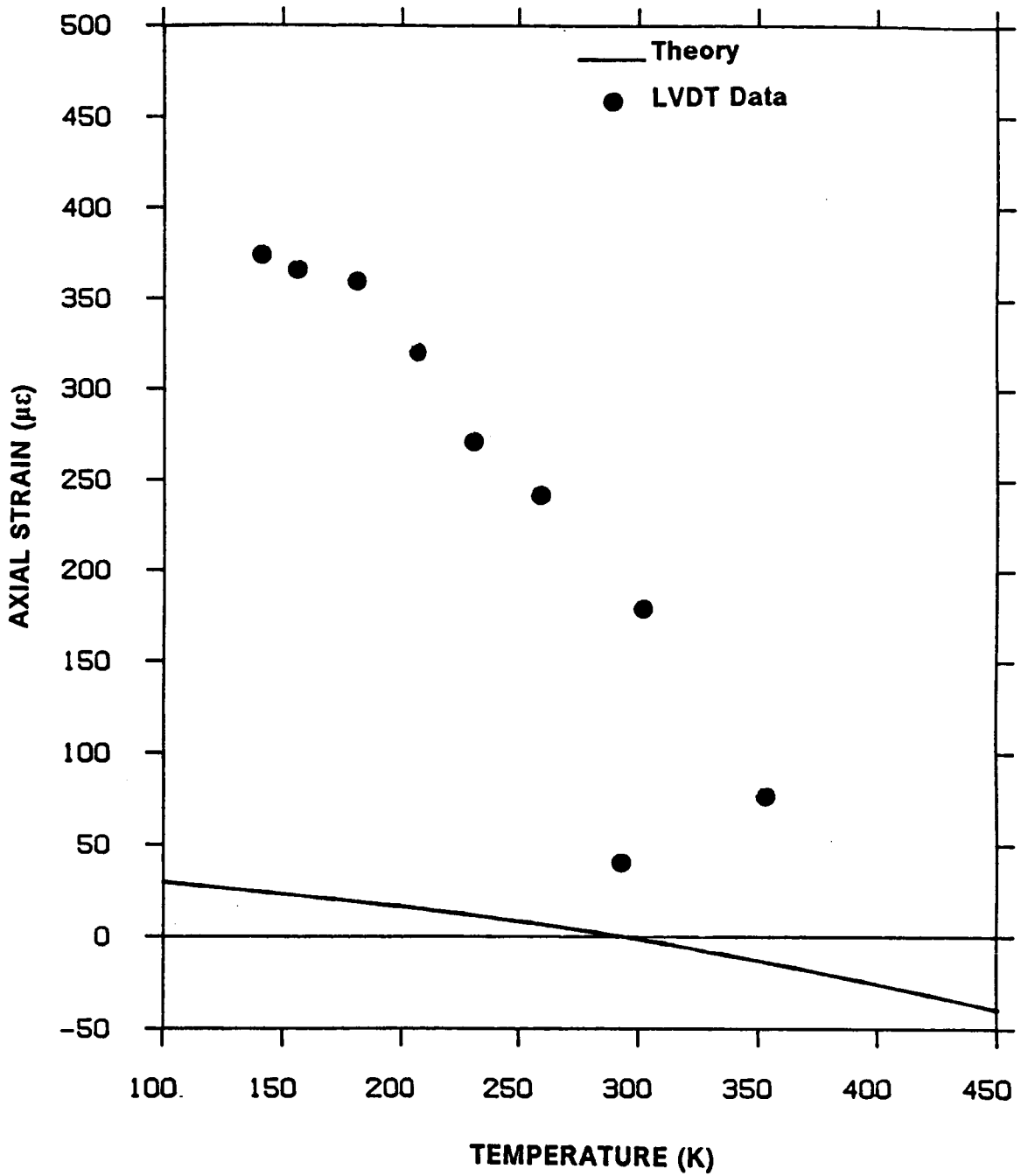


Figure 81. Axial Strain vs. Temperature, Specimen 28: [-10 / 0<sub>3</sub> / 20<sub>2</sub> / 0<sub>3</sub> / -10 ]. Experiment and Theory, Temperature-dependent material properties.

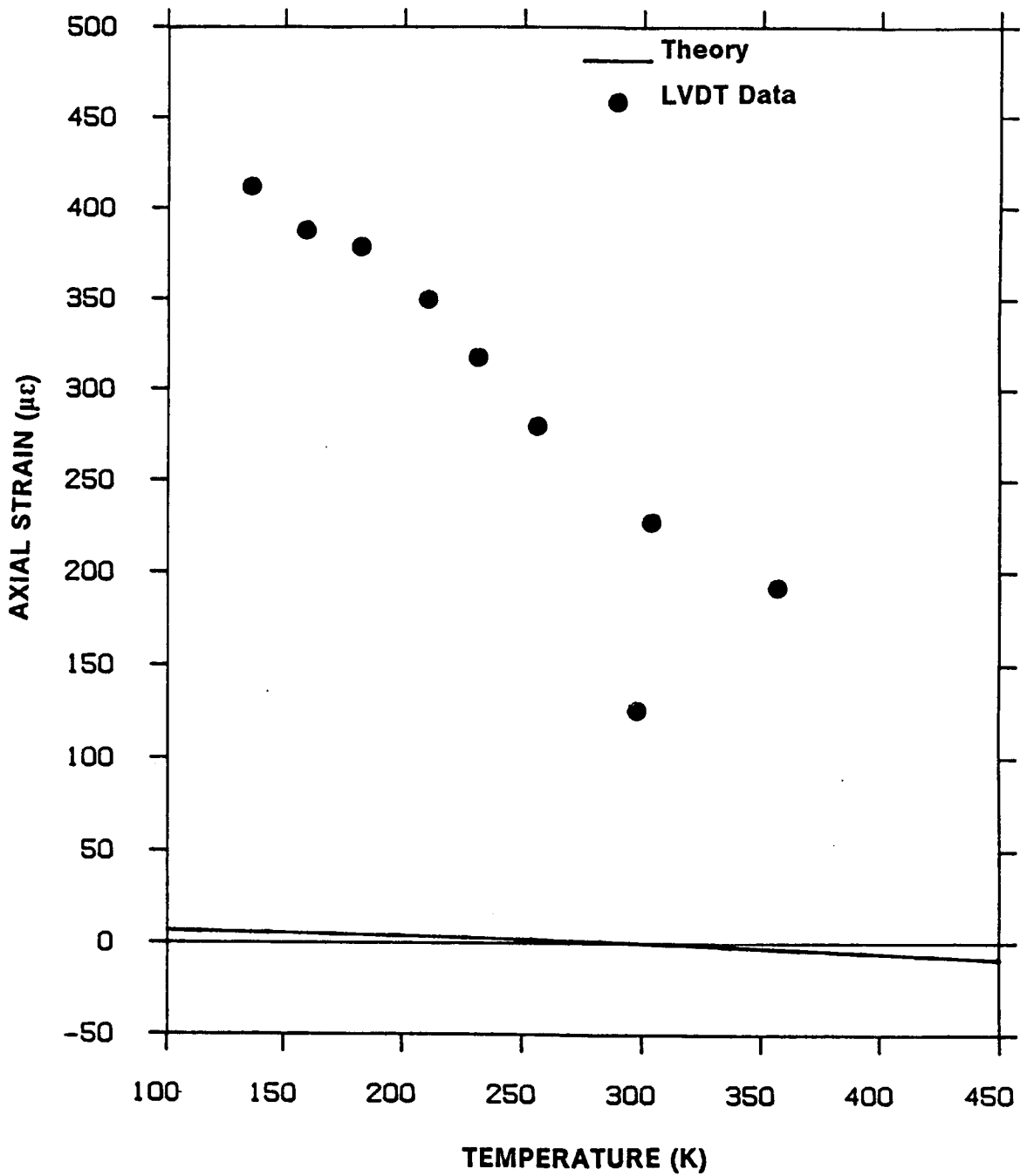


Figure 82. Axial Strain vs. Temperature, Specimen 31:  $[-10_2 / 0_{1,2}]$ . Experiment and Theory, Temperature-dependent material properties.

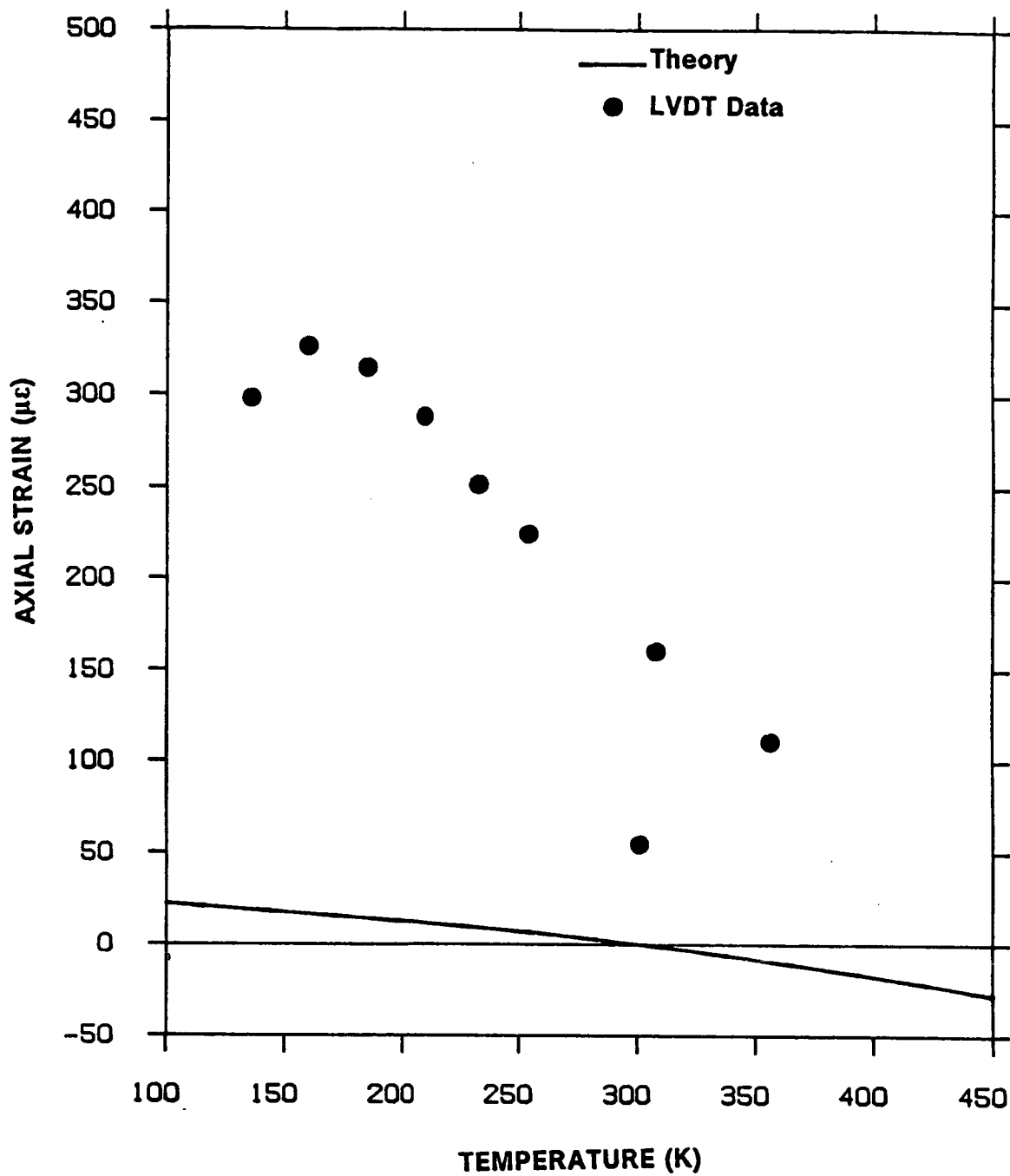


Figure 83. Axial Strain vs. Temperature, Specimen 32:  $[-10_2 / 0_{10} / 10_2]$ . Experiment and Theory, Temperature-dependent material properties.

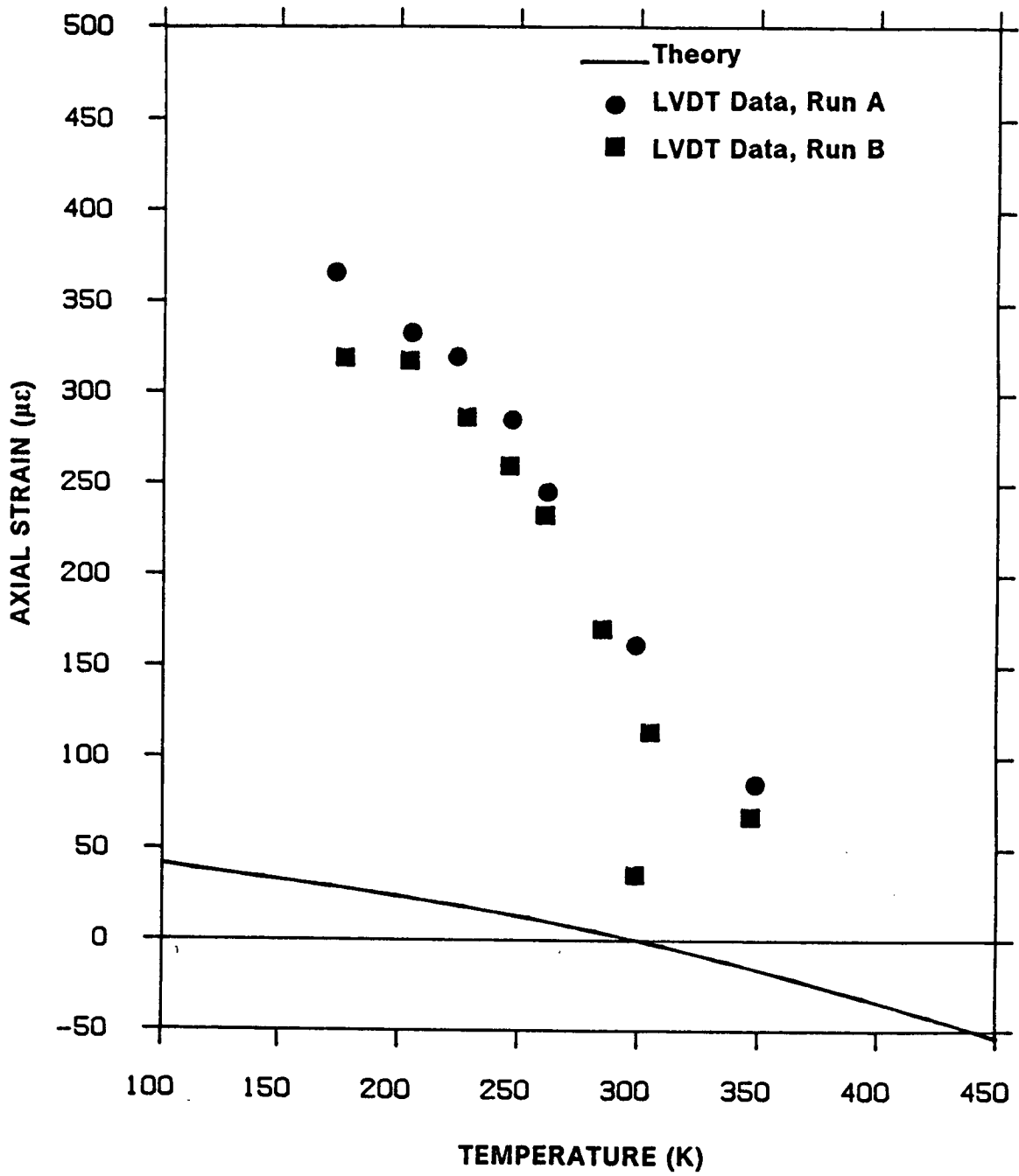


Figure 84. Axial Strain vs. Temperature, Specimen 34:  $[-10_2 / 0_{10} / 20_2]$ . Experiment and Theory, Temperature-dependent material properties.

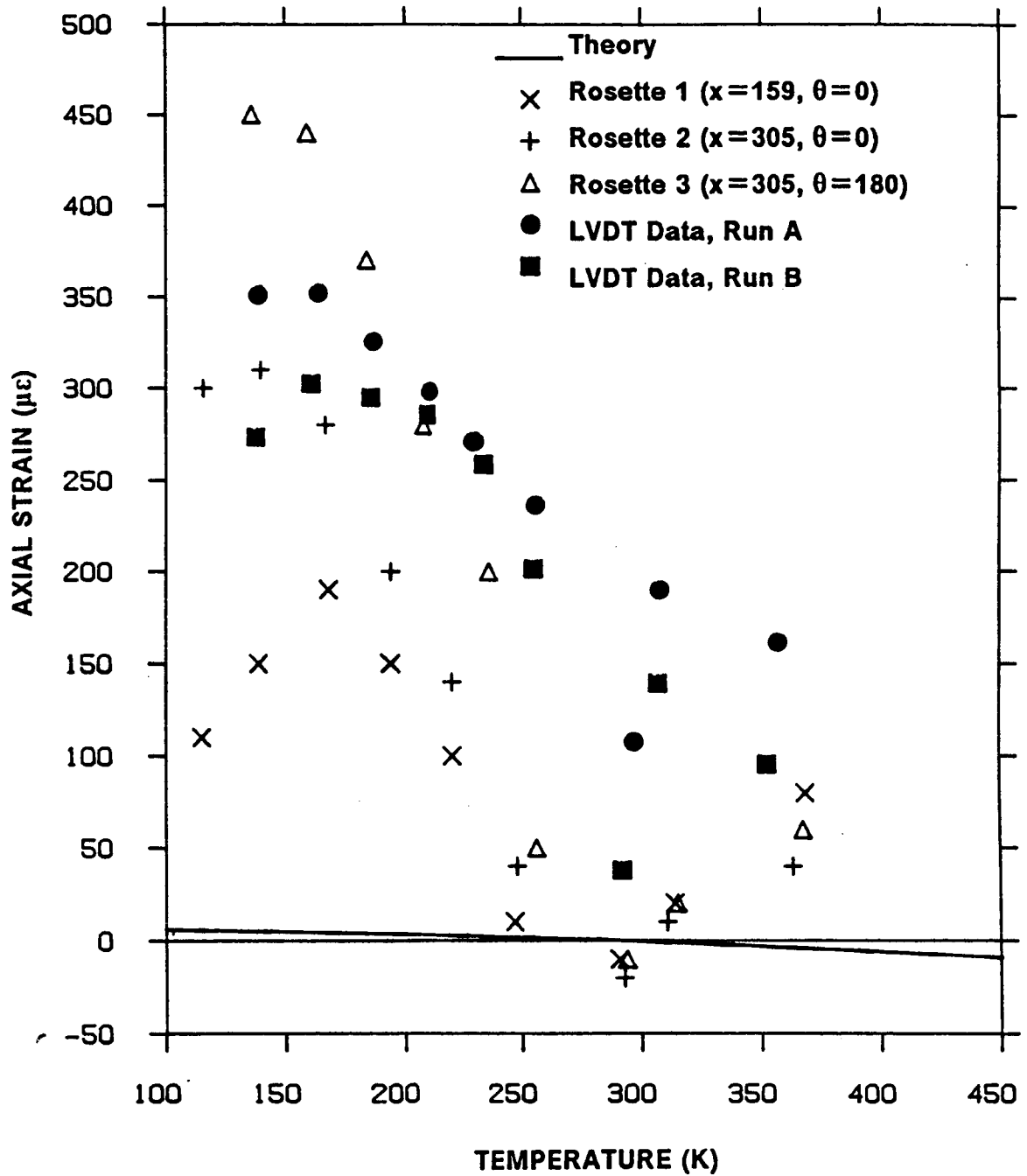


Figure 85. Axial Strain vs. Temperature, Specimen 35:  $[-10 / 0_{12} / -10]$ . Experiment and Theory. Temperature-dependent material properties.

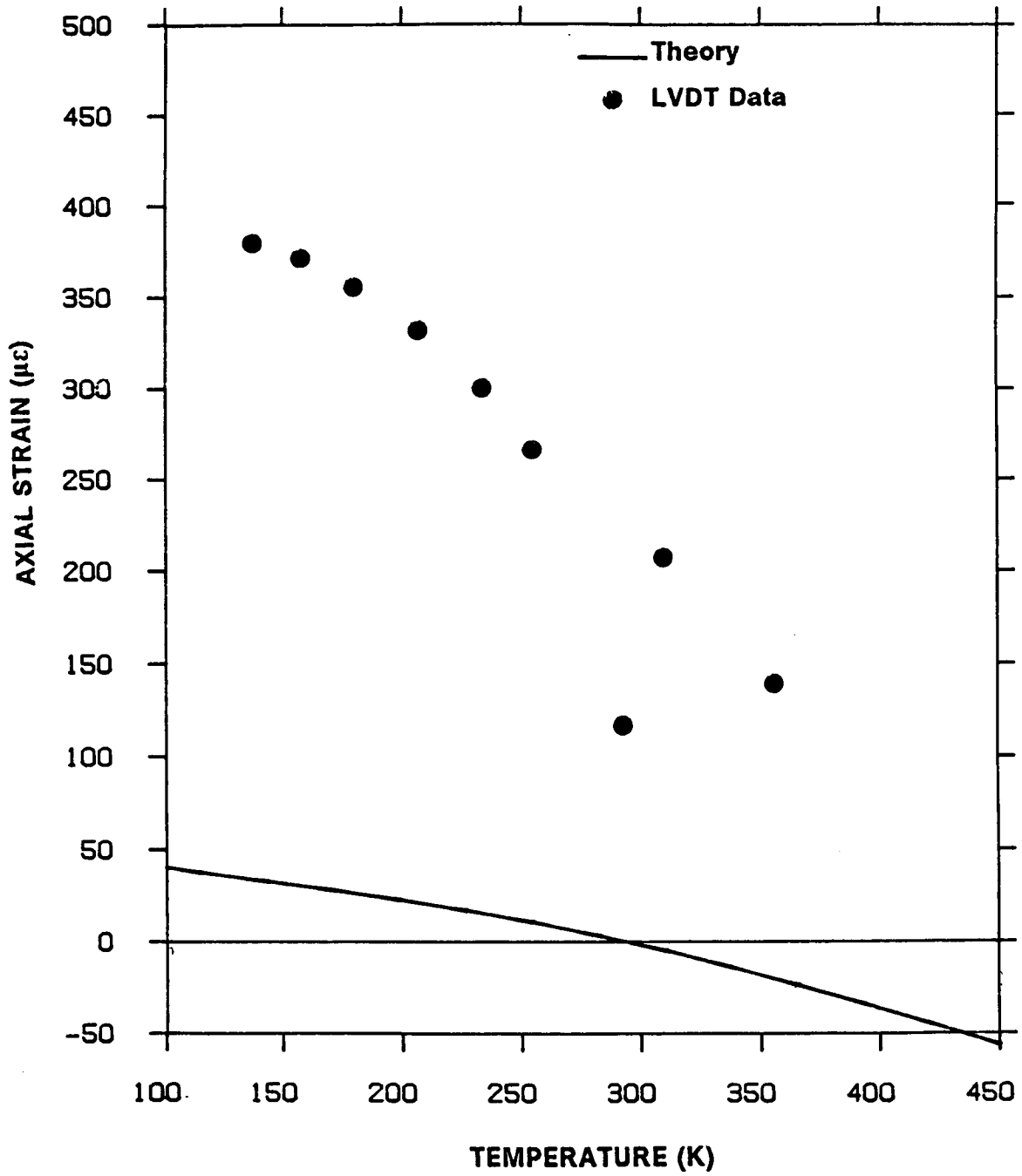


Figure 86. Axial Strain vs. Temperature, Specimen 38: [-10 / 0<sub>s</sub> / 20<sub>2</sub> / 0<sub>s</sub> / -10]. Experiment and Theory, Temperature-dependent material properties.

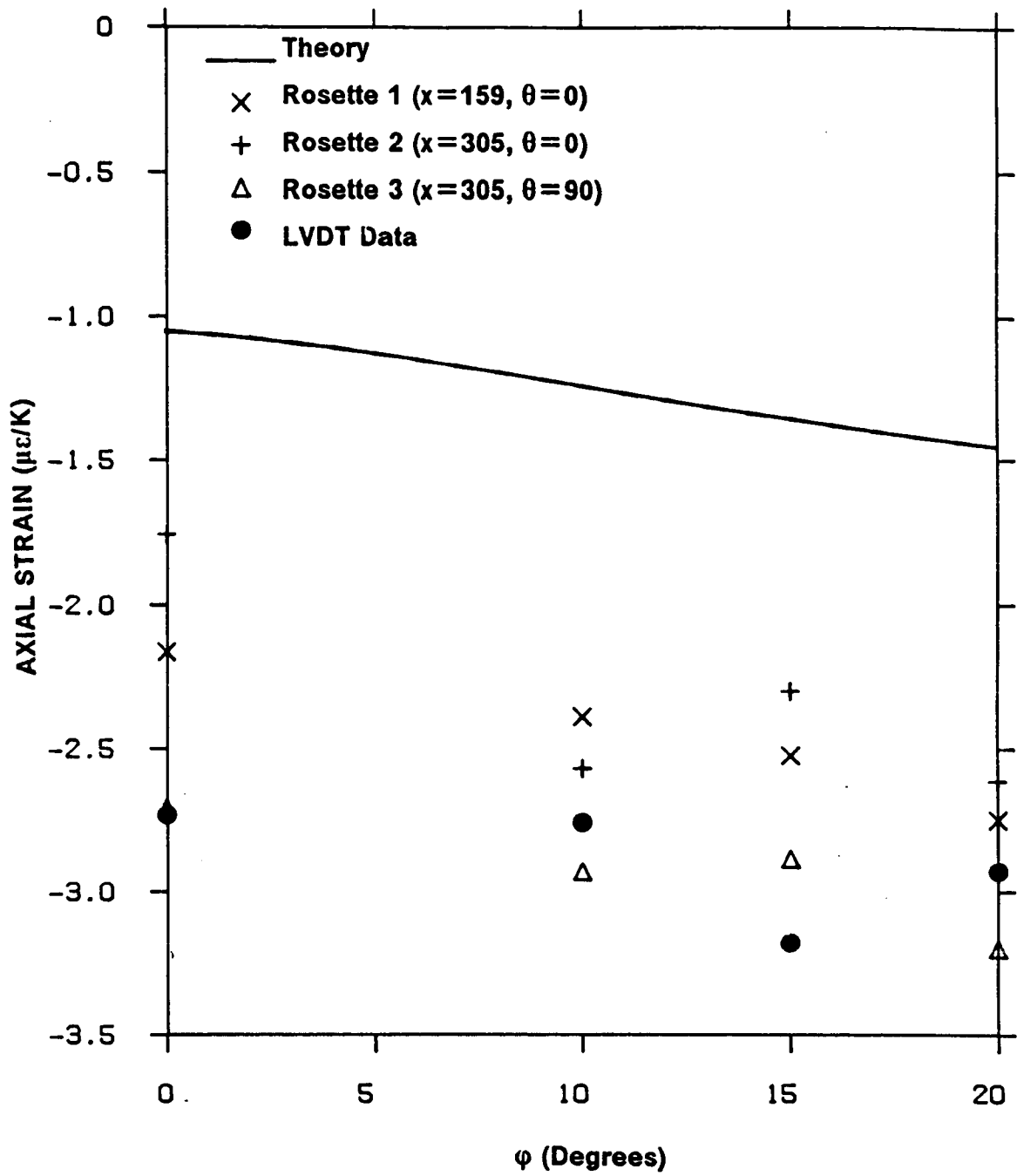


Figure 87. Axial Strain vs. Ply Orientation Angle (Specimens 11 - 14): Family 1 :  $[-10_2 / 0_{10} / \phi_2]$ . Experiment and Theory. Temperature-independent material properties. material system : P75S/ERLX1962A.

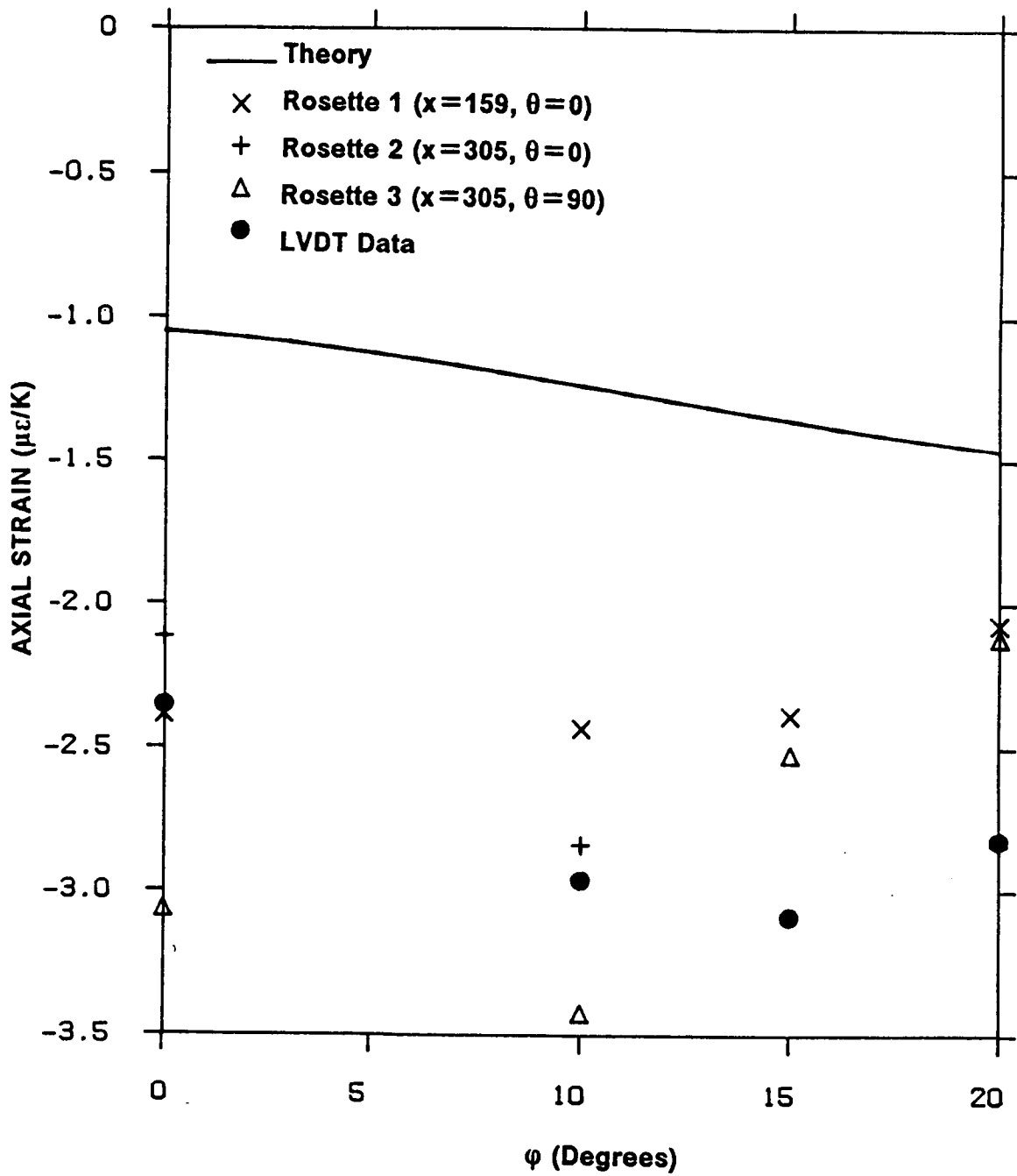


Figure 88. Axial Strain vs. Ply Orientation Angle (Specimens 15 - 18): Family 2 : [-10 / 0<sub>s</sub> /  $\phi_2$  / 0<sub>s</sub> / -10 ]. Experiment and Theory, Temperature-independent material properties, material system : P75S/ERLX1962A.

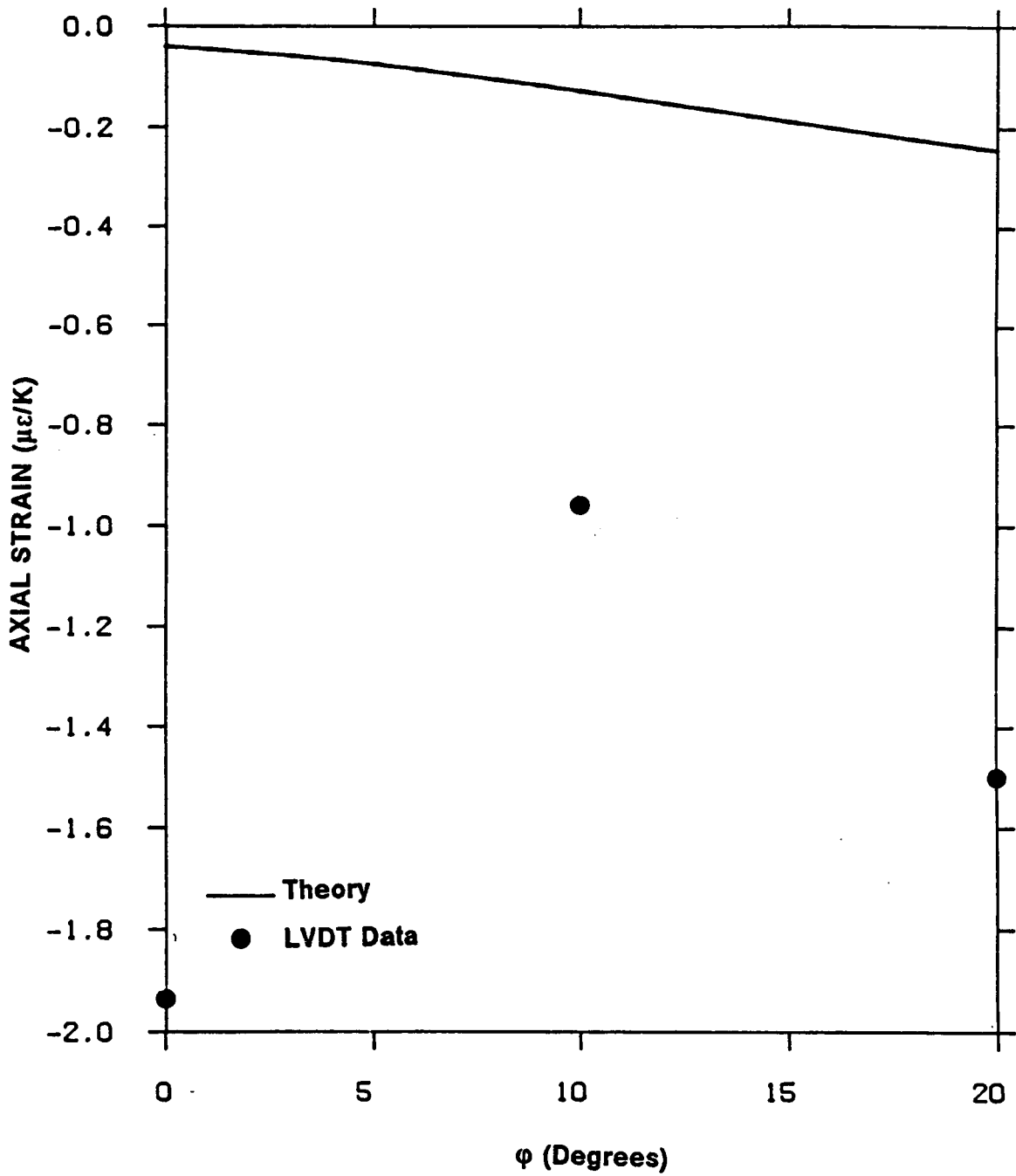


Figure 89. Axial Strain vs. Ply Orientation Angle (Specimens 21, 22, and 24): Family 1 :  $[-10_2 / 0_{10} / \phi_2]$ . Experiment and Theory, Temperature-independent material properties. material system : T300/ERLX1962A.

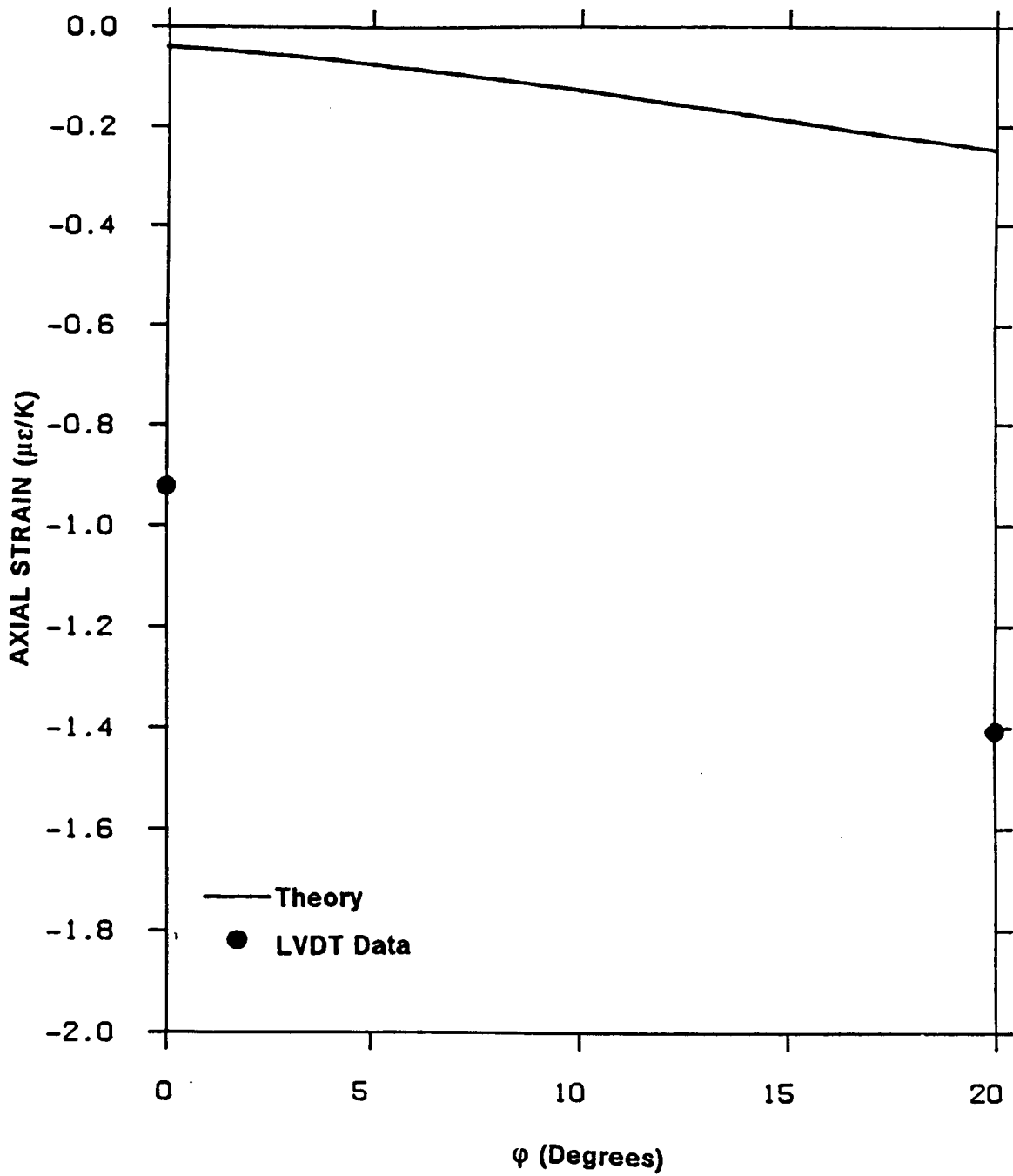


Figure 90. Axial Strain vs. Ply Orientation Angle (Specimens 25 and 28): Family 2 : [-10 / 0<sub>s</sub> / φ<sub>2</sub> / 0<sub>s</sub> / -10 ]. Experiment and Theory, Temperature-independent material properties, material system : T300/ERLX1962A.

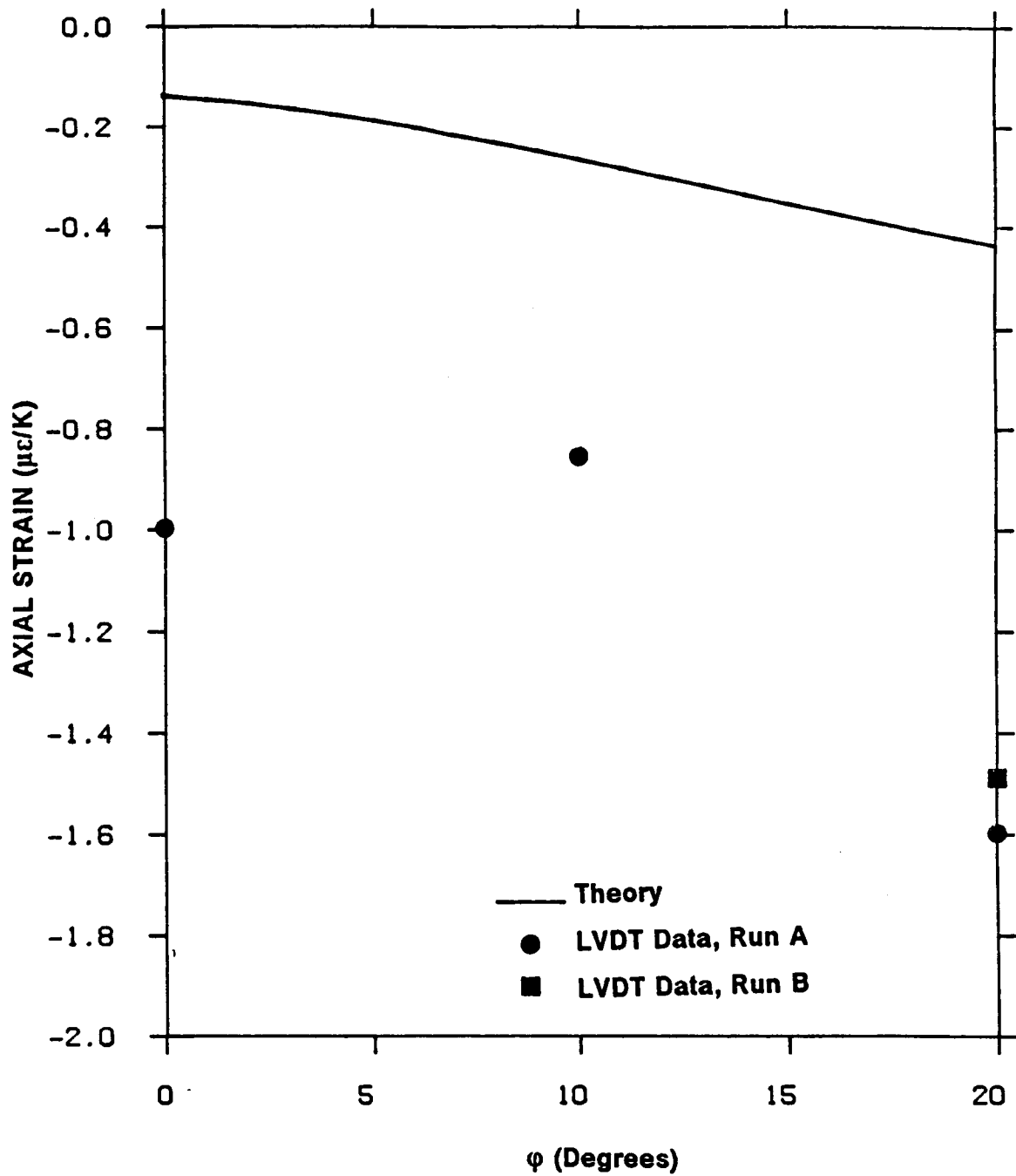


Figure 91. Axial Strain vs. Ply Orientation Angle (Specimens 31, 32, and 34): Family 1 :  $[-10_2 / 0_{10} / \varphi_2]$ . Experiment and Theory, Temperature-independent material properties. material system : AS4/976.

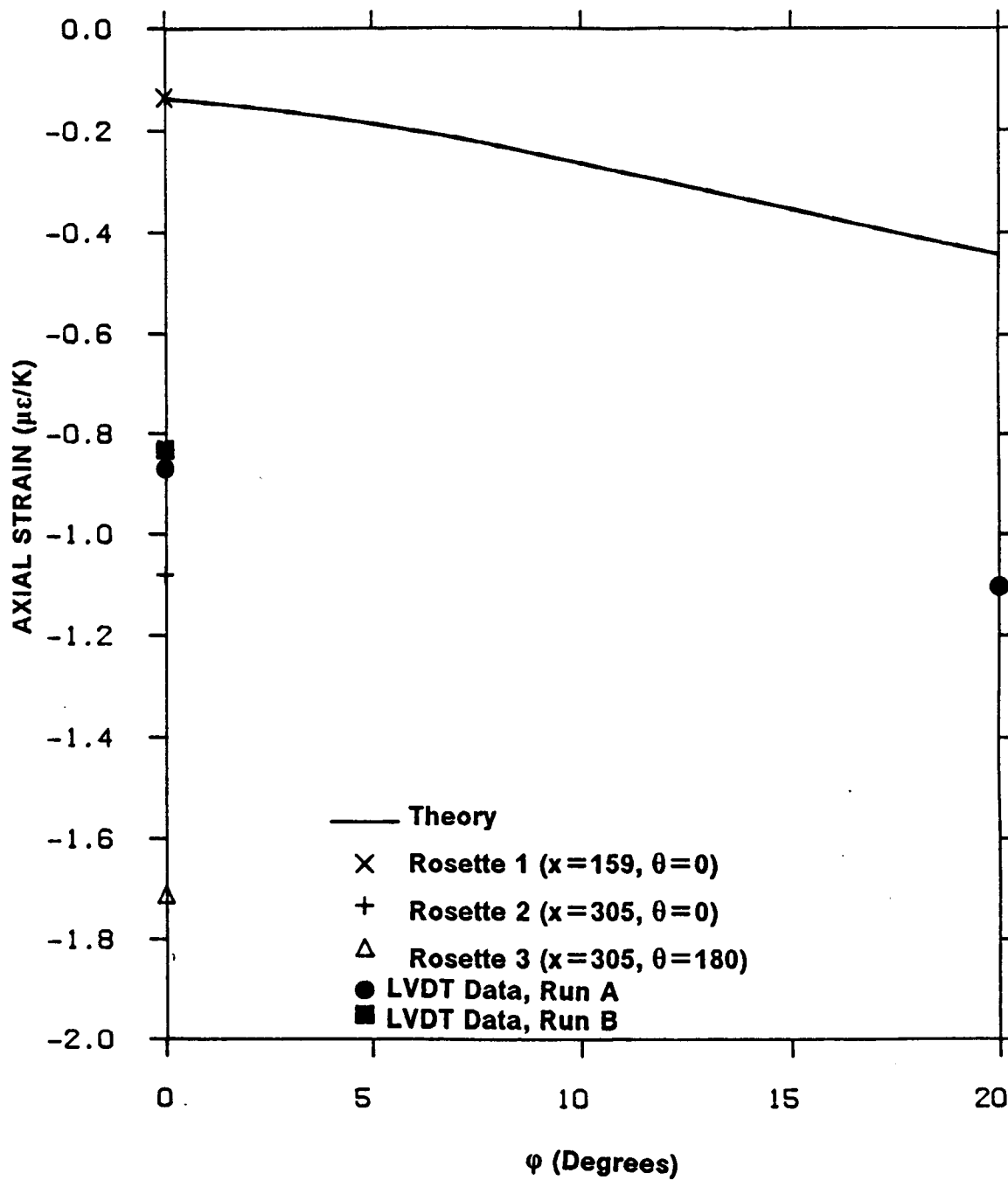


Figure 92. Axial Strain vs. Ply Orientation Angle (Specimens 35 and 38): Family 2 : [-10 / 0<sub>s</sub> / ϕ<sub>2</sub> / 0<sub>s</sub> / -10 ]. Experiment and Theory, Temperature-independent material properties. material system : AS4/976.

The reason for this lack of correlation with theory is not clear. Obviously, uncertainties in the material property data could be responsible for a portion of this. The dashed line in Figure 69 illustrates the effect of changing the axial thermal expansion coefficient from  $\alpha_1 = -1.03 \mu\epsilon/^\circ\text{C}$  to  $\alpha_1 = -2.0 \mu\epsilon/^\circ\text{C}$ . While this does much to improve the correlation between experiment and theory, a factor of two error in the value of  $\alpha_1$  is thought to be highly unlikely. One fact that should be kept in mind when considering this problem is that the theory assumes no stress or strain variation with  $x$ . This, of course, is not the case with the experimental data that are being modelled. A piecewise-linear axial temperature variation is used in order to arrive at an average temperature along the entire length of the tube. This simplification neglects axially-varying effects of material temperature dependency, and fails to account for the fact that temperature also varies circumferentially and radially. Another aspect of the temperature variation that is not accounted for by the theory involves the anisotropic nature of the thermal conductivity of graphite-epoxy. The material exhibits a high thermal conductivity in the fiber-direction and a much lower value transverse to the fibers. For the angle-ply laminates used in this study, a variation in axial thermal conductivity through the tube-wall could result in a steady-state radial temperature gradient. Effects of this temperature gradient could include a magnified Poisson effect from the off-axis layers, or the domination of tube response by the axial fibers; either of these effects could contribute to the larger-than-expected axial response. A final possible cause of poor agreement between experiment and theory might be spatial nonuniformities in the material properties of the tubes. This effect is often found in cylindrical composite structures. It is hoped that further experimental investigation in this area will shed more light on the nature of this discrepancy.

Disregarding the lack of theoretical and experimental agreement, several interesting aspects of axial response are nonetheless apparent. Consistent with the temperature-dependent character of  $\epsilon_1^T$  for P75S/ERLX1962A, Figure 69 - Figure 76 show that the axial response is fairly linear with temperature. On the other hand, Figure 77 - Figure 86 exhibit axial responses that are somewhat lower in magnitude than that of the high modulus fiber tubes, and

the T300 and AS4 specimens show a significant temperature-dependent axial response. This temperature dependency also exhibits the same S-shaped trend that  $\epsilon_T^1$  for low modulus fibers has been observed to have<sup>18 24 25</sup>. It is also interesting to note that the measured axial responses for all tubes in each material system are quite similar. In fact the differences in measured axial response between tubes of different materials is not as great as the difference in their respective material properties.

The axial responses of all tubes seems to also be somewhat insensitive to off-axis ply orientation angle, as is predicted theoretically. This aspect is best seen in Figure 87 - Figure 92, which like the previous illustrations of twist vs.  $\phi$ , are linear approximations of each set of test data. These figures show the axial strain per unit temperature change ( $\Delta\epsilon^\circ/K$ ). Although these figures illustrate the linear approximations of tube response, this does not mask the effect of off-axis angle on axial response. As can be seen in Figure 87, for example, the off-axis angle has little influence on the axial response. The surprising result is that the contraction tendencies (i.e., negative coefficient of thermal expansion) **increase** slightly with increasing off-axis angle. Also, except for a significant vertical shift, the experimental data and the theoretical data parallel each other. That the strain gage data and the displacement transducer data give similar trends, despite the fact that they are independent measures, adds to the validity of the experimental data. It would appear that the theoretical predictions do not correlate well because some of the assumptions (specifically, that the temperature distribution is uniform) in the theory are not satisfied and because of shortcomings in the material properties used.

### **5.3 Hoop Strain Response**

Finally, Figure 93 - Figure 103 illustrate the hoop strain characteristics of the test specimens. Though it has not been emphasized previously, the hoop strain was measured as part of the strain gage measurements. If dimensional changes in the tube diameter are deemed important, these data are important. As can be seen in Figure 93 - Figure 101, the correlation between theory and experiment is very good. There is some deviation at low temperatures. The temperature-dependent theory predicted that the slope of the hoop strain vs. temperature relation would increase as the temperature decreased below about 200 K. On the other hand, the experimental data below 200 K showed that the slope of  $\epsilon_\theta(T)$  decreased. Except for specimens 16, 18 and 35, the data from the three rosettes are in close agreement. The data show that all tubes expanded in diameter when heated. By examining the figures, it is clear that there is little difference in the circumferential expansion characteristics of the various tubes. This finding is further supported by Figure 102 and Figure 103. These figures show the influence of off-axis angle on circumferential strain per unit temperature change ( $\Delta\epsilon_\theta/K$ ). It is seen that there is little predicted or measured dependence of off-axis angle on circumferential response, and that the linear theory overpredicts the response. The fact that the measured hoop strain diverged even from the temperature-dependent theory at low temperatures also influenced the lower than predicted strains in Figure 102 and Figure 103.

### **5.4 Summary of Experimental Results**

In summary, this experimental investigation succeeded in its primary goal of verifying the theoretical prediction that composite tubes, even those with balanced symmetric lamination sequences, will twist when subjected to a thermal load. In general, the agreement between

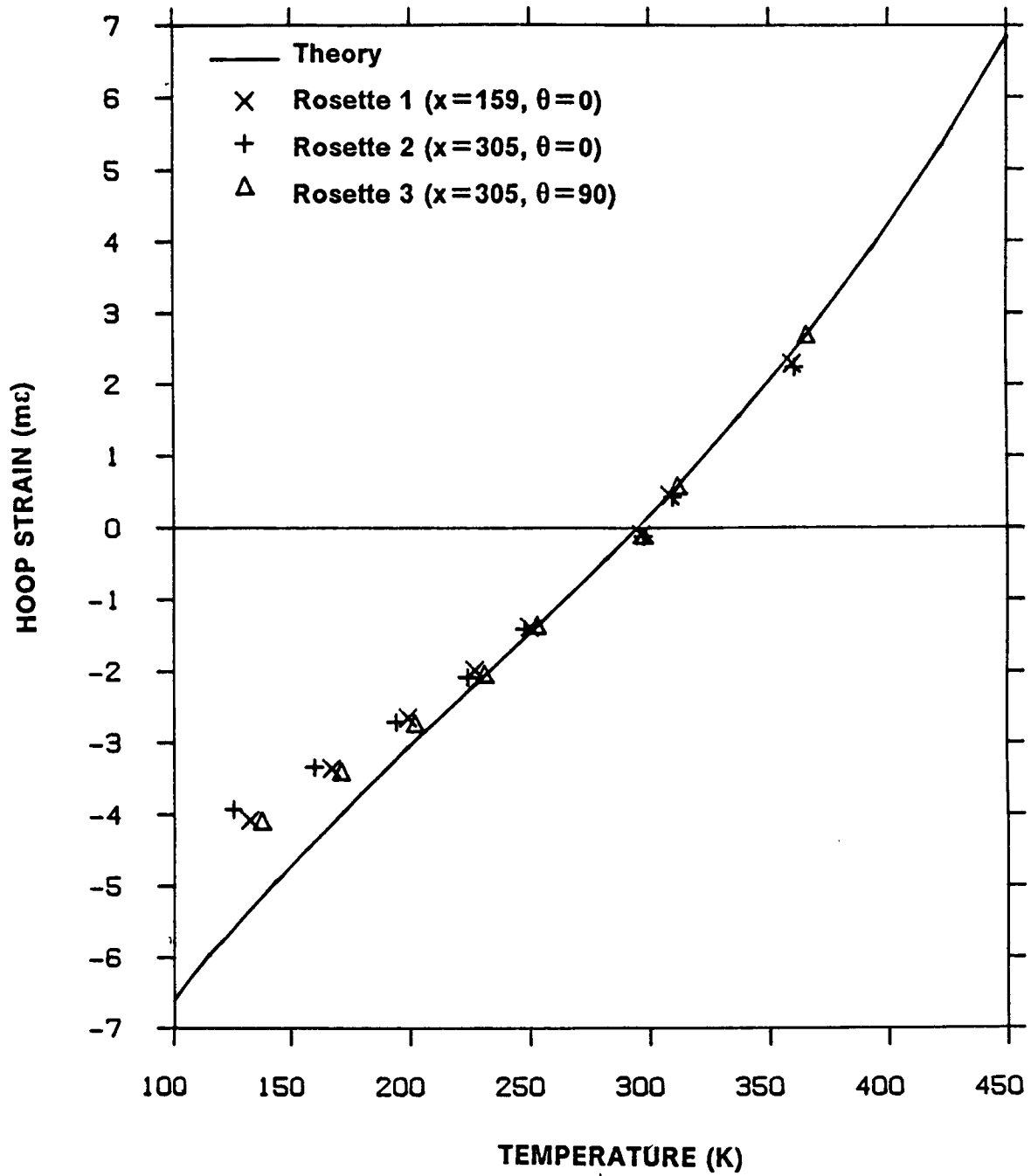


Figure 93. Hoop Strain vs. Temperature, Specimen 11:  $[-10_2 / 0_{12}]$ . Experiment and Theory, Temperature-dependent material properties.

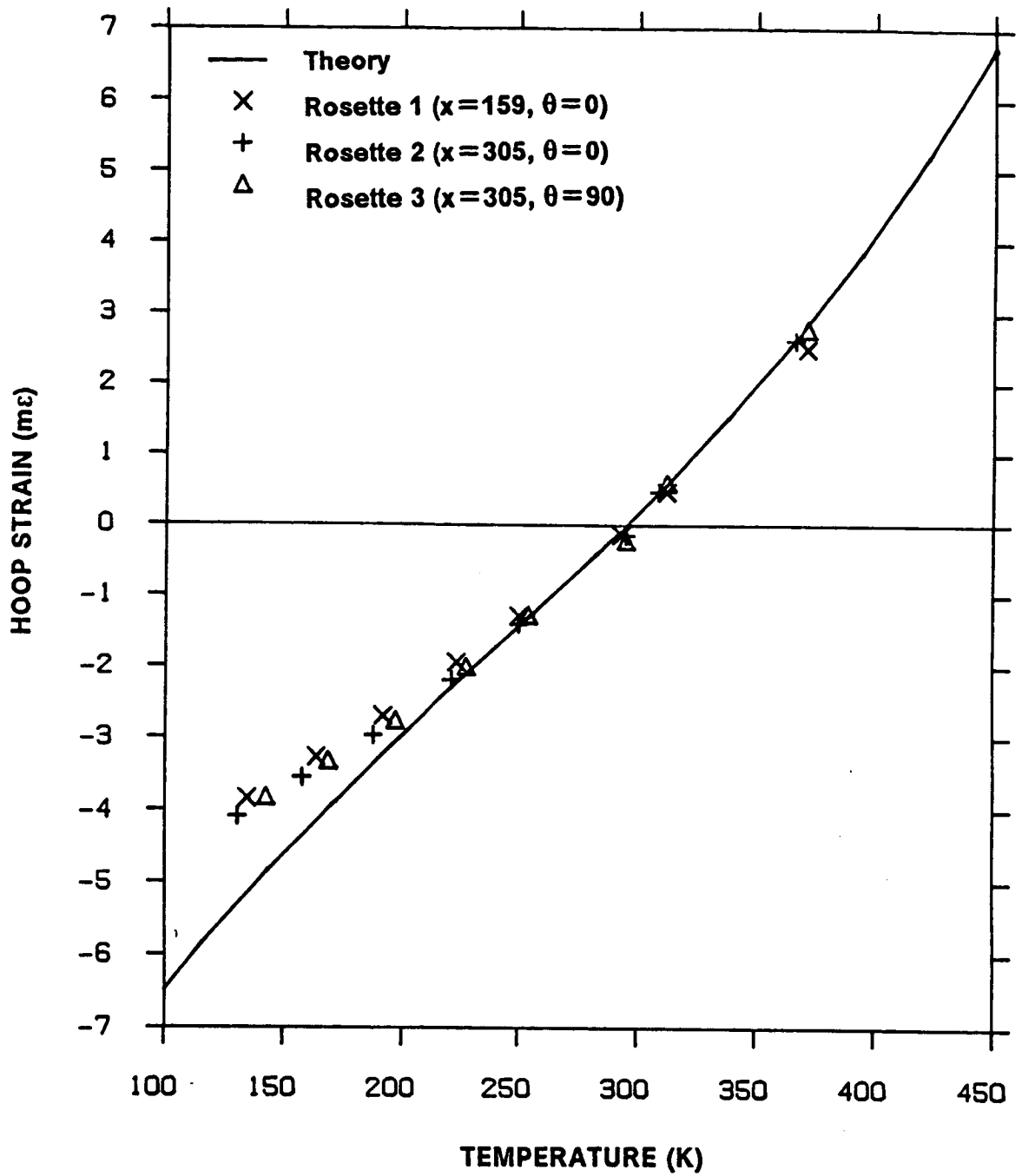


Figure 94. Hoop Strain vs. Temperature, Specimen 12:  $[-10_2 / 0_{10} / 10_2]$ . Experiment and Theory, Temperature-dependent material properties.

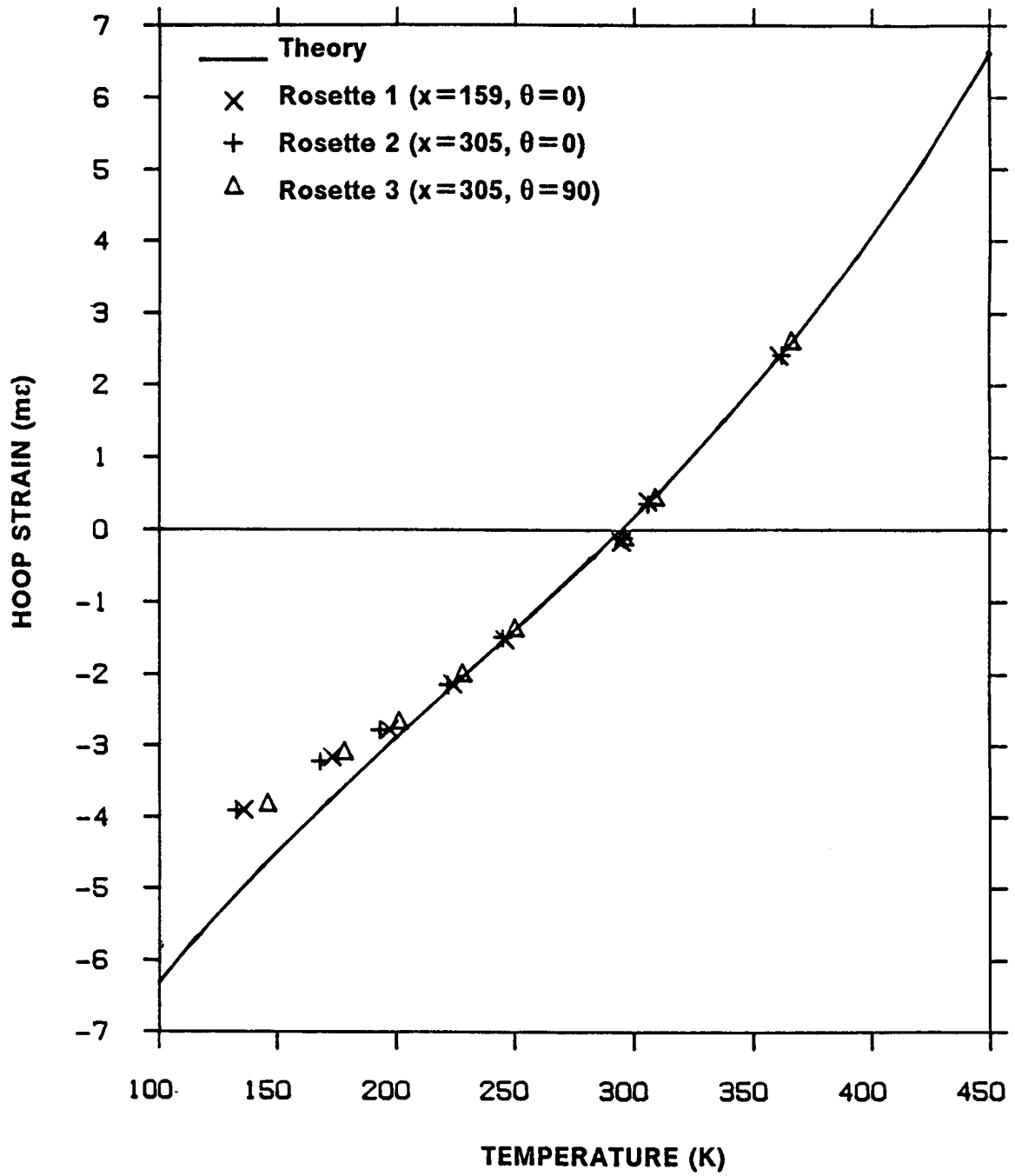


Figure 95. Hoop Strain vs. Temperature, Specimen 13:  $[-10_2 / 0_{10} / 15_2]$ . Experiment and Theory, Temperature-dependent material properties.

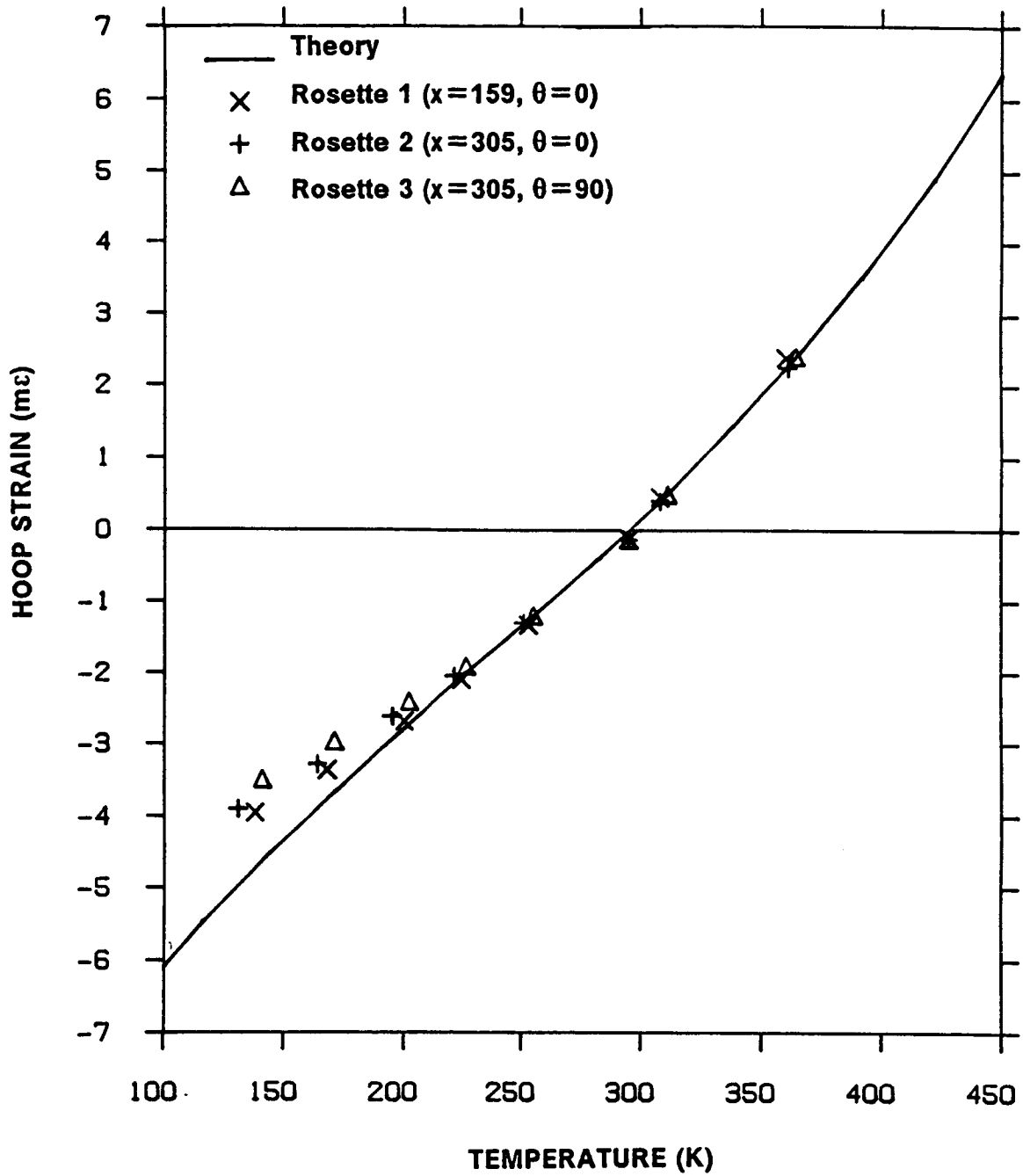


Figure 96. Hoop Strain vs. Temperature, Specimen 14:  $[-10_2 / 0_{10} / 20_2]$ . Experiment and Theory, Temperature-dependent material properties.

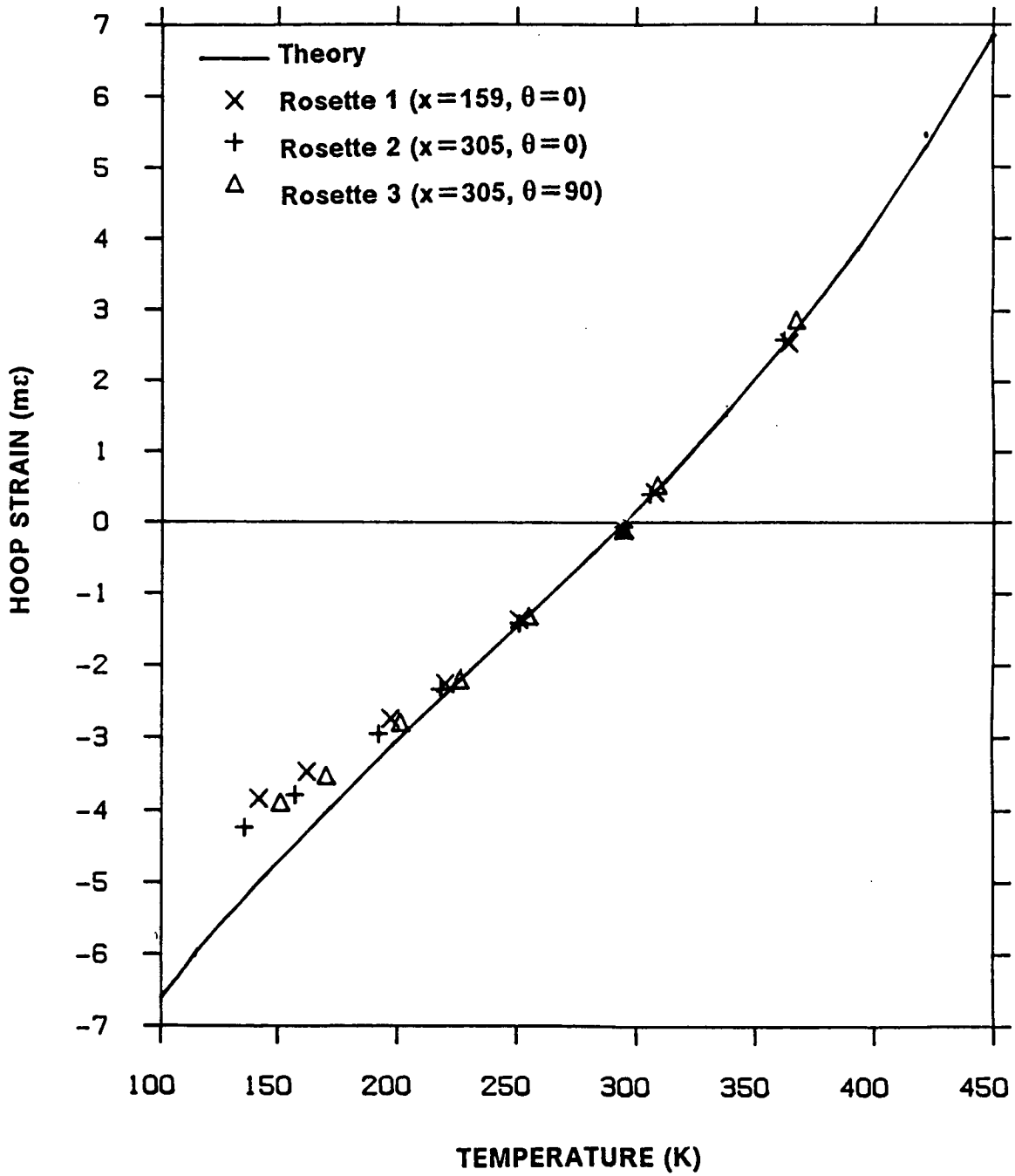


Figure 97. Hoop Strain vs. Temperature, Specimen 15:  $[-10 / 0_{12} / -10]$ . Experiment and Theory, Temperature-dependent material properties.

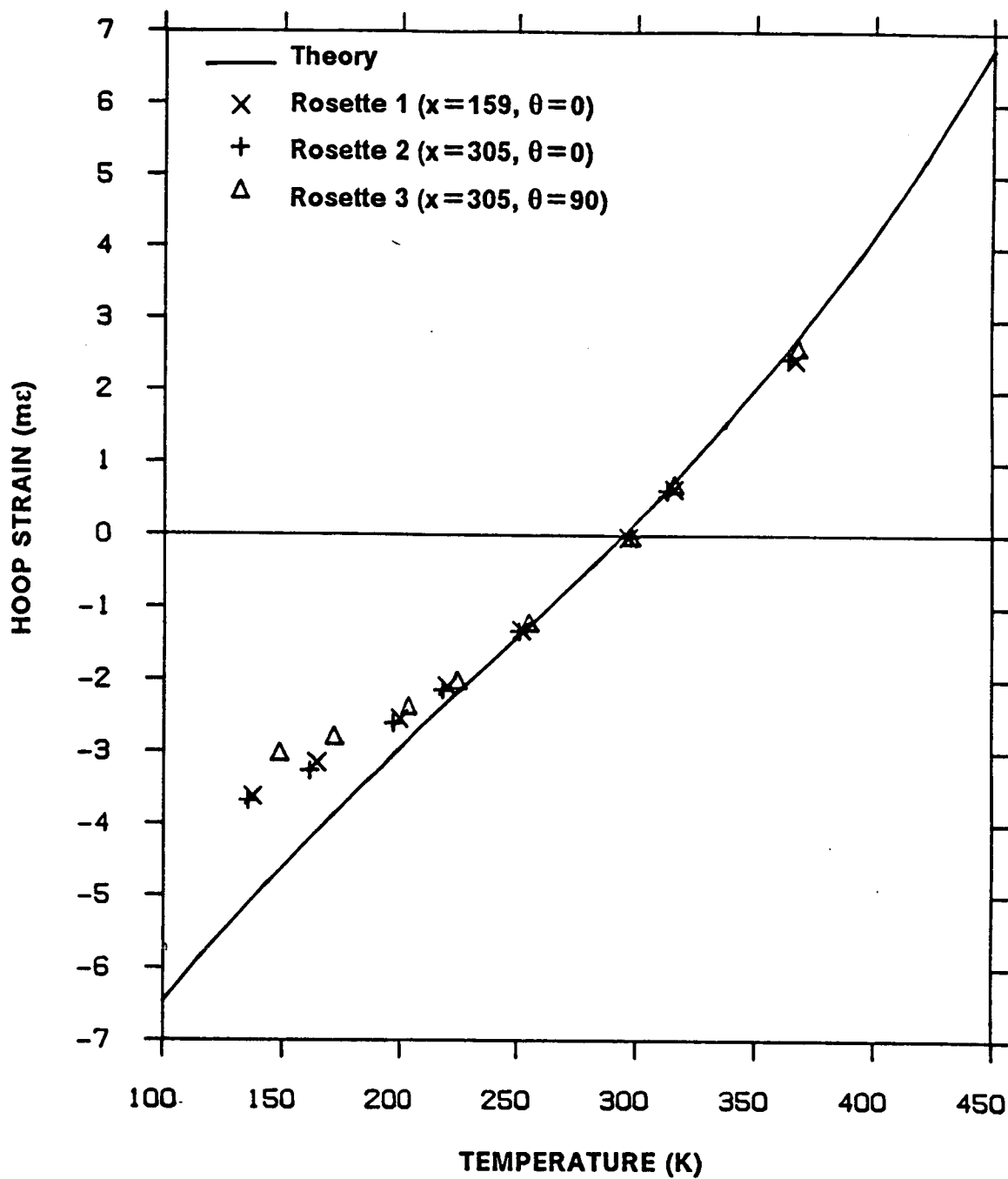


Figure 98. Hoop Strain vs. Temperature, Specimen 16:  $[-10 / 0_s / 10_s / 0_s / -10]$ . Experiment and Theory, Temperature-dependent material properties.

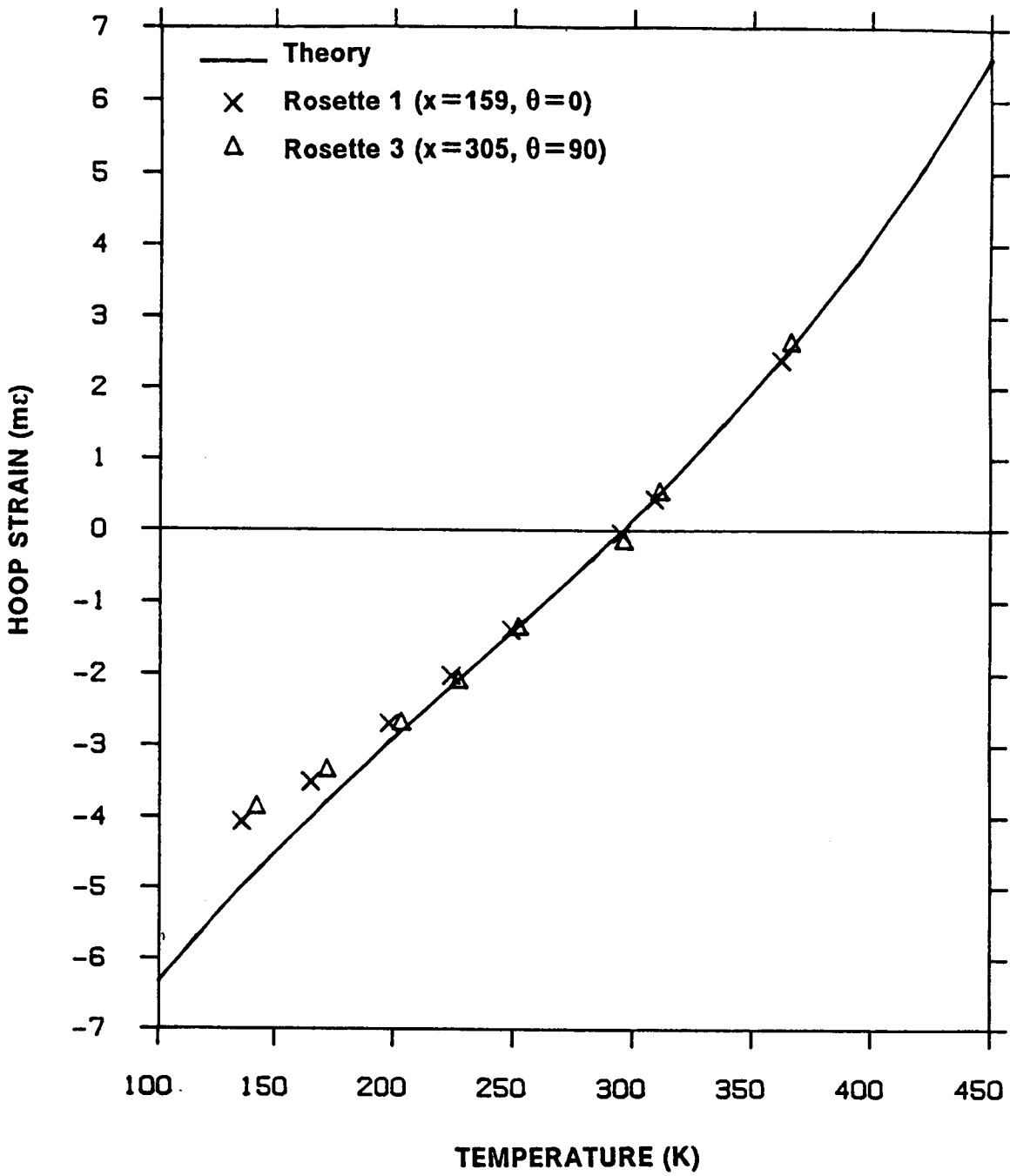


Figure 99. Hoop Strain vs. Temperature, Specimen 17:  $[-10 / 0_s / 15_2 / 0_s / -10]$ . Experiment and Theory, Temperature-dependent material properties.

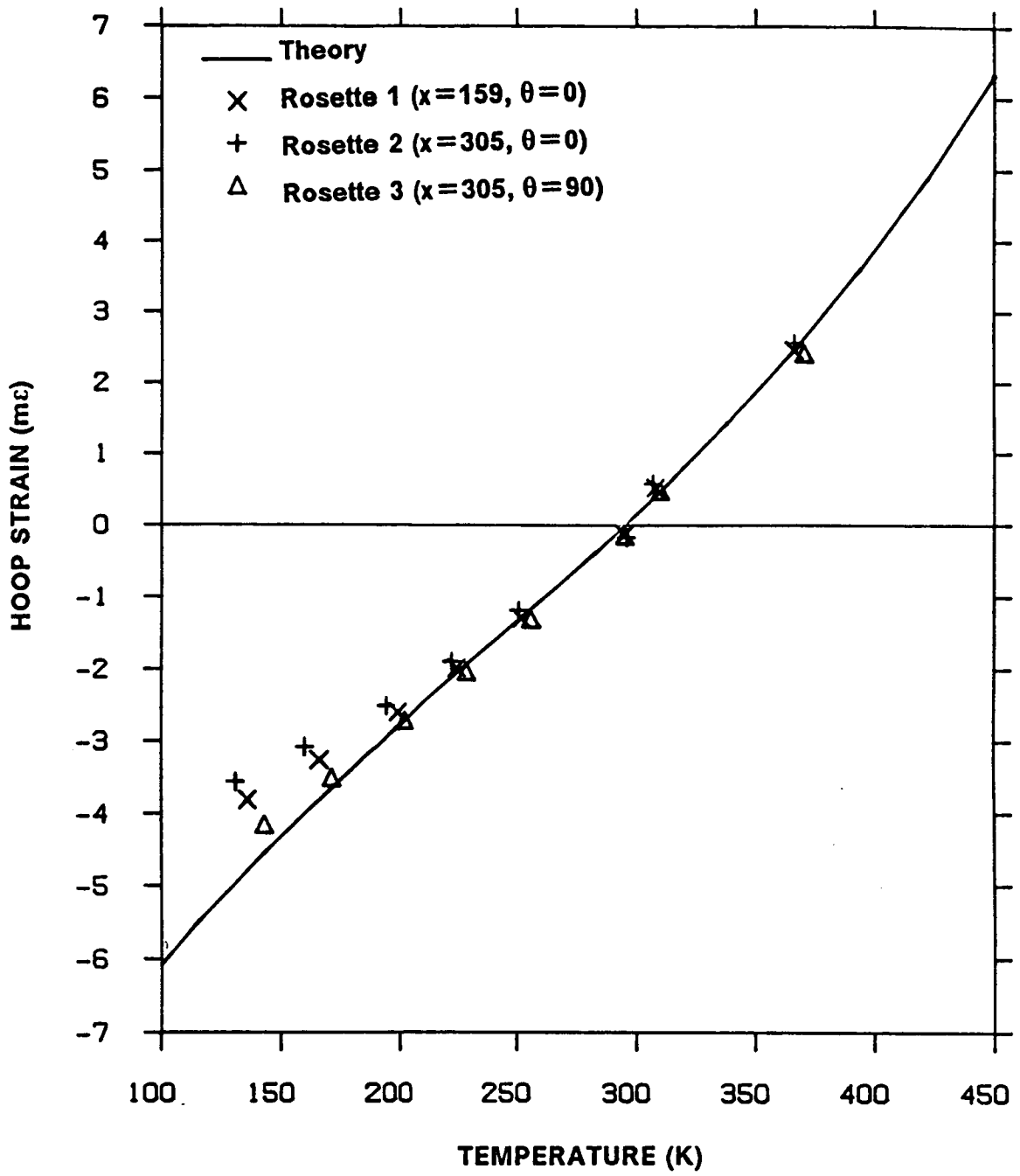


Figure 100. Hoop Strain vs. Temperature, Specimen 18:  $[-10 / 0_s / 20_2 / 0_s / -10]$ . Experiment and Theory, Temperature-dependent material properties.

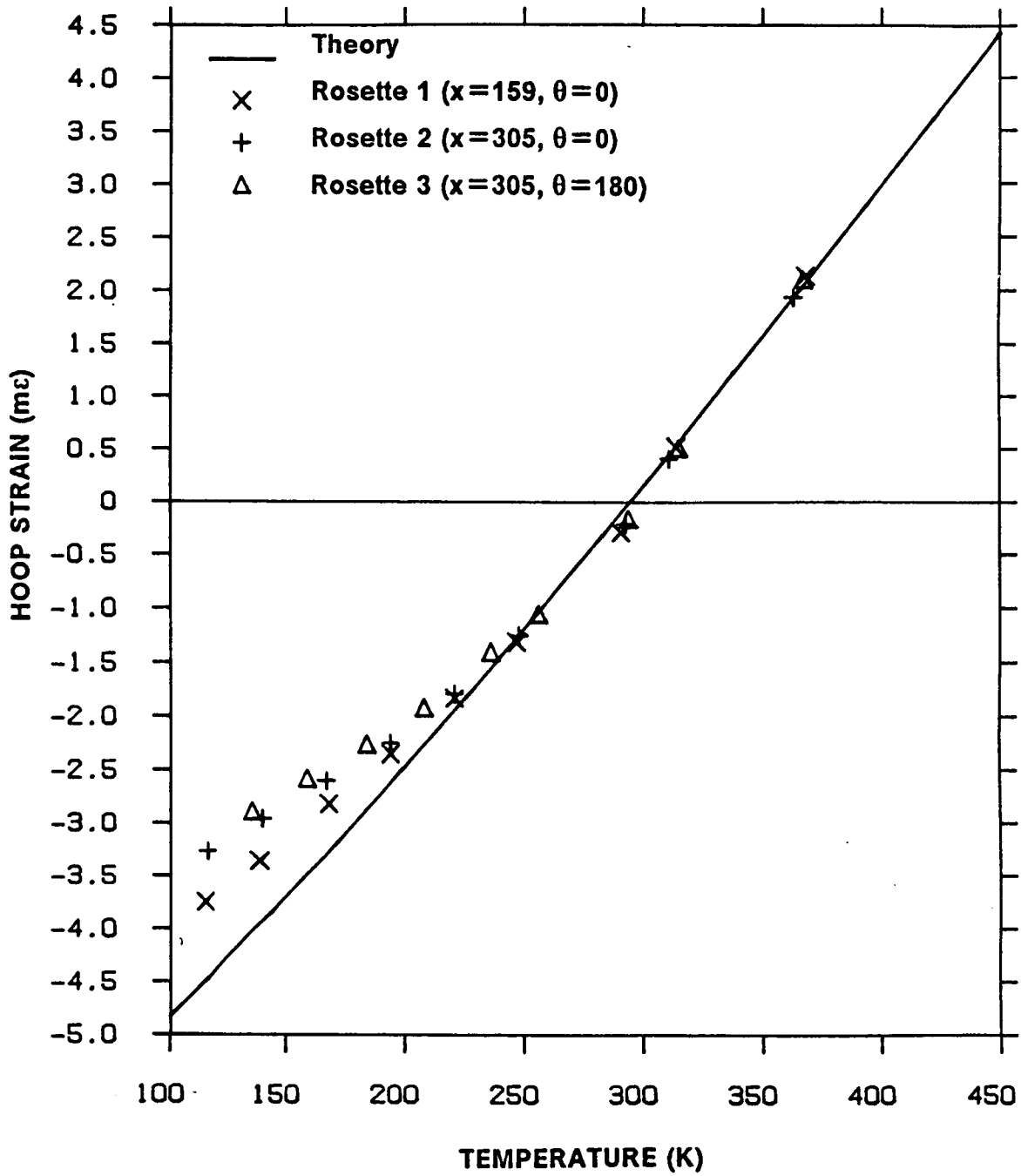


Figure 101. Hoop Strain vs. Temperature, Specimen 35: [-10 / 0<sub>12</sub> / -10]. Experiment and Theory, Temperature-dependent material properties.

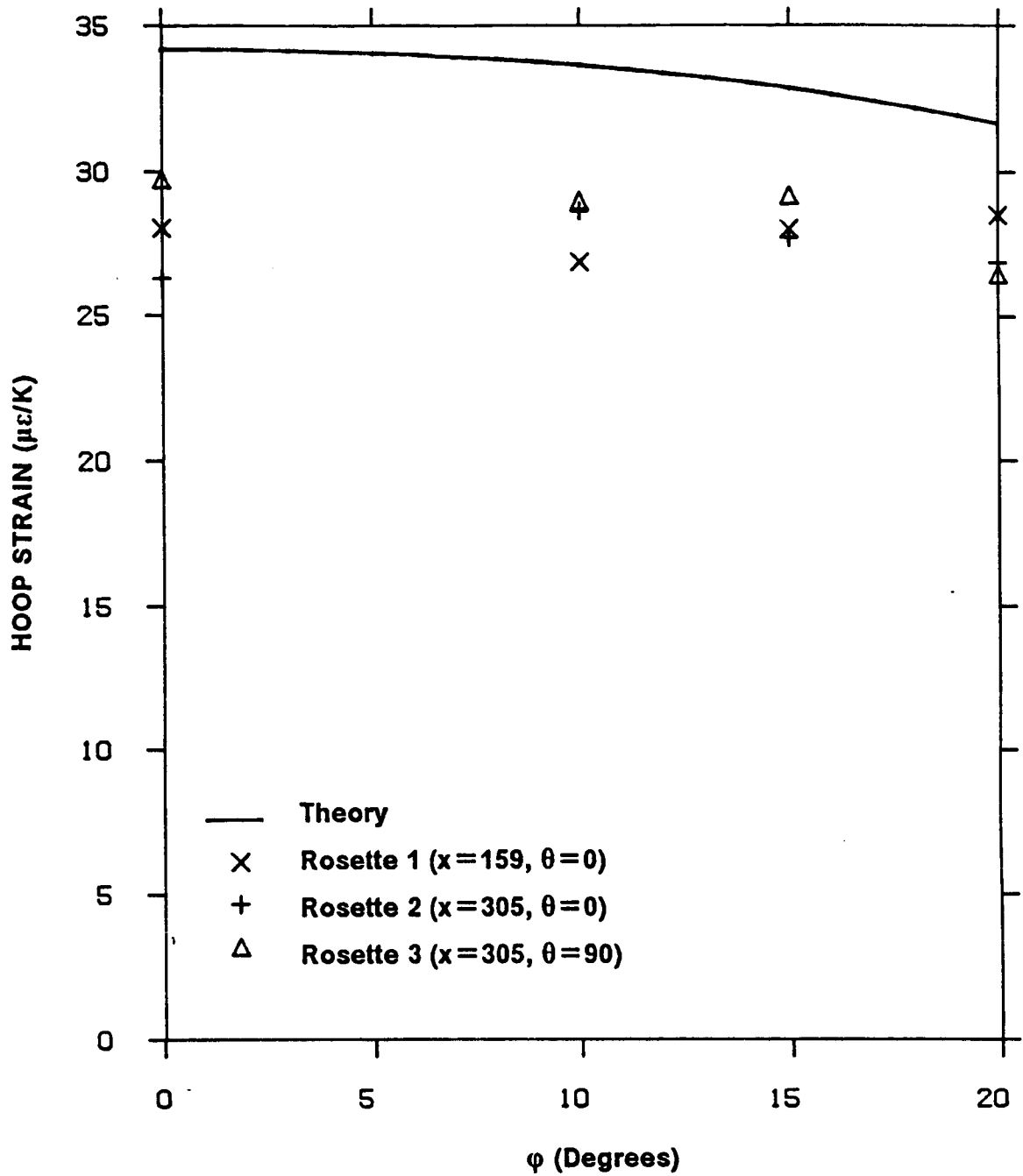


Figure 102. Hoop Strain vs. Ply Orientation Angle (Specimens 11 - 14): Family 1 :  $[-10_2 / 0_{10} / \phi_2]$ . Experiment and Theory, Temperature-independent material properties. material system : P75S/ERLX1962A.

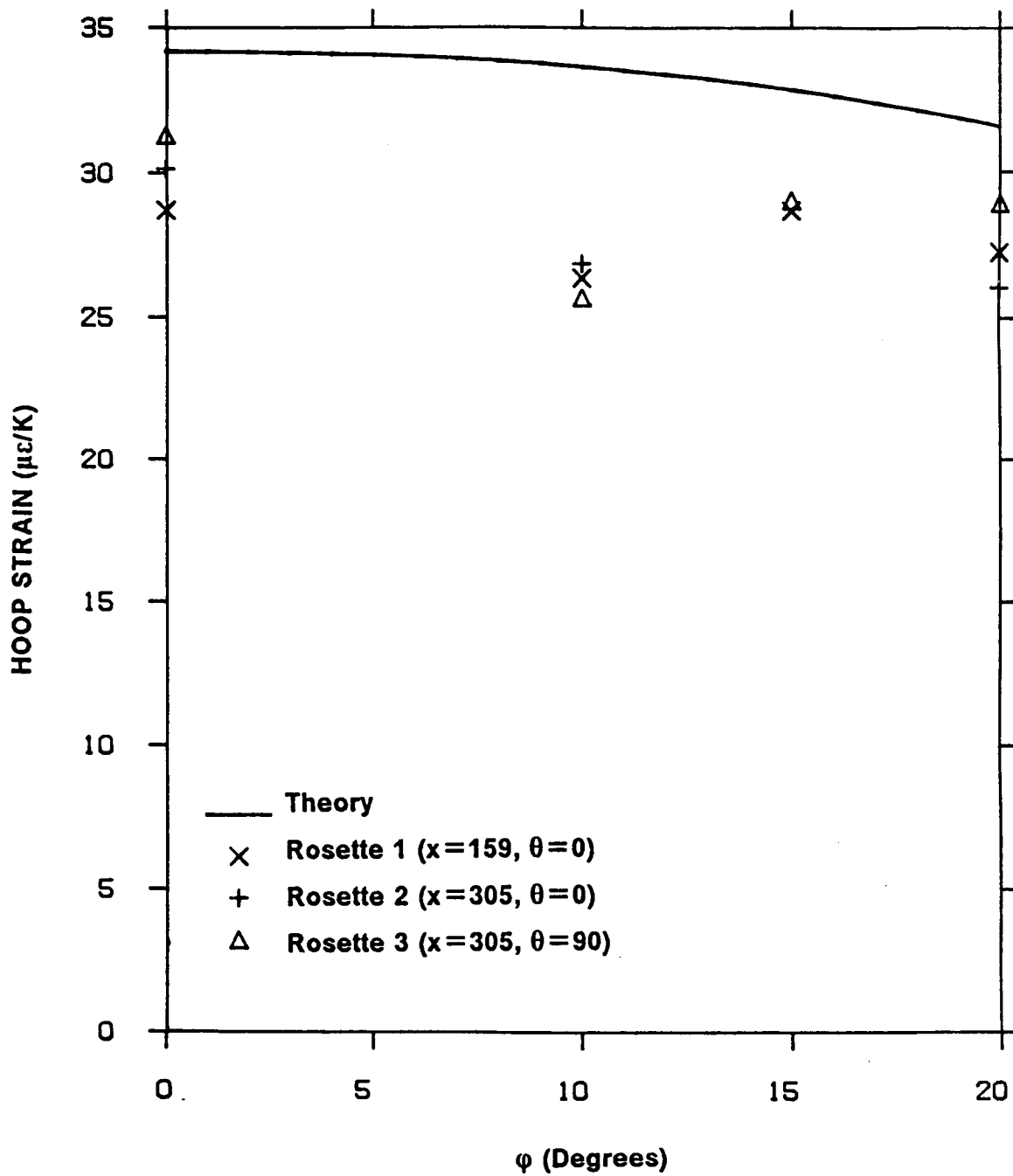


Figure 103. Hoop Strain vs. Ply Orientation Angle (Specimens 15 - 18): Family 2 : [-10 / 0<sub>s</sub> /  $\phi_2$  / 0<sub>s</sub> / -10 ]. Experiment and Theory, Temperature-independent material properties. material system : P75S/ERLX1962A.

theory and experiment of the twist response of the tubes was good. The agreement between measured and predicted twist response was believed to be sensitive to tube fabrication anomalies such as the accuracy of the off-axis ply orientation angles. The strain gage measurements made in this investigation were found to be somewhat erratic. The graphite-epoxy material systems studied here were shown to exhibit temperature-dependent material behavior over the range of temperatures studied. The axial response of the tubes tested was observed to be greater than predicted by a factor of three. It is not clear whether this effect was due to axial variations in the experiment which the theory did not account for, lack of accurate material properties, or the axial temperature variations present in the test apparatus used.

In the final chapter, the results of this, and earlier chapters are summarized. Overall conclusions and recommendations for this investigation are presented.

## 6.0 Conclusions and Recommendations

The specific objectives of this study were as follows:

1. To develop an analytical methodology to study the stresses and deformations in tubes of circular cross-section and which consisted of layers of anisotropic material. The loading was primarily thermal and temperature-dependent material properties were included in the methodology. Only axisymmetric tube responses were considered.
2. To use the analysis to study the effect, on predicted stresses and deformations, of including the temperature dependence of material properties.
3. To use the analysis to study the effect, on the predicted stresses and deformations, of metallic coatings.
4. To develop an experimental apparatus for measuring thermally-induced deformations in uniformly heated and cooled angle-ply composite tubes, particularly the phenomenon of thermally-induced twist.

5. To measure the thermally-induced deformations in a series of tubes to validate the findings of the analysis, and to correlate the experimental results with the analytical results.

Objectives 1-3 were met by developing an analysis based on elasticity theory. The analysis was developed from first principles, the inclusion of temperature-dependent properties being relatively straightforward with this approach. An elasticity solution was used, as opposed to a shell-like theory, to account for any through-the-thickness effects that may prevail. As it turned out, one of these prevailing effects was thermally-induced twist. A shell-like approach would not have revealed this phenomenon. The derivation of the governing equations of elasticity and the boundary conditions appropriate for this problem were presented in Ch. 2. An analytical investigation, satisfying Objectives 2 and 3, was presented in Ch. 3.

The analytical predictions obtained indicated that off-axis ply orientation can cause significant stresses when the temperature approaches the values encountered in the orbital environment. While the predicted fiber direction stresses were low, relative to the fiber strength, the transverse stress  $\sigma_2$  could exceed values that would cause cracking in the epoxy. These transverse stresses were, for the most part, the same for both tube designs considered and were, as expected, a strong function of fiber angle. From the results presented, it did appear, however, that low off-axis fiber angles could be used to minimize the thermally-induced stresses. For application to the space station, the most critical design considerations should involve minimizing the transverse stress in the off-axis plies and maximizing the transverse tensile strength of the graphite-epoxy material system used. The effect of temperature-dependent material properties was found to be significant. Off-axis ply orientation angle and lamination sequence were found to play an important role in determining tube response. However, composites provide enough variable design parameters that a satisfactory design can be achieved.

It appeared that the coatings had no detrimental effect on the response of the tube. The contraction of the outer coating was found to have a beneficial effect on the stresses in the graphite-epoxy. The coating generally caused a decrease in transverse tensile stresses and radial stresses in the graphite-epoxy, for the designs considered in this investigation. However, the inner coating showed a tendency to pull away from the tube and possibly delaminate. The stresses in the coatings were predicted to be quite high. This was due primarily to the assumption that the coating material behaved as a linear elastic material. Yielding and subsequent plastic deformations could well alter the stress state in the foil. However, this behavior would not be expected to adversely influence the response of the tube, particularly the stresses.

One of the more interesting findings related to the twist response of the tube. It was shown that the tube would twist due to a temperature change despite the fact that the wall in both designs was of a balanced construction. It was shown that the thermally-induced twist was due to the fact that the different off-axis layers had different radial positions. A single off-axis layer would obviously twist, but adding a second off-axis layer with exactly the opposite sign did not exactly cancel the twist of the first layer. The further apart the two balancing off-axis layers are in the radial direction, the larger is the net twist effect from the two off-axis layers. The fact that a tube fabricated with a balanced lamination sequence exhibits twist has serious consequences if the tube is part of a structure in which dimensional stability and longevity are issues. If the tube is long enough and the temperature change substantial, the rotation of one end of the tube relative to the other can become significant. On the other hand, if both ends of the tube are firmly attached to some other part of the structure, a temperature change can induce torsional loads in the tube. If the temperature change is cyclic, as well may be the case in an orbiting structure, the torsional loads will be cyclic and they could eventually lead to material failure in the form of fatigue.

Because of the serious implications of thermally-induced twist, it was felt to be important to study the phenomenon experimentally. In addition, other thermally-induced responses, e.g.

axial deformations and strains, could be studied at the same time. This led to Objectives 4 and 5. They required the design and fabrication of a test apparatus. The twist phenomenon was felt to be so fundamental, and for some situations so pronounced, that the apparatus did not have to employ sophisticated thermal equipment or high resolution techniques. Thus, electromechanical transducers and a slightly modified standard environmental chamber were the basis for the design. The specimens used were similar in design to those being considered for use on the space station. The specimens included three types of graphite-epoxy material, eight lamination sequences, and three off-axis ply orientation angles.

A detailed description of the experimental apparatus was presented in Ch.4. Eighteen test specimens were tested in this apparatus, and the experimental results were presented in Ch. 5 and compared to theoretical predictions. This experimental investigation succeeded in its primary goal of verifying the theoretical prediction that composite tubes, even those with balanced symmetric lamination sequences, would twist when subjected to a thermal load. In general, the agreement between theory and experiment of the twist response of the tubes was good. The agreement between measured and predicted twist response was found to be sensitive to tube fabrication anomalies such as the accuracy of the off-axis ply orientation angles. The strain gage measurements made in this investigation were found to be somewhat erratic. The graphite-epoxy material systems studied here were shown to exhibit temperature-dependent material behavior over the range of temperatures studied. Correlation between theory and experiment was, in many cases, worse at low temperatures. From this it is concluded that the temperature-dependent material property data used in this investigation is not reliable at cryogenic temperatures. The axial response of the tubes tested was observed to be greater than predicted by a factor of three. It is not clear whether this effect was due to axial variations in the experiment which the theory did not account for, lack of accurate material properties, or the axial temperature variations present in the test apparatus used. It is recommended that the problem of thermally-induced axial deformations be investigated further, both experimentally and analytically. A test apparatus that fully encloses the test spec-

imen and thereby eliminates any large axial variations in temperature is suggested. Finally, although the specimens were not dried before testing, moisture loss was not found to be an issue. The reason for this is felt to be the short length of time that the specimens were subjected to temperatures higher than room temperature.

In general, the problem of a thermally-loaded laminated tube presents many interesting aspects in design and analysis. In many applications, a composite tube can be an efficient and versatile structural component. Care should be taken to consider the unique analytical aspects of the the tubular geometry. Further study is warranted, in order to realize the full potential of this type of structural member.

PRECEDING PAGE BLANK NOT FILMED

## References

- <sup>1</sup> Hagaman, Jane A., "A Survey of Structural Material Issues for a Space Station," NASA-TM-86385 (August 1985).
- <sup>2</sup> Cohen, D., Hyer, M. W., and Tompkins, S. S., "The Effect of Thermal Cycling on Matrix Cracking and Stiffness Changes in Cross-Ply Graphite-Epoxy Tubes," CCMS-84-12, Virginia Tech Center for Composite Materials and Structures Report (August 1984).
- <sup>3</sup> Cohen, D. and Hyer, M. W., "Residual Stresses in Cross-Ply Composite Tubes," CCMS-84-04, Virginia Tech Center for Composite Materials and Structures Report (June 1984).
- <sup>4</sup> Whitney, J. M. and Halpin, J. C., "Analysis of Laminated Anisotropic Tubes Under Combined Loading," *J. Composite Materials*, Vol. 2, No. 3 (July 1968), p.360.
- <sup>5</sup> Pao, Y. C., "On Higher Order Theory for Thermoelastic Analysis of Heterogeneous Orthotropic Cylindrical Shells," *Developments of Theoretical and Applied Mechanics*, Vol. 6 (1972), Proc. of the Sixth Southeastern Conference on Theoretical and Applied Mechanics, eds. E. G. Henneke and S. C. Kranc, published by University Microfilms International, Ann Arbor, MI., p. 787.
- <sup>6</sup> Pao, Y. C., and Peterson, K., "Optimal Study of Interface Axial Shear Stresses in Two-Layer Axisymmetric Shell Induced During Curing Treatment," *J. Composite Materials*, Vol. 16 (May 1982), p. 204.
- <sup>7</sup> Whitney, J. M., "On the Use of Shell Theory for Determining Stresses in Composite Cylinders," *J. Composite Materials*, Vol. 5 (July 1971), p. 340.
- <sup>8</sup> Sherrer, R. E., "Filament Wound Cylinders with Axial-Symmetric Loads," *J. Composite Materials*, Vol.1 (1967), p. 344.
- <sup>9</sup> Pagano, N. J. and Whitney, J. M., "Geometric Design of Composite Cylindrical Characterization Specimens," *J. Composite Materials*, Vol. 4 (July 1970), p. 360.

- 10 Weng, Tu-Lung, "Thermal Stresses in Anisotropic Hollow Cylinder," *J. Basic Engineering* (June 1965), p. 391.
- 11 Carter, R. J., and Brzezinski, A. J., "Design, Fabrication, and CTE Testing of a Low Coefficient of Thermal Expansion Tube," Proc. from the 17th National SAMPE Technical Conference, Kiamesha Lake, N.Y. (October 22-24, 1985) pp. 524-531.
- 12 Uemura, M., and Fukunaga, H., "Burst Strength of Filament- Wound Cylinders Subjected to Internal Pressure", *Composite Materials: Mechanics, Mechanical Properties, and Fabrication*, Proc., Japan-U.S. Composite Materials Conference, Tokyo (1982), published by Barking Essex Applied Science Publishers for Japan Society for Composite Materials.
- 13 Lekhnitskii, S. G., *Theory of Elasticity of an Anisotropic Body*, Translated by P. Fern, Holden-Day, Inc. San Fransisco, 1963.
- 14 Pagano, N. J., "Stress Gradients in Laminated Composite Cylinders," *J. Composite Materials*, Vol. 5 (1971) p. 340.
- 15 Pagano, N. J., Personal Communication with M. W. Hyer.
- 16 Hyer, M. W. and Cooper, D. E., "Stresses and Deformations in Composite Tubes Due to Circumferential Temperature Gradients," *J. Applied Mechanics*, Vol. 53, No. 4 (1986) pp. 757-764.
- 17 Hyer, M. W. and Rousseau, C. Q., "Thermally Induced Stresses and Deformations in Angle-Ply Composite Tubes," *J. Composite Materials* (in press).
- 18 Milkovich, Scott Milan, Herakovich, Carl T., and Sykes, George F., Jr., "Space Radiation Effects on Graphite- Epoxy Composite Materials," CCMS-84-08, Virginia Tech Center for Composite Materials and Structures Report (June 1984).
- 19 Datta, S. K., Ledbetter, H. M., and Kriz, R. D., "Predicted Elastic Constants of Transversely Isotropic Composites Containing Anisotropic Fibers." *Progress in Science and Engineering of Composites*, Proc. of the Fourth International Conference on Composite Materials (1982), eds. T. Hayashi, K. Kawata, and S. Umekawa, Vol. I, p. 349, published by The Japan Society for Composite Materials, c/o Business Center for Academic Societies of Japan, 2-4-6 Yayoi, Bunkyo-ku, Tokyo 113, Japan.
- 20 Tsai, S. W., *Composites Design 1986*, Think Composites, 3033 Locust Camp Rd. (Box 581), Dayton, OH, 45419, p. 10-8 (1986).
- 21 Schott Optical Glass, Inc. Zerodur data sheet.
- 22 Wolfendale, P. C. F., "Capacitive Displacement Transducers with High Accuracy and Resolution," *J. Scientific Instruments*, Vol. 1, Series 2 (1968) pp. 817-818.
- 23 "Errors Due to Transverse Sensitivities in Strain Gages," Measurements Group, Inc. Tech Note, TN-509 (1982).
- 24 Hyer, M. W., Herakovich, C. T., Milkovich, S. M., and Short, J. S., "Temperature Dependence of Mechanical and Thermal Expansion Properties of T300/5208 Graphite-Epoxy," *Composites*, Vol. 14, No. 3, (July 1983) pp. 276-280.
- 25 Bowles, David E. and Tompkins, Steven S., Personal Communication.

## Appendix A. Material Properties

This Appendix contains the temperature-independent and temperature-dependent material properties used in the analytical portions of this investigation. Temperature-independent properties are presented in both SI and U. S. Customary units. The polynomials that constitute the temperature-dependent material properties are in U. S. Customary units only. Also included is a discussion of the method used to calculate the temperature-dependent properties. The graphite-epoxy composite material systems considered are T300/934, P75S/ERLX1962A, T300/ERLX1962A, and AS4/976. Also shown are 6061 Aluminum and a typical aerospace epoxy adhesive.

Tables A.2 - A.7 present temperature-independent engineering constants for all materials. The source of the data is referenced in the Tables. If no reference is given for a particular number, it was either assumed, or derived from other data. For three of the graphite-epoxies,  $\nu_{23}$  was assumed to be 0.49, on the basis of Datta, et al.[A1]. It should be noted that if  $E_2 = E_3$ , the elasticity analysis would have division by zero in the expression for  $w(r)$ . To avoid this, the analysis could have been conducted assuming the material was transversely isotropic in the  $\theta$ - $r$  plane, or  $E_3$  could have been made slightly different than  $E_2$ . Here, the latter approach was used, with  $E_3 = 0.90 E_2$ . This resulted in  $S_{33} = 1.11 S_{22}$ . The temperature-independent compliance matrices may, of course, be calculated from the engineering properties.

Temperature-dependent mechanical and thermal expansion data for T300/5208 graphite-epoxy were presented by Hyer, et. al.[A2]. Cooper [A3] used the results of Hyer, et. al.[A2] to derive general expressions for the temperature-dependent compliance matrix,  $S_{ij}$ , for graphite-epoxy. Cooper assumed that all types of graphite-epoxies would exhibit temperature-dependent behavior similar to that of T300/5208, thus, a general polynomial form of the  $S_{ij}$  matrix could be written for graphite-epoxy which could be modified to describe any specific type of graphite-epoxy, given specific temperature-independent compliances. While this method of finding temperature-dependent material properties is somewhat arbitrary, it is felt that analytical results using these properties are still more accurate than those employing temperature-independent properties. In this investigation, the temperature-independent, and temperature-dependent engineering properties reported by Milkovich, et al.[A4] are used for T300/934. This T300/934 temperature-dependent data is then used to derive a general form for the compliances, in a manner similar to that employed by Cooper [A3]. The general form of the compliances is, therefore, given in Table A.1. The temperature-dependent compliances for P75S/ERLX1962A and AS4/976, presented in Tables A.9 and A.10, are derived using this method. For T300/ERLX1962A, the temperature-dependent compliances of T300/934 are used.

Conventional thermal expansion coefficients ( $\alpha_i$ ) are used for the temperature-independent data, however, temperature-dependent properties are presented in terms of thermally-induced strains. It is felt that thermal strain is a more straight-forward way of presenting these temperature-dependent properties than temperature-dependent forms of CTE's. The polynomials for thermal strain for T300/934 were derived from experimental data [A5]. Thermal strain data for P75S/934 was obtained from the same source and used for P75S/ERLX1962A. The T300/934 data was used for T300/ERLX1962A. For the AS4/976 temperature-dependent thermal strains, the T300/934 data was used to derive general forms for thermal strain in a manner similar to that used for the compliances. These general polynomials are presented in Table A.1. Temperature-dependent values of  $E$ ,  $\nu$ , and  $\alpha$  for 6061 aluminum were reported by Barrett and Beusking [A6]. From this data, the

temperature-dependent compliances and thermal strains for 6061 are calculated and are given in Table A.11. Note that for computational purposes,  $S_{33} = 1.11 S_{22}$  for 6061. No temperature-dependent data was available for the epoxy adhesive.

## Appendix A. References

1. Datta, S. K., Ledbetter, H. M., and Kriz, R. D., "Predicted Elastic Constants of Transversely Isotropic Composites Containing Anisotropic Fibers." *Progress in Science and Engineering of Composites*, Proc. of the Fourth International Conference on Composite Materials (1982), eds. T. Hayashi, K. Kawata, and S. Umekawa, Vol. I, p. 349, published by The Japan Society for Composite Materials, c/o Business Center for Academic Societies of Japan, 2-4-6 Yayoi, Bunkyo-ku, Tokyo 113, Japan.
2. Hyer, M. W., Herakovich, C. T., Milkovich, S. M., and Short, J. S., "Temperature Dependence of Mechanical and Thermal Expansion Properties of T300/5208 Graphite-Epoxy," *Composites*, Vol. 14, No. 3, (July 1983) pp. 276-280.
3. Cooper, D. E., "Stress Gradients in Cross-Ply Composite Tubes Subjected to Circumferential Temperature Gradients", M. S. Thesis, Department of Engineering Mechanics, Virginia Polytechnic Institute and State University, Blacksburg, VA, 24061 (July 1985).
4. Milkovich, Scott Milan, Herakovich, Carl T., and Sykes, George F., Jr., "Space Radiation Effects on Graphite- Epoxy Composite Materials," CCMS-84-08, Virginia Tech Center for Composite Materials and Structures Report (June 1984).
5. Bowles, David E. and Tompkins, Steven S., Personal Communication.
6. Barrett, David J. and Beusking, Kent W., "Temperature Dependent Nonlinear Metal Matrix Laminate Behavior," NASA-CR-4016 (1986).
7. Mincho, M. J., Jr., "High Modulus Composite Properties," Proc. from AIAA Space Systems Technology Conference, San Diego, CA (June 1986), published by AIAA Publications, 1633 Broadway, New York, N.Y., 10019.
8. Bacon, R., Eckstein, B. H., Kowalski, I. M., Schulz, D. A., Strong, S. L., Towne, M. K., and Wagoner, G., "Thermal Expansion Behavior of Unidirectional Composites of Ultra High Modulus Carbon Fibers in Epoxy Resin," First European Conference on Composite Materials and Exhibition - European Assoc. for Composite Materials, Bordeaux, France (September 1985).
9. Hyer, M. W., Personal Communication.

PRECEDING PAGE BLANK, NOT FILMED

**Table A.1. General Form of Temperature-Dependent Material Properties**

$$S_{11} = S_{11}(70)$$

$$S_{12}(T) = S_{12}(70) (9.8353 \times 10^{-1} + 1.5859 \times 10^{-4} T + 1.0959 \times 10^{-6} T^2)$$

$$S_{13}(T) = S_{13}(70) (9.8353 \times 10^{-1} + 1.5859 \times 10^{-4} T + 1.0959 \times 10^{-6} T^2)$$

$$S_{22}(T) = S_{22}(70) (9.4279 \times 10^{-1} + 7.7375 \times 10^{-4} T + 6.2146 \times 10^{-6} T^2)$$

$$S_{23}(T) = S_{23}(70) (9.4279 \times 10^{-1} + 7.7375 \times 10^{-4} T + 6.2146 \times 10^{-6} T^2)$$

$$S_{33}(T) = S_{33}(70) (9.4279 \times 10^{-1} + 7.7375 \times 10^{-4} T + 6.2146 \times 10^{-6} T^2)$$

$$S_{66}(T) = S_{66}(70) (8.8484 \times 10^{-1} + 1.4846 \times 10^{-3} T + 2.2934 \times 10^{-6} T^2)$$

$$\varepsilon_1^T = 0$$

$$\varepsilon_2^T(T) = \alpha_2(70) (-346.05 + 0.92829 T + 2.2853 \times 10^{-6} T^2 - 1.5977 \times 10^{-7} T^3)$$

$$\varepsilon_3^T(T) = \alpha_3(70) (-346.05 + 0.92829 T + 2.2853 \times 10^{-6} T^2 - 1.5977 \times 10^{-7} T^3)$$

Temperature, T, is in degrees Fahrenheit.

The thermal strain polynomials are only valid for composites with low modulus (pan based) fibers.

**Table A.2. Temperature-Independent Material Properties for T300/934**

$$E_1 = 18.9 \text{ Msi (130 GPa) [A4] †}$$

$$E_2 = 1.38 \text{ Msi (9.52 GPa) [A4]}$$

$$E_3 = 1.24 \text{ Msi (8.55 GPa)}$$

$$G_{12} = 0.69 \text{ Msi (4.76 GPa) [A4]}$$

$$\nu_{23} = 0.49$$

$$\nu_{13} = 0.31$$

$$\nu_{12} = 0.31 \text{ [A4]}$$

$$\alpha_1 = 0 \text{ [A5]}$$

$$\alpha_2 = 10.5 \mu\epsilon/^\circ\text{F (18.9 } \mu\epsilon/^\circ\text{C) [A5]}$$

$$\alpha_3 = 10.5 \mu\epsilon/^\circ\text{F (18.9 } \mu\epsilon/^\circ\text{C)}$$

† Brackets indicate reference number from which datum was obtained

**Table A.3. Temperature-Independent Material Properties for P75S/ERLX1962A**

$$E_1 = 49.0 \text{ Msi (338 GPa) [A7] †}$$

$$E_2 = 1.00 \text{ Msi (6.90 GPa) [A7]}$$

$$E_3 = 0.90 \text{ Msi (6.21 GPa)}$$

$$G_{12} = 0.79 \text{ Msi (5.45 GPa) [A7]}$$

$$\nu_{23} = 0.49$$

$$\nu_{13} = 0.30$$

$$\nu_{12} = 0.30 \text{ [A7]}$$

$$\alpha_1 = -0.54 \text{ } \mu\epsilon/\text{ }^\circ\text{F (-0.97 } \mu\epsilon/\text{ }^\circ\text{C) [A8]}$$

$$\alpha_2 = 19.2 \text{ } \mu\epsilon/\text{ }^\circ\text{F (34.6 } \mu\epsilon/\text{ }^\circ\text{C) [A5]}$$

$$\alpha_3 = 19.2 \text{ } \mu\epsilon/\text{ }^\circ\text{F (34.6 } \mu\epsilon/\text{ }^\circ\text{C)}$$

† Brackets indicate reference number from which datum was obtained

**Table A.4. Temperature-Independent Material Properties for T300/ERLX1962A**

$$E_1 = 18.9 \text{ Msi (130 GPa) [A4] †}$$

$$E_2 = 1.38 \text{ Msi (9.52 GPa) [A4]}$$

$$E_3 = 1.24 \text{ Msi (8.55 GPa)}$$

$$G_{12} = 0.69 \text{ Msi (4.76 GPa) [A4]}$$

$$\nu_{23} = 0.49$$

$$\nu_{13} = 0.31$$

$$\nu_{12} = 0.31 \text{ [A4]}$$

$$\alpha_1 = 0 \text{ [A5]}$$

$$\alpha_2 = 10.5 \mu\text{E}/^\circ\text{F (18.9 } \mu\text{E}/^\circ\text{C) [A5]}$$

$$\alpha_3 = 10.5 \mu\text{E}/^\circ\text{F (18.9 } \mu\text{E}/^\circ\text{C)}$$

† Brackets indicate reference number from which datum was obtained

**Table A.5. Temperature-Independent Material Properties for AS4/976**

$$E_1 = 19.1 \text{ Msi (132 GPa) [A9] †}$$

$$E_2 = 1.36 \text{ Msi (9.38 GPa) [A9]}$$

$$E_3 = 1.22 \text{ Msi (8.41 GPa)}$$

$$G_{12} = 0.836 \text{ Msi (5.77 GPa) [A9]}$$

$$\nu_{23} = 0.34 \text{ [A9]}$$

$$\nu_{13} = 0.28$$

$$\nu_{12} = 0.28 \text{ [A9]}$$

$$\alpha_1 = -0.044 \text{ } \mu\text{E}/^\circ\text{F} \text{ (-0.079 } \mu\text{E}/^\circ\text{C) [A9]}$$

$$\alpha_2 = 16.0 \text{ } \mu\text{E}/^\circ\text{F} \text{ (28.8 } \mu\text{E}/^\circ\text{C) [A9]}$$

$$\alpha_3 = 16.0 \text{ } \mu\text{E}/^\circ\text{F} \text{ (28.8 } \mu\text{E}/^\circ\text{C)}$$

† Brackets indicate reference number from which datum was obtained

**Table A.6. Temperature-Independent Material Properties for 6061 Aluminum**

$$E = 9.9 \text{ Msi (68.3 GPa) [A6] †}$$

$$\nu = 0.33 \text{ [A6]}$$

$$\alpha = 12.9 \text{ } \mu\text{ε/}^\circ\text{F (23.2 } \mu\text{ε/}^\circ\text{C) [A6]}$$

† Brackets indicate reference number from which datum was obtained

**Table A.7. Temperature-Independent Material Properties for Epoxy Adhesive**

$$E = 0.54 \text{ Msi (3.72 GPa) [A5] †}$$

$$\nu = 0.35 \text{ [A5]}$$

$$\alpha = 21.8 \text{ } \mu\epsilon/\text{ }^\circ\text{F (39.3 } \mu\epsilon/\text{ }^\circ\text{C) [A5]}$$

† Brackets indicate reference number from which datum was obtained

**Table A.8. Temperature-Dependent Material Properties for T300/934**

The polynomials in this table all have the form:

$$A(T) = a_0 + a_1T + a_2T^2 + a_3T^3$$

where temperature, T, is in degrees Fahrenheit.

$A(T)$	$a_0$	$a_1$	$a_2$	$a_3$
$S_{11}$	$5.2910 \times 10^{-8}$	0	0	0
$S_{12}$	$-1.6319 \times 10^{-8}$	$-2.6314 \times 10^{-12}$	$-1.8184 \times 10^{-14}$	0
$S_{13}$	$-1.6319 \times 10^{-8}$	$-2.6314 \times 10^{-12}$	$-1.8184 \times 10^{-14}$	0
$S_{22}$	$6.6036 \times 10^{-7}$	$5.4196 \times 10^{-10}$	$4.3529 \times 10^{-13}$	0
$S_{23}$	$-3.2356 \times 10^{-7}$	$-2.6556 \times 10^{-10}$	$-2.1329 \times 10^{-13}$	0
$S_{33}$	$7.3373 \times 10^{-7}$	$6.0218 \times 10^{-10}$	$4.8366 \times 10^{-13}$	0
$S_{66}$	$1.1856 \times 10^{-6}$	$1.9892 \times 10^{-9}$	$3.0729 \times 10^{-12}$	0
$\epsilon_1^T$	0	0	0	0
$\epsilon_2^T$	$-3.7751 \times 10^{-3}$	$1.0127 \times 10^{-5}$	$2.4931 \times 10^{-7}$	$-1.7430 \times 10^{-12}$
$\epsilon_3^T$	$-3.7751 \times 10^{-3}$	$1.0127 \times 10^{-5}$	$2.4931 \times 10^{-7}$	$-1.7430 \times 10^{-12}$

**Table A.9. Temperature-Dependent Material Properties for P75S/ERLX1962A**

The polynomials in this table all have the form:

$$A(T) = a_0 + a_1T + a_2T^2 + a_3T^3$$

where temperature, T, is in degrees Fahrenheit.

A(T)	$a_0$	$a_1$	$a_2$	$a_3$
$S_{11}$	$2.0408 \times 10^{-8}$	0	0	0
$S_{12}$	$-6.0216 \times 10^{-9}$	$-9.7096 \times 10^{-13}$	$-6.7096 \times 10^{-15}$	0
$S_{13}$	$-6.0216 \times 10^{-9}$	$-9.7096 \times 10^{-13}$	$-6.7096 \times 10^{-15}$	0
$S_{22}$	$9.4279 \times 10^{-7}$	$7.7375 \times 10^{-10}$	$6.2146 \times 10^{-13}$	0
$S_{23}$	$-4.6197 \times 10^{-7}$	$-3.7914 \times 10^{-10}$	$-3.0452 \times 10^{-13}$	0
$S_{33}$	$1.0475 \times 10^{-6}$	$8.5972 \times 10^{-10}$	$6.9051 \times 10^{-13}$	0
$S_{66}$	$1.1201 \times 10^{-6}$	$1.8792 \times 10^{-9}$	$2.9030 \times 10^{-12}$	0
$\epsilon_1^T$	$1.5725 \times 10^{-4}$	$-6.1300 \times 10^{-7}$	$6.5270 \times 10^{-11}$	$1.1500 \times 10^{-12}$
$\epsilon_2^T$	$-8.2619 \times 10^{-3}$	$1.7937 \times 10^{-5}$	$4.5310 \times 10^{-9}$	$3.3333 \times 10^{-11}$
$\epsilon_3^T$	$-8.2619 \times 10^{-3}$	$1.7937 \times 10^{-5}$	$4.5310 \times 10^{-9}$	$3.3333 \times 10^{-11}$

**Table A.10. Temperature-Dependent Material Properties for AS4/976**

The polynomials in this table all have the form:

$$A(T) = a_0 + a_1T + a_2T^2 + a_3T^3$$

where temperature, T, is in degrees Fahrenheit.

A(T)	$a_0$	$a_1$	$a_2$	$a_3$
$S_{11}$	$5.2356 \times 10^{-8}$	0	0	0
$S_{12}$	$-1.4418 \times 10^{-8}$	$-2.3249 \times 10^{-12}$	$-1.6066 \times 10^{-14}$	0
$S_{13}$	$-1.4418 \times 10^{-8}$	$-2.3249 \times 10^{-12}$	$-1.6066 \times 10^{-14}$	0
$S_{22}$	$6.9323 \times 10^{-7}$	$5.6893 \times 10^{-10}$	$4.5696 \times 10^{-13}$	0
$S_{23}$	$-2.3570 \times 10^{-7}$	$-1.9344 \times 10^{-10}$	$-1.5537 \times 10^{-13}$	0
$S_{33}$	$7.7025 \times 10^{-7}$	$6.3215 \times 10^{-10}$	$5.0773 \times 10^{-13}$	0
$S_{66}$	$1.0584 \times 10^{-6}$	$1.7758 \times 10^{-9}$	$2.7433 \times 10^{-12}$	0
$\epsilon_1^T$	0	0	0	0
$\epsilon_2^T$	$-5.5368 \times 10^{-3}$	$1.4853 \times 10^{-5}$	$3.6565 \times 10^{-9}$	$-2.5563 \times 10^{-12}$
$\epsilon_3^T$	$-5.5368 \times 10^{-3}$	$1.4853 \times 10^{-5}$	$3.6565 \times 10^{-9}$	$-2.5563 \times 10^{-12}$

**Table A.11. Temperature-Dependent Material Properties for 6061 Aluminum**

The polynomials in this table all have the form:

$$A(T) = a_0 + a_1T + a_2T^2 + a_3T^3$$

where temperature, T, is in degrees Fahrenheit.

A(T)	$a_0$	$a_1$	$a_2$	$a_3$
$S_{11}$	$9.8870 \times 10^{-8}$	$2.5190 \times 10^{-11}$	0	0
$S_{12}$	$-3.2630 \times 10^{-8}$	$-8.3070 \times 10^{-12}$	0	0
$S_{13}$	$-3.2630 \times 10^{-8}$	$-8.3070 \times 10^{-12}$	0	0
$S_{22}$	$9.8870 \times 10^{-8}$	$2.5190 \times 10^{-11}$	0	0
$S_{23}$	$-3.2630 \times 10^{-8}$	$-8.3070 \times 10^{-12}$	0	0
$S_{33}$	$1.0990 \times 10^{-7}$	$2.8000 \times 10^{-11}$	0	0
$S_{66}$	$2.6300 \times 10^{-7}$	$6.6930 \times 10^{-11}$	0	0
$\epsilon_1^T$	$-4.4798 \times 10^{-3}$	$1.2029 \times 10^{-5}$	$2.2943 \times 10^{-9}$	0
$\epsilon_2^T$	$-4.4798 \times 10^{-3}$	$1.2029 \times 10^{-5}$	$2.2943 \times 10^{-9}$	0
$\epsilon_3^T$	$-4.4798 \times 10^{-3}$	$1.2029 \times 10^{-5}$	$2.2943 \times 10^{-9}$	0

## Appendix B. Test Specimen Information

This Appendix contains details of test specimen geometry, testing sequence, and strain gage specifications. Table B.1 lists specimen length, average inside diameter (measured at two circumferential locations in each end of the tube), and average tube wall thickness (measured at four circumferential locations at each end of the tube) for the P75S/ERLX1962A and AS4/976 tubes. Not shown in Table B.1 are measurements of overall specimen straightness. No appreciable warping along the length of the specimens was observed, however, the outside diameter was found to be somewhat (less than 0.20 mm) smaller near the center of some of the test specimens than at the ends. Due to time constraints and the uniformity of the first two sets of test specimens, the dimensions of the T300/ERLX1962A tubes were not checked.

Table B.2 lists the tests that were conducted, in the order in which they were done. The weight of each test specimen before, and immediately after testing is shown. Even though the specimens were not dried before testing, the weight changes can be seen to be no more than  $\pm 0.2\%$ , thus supporting the conclusion that moisture loss/gain was not a factor in overall tube response. The notes appended to Table B.2 include whether or not the test specimen was strain gaged, whether or not useable strain gage data were obtained, and any observed peculiarities in the test.

Finally, Table B.3 presents the gage factors and transverse sensitivities of the strain gages. All WK-00-125AD-350 and all WK-00-125RA-350 gages came from the same lots, therefore, the gage factors and transverse sensitivities for all gages of each type were the same on all test specimens.

**Table B.1. Test Specimen Dimensions**

Specimen	Length (mm)	Avg. I.D. (mm)	Avg. Thickness (mm)
11	609.60	50.67	1.80
12	609.60	50.52	1.83
13	609.60	50.52	1.83
14	609.60	50.57	1.78
15	609.60	50.57	1.80
16	609.60	50.62	1.80
17	608.84	50.55	1.80
18	609.60	50.55	1.80
31	609.60	50.62	1.57
32	609.60	50.60	1.70
34	610.11	50.65	1.65
35	610.36	50.60	1.68
38	609.60	50.57	1.70

**Table B.2. Test Sequence and Miscellaneous Notes**

Test	Wt. Before (gms)	Wt. After (gms)	Wt. Gain (%)	
34A	-	-	-	⊕
34B	-	-	-	† † §
31	311.55	311.60	0.0	† †
32	340.50	340.90	0.1	† † £
35A	320.75	320.00	-0.2	† †
38	320.35	320.40	0.0	† †
35B	320.30	321.00	0.2	†
16	373.85	374.40	0.1	†
12	373.80	-	-	†
14	366.10	365.90	-0.1	† §
18	367.70	368.10	0.1	†
11	371.20	371.30	0.0	† §
17	369.20	369.20	0.0	† £
13	371.30	371.75	0.1	† §
15	367.70	367.30	-0.1	† §
21	295.10	294.60	-0.2	
22	294.35	294.90	0.2	§
24	293.60	293.90	0.1	
25	297.00	297.70	0.2	§
28	294.00	294.70	0.2	

⊕ Weight includes thermocouples and RTV bonding agent, strain gages and wiring, and tape securing thermocouple and strain gage wire.

† Specimen was strain gaged.

‡ Strain gage data was not acquired do to hardware error.

§ LVDT plunger(s) observed to stick (see discussion in Ch. 4).

£ One strain gage channel open.

**Table B.3. Strain Gage Specifications**

Gage	Element†	Gage Factor	Transverse Sensitivity (%)
125AD	‡	2.01 ± 1 %	-2.3
125RA	1	1.97 ± 1 %	-1.0
125RA	2	2.02 ± 1 %	-1.4
125RA	3	1.97 ± 1 %	-1.0

† For the WK-00-125RA-350 rosette, element 1 was oriented axially on the test specimen, element 2 was 45° off-axis, and element 3 was oriented in the hoop direction.

‡ The WK-00-125AD-350 gage was a single element and the rosettes built using these gages had the same gage factors and transverse sensitivities on all arms.

## Appendix C. Program Listings

This appendix contains the FORTRAN 77 source codes for two versions of the generalized plane strain cylindrically anisotropic elasticity solution presented in this investigation. The first program, ELAS2, is configured to accept temperature-independent engineering properties. The second program, ELAST1, uses temperature-dependent polynomial forms of compliances and thermal strains as input material properties. Both programs assume all input and output data will be in U. S. Customary units.

**PRECEDING PAGE BLANK NOT FILMED**

```

C ELAS2
C
C ELASTICITY SOLUTION FOR AN ANGLE-PLY COMPOSITE TUBE W/THERMAL
C AND MECHANICAL LOADS
C
C CARL ROUSSEAU AND DR. MIKE HYER
C ESM DEPT.
C VIRGINIA TECH
C
      IMPLICIT REAL*8 (A-H,M-Z)
      COMMON /IN/ ANGLE(15),T(15),CB11(15),CB12(15),CB13(15),CB16(15),
$         CB22(15),CB23(15),CB26(15),CB33(15),CB36(15),CB66(15),RO(15),
$         RI(15),ALPAX(15),ALPAO(15),ALPAR(15),ALPAXO(15),DT,P,TW,J
      COMMON /SOLN/BC(32,32),ET(32,1),V(15),V1(15),V2(15),V3(15),V4(15),
$         Z1(15),Z2(15),Z3(15),Z4(15),Z5(15),Z6(15),Z7(15)
      COMMON/OUT/ R(150),EPSX(10,15),EPSO(10,15),EPSR(10,15),
$         GAMXO(10,15),SIGX(10,15),SIGO(10,15),SIGR(10,15),TAUXO(10,15),
$         EPS1(10,15),EPS2(10,15),EPS3(10,15),GAM12(10,15),
$         SIG1(10,15),SIG2(10,15),SIG3(10,15),TAU12(10,15),
$         RR(10,15)
      DIMENSION SIGB(15),ZZ(15)
      PI = 3.1415927

C
      CALL INPUT

C
      DO 10 I=1,J

C
      SIGB(I) = ((CB23(I) - CB22(I))*ALPAO(I) + (CB33(I) - CB23(I))*
$         ALPAR(I) + (CB13(I) - CB12(I))*ALPAX(I) + (CB36(I) -
$         CB26(I))*ALPAXO(I)) * DT
      V(I) = DSQRT (CB22(I) / CB33(I))
      V1(I) = 1. + V(I)
      V2(I) = 1. - V(I)
      V3(I) = 2. + V(I)
      V4(I) = 2. - V(I)
      ZZ(I) = CB33(I) - CB22(I)
      Z1(I) = (CB12(I) - CB13(I)) / ZZ(I)
      Z2(I) = (CB26(I) - 2*CB36(I)) / (3*CB33(I) + ZZ(I))
      Z3(I) = SIGB(I) / ZZ(I)
      Z4(I) = CB12(I) + CB13(I)
      Z5(I) = CB26(I) + CB36(I)
      Z6(I) = CB23(I) + CB33(I)
10     Z7(I) = CB22(I) + CB23(I)
C
      BC(1,1) = CB13(1) + Z6(1)*Z1(1)
      BC(1,2) = ((Z6(1) + CB33(1))*Z2(1) + CB36(1)) * RI(1)
      BC(1,3) = (CB23(1) + V(1)*CB33(1)) * RI(1)**(-V2(1))
      BC(1,4) = (CB23(1) - V(1)*CB33(1)) * RI(1)**(-V1(1))
      ET(1,1) = (CB13(1)*ALPAX(1) + CB23(1)*ALPAO(1) + CB33(1)*ALPAR(1)
$         + CB36(1)*ALPAXO(1))*DT - Z6(1)*Z3(1)

```

```

DO 12 I1=5,2*J+2
BC(1,I1) = 0.
BC(2,1) = CB13(J) + Z6(J)*Z1(J)
BC(2,2) = ((Z6(J) + CB33(J))*Z2(J) + CB36(J)) * RO(J)
12 BC(2,(I1-2)) = 0.
BC(2,(2*J+1)) = (CB23(J) + V(J)*CB33(J)) * RO(J)**(-V2(J))
BC(2,(2*J+2)) = (CB23(J) - V(J)*CB33(J)) * RO(J)**(-V1(J))
ET(2,1) = (CB13(J)*ALPAX(J) + CB23(J)*ALPA0(J) + CB33(J)*ALPAR(J)
$      + CB36(J)*ALPAX0(J))*DT - Z6(J)*Z3(J)
BC(3,1) = 0.
BC(3,2) = 0.
BC(4,1) = 0.
BC(4,2) = 0.
ET(3,1) = P / 2 / PI
ET(4,1) = TW / 2 / PI
DO 30 I=1,J
BC(3,1) = BC(3,1) + (CB11(I) + Z1(I)*Z4(I)) * (RO(I)**2 -
$      RI(I)**2) / 2.
BC(3,2) = BC(3,2) + ((CB13(I) + Z4(I)) * Z2(I) + CB16(I))
$      * (RO(I)**3 - RI(I)**3) / 3.
BC(3,(1+2*I)) = (CB12(I) + V(I) * CB13(I)) * (RO(I)**V1(I) -
$      RI(I)**V1(I)) / V1(I)
BC(3,(2+2*I)) = (CB12(I) - V(I) * CB13(I)) * (RO(I)**V2(I) -
$      RI(I)**V2(I)) / V2(I)
ET(3,1) = ET(3,1) + (DT*(CB11(I)*ALPAX(I) + CB12(I)*ALPA0(I) +
$      CB13(I)*ALPAR(I) + CB16(I)*ALPAX0(I)) - Z3(I)*Z4(I))*
$      (RO(I)**2 - RI(I)**2) / 2.
BC(4,1) = BC(4,1) + (CB16(I) + Z1(I)*Z5(I)) * (RO(I)**3 -
$      RI(I)**3) / 3.
BC(4,2) = BC(4,2) + (CB66(I) + Z2(I) * (Z5(I) +CB36(I)))*
$      (RO(I)**4 - RI(I)**4) / 4.
BC(4,(1+2*I)) = (CB26(I) + V(I) * CB36(I)) * (RO(I)**V3(I) -
$      RI(I)**V3(I)) / V3(I)
BC(4,(2+2*I)) = (CB26(I) - V(I) * CB36(I)) * (RO(I)**V4(I) -
$      RI(I)**V4(I)) / V4(I)
30 ET(4,1) = ET(4,1) + (DT*(CB16(I)*ALPAX(I) + CB26(I)*ALPA0(I) +
$      CB36(I)*ALPAR(I) + CB66(I)*ALPAX0(I)) - Z3(I)*Z5(I))*
$      (RO(I)**3 - RI(I)**3) / 3.
DO 34 KK=5,2*J+2
DO 34 LL=1,2*J+2
34 BC(KK,LL) = 0.
DO 40 K=1,J-1
BC((4+K),1) = (Z1(K) - Z1(K+1)) * RO(K)
BC((4+K),2) = (Z2(K) - Z2(K+1)) * RO(K)**2
BC((4+K),(1+2*K)) = RO(K)**V(K)
BC((4+K),(2+2*K)) = RO(K)**(-V(K))
BC((4+K),(3+2*K)) = -RO(K)**V(K+1)
BC((4+K),(4+2*K)) = -RO(K)**(-V(K+1))
ET((4+K),1) = (Z3(K+1) - Z3(K)) * RO(K)
BC((3+J+K),1) = CB13(K)+Z6(K)*Z1(K)-CB13(K+1)-Z6(K+1)*Z1(K+1)

```

```

BC((3+J+K),2) = ((Z6(K) + CB33(K))*Z2(K) + CB36(K) - (Z6(K+1)
$          + CB33(K+1))*Z2(K+1) - CB36(K+1)) * RO(K)
BC((3+J+K),(1+2*K)) = (CB23(K) + V(K)*CB33(K)) * RO(K)**(-V2(K))
BC((3+J+K),(2+2*K)) = (CB23(K) - V(K)*CB33(K)) * RO(K)**(-V1(K))
BC((3+J+K),(3+2*K)) = -(CB23(K+1) + V(K+1)*CB33(K+1)) *
$          RO(K)**(-V2(K+1))
BC((3+J+K),(4+2*K)) = -(CB23(K+1) - V(K+1)*CB33(K+1)) *
$          RO(K)**(-V1(K+1))
40 ET((3+J+K),1) = DT * (CB13(K)*ALPAX(K) - CB13(K+1)*ALPAX(K+1) +
$          CB23(K)*ALPA0(K) - CB23(K+1)*ALPA0(K+1) +
$          CB33(K)*ALPAR(K) - CB33(K+1)*ALPAR(K+1) +
$          CB36(K)*ALPAX0(K) - CB36(K+1)*ALPAX0(K+1)) -
$          Z6(K)*Z3(K) + Z6(K+1)*Z3(K+1)
C
WRITE(6,19)
19 FORMAT('PLY    LAMBDA'//)
DO 52 I=1,J
WRITE(6,20) I, V(I)
52 CONTINUE
20 FORMAT(I2,D16.8)
WRITE(6,22)
22 FORMAT(//'BC(I,J)    EPS-0    GAM-0    A(1 THRU 2J)'//)
DO 35 K9=1,2*J+2
WRITE(6,45) (BC(K9,L9),L9=1,(2*J+2))
35 CONTINUE
45 FORMAT(6D16.8)
WRITE(6,32)
32 FORMAT(//'ET(I,1)'//)
WRITE(6,42) (ET(K8,1),K8=1,(2*J+2))
42 FORMAT(D16.8)
C
C SOLVE BC*X=ET USING GASJON (REDDY)
C
CALL GASJON (2*J+2,BC,32,ET,32)
C
CALL OUTPUT
C
CALL RESLTN
C
C
C SUBROUTINE FAIL ONLY WORKS FOR LAMINATES OF ONE MATERIAL
C
C READ FLAG  0 = NO FAILURE CRITERIA ; 1 = TSAI-WU; INPUT FI & FIJ
C
READ(5,*) FL
IF (FL.EQ.0) GOTO 101
CALL FAIL (FL,J)
101 CONTINUE
C
STOP

```

```

END
C
C
C
SUBROUTINE INPUT
C
  IMPLICIT REAL*8 (A-H,M-Z)
  COMMON /IN/ ANGLE(15),T(15),CB11(15),CB12(15),CB13(15),CB16(15),
$   CB22(15),CB23(15),CB26(15),CB33(15),CB36(15),CB66(15),RO(15),
$   RI(15),ALPAX(15),ALPA0(15),ALPAR(15),ALPAX0(15),DT,P,TW,J
  DIMENSION E1(15),E2(15),E3(15),G12(15),NU23(15),NU32(15),NU13(15),
$   NU31(15),NU12(15),NU21(15),ALPA1(15),ALPA2(15),ALPA3(15),
$   C11(15),C12(15),C13(15),C22(15),C23(15),C33(15),C66(15),
$   B11(15),B12(15),B13(15),B22(15),B23(15),B33(15),B66(15),
$   THETA(15),ALFA1(15),ALFA2(15),ALFA3(15),KMAT(15)
  PI = 3.14159265
C
C MATERIAL PROPERTIES
C
  READ(5,*) J, JMAT, RI(1), DT, P, TW
  WRITE(6,15)
15  FORMAT(////'MATERIAL PROPERTIES'//'MATL',6X,'E1',10X,'E2',10X,
$   'E3',10X,'G12',5X,'NU23',4X,'NU13',4X,'NU12',4X,'ALPHA 1',
$   5X,'ALPHA 2',5X,'ALPHA 3'/)
30  FORMAT(I3,4D12.4,3F8.4,3D12.4)
  DO 20 I=1,JMAT
  READ(5,*) E1(I), E2(I), E3(I), G12(I), NU23(I), NU13(I),
$   NU12(I), ALPA1(I), ALPA2(I), ALPA3(I)
  WRITE(6,30) I,E1(I),E2(I),E3(I),G12(I),NU23(I),NU13(I),NU12(I),
$   ALPA1(I),ALPA2(I),ALPA3(I)
C
  NU32(I) = NU23(I) * E3(I) / E2(I)
  NU31(I) = NU13(I) * E3(I) / E1(I)
  NU21(I) = NU12(I) * E2(I) / E1(I)
  Z1 = (1. - NU23(I)*NU32(I) - NU13(I)*NU31(I) - NU12(I)*NU21(I)
$   - 2*NU32(I)*NU13(I)*NU21(I)) / (E1(I)*E2(I)*E3(I))
  C11(I) = (1. - NU23(I)*NU32(I)) / (E2(I)*E3(I)*Z1)
  C12(I) = (NU12(I) + NU32(I)*NU13(I)) / (E1(I)*E3(I)*Z1)
  C13(I) = (NU13(I) + NU12(I)*NU23(I)) / (E1(I)*E2(I)*Z1)
  C22(I) = (1. - NU13(I)*NU31(I)) / (E1(I)*E3(I)*Z1)
  C23(I) = (NU23(I) + NU21(I)*NU13(I)) / (E1(I)*E2(I)*Z1)
  C33(I) = (1. - NU12(I)*NU21(I)) / (E1(I)*E2(I)*Z1)
20  C66(I) = G12(I)
  DO 22 K=1,JMAT
  WRITE(6,23) K,C11(K),C12(K),C13(K),C22(K),C23(K),C33(K),C66(K)
22  CONTINUE
23  FORMAT('/C MATRIX FOR MATL',I2//3D16.8/16X,2D16.8/32X,D16.8/
$   48X,D16.8/)
  WRITE(6,25)
25  FORMAT('LAYER PROPERTIES'//'PLY MATL PHI THICKNESS RI',6X,

```

```

$      'RO' /)
DO 21 I=1,J
READ(5,*) KMAT(I),T(I),ANGLE(I)
IF (I.EQ.1) GO TO 40
RI(I) = RO(I-1)
40  RO(I) = RI(I) + T(I)
    B11(I) = C11(KMAT(I))
    B12(I) = C12(KMAT(I))
    B13(I) = C13(KMAT(I))
    B22(I) = C22(KMAT(I))
    B23(I) = C23(KMAT(I))
    B33(I) = C33(KMAT(I))
    B66(I) = C66(KMAT(I))
    ALFA1(I) = ALPA1(KMAT(I))
    ALFA2(I) = ALPA2(KMAT(I))
    ALFA3(I) = ALPA3(KMAT(I))
    THETA(I) = ANGLE(I) * PI / 180.
    TAYTA = THETA(I)
    M = DCOS (TAYTA)
    N = DSIN (TAYTA)
    Z2 = B12(I) + 2*B66(I)
    CB11(I) = B11(I)*M**4 + 2*M**2*N**2*Z2 + B22(I)*N**4
    CB12(I) = (B11(I) + B22(I) - 4*B66(I))*M**2*N**2 + (N**4 +
$      M**4)*B12(I)
    CB13(I) = M**2*B13(I) + N**2*B23(I)
    CB22(I) = B11(I)*N**4 + 2*M**2*N**2*Z2 + B22(I)*M**4
    CB23(I) = B13(I)*N**2 + B23(I)*M**2
    CB33(I) = B33(I)
    CB16(I) = ((B11(I) - Z2)*M**2 + (Z2 - B22(I))*N**2) * M * N
    CB26(I) = ((B11(I) - Z2)*N**2 + (Z2 - B22(I))*M**2) * M * N
    CB36(I) = (B13(I) - B23(I)) * M * N
    CB66(I) = M**2*N**2*(B11(I)-2*B12(I)+B22(I)) + B66(I)*(M*M-N*N)**2
    ALPAX(I) = ALFA1(I)*M**2 + ALFA2(I)*N**2
    ALPA0(I) = ALFA1(I)*N**2 + ALFA2(I)*M**2
    ALPAR(I) = ALFA3(I)
    ALPAX0(I) = 2*N*M*(ALFA1(I) - ALFA2(I))
    WRITE(6,45) I,KMAT(I),ANGLE(I),T(I),RI(I),RO(I)
21  CONTINUE
45  FORMAT(I2,I5,F7.0,2X,3F8.5)
    WRITE(6,46)
46  FORMAT(//' PLY',26X,'CBAR MATRIX'//)
    DO 32 I=1,J
    WRITE(6,50) I,CB11(I),CB12(I),CB13(I),CB16(I),CB22(I),CB23(I),
$      CB26(I),CB33(I),CB36(I),CB66(I)
32  CONTINUE
50  FORMAT(I2,3X,4D16.8/21X,3D16.8/37X,2D16.8/53X,D16.8/)
    WRITE(6,52)
52  FORMAT('/ PLY',5X,'ALPHA-X',7X,'ALPHA-THETA',7X,'ALPHA-R'
$      ,5X,'ALPHA-X,THETA'//)
    DO 33 I=1,J

```

```

WRITE(6,51) I,ALPAX(I),ALPAO(I),ALPAR(I),ALPAXO(I)
33 CONTINUE
51 FORMAT(I2,4D16.8)
WRITE(6,60) DT,P,TW
60 FORMAT('/DELTA-TEMPERATURE LOAD =',F5.0,' F'// 'AXIAL LOAD=',
$ D14.8,' LB'// 'TORSION =',D14.8,' IN-LB'/)
RETURN
END

C
C
C

SUBROUTINE OUTPUT
IMPLICIT REAL*8 (A-H,M-Z)
COMMON /IN/ ANGLE(15),T(15),CB11(15),CB12(15),CB13(15),CB16(15),
$ CB22(15),CB23(15),CB26(15),CB33(15),CB36(15),CB66(15),RO(15),
$ RI(15),ALPAX(15),ALPAO(15),ALPAR(15),ALPAXO(15),DT,P,TW,J
COMMON /SOLN/BC(32,32),ET(32,1),V(15),V1(15),V2(15),V3(15),V4(15),
$ Z1(15),Z2(15),Z3(15),Z4(15),Z5(15),Z6(15),Z7(15)
COMMON/OUT/ R(150),EPSX(10,15),EPSO(10,15),EPSR(10,15),
$ GAMXO(10,15),SIGX(10,15),SIGO(10,15),SIGR(10,15),TAUXO(10,15),
$ EPS1(10,15),EPS2(10,15),EPS3(10,15),GAM12(10,15),
$ SIG1(10,15),SIG2(10,15),SIG3(10,15),TAU12(10,15),
$ RR(10,15)
DIMENSION EMX(10,15),EMO(10,15),EMR(10,15),EMXO(10,15)
PI = 3.14159265
WRITE(6,10) (ET(I1,1),I1=1,(2*J+2))
10 FORMAT('//ELASTICITY CONSTANTS'//
$ 'EPSILON-0 = ',D14.8// 'GAMMA-0 = ',D14.8//7X,'A1',16X,
$ 'A2'/8(2D16.8/))
DO 20 L=1,J
TAYTA = ANGLE(L) * PI / 180.
M = DCOS(TAYTA)
N = DSIN(TAYTA)
T9 = T(L)/9
DO 20 K=1,10
R(K) = RI(L) + (K-1)*T9
EPSX(K,L) = ET(1,1)
EPSO(K,L) = Z1(L)*ET(1,1) + Z2(L)*ET(2,1)*R(K) + Z3(L) +
$ ET((1+2*L),1)*R(K)**(-V2(L)) + ET((2+2*L),1)*
$ R(K)**(-V1(L))
EPSR(K,L) = Z1(L)*ET(1,1) + 2*Z2(L)*ET(2,1)*R(K) + Z3(L) +
$ ET((1+2*L),1)*V(L)*R(K)**(-V2(L)) - ET((2+2*L),1)*
$ V(L)*R(K)**(-V1(L))
GAMXO(K,L) = ET(2,1)*R(K)
EA1 = ET(1,1) - ALPAX(L)*DT
EA2 = EPSO(K,L) - ALPAO(L)*DT
EA3 = EPSR(K,L) - ALPAR(L)*DT
EA4 = GAMXO(K,L) - ALPAXO(L)*DT
EMX(K,L) = EA1
EMO(K,L) = EA2

```

```

EMR(K,L) = EA3
EMX0(K,L) = EA4
SIGX(K,L) = CB11(L)*EA1+CB12(L)*EA2+CB13(L)*EA3+CB16(L)*EA4
SIG0(K,L) = CB12(L)*EA1+CB22(L)*EA2+CB23(L)*EA3+CB26(L)*EA4
SIGR(K,L) = CB13(L)*EA1+CB23(L)*EA2+CB33(L)*EA3+CB36(L)*EA4
TAUX0(K,L) = CB16(L)*EA1+CB26(L)*EA2+CB36(L)*EA3+CB66(L)*EA4
EPS1(K,L) = EPSX(K,L)*M*M + EPS0(K,L)*N*N + GAMX0(K,L)*M*N
EPS2(K,L) = EPSX(K,L)*N*N + EPS0(K,L)*M*M - GAMX0(K,L)*M*N
EPS3(K,L) = EPSR(K,L)
GAM12(K,L) = -EPSX(K,L)*2*M*N + EPS0(K,L)*2*M*N + GAMX0(K,L)
$
          *(M*M -N*N)
SIG1(K,L) = SIGX(K,L)*M*M + SIG0(K,L)*N*N + TAUX0(K,L)*2*M*N
SIG2(K,L) = SIGX(K,L)*N*N + SIG0(K,L)*M*M - TAUX0(K,L)*2*M*N
SIG3(K,L) = SIGR(K,L)
TAU12(K,L) = -SIGX(K,L)*M*N + SIG0(K,L)*M*N + TAUX0(K,L)
$
          *(M*M -N*N)
20  CONTINUE
    WRITE (6,30)
30  FORMAT (/'TOTAL STRAINS IN X-Y SYSTEM...LAYER...PHI...R/R...'
$      , 'EPS-X...EPS-THETA...EPS-R...GAMMA-X,THETA'//)
50  FORMAT(I2,F5.0,F8.5,4D15.7)
    DO 40 L=1,J
    DO 40 K=1,10
    R(K) = RI(L) + (K-1)*T(L)/9
    RR(K,L) = (R(K)-RI(1))/(RO(J)-RI(1))
    WRITE (6,50) L,ANGLE(L),RR(K,L),EPSX(K,L),EPS0(K,L),EPSR(K,L),
$      GAMX0(K,L)
40  CONTINUE
    WRITE (6,31)
31  FORMAT (/'MECHANICAL STRAINS IN X-Y SYSTEM...LAYER...PHI...R/R'
$      , '...EPS-X...EPS-THETA...EPS-R...GAMMA-X,THETA'//)
    DO 41 L=1,J
    DO 41 K=1,10
    R(K) = RI(L) + (K-1)*T(L)/9
    RR(K,L) = (R(K)-RI(1))/(RO(J)-RI(1))
    WRITE (6,50) L,ANGLE(L),RR(K,L),EMX(K,L),EMO(K,L),EMR(K,L),
$      EMX0(K,L)
41  CONTINUE
    WRITE (6,60)
60  FORMAT (/'STRESSES IN X-Y SYSTEM...LAYER...PHI...R/R...'
$      , 'SIG-X...SIG-THETA...SIG-R...TAU-X,THETA'//)
    DO 70 L=1,J
    DO 70 K=1,10
    WRITE (6,50) L,ANGLE(L),RR(K,L),SIGX(K,L),SIG0(K,L),SIGR(K,L),
$      TAUX0(K,L)
70  CONTINUE
    WRITE (6,90)
90  FORMAT (/'TOTAL STRAINS IN 1-2 SYSTEM...LAYER...PHI...R/R...'
$      , 'EPS-1...EPS-2...EPS-3...GAMMA-1,2'//)
    DO 100 L=1,J

```

```

DO 100 K=1,10
WRITE (6,50) L,ANGLE(L),RR(K,L),EPS1(K,L),EPS2(K,L),EPS3(K,L),
$          GAM12(K,L)
100 CONTINUE
WRITE (6,120)
120 FORMAT (/'STRESSES IN 1-2 SYSTEM...LAYER...PHI...R/R...',
$          'SIG-1...SIG-2...SIG-3...TAU-1,2'//)
DO 130 L=1,J
DO 130 K=1,10
WRITE (6,50) L,ANGLE(L),RR(K,L),SIG1(K,L),SIG2(K,L),SIG3(K,L),
$          TAU12(K,L)
130 CONTINUE
RETURN
END

```

C

```

SUBROUTINE GASJON (N,A,NRMAX,B,NBMAX)
IMPLICIT REAL*8(A-H,O-Z)
DIMENSION A(NRMAX,NRMAX),B(NBMAX,1),INDEX(32,2),IPVOT(32)
M=1
MM=1
1 DET=1.
DO 2 J=1,N
2 IPVOT(J)=0.
DO 14 I=1,N
T=0.
DO 5 J=1,N
IF (IPVOT(J).EQ.1) GO TO 5
DO 4 K=1,N
IF (IPVOT(K)-1) 3,4,17
3 IF (DABS(T).GE.DABS(A(J,K))) GO TO 4
IROW=J
ICOL=K
T=A(J,K)
4 CONTINUE
5 CONTINUE
IPVOT(ICOL)=IPVOT(ICOL)+1
IF (IROW.EQ.ICOL) GO TO 8
DET=-DET
DO 6 L=1,N
T=A(IROW,L)
A(IROW,L)=A(ICOL,L)
6 A(ICOL,L)=T
IF (MM.LE.0) GO TO 8
DO 7 L=1,M
T=B(IROW,L)
B(IROW,L)=B(ICOL,L)
7 B(ICOL,L)=T
8 INDEX(I,1)=IROW
INDEX(I,2)=ICOL
PIVOT=A(ICOL,ICOL)

```

```

DET=DET*PIVOT
A(ICOL,ICOL)=1.
DO 9 L=1,N
9 A(ICOL,L)=A(ICOL,L)/PIVOT
IF (MM.LE.0) GO TO 11
DO 10 L=1,M
10 B(ICOL,L)=B(ICOL,L)/PIVOT
11 DO 14 LI=1,N
IF (LI.EQ.ICOL) GO TO 14
T=A(LI,ICOL)
A(LI,ICOL)=0.
DO 12 L=1,N
12 A(LI,L)=A(LI,L)-A(ICOL,L)*T
IF (MM.LE.0) GO TO 14
DO 13 L=1,M
13 B(LI,L)=B(LI,L)-B(ICOL,L)*T
14 CONTINUE
IF (MM.EQ.1) RETURN
DO 16 I=1,N
L=N-I+1
IF (INDEX(L,1).EQ.INDEX(L,2)) GO TO 16
JROW=INDEX(L,1)
JCOL=INDEX(L,2)
DO 15 K=1,N
T=A(K,JROW)
A(K,JROW)=A(K,JCOL)
A(K,JCOL)=T
15 CONTINUE
16 CONTINUE
17 RETURN
END

```

C  
C

```

SUBROUTINE FAIL(FL,J)

```

C

```

IMPLICIT REAL*8 (A-H,M-Z)
COMMON/OUT/ R(150),EPSX(10,15),EPS0(10,15),EPSR(10,15),
$ GAMX0(10,15),SIGX(10,15),SIG0(10,15),SIGR(10,15),TAUX0(10,15),
$ EPS1(10,15),EPS2(10,15),EPS3(10,15),GAM12(10,15),
$ SIG1(10,15),SIG2(10,15),SIG3(10,15),TAU12(10,15),
$ RR(10,15)
DIMENSION TS(15),F1S1(15),F2S2(15),F2S3(15),F11S1(15),F22S2(15),
$ F22S3(15),F66S6(15),F12S12(15),F12S13(15),F23S23(15)

```

C

```

READ(5,*) F1,F2,F11,F22,F66,F12,F23
WRITE(6,45)
45 FORMAT(// 'TSAI-WU' //)
30 DO 40 I=1,J
F1S1(I) = F1 * SIG1(5,I)
F2S2(I) = F2 * SIG2(5,I)

```

```

F2S3(I) = F2 * SIG3(5,I)
F11S1(I) = F11 * SIG1(5,I)**2
F22S2(I) = F22 * SIG2(5,I)**2
F22S3(I) = F22 * SIG3(5,I)**2
F66S6(I) = F66 * TAU12(5,I)**2
F12S12(I) = F12 * SIG1(5,I)*SIG2(5,I)
F12S13(I) = F12 * SIG1(5,I)*SIG3(5,I)
F23S23(I) = F23 * SIG2(5,I)*SIG3(5,I)
40 TS(I) = F1S1(I) + F2S2(I) + F2S3(I) + F11S1(I) + F22S2(I) +
$      F22S3(I) + F66S6(I) + F12S12(I) + F12S13(I) + F23S23(I)
WRITE(6,50) F1,F2,F11,F22,F66,F12,F23
50 FORMAT(7X,'F1',14X,'F2',13X,'F11',13X,'F22',13X,'F66',13X,
$      'F12',13X,'F23'/7D16.8)
WRITE(6,65)
65 FORMAT(//'PLY',6X,'F1S1',12X,'F2S2',12X,'F2S3'/)
DO 80 I=1,J
80 WRITE(6,60) I,F1S1(I),F2S2(I),F2S3(I)
WRITE(6,110)
110 FORMAT(//'PLY',4X,'F11S1S1',9X,'F22S2S2',9X,'F22S3S3',9X,
$      'F66S6S6',9X,'F12S1S2',9X,'F12S1S3',9X,'F23S2S3'/)
DO 90 I=1,J
90 WRITE(6,60) I,F11S1(I),F22S2(I),F22S3(I),F66S6(I),F12S12(I),
$      F12S13(I),F23S23(I)
WRITE(6,120)
120 FORMAT(//'PLY...FAILURE FRACTION,TS'/)
DO 100 I=1,J
100 WRITE(6,60) I,TS(I)
60 FORMAT(I2,7D16.8)
RETURN
END

```

C

C

SUBROUTINE RESLTN

C

C THIS SUBROUTINE CALCULATES THE STRESS RESULTANTS NX, NO, NXO,  
C MX, MO, AND MXO

C

IMPLICIT REAL\*8 (A-H,M-Z)

```

COMMON /IN/ ANGLE(15),T(15),CB11(15),CB12(15),CB13(15),CB16(15),
$      CB22(15),CB23(15),CB26(15),CB33(15),CB36(15),CB66(15),RO(15),
$      RI(15),ALPAX(15),ALPA0(15),ALPAR(15),ALPAX0(15),DT,P,TW,J
COMMON /SOLN/BC(32,32),ET(32,1),V(15),V1(15),V2(15),V3(15),V4(15),
$      Z1(15),Z2(15),Z3(15),Z4(15),Z5(15),Z6(15),Z7(15)

```

C

PI = 3.1415927

NX1 = 0.

NX2 = 0.

NX3 = 0.

NX4 = 0.

NX5 = 0.

```

N01 = 0.
N02 = 0.
N03 = 0.
N04 = 0.
N05 = 0.
NX01 = 0.
NX02 = 0.
NX03 = 0.
NX04 = 0.
NX05 = 0.
MX1 = 0.
MX2 = 0.
MX3 = 0.
MX4 = 0.
MX5 = 0.
M01 = 0.
M02 = 0.
M03 = 0.
M04 = 0.
M05 = 0.
MX01 = 0.
MX02 = 0.
MX03 = 0.
MX04 = 0.
MX05 = 0.
RM = (RO(J) + RI(1))/2.
DO 107 I=1,J
NX1 = NX1 + (CB11(I) + Z1(I)*Z4(I))*(RO(I)**2 - RI(I)**2)/2.
NX2 = NX2 + ((CB13(I) + Z4(I))*Z2(I) + CB16(I))*(RO(I)**3
$ - RI(I)**3)/3.
NX3 = NX3 + (CB12(I) + V(I)*CB13(I))*(RO(I)**V1(I) -
$ RI(I)**V1(I))*ET(2*I+1,1)/V1(I)
NX4 = NX4 + (CB12(I) - V(I)*CB13(I))*(RO(I)**V2(I) -
$ RI(I)**V2(I))*ET(2*I+2,1)/V2(I)
NX5 = NX5 + (DT*(CB11(I)*ALPAX(I) + CB12(I)*ALPA0(I) + CB13(I)*
$ ALPAR(I) + CB16(I)*ALPAX0(I)) - Z3(I)*Z4(I))*
$ (RO(I)**2 - RI(I)**2)/2.
N01 = N01 + (CB12(I) + Z7(I)*Z1(I))*(RO(I)-RI(I))
N02 = N02 + ((CB23(I) + Z7(I))*Z2(I) + CB26(I))*(RO(I)**2
$ - RI(I)**2)/2.
N03 = N03 + (CB22(I) + V(I)*CB23(I))*(RO(I)**V(I) -
$ RI(I)**V(I))*ET(2*I+1,1)/V(I)
N04 = N04 + (CB22(I) - V(I)*CB23(I))*(RO(I)**(-V(I)) -
$ RI(I)**(-V(I)))*ET(2*I+2,1)/(-V(I))
N05 = N05 + (DT*(CB12(I)*ALPAX(I) + CB22(I)*ALPA0(I) + CB23(I)*
$ ALPAR(I) + CB26(I)*ALPAX0(I)) - Z3(I)*Z7(I))*(RO(I) - RI(I))
NX01 = NX01 + (CB16(I) + Z5(I)*Z1(I))*(RO(I)**2 -
$ RI(I)**2)/2.
NX02 = NX02 + ((CB36(I) + Z5(I))*Z2(I) + CB66(I))*(RO(I)**3
$ - RI(I)**3)/3.

```

```

NX03 = NX03 + (CB26(I) + V(I)*CB36(I))*(RO(I)**V1(I) -
$   RI(I)**V1(I))*ET(2*I+1,1)/V1(I)
NX04 = NX04 + (CB26(I) - V(I)*CB36(I))*(RO(I)**V2(I) -
$   RI(I)**V2(I))*ET(2*I+2,1)/V2(I)
NX05 = NX05 + (DT*(CB16(I)*ALPAX(I) + CB26(I)*ALPA0(I) + CB36(I)*
$   ALPAR(I) + CB66(I)*ALPAX0(I)) - Z3(I)*Z5(I))*
$   (RO(I)**2 - RI(I)**2)/2.
MX1 = MX1 + (CB11(I) + Z4(I)*Z1(I))*(RO(I)**3 -
$   RI(I)**3)/3.
MX2 = MX2 + ((CB13(I) + Z4(I))*Z2(I) + CB16(I))*(RO(I)**4
$   - RI(I)**4)/4.
MX3 = MX3 + (CB12(I) + V(I)*CB13(I))*(RO(I)**V3(I) -
$   RI(I)**V3(I))*ET(2*I+1,1)/V3(I)
MX4 = MX4 + (CB12(I) - V(I)*CB13(I))*(RO(I)**V4(I) -
$   RI(I)**V4(I))*ET(2*I+2,1)/V4(I)
MX5 = MX5 + (DT*(CB11(I)*ALPAX(I) + CB12(I)*ALPA0(I) + CB13(I)*
$   ALPAR(I) + CB16(I)*ALPAX0(I)) - Z3(I)*Z4(I))*
$   (RO(I)**3 - RI(I)**3)/3.
M01 = M01 + (CB12(I) + Z7(I)*Z1(I))*(RO(I)**2 -
$   RI(I)**2)/2.
M02 = M02 + ((CB23(I) + Z7(I))*Z2(I) + CB26(I))*(RO(I)**3
$   - RI(I)**3)/3.
M03 = M03 + (CB22(I) + V(I)*CB23(I))*(RO(I)**V1(I) -
$   RI(I)**V1(I))*ET(2*I+1,1)/V1(I)
M04 = M04 + (CB22(I) - V(I)*CB23(I))*(RO(I)**V2(I) -
$   RI(I)**V2(I))*ET(2*I+2,1)/V2(I)
M05 = M05 + (DT*(CB12(I)*ALPAX(I) + CB22(I)*ALPA0(I) + CB23(I)*
$   ALPAR(I) + CB26(I)*ALPAX0(I)) - Z3(I)*Z7(I))*
$   (RO(I)**2 - RI(I)**2)/2.
MX01 = MX01 + (CB16(I) + Z5(I)*Z1(I))*(RO(I)**3 -
$   RI(I)**3)/3.
MX02 = MX02 + ((CB36(I) + Z5(I))*Z2(I) + CB66(I))*(RO(I)**4
$   - RI(I)**4)/4.
MX03 = MX03 + (CB26(I) + V(I)*CB36(I))*(RO(I)**V3(I) -
$   RI(I)**V3(I))*ET(2*I+1,1)/V3(I)
MX04 = MX04 + (CB26(I) - V(I)*CB36(I))*(RO(I)**V4(I) -
$   RI(I)**V4(I))*ET(2*I+2,1)/V4(I)
107 MX05 = MX05 + (DT*(CB16(I)*ALPAX(I) + CB26(I)*ALPA0(I) + CB36(I)*
$   ALPAR(I) + CB66(I)*ALPAX0(I)) - Z3(I)*Z5(I))*
$   (RO(I)**3 - RI(I)**3)/3.
NX = (NX1*ET(1,1) + NX2*ET(2,1) + NX3 + NX4 - NX5)/RM
NO = (NO1*ET(1,1) + NO2*ET(2,1) + NO3 + NO4 - NO5)
NX0 = (NX01*ET(1,1) + NX02*ET(2,1) + NX03 + NX04 - NX05)/RM
MX = (MX1*ET(1,1) + MX2*ET(2,1) + MX3 + MX4 - MX5)/RM - NX*RM
MO = (M01*ET(1,1) + M02*ET(2,1) + M03 + M04 - M05) - NO*RM
MX0 = (MX01*ET(1,1)+MX02*ET(2,1)+MX03+MX04-MX05)/RM - NX0*RM
WRITE(6,106)
106 FORMAT(// 'STRESS RESULTANTS' /)
WRITE(6,108) NX,NO,NX0,MX,MO,MX0
108 FORMAT(7X, 'NX',14X, 'NO',14X, 'NX0',3D16.8/3D16.8/7X, 'MX',14X, 'MO',

```

```
$      14X, 'MXO' //)  
RETURN  
END
```

```

C
C ELAST1
C
C ELASTICITY SOLUTION FOR AN ANGLE-PLY COMPOSITE TUBE W/THERMAL
C AND MECHANICAL LOADS
C INCLUDES TEMPERATURE-DEPENDENT MATERIAL PROPERTIES
C ASSUMES 350 F-CURE RESIN SYSTEM
C
C CARL ROUSSEAU AND DR. MIKE HYER
C ESM DEPT.
C VIRGINIA TECH
C
      IMPLICIT REAL*8 (A-H,M-Z)
      COMMON /IN/ ANGLE(30),T(30),CB11(30),CB12(30),CB13(30),CB16(30),
$      CB22(30),CB23(30),CB26(30),CB33(30),CB36(30),CB66(30),RO(30),
$      RI(30),EPSTX(30),EPSTO(30),EPSTR(30),EPSTXO(30),DT,P,TW,J
      COMMON/SOLN/BC(62,62),ET(62,1),V(30),V1(30),V2(30),V3(30),V4(30),
$      Z1(30),Z2(30),Z3(30),Z4(30),Z5(30),Z6(30),Z7(30)
      COMMON/OUT/ R(300),EPSX(10,30),EPSO(10,30),EPSR(10,30),
$      GAMXO(10,30),SIGX(10,30),SIGO(10,30),SIGR(10,30),TAUXO(10,30),
$      EPS1(10,30),EPS2(10,30),EPS3(10,30),GAM12(10,30),
$      SIG1(10,30),SIG2(10,30),SIG3(10,30),TAU12(10,30),
$      RR(10,30)
      DIMENSION SIGB(30),ZZ(30)
      PI = 3.1415927
C
      CALL INPUT
C
      DO 10 I=1,J
C
      SIGB(I) = (CB23(I) - CB22(I))*EPSTO(I) + (CB33(I) - CB23(I))*
$      EPSTR(I) + (CB13(I) - CB12(I))*EPSTX(I) + (CB36(I) -
$      CB26(I))*EPSTXO(I)
      V(I) = DSQRT (CB22(I) / CB33(I))
      V1(I) = 1. + V(I)
      V2(I) = 1. - V(I)
      V3(I) = 2. + V(I)
      V4(I) = 2. - V(I)
      ZZ(I) = CB33(I) - CB22(I)
      Z1(I) = (CB12(I) - CB13(I)) / ZZ(I)
      Z2(I) = (CB26(I) - 2*CB36(I)) / (3*CB33(I) + ZZ(I))
      Z3(I) = SIGB(I) / ZZ(I)
      Z4(I) = CB12(I) + CB13(I)
      Z5(I) = CB26(I) + CB36(I)
      Z6(I) = CB23(I) + CB33(I)
10     Z7(I) = CB22(I) + CB23(I)
C
      BC(1,1) = CB13(1) + Z6(1)*Z1(1)
      BC(1,2) = ((Z6(1) + CB33(1))*Z2(1) + CB36(1)) * RI(1)
      BC(1,3) = (CB23(1) + V(1)*CB33(1)) * RI(1)**(-V2(1))

```

```

BC(1,4) = (CB23(1) - V(1)*CB33(1)) * RI(1)**(-V1(1))
ET(1,1) = CB13(1)*EPSTX(1) + CB23(1)*EPSTO(1) + CB33(1)*EPSTR(1)
$      + CB36(1)*EPSTX0(1) - Z6(1)*Z3(1)
DO 12 I1=5,2*J+2
BC(1,I1) = 0.
BC(2,1) = CB13(J) + Z6(J)*Z1(J)
BC(2,2) = ((Z6(J) + CB33(J))*Z2(J) + CB36(J)) * RO(J)
12 BC(2,(I1-2)) = 0.
BC(2,(2*J+1)) = (CB23(J) + V(J)*CB33(J)) * RO(J)**(-V2(J))
BC(2,(2*J+2)) = (CB23(J) - V(J)*CB33(J)) * RO(J)**(-V1(J))
ET(2,1) = CB13(J)*EPSTX(J) + CB23(J)*EPSTO(J) + CB33(J)*EPSTR(J)
$      + CB36(J)*EPSTX0(J) - Z6(J)*Z3(J)
BC(3,1) = 0.
BC(3,2) = 0.
BC(4,1) = 0.
BC(4,2) = 0.
ET(3,1) = P / 2 / PI
ET(4,1) = TW / 2 / PI
DO 30 I=1,J
BC(3,1) = BC(3,1) + (CB11(I) + Z1(I)*Z4(I)) * (RO(I)**2 -
$      RI(I)**2) / 2.
BC(3,2) = BC(3,2) + ((CB13(I) + Z4(I)) * Z2(I) + CB16(I))
$      * (RO(I)**3 - RI(I)**3) / 3.
BC(3,(1+2*I)) = (CB12(I) + V(I) * CB13(I)) * (RO(I)**V1(I) -
$      RI(I)**V1(I)) / V1(I)
BC(3,(2+2*I)) = (CB12(I) - V(I) * CB13(I)) * (RO(I)**V2(I) -
$      RI(I)**V2(I)) / V2(I)
ET(3,1) = ET(3,1) + (CB11(I)*EPSTX(I) + CB12(I)*EPSTO(I) +
$      CB13(I)*EPSTR(I) + CB16(I)*EPSTX0(I) - Z3(I)*Z4(I))*
$      (RO(I)**2 - RI(I)**2) / 2.
BC(4,1) = BC(4,1) + (CB16(I) + Z1(I)*Z5(I)) * (RO(I)**3 -
$      RI(I)**3) / 3.
BC(4,2) = BC(4,2) + (CB66(I) + Z2(I) * (Z5(I) +CB36(I)))*
$      (RO(I)**4 - RI(I)**4) / 4.
BC(4,(1+2*I)) = (CB26(I) + V(I) * CB36(I)) * (RO(I)**V3(I) -
$      RI(I)**V3(I)) / V3(I)
BC(4,(2+2*I)) = (CB26(I) - V(I) * CB36(I)) * (RO(I)**V4(I) -
$      RI(I)**V4(I)) / V4(I)
30 ET(4,1) = ET(4,1) + (CB16(I)*EPSTX(I) + CB26(I)*EPSTO(I) +
$      CB36(I)*EPSTR(I) + CB66(I)*EPSTX0(I) - Z3(I)*Z5(I))*
$      (RO(I)**3 - RI(I)**3) / 3.
DO 34 KK=5,2*J+2
DO 34 LL=1,2*J+2
34 BC(KK,LL) = 0.
DO 40 K=1,J-1
BC((4+K),1) = (Z1(K) - Z1(K+1)) * RO(K)
BC((4+K),2) = (Z2(K) - Z2(K+1)) * RO(K)**2
BC((4+K),(1+2*K)) = RO(K)**V(K)
BC((4+K),(2+2*K)) = RO(K)**(-V(K))
BC((4+K),(3+2*K)) = -RO(K)**V(K+1)

```

```

BC((4+K),(4+2*K)) = -RO(K)**(-V(K+1))
ET((4+K),1) = (Z3(K+1) - Z3(K)) * RO(K)
BC((3+J+K),1) = CB13(K)+Z6(K)*Z1(K)-CB13(K+1)-Z6(K+1)*Z1(K+1)
BC((3+J+K),2) = ((Z6(K) + CB33(K))*Z2(K) + CB36(K) - (Z6(K+1)
$           + CB33(K+1))*Z2(K+1) - CB36(K+1)) * RO(K)
BC((3+J+K),(1+2*K)) = (CB23(K) + V(K)*CB33(K)) * RO(K)**(-V2(K))
BC((3+J+K),(2+2*K)) = (CB23(K) - V(K)*CB33(K)) * RO(K)**(-V1(K))
BC((3+J+K),(3+2*K)) = -(CB23(K+1) + V(K+1)*CB33(K+1)) *
$           RO(K)**(-V2(K+1))
BC((3+J+K),(4+2*K)) = -(CB23(K+1) - V(K+1)*CB33(K+1)) *
$           RO(K)**(-V1(K+1))
40 ET((3+J+K),1) = CB13(K)*EPSTX(K) - CB13(K+1)*EPSTX(K+1) +
$           CB23(K)*EPSTO(K) - CB23(K+1)*EPSTO(K+1) +
$           CB33(K)*EPSTR(K) - CB33(K+1)*EPSTR(K+1) +
$           CB36(K)*EPSTX0(K) - CB36(K+1)*EPSTX0(K+1) -
$           Z6(K)*Z3(K) + Z6(K+1)*Z3(K+1)
C
  WRITE(6,19)
19  FORMAT(1X,'PLY   LAMBDA'//)
  DO 52 I=1,J
  WRITE(6,20) I, V(I)
52  CONTINUE
20  FORMAT(1X,I3,D16.8)
  WRITE(6,22)
22  FORMAT(//1X,'BC(I,J)   EPS-0   GAM-0   A(1 THRU 2J)'//)
  DO 35 K9=1,2*J+2
  WRITE(6,45) (BC(K9,L9),L9=1,(2*J+2))
35  CONTINUE
45  FORMAT(6D16.8)
  WRITE(6,32)
32  FORMAT(//1X,'ET(I,1)'//)
  WRITE(6,42) (ET(K8,1),K8=1,(2*J+2))
42  FORMAT(1X,D16.8)
C
C  SOLVE BC*X=ET USING GASJON (REDDY)
C
  CALL GASJON (2*J+2,BC,62,ET,62)
C
  CALL OUTPUT
C
  CALL RESLTN
C
C
C  SUBROUTINE FAIL ONLY WORKS FOR LAMINATES OF ONE MATERIAL
C
C  READ FLAG 0 = NO FAILURE CRITERIA ; 1 = TSAI-WU;INPUT FI & FIJ
C
  READ(5,*) FL
  IF (FL.EQ.0) GOTO 101

```

```

CALL FAIL (FL,J)
101 CONTINUE
C
STOP
END
C
C
C
SUBROUTINE INPUT
C
IMPLICIT REAL*8 (A-H,M-Z)
COMMON /IN/ ANGLE(30),T(30),CB11(30),CB12(30),CB13(30),CB16(30),
$ CB22(30),CB23(30),CB26(30),CB33(30),CB36(30),CB66(30),RO(30),
$ RI(30),EPSTX(30),EPSTO(30),EPSTR(30),EPSTXO(30),DT,P,TW,J
DIMENSION S(4,4),A(7,3),EPST1(30),EPST2(30),EPST3(30),
$ C11(30),C12(30),C13(30),C22(30),C23(30),C33(30),
$ C66(30),B11(30),B12(30),B13(30),B22(30),B23(30),B33(30),
$ B66(30),THETA(30),EPS1T(30),EPS2T(30),EPS3T(30),KMAT(30)
PI = 3.14159265
C
C MATERIAL PROPERTIES
C
WRITE(6,1)
1 FORMAT('C')
READ(5,*) J, JMAT, RI(1), TF, P, TW
WRITE(6,15)
15 FORMAT('//1X,'MATERIAL PROPERTIES'/1X,'-----')
DT = TF - 350.
DO 20 I=1,JMAT
K1 = 0
DO 19 K=1,4
DO 19 L=1,4
S(K,L) = 0.
19 CONTINUE
READ(5,*) ((A(K,L),L=1,3),K=1,7)
DO 22 I1=1,3
DO 22 J1=I1,3
K1 = K1 + 1
S(I1,J1) = A(K1,1) + A(K1,2)*TF + A(K1,3)*TF*TF
S(J1,I1) = S(I1,J1)
22 CONTINUE
S(4,4) = A(7,1) + A(7,2)*TF + A(7,3)*TF*TF
READ(5,*) A11,A12,A13,A14,A21,A22,A23,A24,A31,A32,A33,A34
EPST1(I) = A11 + A12*TF + A13*TF*TF + A14*TF**3
EPST2(I) = A21 + A22*TF + A23*TF*TF + A24*TF**3
EPST3(I) = A31 + A32*TF + A33*TF*TF + A34*TF**3
WRITE(6,12) I
WRITE(6,14)
WRITE(6,10) ((A(K,L),L=1,3),K=1,7)
WRITE(6,11) A11,A12,A13,A14,A21,A22,A23,A24,A31,A32,A33,A34

```

```

WRITE(6,16)
WRITE(6,17) ((S(K,L),L=1,4),K=1,4)
C INVERT THE S MATRIX
SD = S(1,1)*S(2,2)*S(3,3) - S(1,1)*S(2,3)*S(2,3) -
$ S(2,2)*S(1,3)*S(1,3) - S(3,3)*S(1,2)*S(1,2) +
$ 2*S(2,3)*S(1,3)*S(1,2)
C11(I) = (S(2,2)*S(3,3) - S(2,3)*S(2,3)) / SD
C12(I) = (S(1,3)*S(2,3) - S(1,2)*S(3,3)) / SD
C13(I) = (S(1,2)*S(2,3) - S(1,3)*S(2,2)) / SD
C22(I) = (S(3,3)*S(1,1) - S(1,3)*S(1,3)) / SD
C23(I) = (S(1,2)*S(1,3) - S(2,3)*S(1,1)) / SD
C33(I) = (S(1,1)*S(2,2) - S(1,2)*S(1,2)) / SD
C66(I) = 1./S(4,4)
WRITE(6,18) C11(I),C12(I),C13(I),C22(I),C23(I),C33(I),C66(I)
WRITE(6,30) EPST1(I),EPST2(I),EPST3(I)
20 CONTINUE
12 FORMAT(//1X,'***** MATERIAL',I3,'*****'//)
14 FORMAT(1X,'POLYNOMIAL COEFFICIENTS'//)
10 FORMAT(1X,3D16.8)
11 FORMAT(1X,4D16.8)
16 FORMAT(/1X,'COMPLIANCE MATRIX'//)
17 FORMAT(1X,4D16.8)
18 FORMAT(/1X,'STIFFNESS MATRIX'//1X,3D16.8/17X,2D16.8/33X,D16.8/
$ 49X,D16.8)
30 FORMAT(//1X,'THERMAL STRAINS'//4X,'EPSILON-T,1',5X,
$ 'EPSILON-T,2',5X,'EPSILON-T,3'//1X,3D16.8)
WRITE(6,25)
25 FORMAT(///1X,'LAYER PROPERTIES'//1X,'PLY MATL PHI THICKNESS',
$ 3X,'RI',6X,'RO'//)
DO 21 I=1,J
READ(5,*) KMAT(I),T(I),ANGLE(I)
IF (I.EQ.1) GO TO 40
RI(I) = RO(I-1)
40 RO(I) = RI(I) + T(I)
B11(I) = C11(KMAT(I))
B12(I) = C12(KMAT(I))
B13(I) = C13(KMAT(I))
B22(I) = C22(KMAT(I))
B23(I) = C23(KMAT(I))
B33(I) = C33(KMAT(I))
B66(I) = C66(KMAT(I))
EPS1T(I) = EPST1(KMAT(I))
EPS2T(I) = EPST2(KMAT(I))
EPS3T(I) = EPST3(KMAT(I))
THETA(I) = ANGLE(I) * PI / 180.
TAYTA = THETA(I)
M = DCOS (TAYTA)
N = DSIN (TAYTA)
Z2 = B12(I) + 2*B66(I)
CB11(I) = B11(I)*M**4 + 2*M**2*N**2*Z2 + B22(I)*N**4

```

```

CB12(I) = (B11(I) + B22(I) - 4*B66(I))*M**2*N**2 + (N**4 +
$      M**4)*B12(I)
CB13(I) = M**2*B13(I) + N**2*B23(I)
CB22(I) = B11(I)*N**4 + 2*M**2*N**2*Z2 + B22(I)*M**4
CB23(I) = B13(I)*N**2 + B23(I)*M**2
CB33(I) = B33(I)
CB16(I) = ((B11(I) - Z2)*M**2 + (Z2 - B22(I))*N**2) * M * N
CB26(I) = ((B11(I) - Z2)*N**2 + (Z2 - B22(I))*M**2) * M * N
CB36(I) = (B13(I) - B23(I)) * M * N
CB66(I) = M**2*N**2*(B11(I)-2*B12(I)+B22(I)) + B66(I)*(M*M-N*N)**2
EPSTX(I) = EPS1T(I)*M**2 + EPS2T(I)*N**2
EPSTO(I) = EPS1T(I)*N**2 + EPS2T(I)*M**2
EPSTR(I) = EPS3T(I)
EPSTXO(I) = 2*N*M*(EPS1T(I) - EPS2T(I))
WRITE(6,45) I,KMAT(I),ANGLE(I),T(I),RI(I),RO(I)
21 CONTINUE
45 FORMAT(1X,I3,I5,F7.0,2X,3F8.5)
WRITE(6,46)
46 FORMAT(/1X,'PLY',27X,'CBAR MATRIX'//)
DO 32 I=1,J
WRITE(6,50) I,CB11(I),CB12(I),CB13(I),CB16(I),CB22(I),CB23(I),
$      CB26(I),CB33(I),CB36(I),CB66(I)
32 CONTINUE
50 FORMAT(1X,I3,3X,4D16.8/23X,3D16.8/39X,2D16.8/55X,D16.8/)
WRITE(6,52)
52 FORMAT(/1X,'PLY',6X,'EPS-T-X',7X,'EPS-T-THETA',7X,'EPS-T-R'
$      ,5X,'EPS-T-X,THETA'//)
DO 33 I=1,J
WRITE(6,51) I,EPSTX(I),EPSTO(I),EPSTR(I),EPSTXO(I)
33 CONTINUE
51 FORMAT(1X,I3,4D16.8)
WRITE(6,60) TF,DT,P,TW
60 FORMAT(/1X,'OPERATING TEMPERATURE =',F5.0,' F'//1X,
$      'DELTA-TEMPERATURE LOAD =',F5.0,' F'//1X,'AXIAL LOAD=',
$      D14.8,' LB'//1X,'TORSION =',D14.8,' IN-LB'//)
RETURN
END

```

C  
C  
C

```

SUBROUTINE OUTPUT
IMPLICIT REAL*8 (A-H,M-Z)
COMMON /IN/ ANGLE(30),T(30),CB11(30),CB12(30),CB13(30),CB16(30),
$      CB22(30),CB23(30),CB26(30),CB33(30),CB36(30),CB66(30),RO(30),
$      RI(30),EPSTX(30),EPSTO(30),EPSTR(30),EPSTXO(30),DT,P,TW,J
COMMON/SOLN/BC(62,62),ET(62,1),V(30),V1(30),V2(30),V3(30),V4(30),
$      Z1(30),Z2(30),Z3(30),Z4(30),Z5(30),Z6(30),Z7(30)
COMMON/OUT/ R(300),EPSX(10,30),EPSO(10,30),EPSR(10,30),
$      GAMXO(10,30),SIGX(10,30),SIGO(10,30),SIGR(10,30),TAUXO(10,30),
$      EPS1(10,30),EPS2(10,30),EPS3(10,30),GAM12(10,30),

```

```

$          SIG1(10,30),SIG2(10,30),SIG3(10,30),TAU12(10,30),
$          RR(10,30)
DIMENSION EMX(10,30),EMO(10,30),EMR(10,30),EMX0(10,30)
PI = 3.14159265
WRITE(6,10) (ET(I1,1),I1=1,(2*J+2))
10  FORMAT(//1X,'ELASTICITY CONSTANTS'//1X,
$       'EPSILON-0 = ',D14.8//1X,'GAMMA-0 = ',D14.8//8X,'A1',16X,
$       'A2'/30(1X,2D16.8/))
DO 20  L=1,J
TAYTA = ANGLE(L) * PI / 180.
M = DCOS(TAYTA)
N = DSIN(TAYTA)
T9 = T(L)/9
DO 20  K=1,10
R(K) = RI(L) + (K-1)*T9
EPSX(K,L) = ET(1,1)
EPSO(K,L) = Z1(L)*ET(1,1) + Z2(L)*ET(2,1)*R(K) + Z3(L) +
$          ET((1+2*L),1)*R(K)**(-V2(L)) + ET((2+2*L),1)*
$          R(K)**(-V1(L))
EPSR(K,L) = Z1(L)*ET(1,1) + 2*Z2(L)*ET(2,1)*R(K) + Z3(L) +
$          ET((1+2*L),1)*V(L)*R(K)**(-V2(L)) - ET((2+2*L),1)*
$          V(L)*R(K)**(-V1(L))
GAMXO(K,L) = ET(2,1)*R(K)
EA1 = ET(1,1) - EPSTX(L)
EA2 = EPSO(K,L) - EPSTO(L)
EA3 = EPSR(K,L) - EPSTR(L)
EA4 = GAMXO(K,L) - EPSTXO(L)
EMX(K,L) = EA1
EMO(K,L) = EA2
EMR(K,L) = EA3
EMX0(K,L) = EA4
SIGX(K,L) = CB11(L)*EA1+CB12(L)*EA2+CB13(L)*EA3+CB16(L)*EA4
SIGO(K,L) = CB12(L)*EA1+CB22(L)*EA2+CB23(L)*EA3+CB26(L)*EA4
SIGR(K,L) = CB13(L)*EA1+CB23(L)*EA2+CB33(L)*EA3+CB36(L)*EA4
TAUXO(K,L) = CB16(L)*EA1+CB26(L)*EA2+CB36(L)*EA3+CB66(L)*EA4
EPS1(K,L) = EPSX(K,L)*M*M + EPSO(K,L)*N*N + GAMXO(K,L)*M*N
EPS2(K,L) = EPSX(K,L)*N*N + EPSO(K,L)*M*M - GAMXO(K,L)*M*N
EPS3(K,L) = EPSR(K,L)
GAM12(K,L) = -EPSX(K,L)*2*M*N + EPSO(K,L)*2*M*N + GAMXO(K,L)
$          *(M*M -N*N)
SIG1(K,L) = SIGX(K,L)*M*M + SIGO(K,L)*N*N + TAUXO(K,L)*2*M*N
SIG2(K,L) = SIGX(K,L)*N*N + SIGO(K,L)*M*M - TAUXO(K,L)*2*M*N
SIG3(K,L) = SIGR(K,L)
TAU12(K,L) = -SIGX(K,L)*M*N + SIGO(K,L)*M*N + TAUXO(K,L)
$          *(M*M -N*N)
20  CONTINUE
WRITE (6,30)
30  FORMAT (//1X,'TOTAL STRAINS IN X-Y SYSTEM...LAYER...PHI...R/R...'
$          , 'EPS-X...EPS-THETA...EPS-R...GAMMA-X,THETA'//)
50  FORMAT(1X,I3,F5.0,F8.5,4D15.7)

```

```

DO 40 L=1,J
DO 40 K=1,10
R(K) = RI(L) + (K-1)*T(L)/9
RR(K,L) = (R(K)-RI(1))/(RO(J)-RI(1))
WRITE (6,50) L,ANGLE(L),RR(K,L),EPSX(K,L),EPSO(K,L),EPSR(K,L),
$          GAMXO(K,L)
40  CONTINUE
WRITE (6,31)
31  FORMAT (//1X,'MECHANICAL STRAINS IN X-Y SYSTEM...LAYER...PHI...'
$          , 'R/R...EPS-X...EPS-THETA...EPS-R...GAMMA-X,THETA'//)
DO 41 L=1,J
DO 41 K=1,10
R(K) = RI(L) + (K-1)*T(L)/9
RR(K,L) = (R(K)-RI(1))/(RO(J)-RI(1))
WRITE (6,50) L,ANGLE(L),RR(K,L),EMX(K,L),EMO(K,L),EMR(K,L),
$          EMXO(K,L)
41  CONTINUE
WRITE (6,60)
60  FORMAT (//1X,'STRESSES IN X-Y SYSTEM...LAYER...PHI...R/R...'
$          , 'SIG-X...SIG-THETA...SIG-R...TAU-X,THETA'//)
DO 70 L=1,J
DO 70 K=1,10
WRITE (6,50) L,ANGLE(L),RR(K,L),SIGX(K,L),SIGO(K,L),SIGR(K,L),
$          TAU XO(K,L)
70  CONTINUE
WRITE (6,90)
90  FORMAT (//1X,'TOTAL STRAINS IN 1-2 SYSTEM...LAYER...PHI...R/R...'
$          , 'EPS-1...EPS-2...EPS-3...GAMMA-1,2'//)
DO 100 L=1,J
DO 100 K=1,10
WRITE (6,50) L,ANGLE(L),RR(K,L),EPS1(K,L),EPS2(K,L),EPS3(K,L),
$          GAM12(K,L)
100 CONTINUE
WRITE (6,120)
120 FORMAT (//1X,'STRESSES IN 1-2 SYSTEM...LAYER...PHI...R/R...'
$          , 'SIG-1...SIG-2...SIG-3...TAU-1,2'//)
DO 130 L=1,J
DO 130 K=1,10
WRITE (6,50) L,ANGLE(L),RR(K,L),SIG1(K,L),SIG2(K,L),SIG3(K,L),
$          TAU12(K,L)
130 CONTINUE
RETURN
END

C
SUBROUTINE GASJON (N,A,NRMAX,B,NBMAX)
IMPLICIT REAL*8(A-H,O-Z)
DIMENSION A(NRMAX,NRMAX),B(NBMAX,1),INDEX(62,2),IPVOT(62)
M=1
MM=1
1 DET=1.

```

```

DO 2 J=1,N
2 IPVOT(J)=0.
DO 14 I=1,N
T=0.
DO 5 J=1,N
IF (IPVOT(J).EQ.1) GO TO 5
DO 4 K=1,N
IF (IPVOT(K)-1) 3,4,17
3 IF (DABS(T).GE.DABS(A(J,K))) GO TO 4
IROW=J
ICOL=K
T=A(J,K)
4 CONTINUE
5 CONTINUE
IPVOT(ICOL)=IPVOT(ICOL)+1
IF (IROW.EQ.ICOL) GO TO 8
DET=-DET
DO 6 L=1,N
T=A(IROW,L)
A(IROW,L)=A(ICOL,L)
6 A(ICOL,L)=T
IF (MM.LE.0) GO TO 8
DO 7 L=1,M
T=B(IROW,L)
B(IROW,L)=B(ICOL,L)
7 B(ICOL,L)=T
8 INDEX(I,1)=IROW
INDEX(I,2)=ICOL
PIVOT=A(ICOL,ICOL)
DET=DET*PIVOT
A(ICOL,ICOL)=1.
DO 9 L=1,N
9 A(ICOL,L)=A(ICOL,L)/PIVOT
IF (MM.LE.0) GO TO 11
DO 10 L=1,M
10 B(ICOL,L)=B(ICOL,L)/PIVOT
11 DO 14 LI=1,N
IF (LI.EQ.ICOL) GO TO 14
T=A(LI,ICOL)
A(LI,ICOL)=0.
DO 12 L=1,N
12 A(LI,L)=A(LI,L)-A(ICOL,L)*T
IF (MM.LE.0) GO TO 14
DO 13 L=1,M
13 B(LI,L)=B(LI,L)-B(ICOL,L)*T
14 CONTINUE
IF (MM.EQ.1) RETURN
DO 16 I=1,N
L=N-I+1
IF (INDEX(L,1).EQ.INDEX(L,2)) GO TO 16

```

```

JROW=INDEX(L,1)
JCOL=INDEX(L,2)
DO 15 K=1,N
T=A(K,JROW)
A(K,JROW)=A(K,JCOL)
A(K,JCOL)=T
15 CONTINUE
16 CONTINUE
17 RETURN
END

C
C
SUBROUTINE FAIL(FL,J)
C
IMPLICIT REAL*8 (A-H,M-Z)
COMMON/OUT/ R(300),EPSX(10,30),EPS0(10,30),EPSR(10,30),
$ GAMX0(10,30),SIGX(10,30),SIG0(10,30),SIGR(10,30),TAUX0(10,30),
$ EPS1(10,30),EPS2(10,30),EPS3(10,30),GAM12(10,30),
$ SIG1(10,30),SIG2(10,30),SIG3(10,30),TAU12(10,30),
$ RR(10,30)
DIMENSION TS(30),F1S1(30),F2S2(30),F2S3(30),F11S1(30),F22S2(30),
$ F22S3(30),F66S6(30),F12S12(30),F12S13(30),F23S23(30)
C
READ(5,*) F1,F2,F11,F22,F66,F12,F23
WRITE(6,45)
45 FORMAT(//1X,'TSAI-WU'//)
30 DO 40 I=1,J
F1S1(I) = F1 * SIG1(5,I)
F2S2(I) = F2 * SIG2(5,I)
F2S3(I) = F2 * SIG3(5,I)
F11S1(I) = F11 * SIG1(5,I)**2
F22S2(I) = F22 * SIG2(5,I)**2
F22S3(I) = F22 * SIG3(5,I)**2
F66S6(I) = F66 * TAU12(5,I)**2
F12S12(I) = F12 * SIG1(5,I)*SIG2(5,I)
F12S13(I) = F12 * SIG1(5,I)*SIG3(5,I)
F23S23(I) = F23 * SIG2(5,I)*SIG3(5,I)
40 TS(I) = F1S1(I) + F2S2(I) + F2S3(I) + F11S1(I) + F22S2(I) +
$ F22S3(I) + F66S6(I) + F12S12(I) + F12S13(I) + F23S23(I)
WRITE(6,50) F1,F2,F11,F22,F66,F12,F23
50 FORMAT(8X,'F1',14X,'F2',13X,'F11',13X,'F22',13X,'F66',13X,
$ 'F12',13X,'F23'/1X,7D16.8)
WRITE(6,65)
65 FORMAT(//1X,'PLY',7X,'F1S1',12X,'F2S2',12X,'F2S3'//)
DO 80 I=1,J
80 WRITE(6,60) I,F1S1(I),F2S2(I),F2S3(I)
WRITE(6,110)
110 FORMAT(//1X,'PLY',5X,'F11S1S1',9X,'F22S2S2',9X,'F22S3S3',9X,
$ 'F66S6S6',9X,'F12S1S2',9X,'F12S1S3',9X,'F23S2S3'//)

```

```

DO 90 I=1,J
90 WRITE(6,60) I,F11S1(I),F22S2(I),F22S3(I),F66S6(I),F12S12(I),
  $ F12S13(I),F23S23(I)
  WRITE(6,120)
120 FORMAT(//1X,'PLY...FAILURE FRACTION,TS'/)
  DO 100 I=1,J
100 WRITE(6,60) I,TS(I)
60 FORMAT(1X,I3,7D16.8)
  RETURN
  END

C
C
C SUBROUTINE RESLTN
C
C THIS SUBROUTINE CALCULATES THE STRESS RESULTANTS NX, NO, NXO,
C MX, MO, AND MXO
C
  IMPLICIT REAL*8 (A-H,M-Z)
  COMMON /IN/ ANGLE(30),T(30),CB11(30),CB12(30),CB13(30),CB16(30),
  $ CB22(30),CB23(30),CB26(30),CB33(30),CB36(30),CB66(30),RO(30),
  $ RI(30),EPSTX(30),EPSTO(30),EPSTR(30),EPSTXO(30),DT,P,TW,J
  COMMON/SOLN/BC(62,62),ET(62,1),V(30),V1(30),V2(30),V3(30),V4(30),
  $ Z1(30),Z2(30),Z3(30),Z4(30),Z5(30),Z6(30),Z7(30)

C
  PI = 3.1415927
  NX1 = 0.
  NX2 = 0.
  NX3 = 0.
  NX4 = 0.
  NX5 = 0.
  NO1 = 0.
  NO2 = 0.
  NO3 = 0.
  NO4 = 0.
  NO5 = 0.
  NXO1 = 0.
  NXO2 = 0.
  NXO3 = 0.
  NXO4 = 0.
  NXO5 = 0.
  MX1 = 0.
  MX2 = 0.
  MX3 = 0.
  MX4 = 0.
  MX5 = 0.
  MO1 = 0.
  MO2 = 0.
  MO3 = 0.
  MO4 = 0.
  MO5 = 0.

```

```

MX01 = 0.
MX02 = 0.
MX03 = 0.
MX04 = 0.
MX05 = 0.
RM = (RO(J) + RI(1))/2.
DO 107 I=1,J
NX1 = NX1 + (CB11(I) + Z1(I)*Z4(I))*(RO(I)**2 - RI(I)**2)/2.
NX2 = NX2 + ((CB13(I) + Z4(I))*Z2(I) + CB16(I))*(RO(I)**3
$ - RI(I)**3)/3.
NX3 = NX3 + (CB12(I) + V(I)*CB13(I))*(RO(I)**V1(I) -
$ RI(I)**V1(I))*ET(2*I+1,1)/V1(I)
NX4 = NX4 + (CB12(I) - V(I)*CB13(I))*(RO(I)**V2(I) -
$ RI(I)**V2(I))*ET(2*I+2,1)/V2(I)
NX5 = NX5 + (CB11(I)*EPSTX(I) + CB12(I)*EPST0(I) + CB13(I)*
$ EPSTR(I) + CB16(I)*EPSTX0(I) - Z3(I)*Z4(I))*
$ (RO(I)**2 - RI(I)**2)/2.
N01 = N01 + (CB12(I) + Z7(I)*Z1(I))*(RO(I)-RI(I))
N02 = N02 + ((CB23(I) + Z7(I))*Z2(I) + CB26(I))*(RO(I)**2
$ - RI(I)**2)/2.
N03 = N03 + (CB22(I) + V(I)*CB23(I))*(RO(I)**V(I) -
$ RI(I)**V(I))*ET(2*I+1,1)/V(I)
N04 = N04 + (CB22(I) - V(I)*CB23(I))*(RO(I)**(-V(I)) -
$ RI(I)**(-V(I)))*ET(2*I+2,1)/(-V(I))
N05 = N05 + (CB12(I)*EPSTX(I) + CB22(I)*EPST0(I) + CB23(I)*
$ EPSTR(I) + CB26(I)*EPSTX0(I)-Z3(I)*Z7(I))*(RO(I) - RI(I))
NX01 = NX01 + (CB16(I) + Z5(I)*Z1(I))*(RO(I)**2 -
$ RI(I)**2)/2.
NX02 = NX02 + ((CB36(I) + Z5(I))*Z2(I) + CB66(I))*(RO(I)**3
$ - RI(I)**3)/3.
NX03 = NX03 + (CB26(I) + V(I)*CB36(I))*(RO(I)**V1(I) -
$ RI(I)**V1(I))*ET(2*I+1,1)/V1(I)
NX04 = NX04 + (CB26(I) - V(I)*CB36(I))*(RO(I)**V2(I) -
$ RI(I)**V2(I))*ET(2*I+2,1)/V2(I)
NX05 = NX05 + (CB16(I)*EPSTX(I) + CB26(I)*EPST0(I) + CB36(I)*
$ EPSTR(I) + CB66(I)*EPSTX0(I)- Z3(I)*Z5(I))*
$ (RO(I)**2 - RI(I)**2)/2.
MX1 = MX1 + (CB11(I) + Z4(I)*Z1(I))*(RO(I)**3 -
$ RI(I)**3)/3.
MX2 = MX2 + ((CB13(I) + Z4(I))*Z2(I) + CB16(I))*(RO(I)**4
$ - RI(I)**4)/4.
MX3 = MX3 + (CB12(I) + V(I)*CB13(I))*(RO(I)**V3(I) -
$ RI(I)**V3(I))*ET(2*I+1,1)/V3(I)
MX4 = MX4 + (CB12(I) - V(I)*CB13(I))*(RO(I)**V4(I) -
$ RI(I)**V4(I))*ET(2*I+2,1)/V4(I)
MX5 = MX5 + (CB11(I)*EPSTX(I) + CB12(I)*EPST0(I) + CB13(I)*
$ EPSTR(I) + CB16(I)*EPSTX0(I) - Z3(I)*Z4(I))*
$ (RO(I)**3 - RI(I)**3)/3.
M01 = M01 + (CB12(I) + Z7(I)*Z1(I))*(RO(I)**2 -
$ RI(I)**2)/2.

```

```

M02 = M02 + ((CB23(I) + Z7(I))*Z2(I) + CB26(I))*(RO(I)**3
$ - RI(I)**3)/3.
M03 = M03 + (CB22(I) + V(I)*CB23(I))*(RO(I)**V1(I) -
$ RI(I)**V1(I))*ET(2*I+1,1)/V1(I)
M04 = M04 + (CB22(I) - V(I)*CB23(I))*(RO(I)**V2(I) -
$ RI(I)**V2(I))*ET(2*I+2,1)/V2(I)
M05 = M05 + (CB12(I)*EPSTX(I) + CB22(I)*EPSTO(I) + CB23(I)*
$ EPSTR(I) + CB26(I)*EPSTXO(I) - Z3(I)*Z7(I))*
$ (RO(I)**2 - RI(I)**2)/2.
MX01 = MX01 + (CB16(I) + Z5(I)*Z1(I))*(RO(I)**3 -
$ RI(I)**3)/3.
MX02 = MX02 + ((CB36(I) + Z5(I))*Z2(I) + CB66(I))*(RO(I)**4
$ - RI(I)**4)/4.
MX03 = MX03 + (CB26(I) + V(I)*CB36(I))*(RO(I)**V3(I) -
$ RI(I)**V3(I))*ET(2*I+1,1)/V3(I)
MX04 = MX04 + (CB26(I) - V(I)*CB36(I))*(RO(I)**V4(I) -
$ RI(I)**V4(I))*ET(2*I+2,1)/V4(I)
107 MX05 = MX05 + (CB16(I)*EPSTX(I) + CB26(I)*EPSTO(I) + CB36(I)*
$ EPSTR(I) + CB66(I)*EPSTXO(I) - Z3(I)*Z5(I))*
$ (RO(I)**3 - RI(I)**3)/3.
NX = (NX1*ET(1,1) + NX2*ET(2,1) + NX3 + NX4 - NX5)/RM
NO = (NO1*ET(1,1) + NO2*ET(2,1) + NO3 + NO4 - NO5)
NXO = (NXO1*ET(1,1) + NXO2*ET(2,1) + NXO3 + NXO4 - NXO5)/RM
MX = (MX1*ET(1,1) + MX2*ET(2,1) + MX3 + MX4 - MX5)/RM - NX*RM
MO = (MO1*ET(1,1) + MO2*ET(2,1) + MO3 + MO4 - MO5) - NO*RM
MXO = (MXO1*ET(1,1)+MXO2*ET(2,1)+MXO3+MXO4-MXO5)/RM - NXO*RM
WRITE(6,106)
106 FORMAT(//1X,'STRESS RESULTANTS'//)
WRITE(6,108) NX,NO,NXO,MX,MO,MXO
108 FORMAT(7X,'NX',14X,'NO',14X,'NXO'/3D16.8/3D16.8/7X,'MX',14X,'MO',
$ 14X,'MXO'//)
RETURN
END

```

<b>BIBLIOGRAPHIC DATA SHEET</b>	<b>1. Report No.</b> CCMS-87-04, VPI-E-87-3	<b>2.</b>	<b>3. Recipient's Accession No.</b>
<b>4. Title and Subtitle</b> Stresses and Deformations in Angle-Ply Composite Tubes		<b>5. Report Date</b> March 1987	
<b>7. Author(s)</b> C. Q. Rousseau, M. W. Hyer, S. S. Tompkins		<b>6.</b>	
<b>9. Performing Organization Name and Address</b> Virginia Polytechnic Institute and State University Engineering Science and Mechanics Blacksburg, Virginia 24061		<b>8. Performing Organization Rept. No.</b> VPI-E-87-3	
<b>12. Sponsoring Organization Name and Address</b> National Aeronautics and Space Administration Langley Research Center Hampton, Virginia 23665		<b>10. Project/Task/Work Unit No.</b>	
		<b>11. Contract/Grant No.</b> NAG-1-343	
		<b>13. Type of Report &amp; Period Covered</b>	
<b>15. Supplementary Notes</b>		<b>14.</b>	
<b>16. Abstracts</b> The objective of this study was to investigate, both experimentally and analytically, the stresses and deformations in angle-ply composite tubes subjected to axisymmetric thermal loading. For the theoretical portion a generalized plane strain elasticity analysis was developed. The analysis included mechanical and thermal loading, and temperature-dependent material properties. Using the elasticity analysis and a temperature range of 116 K to 450 K, stress levels were found to be high for the specific designs considered, compared to material failure levels. In addition, the use of temperature-dependent material properties was found to have a significant effect on the predicted stresses and deformations. The elasticity analysis was also used to study the effect of including a thin metallic coating on a graphite-epoxy tube. The stresses in the coatings were found to be quite high, exceeding the yield (continued on next page)			
<b>17. Key Words and Document Analysis. 17a. Descriptors</b> angle-ply tubes, graphite-epoxy tubes, thermo-mechanical elasticity solution, cylindrically anisotropic elasticity solution, temperature-dependent material properties, protective coatings, thermally induced stresses, thermal expansion, thermally-induced twist, LVDT			
<b>17b. Identifiers/Open-Ended Terms</b>			
<b>17c. COSATI Field/Group</b>			
<b>18. Availability Statement</b> unlimited		<b>19. Security Class (This Report)</b> UNCLASSIFIED	<b>21. No. of Pages</b> 243
		<b>20. Security Class (This Page)</b> UNCLASSIFIED	<b>22. Price</b>

## Abstracts (cont.)

stress of aluminum. An important finding in the analytical studies was the fact that even tubes with a balanced-symmetric lamination sequence exhibited shear deformation, or twist. The radial location of an off-axis ply was found to influence its effect on the overall torsional tube response. For the experimental portion an apparatus was developed to measure torsional and axial response in the temperature range of 140 K to 360 K. Eighteen specimens were tested, combining three material systems, eight lamination sequences, and three off-axis ply orientation angles. For the twist response, agreement between analysis and experiment was found to be good. The axial response of the tubes tested was found to be greater than predicted by a factor of three. As a result of the study it is recommended that the thermally-induced axial deformations be investigated further, both experimentally and analytically.